Crystal chemistry and seismic wavespeeds of dense oxyhydroxides: hydrogen transport in Earth's lower mantle

Thesis by
Benjamin Thomas Strozewski

In Partial Fulfillment of the Requirements for the
Degree of
Doctor of Philosophy

Caltech

CALIFORNIA INSTITUTE OF TECHNOLOGY
Pasadena, California

2025
Defended March 5, 2025

ACKNOWLEDGEMENTS

"You can swim all day in the Sea of Knowledge and still come out completely dry.
Most people do."
- Norton Juster, *The Phantom Tollbooth*

This thesis represents a link in a chain of pursuits in my life to satisfy the desire to know things, a desire imbued upon me by numerous mentors, role models, and loved ones who I have been fortunate to have in my life. I hope it is also a useful scientific contribution.

The work in this thesis was supported by the National Science Foundation's (NSF) Collaborative Studies of the Earth's Deep Interior (CSEDI) under EAR-2009935. Portions of this work were performed at sectors 3 and 13-GeoSoilEnviroCARS of the Advanced Photon Source (APS) and the National Synchrotron Light Source II, United States Department of Energy (DOE) facilities. Use of the APS is supported by the U.S. DOE Office of Science (DE-AC02- 06CH11357). Sector 3 operations are partially supported by COMPRES (EAR-1661511). GeoSoilEnviroCARS is supported by NSF – Earth Sciences (EAR-1634415) and DOE-Geosciences (DE-FG02-94ER14466). Use of the COMPRES-GSECARS gas loading system was supported by COMPRES under NSF Cooperative Agreement EAR-1606856. The experiments described in this thesis would have been impossible without the support of beamline staff at these facilities: Thomas Toellner, Barbara Lavina, and Jiyong Zhao at sector 3 of the APS, Stella Chariton and Vitali Prakapenka at sector 13, and Zhenxian Liu at NSLS-II. Thank you to you all.

At Caltech, I have been fortunate to have had wonderful advisors who have given me not only the specific expertise required to complete this thesis, but more importantly taught me many things about the scientific endeavor. First and foremost, I extend my deepest gratitude to my thesis advisor, Jennifer Jackson. These last five and change years have at times been both incredibly fun and also challenging. You have pushed me to become a detail oriented and thorough experimentalist while never losing sight of the larger questions about the Earth that we are trying to answer. Your enthusiasm for what we do is infectious and it is impossible not to respect how willing you are to dive into any scientific topic within geoscience or without. Even during the some of the challenging periods in my time here at Caltech, and especially during crises such as the global pandemic or the fires in Los Angeles

County this winter, I have always felt supported and could ask nothing more of an advisor. I came to geosciences from a physics background and had a lot to learn about the Earth, especially its deepest regions, but you motivated my passion to tackle some of the enigmas of our planet and broaden my knowledge outside of our own niche.

To the other members of my committee, I am extremely grateful that you allowed me to do the same. Zach, thank you for taking me in to your group with essentially no knowledge of seismology in my first year. Through working together, I became much more equipped to have a complete understanding of our field and greatly appreciate everything I learned from you both as a researcher, student, and TA. Mike, you have always showed an inspiring interest in all the different areas of our wider field, including in the experimental side of geophysics. It has been both motivating and encouraging to me that you are humble and curious enough to dive into these topics and ask genuine, insightful questions. George, I always enjoyed coming over to Arms to shoot some photons at my samples with you. Your expertise and mentorship, especially in using Raman and infrared spectroscopy, were invaluable in my analyses. Not only did I learn much about the specific techniques we used, it was also great to soak up some of your accumulated lab wisdom and to share your gung ho attitude towards experimental science.

My time at Caltech could not have been successful without my labmates and the other members of the Jackson lab group. I am extremely fortunate to have been part of a group that was so helpful, supportive, and fun. In particular, I am incredibly grateful to Johannes Buchen, who mentored me throughout my first and second years in understanding how to put together a diamond anvil cell and conduct successful synchrotron experiments. DAC preparation is usually frustrating in the best of circumstances but your patience and diligence in preparing experiments was something that I will carry with me through the rest of my time in research and in science in general. Wolfgang — your expertise has been invaluable in obtaining the results of this thesis and your willingness to help at every stage was infectious in the group. Vasilije — you always provided such an uplifting and optimistic spirit in our group. As anyone who has done synchrotron experiments knows, these are vital characteristics to keep pushing through uncertainty and you were a wonderful role model in that way, as well as being a very productive scientist. Olivia — you were always such a steady and calm presence in the lab and out. Your generosity with your time to help and mentor others molded and maintained our positive, cooperative lab culture. I appreciate all your help with my own experiments, watching the resonant counts roll in through the wee hours of the morning. Cijin — sharing an office with you and working together in the group has made my time at Caltech that much more enjoyable. It is cathartic to share the lows and challenges of the PhD journey with someone who intimately understands them and great to celebrate the successes with someone who knows all the work that went into making things happen.

There are innumerable other people that I was so fortunate to meet here and who I am proud to count among my close friends. To all of you: Jimmy, Maria, Ojashvi, Jack, Valeria, Caifeng, Victor, Alba, Will, Eli, Auden, and everyone else in the seismo lab, the time spent outside of the department has kept me sane and centered. Especially to Jimmy, Maria, and Ojashvi, with whom I have shared much of this PhD journey: your friendship has been truly invaluable.

It is impossible to put into words my gratitude to my family and to my parents, who taught me that nothing is more useful than knowledge and that nothing worth doing is easy. You have given me everything I need throughout my life and it is due to your example that I have been motivated to strive to accomplish everything that I am capable of. You never discouraged me from my goals and spared no effort to help me accomplish them, whether it was training me for soccer in the backyard or indulging my interest in that random astrophysics textbook. Most importantly, you taught me to love to learn, for which I am eternally grateful. To my siblings, Kate and Andy, growing up with you formed my disposition as much as anything in my life. I am lucky to have you in my life and proud to be your brother.

Finally, to my fiancée Jess: you have been there for me for so long and through so much. It hasn't been easy being apart but I could not have done it with anyone else. You inspire me every day to find joy in what I do. I love you so much and am filled with excitement for the rest of our lives together.

ABSTRACT

In this thesis, I perform a thorough investigation of the electronic and elastic properties of the dense oxyhydroxide (Al,Fe)-phase H ($Al_{0.84}Fe^{3+}{}_{0.07}Mg_{0.02}Si_{0.06}OOH$). This phase represents a realistic composition in a solid solution which has been hypothesized to carry 'water', in the form of hydrogen, to the lowermost depths of Earth's mantle. Its propensity for water storage and elastic properties are affected by hydrogen bond symmetrization and a high-low spin crossover of Fe^{3+} atoms, respectively. In order to determine changes in hydrogen bonding environment, I use synchrotron infrared spectroscopy and Raman spectroscopy, which identify O-H vibrational modes in the crystal structure and changes in their frequencies with pressure. These vibrational modes indicate that (Al,Fe)-phase H likely stores additional hydrogen as defects and that hydrogen bonds are disordered at ambient pressure due to the substitution of cations of different valence states. I find that hydrogen atoms become dynamically disordered across sites at 10 GPa and conclude that hydrogen bond symmetrization in (Al,Fe)-phase H takes place at 35 GPa. I use powder X-ray diffraction to constrain the equation of state of this phase, providing fundamental constraints on its incompressibility and density at high pressures. I complement this equation of state with study of the electronic environment around the Fe atoms via nuclear resonant forward scattering in order to constrain the spin crossover of Fe^{3+} atoms between 48 and 63 GPa. I use nuclear resonant inelastic X-ray scattering measurements to determine the seismic wavespeeds of (Al,Fe)-phase H to 120 GPa, the base of the lowermost mantle. The measured seismic wavespeeds are incorporated into whole-rock models which suggest that (Al,Fe)-phase H contributes to seismic heterogeneity in the mid-mantle and that hydrous metabasalt containing (Al,Fe)-phase H could contribute to seismic anomalies associated with the edges of large, low, shear velocity provinces in the lowermost mantle as it heats during descent in the lowermost mantle. The combined results of this thesis elucidate a complete compression pathway during transport of a dense oxyhydroxide into the lower mantle in the context of changes in its electronic and elastic properties. I offer several observables which may be used to detect the presence of this phase in subducted metabasalt and comment on the implications for hydrogen storage in the deep Earth.

PUBLISHED CONTENT AND CONTRIBUTIONS

Strozewski, Benjamin T., Zhenxian Liu, George R. Rossman, Wolfgang Sturhahn, Johannes Buchen, and Jennifer M. Jackson (2025a). "Vibrational spectroscopy of dense oxyhydroxides: hydrogen bond disorder and symmetrization at high pressure ". In: *American Mineralogist [submitted].*
B.S performed the ambient-pressure experimental measurements, conducted the formal analysis, and wrote the original manuscript with J.M.J supervision.

Strozewski, Benjamin T., Ojashvi Rautela, Johannes Buchen, Wolfgang Sturhahn, Takayuki Ishii, Itaru Ohira, Olivia Pardo, Jiyong Zhao, Thomas S Toellner, and Jennifer M Jackson (2025b). "Sound Velocities of (Al,Fe)-phase H and the seismic visibility of dense oxyhydroxides in Earth's lower mantle ". In: *Physics of Earth and Planetary Interiors [submitted].*
B.S performed the experimental measurements, conducted the formal analysis, and wrote the original manuscript with J.M.J supervision.

Strozewski, Benjamin, Johannes Buchen, Wolfgang Sturhahn, Takayuki Ishii, Itaru Ohira, Stella Chariton, Barbara Lavina, Jiyong Zhao, Thomas S Toellner, and Jennifer M Jackson (2023). "Equation of State and Spin Crossover of (Al,Fe)-Phase H". In: *Journal of Geophysical Research : Solid Earth*, pp. 1–20. DOI: `10.1029/2022JB026291`.
B.S prepared the experiments, conducted the formal analysis, and wrote the original manuscript with J.M.J supervision.

TABLE OF CONTENTS

LIST OF ILLUSTRATIONS

LIST OF TABLES

NOMENCLATURE

Core-mantle boundary (CMB). The boundary between Earth's silicate mantle and predominantly Fe core 2900 km below the Earth's surface.

Geotherm. A thermal profile in the Earth which describes how temperature changes with increasing pressure and depth.

Hydrostatic pressure. A state in which the stress applied to a material is uniform across its surface area.

Large, low shear velocity province. Basal mantle structures consistently observed in sesmic imaging with up to 1200 km height and 1000 km spatial extent. Best characterized by their low shear velocity compared to the surrounding mantle.

Late Veneer. The delivery of volatile material to Earth late in the accretion process and after core formation.

Lithosphere. The rigid part of the Earth composed of the crust and a portion of the upper mantle.

Metabasalt. Basaltic rock which has undergone metamorphism due to heat and pressure.

Mid-Ocean Ridge Basalt. A "standard" basaltic rock produced from partial melting of the upper mantle and exhumed at a mid-ocean ridge.

Mineral. An inorganic solid which occurs naturally, has a defined crystal structure, and has a defined composition.

Nominally Anhydrous Minerals. Minerals which do not contain hydrogen in their crystal structure but may nevertheless store hydrogen as defects or in vacancies.

Ocean Island Basalt (OIB). A basaltic rock exhumed from the Earth's mantle away from a mid-ocean ridge. Generally thought to be sourced from a plume, potentially deeper in Earth's mantle than a mid-ocean ridge basalt.

Oxyhydroxide. An inorganic solid whose composition includes OOH and the O-H--O bonding unit.

Phase. An inorganic solid with a defined crystal structure and a defined composition but *not* yet confirmed to occur naturally.

Siderophile. "Iron-loving" elements which are expected to partition into the core rather than the silicate mantle during differentiation of the Earth.

Slab. A part of a tectonic plate that descends into the mantle, generally due to its lower temperature and consequently higher density.

Solid solution. A mixture of two solids in which variable composition is made possible by exchange of cations.

Spin crossover. A reassignment of electrons to different orbitals, changing the net spin of an atom's electrons. In oxides, net spin of transition metals is typically reduced at high pressure.

Ultralow velocity zones. Basal mantle structures less than 100 km in size characterized by drastic ($> 10\%$) decreases in seismic velocity relative to the surrounding mantle.

Chapter 1

INTRODUCTION

1.1 The importance of water in geophysical processes

Earth is a terrestrial planet with 71% of its surface covered by water. The importance of H_2O in all its forms cannot be overstated. Earth has avoided Mars' fate of drying out over geologic time (e.g. Scheller et al., 2021) such that water still significantly impacts processes on the planet. On Earth's surface, glaciers have carved out steep terrains and rivers carry the resulting sediment to the sea. Developments in our understanding of the rheology of glacial ice have necessitated increasingly thorough descriptions of processes involved in deformation of solid H_2O (Ranganathan and Minchew, 2024; Herman, 2022). Draining or filling of pore spaces in rocks — in some cases by water — influences the development of shear zones (Heimisson et al., 2021) while fluid transport in the crust can lead to swarm-like behavior of earthquakes (Ross and Cochran, 2021). Water can be important in controlling postseismic deformation (Fialko, 2004) and the cycle of earthquakes in subduction zones (Dal Zilio and Gerya, 2022). When hydrous minerals exsolve their water as they are subducted, they may encourage seismicity by embrittlement of the rock (Omori et al., 2004; Dobson et al., 2002) and cause fluid to rise bouyantly towards the surface, resulting in arc volcanism (e.g. Turner and Langmuir, 2022; Blackwell et al., 1982). It is therefore clear that the properties of water and its storage in rocks or minerals are an important consideration in many problems within geophysics.

A perhaps less obvious locale for water is in Earth's deep interior. The deep Earth carries the largest uncertainty in terms of hydrogen storage: conservative estimates imply that Earth's lower mantle and core could store between 0.5 and 16 times the total mass of Earth's oceans (see review by Peslier et al., 2017), potentially dwarfing the amount of water in surficial reservoirs. Some of this H may participate in whole-mantle convection (e.g. Spasojevic et al., 2010) while some may partition into the core and contribute to explaining the observed density and seismic velocities, which cannot be obtained under the assumption that the core is composed solely of an Fe-Ni alloy (Poirier, 1994; Stevenson, 1981). However, substantial uncertainties remain regarding the partitioning of H at core-mantle boundary conditions as well as on the light element content of the core, which may contain H, Si, S, or C (Hirose et al., 2013; Allégre et al., 1995). The hydrogen budget of the lower mantle depends critically on the water storage capacities of constituent minerals (Hirschmann, 2006). However, it is challenging to study the hydration of rocks in the lower mantle as these rocks will be chemically processed (i.e. affected by temperature and pressure) before partially melting if they are exhumed at Earth's surface. Therefore, indirect measurement techniques such as seismology are invaluable tools to ascertain the chemical composition and hydration of the lower mantle. This thesis examines the crystal chemistry and seismic wavespeeds of the dense oxyhydroxide (Al,Fe)-phase H ($Al_{0.84}Fe^{3+}{}_{0.07}Mg_{0.02}Si_{0.06}OOH$) and the ($\delta$-AlOOH)-($MgSiO_2(OH)_2$)-($\epsilon$-FeOOH) solid solution. I situate these measurements within the context of constraints from seismology to ask the question: if highly hydrous minerals have been subducted into Earth's lower mantle, would we know?

1.2 Water in Earth's interior

To understand the full picture of hydrogen in Earth's interior, we would like to know how much we have and where it is. A reasonable understanding of hydrogen content in the Earth today requires informed estimates on the total amount of hydrogen in the Earth when it was finished accreting material and differentiating into a mantle and core. There are broadly two ways that hydrogen can be delivered to and sequestered within our planet: during planetary accretion (in small, aggregating planetisimals or by sucking in nebular gas) or in the late stages of accretion and differentiation by impact material. That is, some H could be present in the small planetismals which aggregated and coalesced at the beginning of Earth's formation or within asteroids which impacted the nearly-accreted Earth and contributed their hydrogen, as well as other elements (Albarède, 2009; Halliday and Canup, 2023; Gu et al., 2024). The delivery of volatile elements in chondritic asteroids after core formation is known as the "late veneer" and in part seeks to explain the higher than expected concentration of siderophile ("iron-loving") elements in Earth's mantle, which seemingly should have been removed during core formation (review by Walker, 2009). Observations that achondrite meteorites which would have formed Earth's building blocks are dry (< 1000 ppm H_2O; Newcombe et al., 2023) also seem to require a later delivery of volatile-rich material. Studies of the Mn-Cr isotope system (Trinquier et al., 2008; Qin et al., 2010), U-Pb system (Albarede et al., 2013; Ballhaus et al., 2013), and I-Pu system (Liu et al., 2023) suggest that Earth accreted dry, from planetismals with very little water. Observations that relic, differentiated planetismals are dry (Newcombe et al., 2023) and that a late delivery of volatile-rich material to the Earth could explain the higher $^{182}W/^{184}W$ of the moon (Kruijer et al., 2015) support the need for a late veneer. However, Piani et al. (2020) suggest that hydrated enstatite chondrites as part of accreting material could supply 3.4 to 23.1 ocean masses of water ($1.4x10^{21}$ kg), enough to match low to intermediate estimates of Earth's total hydrogen budget. Study of noble gases (Mukhopadhyay, 2012; Mukhopadhyay and Parai, 2019) imply that volatile accretion was heterogeneous and that signatures of this heterogeneous delivery remain in Earth's interior today. Constraints on Earth's current hydrogen budget are inextricable from initial estimates and planetary formation models, as well as from models of mantle flow and H cycling by plate tectonics today. The more H is stored in the lower mantle, the greater the need for incorporation of hydrated material into the Earth, either during accretion or as part of a late veneer. If H is preferentially delivered to certain regions of Earth's lowermost mantle through geologic time, this may contribute to preservation of heterogenous volatile concentrations or sequester surficial hydrogen in deep reservoirs. Indeed, ocean island basalts (OIBs) sourced from the lower mantle can be more hydrogen-rich (e.g. Simons et al. (2002), review by Bolfan-Casanova (2005)), than mid-ocean ridge basalts (MORBs), suggesting that the deep mantle may either preserve a primordial signature of hydrogen-rich material or a volatile enrichment attributable to subducted material.

The water storage capacities of nominally anyhdrous minerals (NAMs) and the presence of hydrous minerals are affected by pressure and temperature. The *P-T* path of a subducting slab therefore governs to what depths within Earth's mantle hydrogen can be transported in subducted crust (e.g., Barber et al. (2022)), which is more hydrous than the depleted lithosphere (Hirschmann, 2006). The mantle transition zone has generally been considered to be 'wet' (up to 20,000 ppm H_2O or 2 wt.%) relative to the upper (100-200 ppm H_2O) and lower mantle (100-2,000 ppm H_2O), a paradigm (see review Ohtani (2020)) based in part on the water storage capacities of high-pressure olivine polymorphs and the apparent lack of hydrous phases stable at conditions of the lower mantle (Bercovici and Karato, 2003; Karato, 2011). Inclusions in superdeep (> 410 km depth) diamonds support the understanding that the base of the mantle transition zone contains up to 2 wt. % H_2O and is likely a region of metasomatism within Earth's mantle (Gu et al., 2022; Pearson et al., 2014; Tschauner et al., 2018; Wirth et al., 2007).

Most of the hydrous phases formed in subducted lithosphere (e.g. serpentine) are expected to dehydrate within the upper 200 km of Earth's mantle (Ulmer and Trommsdorff, 1995; Kawamoto, 2006), contributing to arc volcanism above a subducted slab.

Dense hydrous magnesium silicate phases are stable at higher pressure and temperatures but are nevertheless expected to dehydrate along typical geotherms in the upper mantle or transition zone (Bolfan-Casanova, 2005). However, recently synthesized hydrous phases such as δ-AlOOH ("delta phase"), $MgSiO_2(OH)_2$ ("phase H"), and ϵ-FeOOH have been observed to be stable at temperatures and pressures relevant to the lowermost mantle and form from the components of hydrous metabasalts (Liu et al., 2019). In particular, a natural equivalent of δ-AlOOH has garnered interest as a candidate carrier of hydrogen to the deep mantle (Ohtani, 2020; Ohtani et al., 2018) due to its stability at temperatures potentially as high as those of the ambient mantle near the core-mantle boundary (Sano et al., 2008; Terasaki et al., 2012).

Recent findings suggest that stishovite (Lin et al., 2020) and other rutile-structured phases may contain up to several wt.% water, even at core-mantle boundary conditions (Tsutsumi et al., 2024), possibly via the occupation of an oxygen vacancy by a hydrogen atom (Palfey et al., 2021) or, in the case of Al-free stishovite, the charge balancing of a Si vacancy by four OH groups (Palfey et al., 2023). The coupled substitution of Al^{3+} and H^+ for Si^{4+} likely enhances the water storage capacity of stishovite (Ishii et al., 2022a; Takaichi et al., 2024). However, it was suggested that stishovite remains dry and alumina depleted when an Al-rich hydrous mineral (δ-AlOOH) coexists (Ishii et al., 2024), implying that such a hydrous mineral is an important carrier of water as long as it is thermally stable. Indeed, recent synthesis experiments have revealed δ-AlOOH to be an endmember component of the (δ-AlOOH)-($MgSiO_2(OH)_2$)-(ϵ-FeOOH) solid solution (Komatsu et al., 2011; Liu et al., 2019; Ohira et al., 2014). Therefore, studying the effect of compositional variation in this system will be necessary to understand the seismic signature of subducted lithosphere and distinguish between different hypotheses concerning the origin of seismic reflectors and structure within the lower mantle (e.g., Panero et al. (2020)).

1.3 Lower mantle heterogeneity

While it is often challenging to obtain precise constraints on density and seismic wave speeds of structures in the lower mantle, there exists clear heterogeneity across a wide range of depths (Ritsema et al., 2020). It is now known that portions of tectonic plates that sink into the mantle, often referred to as slabs, can continue descending through the mantle transition zone into the lower mantle (Van Der Hilst et al., 1997; Meer et al., 2018; Tan et al., 2002; Schumacher and Thomas, 2016). Observations and modeling of seismic waveforms have revealed small scale heterogeneity in the mid-lower mantle (600-1500 km depth) that scatters seismic waves (Mao et al., 2022; Kaneshima, 2016; Ritsema et al., 2020; Yuan et al., 2021; Bentham and Rost, 2014). Despite difficulties in determining seismic velocity perturbations, the period of observed scattered waves ($\approx$ 1 s) indicates that such structures are likely thin ($\approx$ 10 km), suggesting the possibility that they are subducted oceanic crust. Oceanic crust also contains SiO_2 as stishovite, which undergoes the post-stishovite phase transition across a broad range of pressures (40-80 GPa; 1000-2000 km depth), depending on its Al and H content (Umemoto et al., 2016; Zhang et al., 2022; Lakshtanov et al., 2007; Wang et al., 2023; Nomura et al., 2010). Therefore, the pressure and temperature of this transition in the Earth will also be affected by the formation of hydrous phases. For example, Liu et al. (2019) found that when dense oxyhydroxides form in subducted basalt, SiO_2 contains very little Al or H. This phase transition may contribute to decreases in seismic velocity, particularly V_S, responsible for the scattering of seismic waves. However, subducted oceanic crust may scatter seismic waves due to its intrinsic differences in velocity relative to the surrounding pyrolitic mantle (Mao et al., 2022), which could be enhanced by hydrous phases. At the moment, uncertainties on the precise velocity anomalies associated with this scattering make precise conclusions about the mineralogy of these structures difficult. As seismic observations and mineral physics experiments advance, it is critical to understand how likely mineralogies in subducted crust will affect its seismic signature in the lower mantle, including the post-stishovite phase transition as well as the spin crossovers in minor phases highlighted in this work.

In the lowermost mantle, the D" region (generally 200 km above the core-mantle boundary) varies laterally in thickness and seismic velocity (Sun et al., 2016) and may host deformation-induced seismic anisotropy in some regions (Pisconti et al., 2023; Creasy et al., 2017). Ultralow velocity zones (ULVZs) 100 km or less in size and with decreases in V_P up to 10% and in V_S up to 50% (Jackson and Thomas, 2021) have been frequently observed in the D" region (e.g. Lai et al., 2022; Kim et al., 2020; Wolf et al., 2024) and in some cases suggested to be related to slab debris. In some areas, ULVZs cluster around two large, low shear velocity provinces (LLSVPs) (e.g. Hosseini et al., 2020; Koelemeijer et al., 2016, reviews by McNamara, 2019; Garnero et al., 2016): enormous structures possibly up to 1200 km in height from the core-mantle boundary and on the order of 1000 km in spatial extent generally characterized by shear-wave speeds 1 to 2% lower than those predicted by 1-D Earth models in this region. Large, low shear velocity provinces observed in seismic imaging could represent compositional differences (Hernlund and Houser, 2008; Ni et al., 2002; Ni and Helmberger, 2003) or a bundle of plumes blurred by tomography (e.g. Schuberth and Bunge, 2009; French and Romanowicz, 2015) and the precise origin of these structures remains a topic of active debate.

The geographical correlation between some ULVZs, LLSVPs, and subducted slabs seem to imply a dynamic relationship (Sun et al., 2019; Li et al., 2022) as the subducted slab may push a ULVZ into the boundary of the LLSVP. Impingement of a subducted slab on the edge of a large, low shear velocity province also implies that subducted oceanic crust can, at least in certain scenarios, be transported to the core-mantle boundary. Dense, cold crust would certainly influence the development of lowermost mantle structures (Jones et al., 2020) and could potentially accumulate over geologic time. The consequently large temperature gradient and diverse mineralogy in this region could also regulate Fe-H exchange across the core-mantle boundary. Even small amounts of Fe enrichment in the lowermost mantle, for example in Fe-rich (Mg,Fe)O, could explain the seismic velocities of ultralow velocity zones (Bower et al., 2011; Wicks et al., 2010; Chen et al., 2012; Wicks et al., 2017; Dobrosavljevic et al., 2019). Experiments have posited that H_2O — exsolved from subducted hydrous minerals — could react with Fe from the core to form hydrous iron-dioxide FeO_2H_x $(0 < x < 1)$ (Nishi et al., 2017; Hu et al., 2017). Kawano et al. (2024) found that iron-water reactions at the CMB would produce Fe-enriched bridgmanite, FeO wustite, and FeH. Despite the disagreement with Hu et al. (2017) in the reaction products, this study also observes that Fe-enrichment in the lowermost mantle could contribute to the formation of ULVZ or a dense, several km thick layer at the base of the mantle. Indeed, Russell et al. (2023) find that the density distribution in the lowermost mantle is best explained by a 1-3 km thick dense layer. Ho et al. (2023) build upon the experimental work of Dobrosavljevic et al. (2023) to demonstrate that in the lowermost mantle, FeO is in a quantum-critical state which could explain elevated electrical conductivities observed in this region and in ULVZs. It is therefore clear that Fe-enrichment is an intriguing hypothesis for several enigmatic features of this complex region. However, a better understanding of water (i.e. hydrogen) transport within the lower mantle is necessary to understand whether Fe-H reactions could lead to Fe enrichment in the lowermost mantle.

1.4 Thesis overview

Hydrogen and water are important in many areas of geophysics and their effects can be seen in every layer of the Earth system, from the atmosphere to the core. This thesis focuses on hydrogen transport within the lower mantle and how we might use geophysical observations, most notably seismology, to ascertain whether hydrogen is carried into the lower mantle by hydrous phases. This problem is tricky as we must rely on indirect observing techniques which often yield non-unique solutions. It is therefore critical to understand precisely the seismic velocities and crystal chemistry of materials in the deep Earth as they ultimately control how seismic waves pass through the deep interior. To these ends, I have conducted experiments on the (δ-AlOOH)-($MgSiO_2(OH)_2$)-(ϵ-FeOOH) solid solution with a particular focus on (Al,Fe)-phase H: ($Al_{0.84}Fe^{3+}{}_{0.07}Mg_{0.02}Si_{0.06}OOH$), with the goal of fully understanding its crystal chemistry and effects on observable geophysical properties of Earth's lowermost mantle.

In Chapter 2, I use infrared and Raman spectroscopy techniques to explore the hydrogen bonding environment of (Al,Fe)-phase H and δ-$Al_{0.87}Fe_{0.13}OOH$ to 42 GPa. Hydrogen bonds in dense oxyhydroxides are likely to become symmetric at high pressure. Symmetric hydrogen bonds are short, strong, and likely necessary to prevent dehydration of these phases at the high temperatures of the lowermost mantle. These measurements clarify that hydrogen bonds in (Al,Fe)-phase H are occupationally disordered at ambient pressure due to the presence of cations of different valence states. That is, there are multiple, defined sites of the H atoms which cannot be discerned from X-ray diffraction methods but are illuminated using vibrational spectroscopy. In both (Al,Fe)-phase H and δ-$Al_{0.87}Fe_{0.13}OOH$, dynamic disorder of hydrogen atoms in the O-H--O bonding unit occurs at approximately 10 GPa. Softening of O-H stretching modes indicate that hydrogen bond symmetrization likely occurs in (Al,Fe)-phase H at approximately 35 GPa.

Chapter 3 describes the results of X-ray diffraction measurements to 120 GPa, which constrain the equation of state of this dense oxyhydroxide. The equation of state is a critical parametrization for determining the density and bulk seismic velocity of this material at high pressure, as well as its incompressibility. Chapter 3 also presents the results of synchrotron Mössbauer spectroscopy (SMS) measurements which constrain the electronic environment around Fe atoms. These measurements compliment the equation of state to identify a Fe^{3+} spin crossover in (Al,Fe)-phase H between 48 and 63 GPa, which leads to a drastically reduced bulk incompressibility and bulk seismic velocity in this pressure region.

In Chapter 4, I present results from nuclear resonant inelastic X-ray scattering measurements. This technique measures the partial phonon density of states — the set of vibrational modes in the crystal structure related to the Fe atoms —

from which the P-wave and S-wave velocities are determined. The results of these measurements are incorporated into whole-rock models of seismic velocities in the lowermost mantle, in collaboration with Ojashvi Rautela, a fellow graduate student at Caltech. The results of these models indicate that the presence of (Al,Fe)-phase H in subducted metabasalt could contribute to scattering of seismic waves in the mid-lower mantle and to the elevated bulk sound velocities (V_Φ) observed at the edges of large, low shear velocity provinces when considering thermal effects.

In Chapter 5, I summarize the results of this thesis and the connection between the crystal chemistry of dense oxyhydroxides and the transport of H within Earth's lower mantle. I discuss potential future measurements and seismological constraints which could elucidate the concentration of H in Earth's largest chemical reservoir.

Chapter 2

VIBRATIONAL SPECTROSCOPY OF DENSE OXYHYDROXIDES: HYDROGEN BOND DISORDER AND SYMMETRIZATION AT HIGH PRESSURE

*This chapter has been submitted and is currently under review:

Strozewski, Benjamin T., Zhenxian Liu, George R. Rossman, Wolfgang Sturhahn, Johannes Buchen, and Jennifer M. Jackson (2025). "Vibrational spectroscopy of dense oxyhydroxides: hydrogen bond disorder and symmetrization at high pressure ". In: *American Mineralogist [submitted].*

2.1 Introduction

Water storage capacities of nominally anhydrous minerals (e.g. Smyth et al., 2003; Férot and Bolfan-Casanova, 2012; Bell and Rossman, 1992) and seismologically determined discontinuities (Kennett and Engdahl, 1991; Kennett et al., 1995; Dziewonski and Anderson, 1981) suggest that Earth's mantle can be divided into three regions based on the level of hydration: a relatively dry upper mantle (100-2000 ppm), a wet mantle transition zone (0.1-2.0 wt.%), and a dry lower mantle (< 0.1 wt. %) (review by Ohtani, 2020). While hydrous minerals often dehydrate within the upper mantle and contribute to arc volcanism, serpentine may retain its hydrogen in cold subduction environments (Rüpke et al., 2004), contributing to the storage of water in a chain of high-pressure hydrous phases (Bolfan-Casanova, 2005). Recent work suggests that dense oxyhydroxide phases could form at conditions of the mantle transition zone (Liu et al., 2019; Ohira et al., 2014; Bindi et al., 2014b; Kawazoe et al., 2017; Nishi et al., 2019), which is at least locally 'wet' (~ 2 wt. % H_2O), as indicated by hydrous inclusions recovered in sublithospheric diamonds (Tschauner et al., 2018; Pearson et al., 2014; Palot et al., 2016; Gu et al., 2022). Dense oxyhydroxide phases (e.g. δ-AlOOH) potentially formed in this region retain hydrogen in their crystal structures at temperatures up to 2200 K at 128 GPa (Ohira et al., 2014; Duan et al., 2018; Panero and Caracas, 2017) and therefore provide a mechanism for transport of hydrogen into the lowermost mantle via subducting slabs.

Hydration of nominally anhydrous minerals or the presence of hydrous minerals have been shown to affect the speed at which seismic waves propagate and alter the depth and topography of key seismic discontinuities in the mantle (e.g. Schmandt et al., 2014; Jacobsen, 2018; Mao et al., 2008; Wang and Wu, 2022; Ohira et al., 2021, Chapter 4). Hydrous phases in the basaltic layer of a slab may contribute to scattering of seismic waves in the mid-lower mantle or to the origin of velocity anomalies at the edges of large, low shear velocity provinces should they accumulate near the core-mantle boundary (Chang et al., 2013; Strozewski et al., 2023; Ohira et al., 2021). The D" region is complex, both in petrology (Jackson and Thomas, 2021) and dynamics, as subducting slabs may flow into basal mantle structures (Sun et al., 2019; Wolf et al., 2024). If hydrous phases are subducted to these depths, they are likely to contribute to the chemical complexity of the D" region. Release of hydrogen from hydrous phases encountering the steep temperature gradient near the core-mantle boundary may affect phase relations and lower the solidus of material in this region, if not partitioned into other phases (e.g. Tsutsumi et al., 2024). Exsolved H may partition into the liquid Fe-rich metal of the outer core (Kim et al., 2023), leading to Fe-enrichment in ultra-low velocity zones (Kawano et al., 2024), which could explain the observed seismic velocities of these structures (Bower et al., 2011; Wicks et al., 2010; Dobrosavljevic et al., 2019; Jackson and Thomas, 2021).

Iron-bearing, Al-rich phases in the (δ-AlOOH)-($MgSiO_2(OH)_2$)-(ϵ-FeOOH) system (hereafter referred to as (δ-H-ϵ) have been observed to form in coexistence with bridgmanite, calcium perovskite (or "davemaoite"), stishovite, and ferropericlase in a natural hydrous basalt composition at the base of the mantle transition zone (Liu et al., 2019). To retain hydrogen at lower mantle conditions, hydrogen bonds in hydrous minerals must be strong enough to not dissociate at high temperatures. In the O-H--O bonding environment, long O-O distances (d > 2.5 Å) are hypothesized to result in two potential wells and likely two defined positions for the hydrogen atom (Kolesov, 2021; Sano-Furukawa et al., 2018). At shorter O-O distances (d $\approx$ 2.5 Å) the two potential wells move closer together and the barrier between them is consequently reduced, provoking disorder due to tunneling between the two sites or due to an asymmetric but wide potential well (Trybel et al., 2021). At even shorter O-O distances a single potential well may form. This is known as hydrogen bond symmetrization and it provides the strong hydrogen bonds which are likely critical in enabling compositions in this system to retain hydrogen at conditions of Earth's lower mantle. Observations of hydrogen bond disorder and symmetrization in phases relevant to Earth's mantle have been reviewed by Tsuchiya and Thompson (2022).

Study of different compositions in the δ-H-ϵ system has revealed the sensitivity of hydrogen bonding environment to end-member proportion (Bindi et al., 2014b; Komatsu et al., 2011; Suzuki, 2010). Disordering of hydrogen bonds in rutile-type oxyhydroxides from an ordered state can increase the symmetry of the crystal structure and cause a $P2_1nm \rightarrow Pnnm$ phase transition, making hydrogen bond disorder inferable with X-ray diffraction methods (Duan et al., 2018; Gleason et al., 2013; Komatsu et al., 2011; Ohira et al., 2019; Thompson et al., 2020). In contrast, hydrogen bond symmetrization will not change the long-range crystal symmetry of compositions with disordered hydrogen bonds and is therefore difficult to detect via X-ray diffraction. Komatsu et al. (2011) observed that the dissolution of even small amounts of Mg and Si into the crystal structure of δ-AlOOH results in disordering of cations at ambient pressure in this phase, a phenomenon that is also observed in topaz-OH and phase egg ($AlSiO_3OH$) (Xue et al., 2006). Cation disorder is not explicitly observed in (Al,Fe)-phase H: (δ-$Al_{0.84}Fe^{3+}{}_{0.07}Mg_{0.02}Si_{0.06}$)OOH (Strozewski et al., 2023) although this phase does adopt disordered hydrogen bonds at ambient pressure and temperature, possibly due to small fluctations in the positions of cations with different sizes and valences. This is in contrast to δ-(Al,Fe)OOH which has ordered, asymmetric hydrogen bonds at ambient pressure but undergoes a hydrogen bond order-disorder transition at ~10 GPa, resulting in a $P2_1nm \rightarrow Pnnm$ phase transition (Ohira et al., 2019; Ohira et al., 2021). A $P2_1nm \rightarrow Pnnm$ phase transition associated with changes in the pressure dependence of infrared-active O-H modes has been observed at approximately 10 GPa in the Fe-free endmember δ-AlOOH (Sano-Furukawa et al., 2009a; Kagi et al., 2010) and at approximately 5 GPa in the structural analogue β-CrOOH (Jahn et al., 2012). The order-disorder transition in ϵ-FeOOH at 18 GPa was inferred from infrared spectroscopy and X-ray diffraction (Thompson et al., 2020). Sano-Furukawa et al. (2018) used neutron diffraction to determine that hydrogen bonds become symmetric in δ-AlOOH at approximately 18 GPa. Nuclear magnetic resonance studies (Meier et al., 2022; Trybel et al., 2021) largely confirm this observation but suggest that the symmetrization of hydrogen bonds does not proceed via proton tunneling and that maximum proton mobility in various oxyhydroxides occurs at an O-O separation of 2.443 Å, regardless of initial electronic structure. In part, the uncertainty at which hydrogen bond symmetrization occurs in the δ-H-ϵ system for non end-member compositions is due to the paucity — relative to X-ray diffraction measurements — of studies which employ techniques explicitly sensitive to hydrogen bonding such as infrared spectroscopy or neutron diffraction. We will revisit this overview of the δ-H-ϵ system in the discussion section.

In this study, we use infrared and Raman spectroscopy to examine vibrational modes associated with hydrogen bonding in (Al,Fe)-phase H and δ-(Al,Fe)OOH to a pressure of 42 GPa. A decrease in the pressure dependence of modes associated with O-H bending and a significant softening of O-H stretching frequencies suggest a change in the hydrogen bonding environment of (Al,Fe)-phase H at 10-12 GPa, attributable to hydrogen bond disorder. Softening of O-H stretching modes in δ-(Al,Fe)OOH agrees with previous observations of a phase transition close to 10 GPa provoked by the disorder of hydrogen bonds. Softening and splitting of O-H bending modes in (Al,Fe)-phase H at approximately 35 GPa are inferred to evidence hydrogen bond symmetrization. We complement these observations with nuclear resonant inelastic X-ray scattering (NRIXS) measurements, presented in the supplementary information to this chapter, which suggest a change in the mean-square displacement of Fe atoms in (Al,Fe)-phase H at 35 GPa.

2.2 Methods

Infrared and Raman Spectroscopy

Infrared spectra at ambient pressure were collected at the California Institute of Technology using a Thermo-Nicolet iS50 Fourier transform infrared spectrometer equipped with a KBr beamsplitter and MCTA liquid nitrogen cooled detector. The absorbance (A) is a measure of the strength of the absorption by the sample and is calculated from transmitted intensities according to the equation:

$$A = -\log(\frac{I}{I_0}) \tag{2.1}$$

where I corresponds to the transmitted intensity recorded through the sample and I_0 to a reference intensity without the sample in the beam path (background). To reduce background in the O-H stretching region, samples were measured on a sapphire slide. The sapphire slide is opaque at wavenumbers below 1500 cm^{-1} but reduces the substantial background associated with an SiO_2 glass slide at higher wavenumbers. Measurements were performed on a large ($\approx$ 300x300 μm^2), unoriented grain of (Al,Fe)-phase H and two small ($\approx$ 100x100 μm^2), unoriented grains of δ-(Al,Fe)OOH. The background and sample spectra were each collected between 1500 and 4000 cm^{-1} using an infrared light source and with a resolution of 0.483 cm^{-1}.

Ambient-pressure Raman spectroscopy measurements were performed on small (100x100 μm^2), unoriented grains of (Al,Fe)-phase H and δ-(Al,Fe)OOH, mounted on SiO_2 glass slides. Measurements were made using a Renishaw Raman InVia spectrometer with a 514 nm green laser, calibrated using a piece of pure Si with a strong Raman line at 520.5 cm^{-1}. Scans were performed in extended mode over the wavenumber range 100-4000 cm^{-1} or 50-4000 cm^{-1}.

A symmetric diamond anvil cell (DAC) with type IIa diamond anvils and 400 μm diameter culets was used for each set of synchrotron infrared spectroscopy (SIR) measurements. A rhenium gasket was pre-indented to a thickness of approximately 50 μm and a 100 μm sample chamber was drilled using an electric discharge machine. A small amount of powdered (Al,Fe)-phase H ((δ-$Al_{0.84}Fe^{3+}{}_{0.07}Mg_{0.02}Si_{0.06}$)OOH) or δ-Fe13 (($Al_{0.87}Fe^{3+}{}_{0.13}$)OOH) was loaded into the sample chamber and diluted with KBr, which also serves as a pressure medium. In each case, a small (~10 μm diameter) ruby was placed within the sample chamber as a pressure calibrant. We calculate pressure using the calibration of Dewaele et al. (2008). The determined uncertainty from fitting an individual ruby spectrum is small ($\approx$ 0.01 GPa). However, we used a conservative estimate of 2.5% uncertainty on the measured pressure to reflect the systematic error arising from the use of different published ruby pressure scales (Shen et al., 2020).

Synchrotron infrared spectroscopy (SIR) measurements at high pressure were performed at beamline 22-IR-1 of the National Synchrotron Light Source II (NSLS-II), Brookhaven National Laboratory, Upton, New York. The synchrotron IR beam is split with a KBr beamsplitter without the use of polarizers or filters. The resultant spot size on the sample is approximately 50x50 μm^2. Infrared spectroscopy measurements are performed with either a Bruker Vertex 80 FTIR spectrometer and a Hyperion 2000 IR microscope with a mid-band (500-6000 cm^{-1}) MCT detector or Bruker Vertex 80v spectrometer and a custom IR164 microscope system with a wide-band (400-7000 cm^{-1}) MCT detector. The mid-band setup is used for pressures from 0 to 42 GPa. The wide-band setup was tested for measurements between 12 and 24 GPa but did not reveal additional vibrational modes. In addition to a spectrum collected on the sample at each pressure, a reference spectrum is collected away from the sample on a region with only the diamond anvil and KBr pressure medium to remove the contribution of diamond phonons in accordance with equation (1). However, residual absorption and noise from this procedure may persist due to the different locations of the measurements within the sample chamber.

Nuclear resonant inelastic X-ray scattering

Two panoramic diamond anvil cells (panDACs) were loaded with grains of (Al,Fe)-phase H for nuclear resonant inelastic X-ray scattering (NRIXS) experiments. NRIXS measurements were performed at sector 3 of the Advanced Photon Source, Argonne National Laboratory (Lemont, IL). One panDAC (run 1) with 400 μm flat culet anvils was loaded with a 20 μm thick, 50x30 μm^2 grain. A Be gasket was pre-indented to a thickness of 62 μm and drilled with a 210 μm diameter hole. Compressed Ne gas was loaded at the California Institute of Technology as a pressure medium. A second panDAC (run 2) with 250 μm beveled culets was loaded with a 30 μm thick, 65 x 60 μm^2 grain. A Be gasket was pre-indented to a thickness of 41 μm and a 140 μm hole was drilled in the center of the indentation. A boron epoxy insert was placed into each drilled Be gasket to stiffen the sample chamber. A ruby sphere approximately 10 μm in diameter was loaded proximal to the sample in each panDAC for pressure determination. Ruby fluorescence measurements were used to determine the pressure in each cell at low pressure (< 35 GPa) using the calibration of Dewaele et al. (2008). Pressure uncertainty is determined from ruby fluorescence measurements performed before and after each series of NRIXS scans. At high pressure (> 35 GPa), diamond edge Raman spectroscopy was used to estimate pressure inside the panDAC with the calibration of Akahama and Kawamura (2010). Pressure uncertainty at high pressure was determined from diamond edge measurements at four different locations of the sample. Additional details on the processing of NRIXS data are described in Chapter 4.

2.3 Results

Band identification and assignments at 1 bar

Raman and infrared (IR) spectra of (Al,Fe)-phase H and δ-Fe13 at ambient pressure (1 bar) are plotted in Figures 1 and 2, respectively. The same ambient pressure Raman spectra are compared to those of δ-AlOOH from the DFT study of Tsuchiya et al. (2008) and the measurement of Ohtani et al. (2001) in Figure 1. The Raman and IR spectra of each oxyhydroxide share the same general features and can be separated into three bands at ambient pressure (Table 1). Band I (0-1000 cm^{-1}) contains at least 5 visible vibrational modes that are associated with cation-oxygen (M-O) vibrations (Jahn et al., 2012; Tsuchiya et al., 2008). Henceforth, we focus on modes associated with O-H bonds. In this work, we use O-H--O to indicate asymmetrically bonded hydrogens and O-H to refer to a bond between a single oxygen and hydrogen atom. Vibrational modes associated with O-H--O bonding are readily identified based on comparison to Kagi et al. (2010) and Jahn et al. (2012), who performed infrared measurements on δ-AlOOH and β-CrOOH, respectively. In these studies, deuterated samples (δ-AlOOD and β-CrOOD) were also measured, revealing 2 O-H bending modes between 1000 and 1500 cm^{-1} (band II). The presence of several O-H bending modes in δ-AlOOH in this wavenumber region was also predicted by the density functional theory (DFT) results of Tsuchiya et al. (2008).

Band III encompasses absorption at wavenumbers > 1500 cm^{-1} and corresponds to O-H stretching vibrations (Tsuchiya et al., 2008; Jahn et al., 2012) or possibly modes which have both bending and stretching components (Table 1). At ambient pressure, the O-O distances in (Al,Fe)-phase H and δ-Fe13 are 2.53 Å (Strozewski et al., 2023) and 2.55 Å (Ohira et al., 2019). Based on these O-O distances, the correlation curve of Libowitzky (1999) predicts O-H stretching frequencies of 2130 and 2335 cm^{-1} (Supplementary Figure S1, Table 1) for (Al,Fe)-phase H and δ-(Al,Fe)OOH, respectively. These predicted frequencies agree well with a Raman and infrared-active vibrational mode in the respective phases. In the rest of this work, we refer to this mode as the primary stretching mode as it most closely corresponds to the predicted O-H stretch from the respective crystal structures.

Although the O-H stretching region is complicated by residual absorption from the diamond anvils, the primary stretching frequency is nevertheless easily tracked as it moves to lower wavenumbers with increasing pressure (Figure 3) and is located well by the measurements at ambient pressure (Figure 2). At higher pressures, an artifact from the diamond absorption persists at $\approx$ 2100 cm^{-1} while the primary stretching mode has shifted from 2130 cm^{-1} to $\approx$ 1800 cm^{-1} (Figure 3). We observe Raman and infrared-active O-H stretching modes in (Al,Fe)-phase H and δ-Fe13 at wavenumbers higher than that of the primary stretching mode in the wavenumber region $\approx$ 2000-3500 cm^{-1}. The existence of several distinct modes at wavenumbers higher than that of the primary O-H stretch inferred from the crystallographic constraints on the O-O distance is a robust observation in dense oxhydroxides. Ohtani et al. (2001) observed additional O-H stretching modes in δ-AlOOH (Figure 1), which were corroborated by the DFT predictions of Tsuchiya et al. (2008), who speculated that several O-O distances exist within the crystal structure. Xue et al. (2006) suggested that instead these modes are caused by Fermi resonances between the fundamental O-H stretching mode and overtones or combination modes. The observation here that vibrational modes in the range $\approx$ 2000-3000 cm^{-1} are generally both Raman and infrared-active confirm that the O-H--O bonding unit is not centrosymmetric in

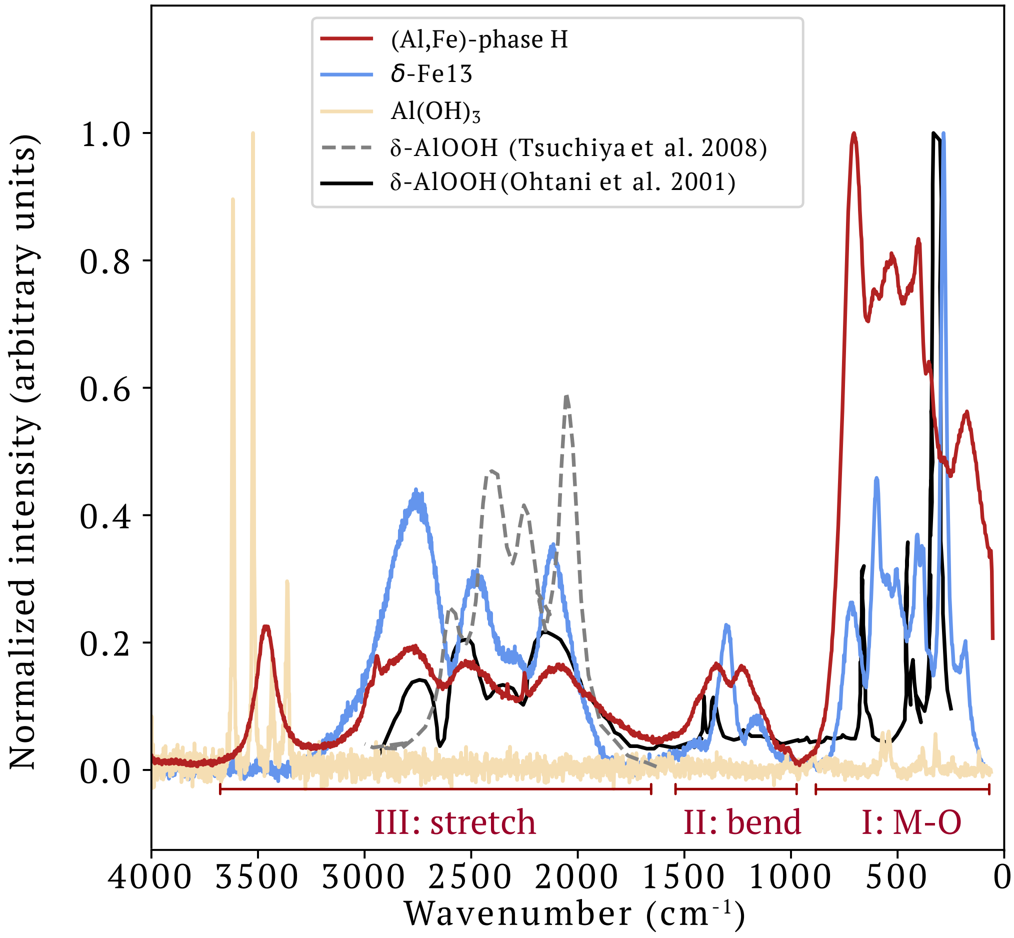

Figure 2.1: (a) Comparison of Raman spectra at ambient pressure of (Al,Fe)-phase H and δ-Fe13 with that of powdered Al(OH)$_3$ gibbsite (this study) and δ-AlOOH (Ohtani et al., 2001). A theoretical prediction of the Raman spectrum of δ-AlOOH in the O-H stretch region from Tsuchiya et al. (2008) (structure 12) is plotted in light gray. Spectra are plotted with decreasing wavenumber on the x-axis for consistency in comparison to infraredspectra throughout the manuscript.

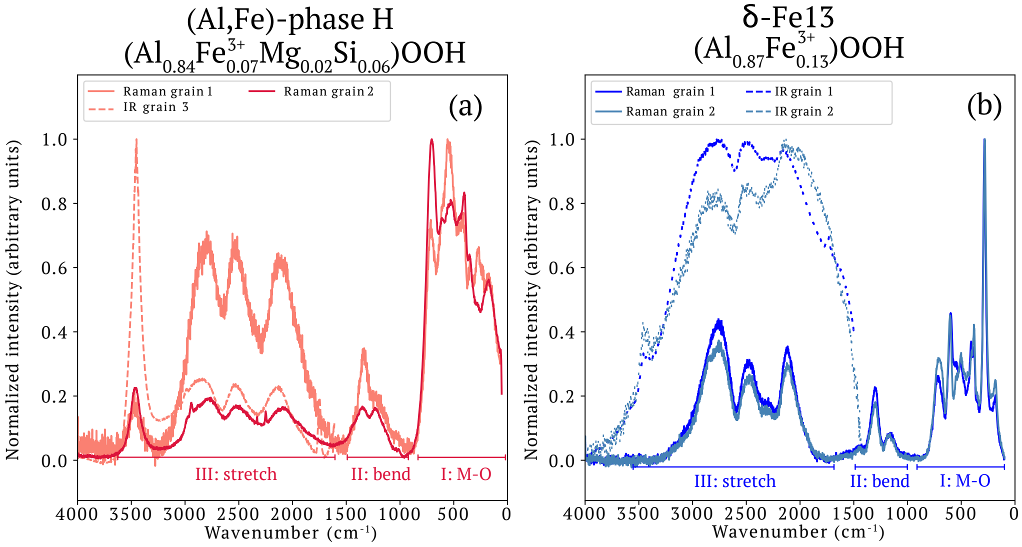

Figure 2.2: Identification of vibrational modes in the measured Raman and infrared spectra of (Al,Fe)-phase H and δ-Fe13. (a) Comparison of Raman and infrared spectra measured on two grains of δ-Fe13 at ambient pressure. Infrared and Raman spectra are collected on the same two grains. (b) Comparison of Raman and infrared spectra measured on three different grains of (Al,Fe)-phase H at ambient pressure.

	Band #	Wavenumber (cm^{-1})	# modes
M-O	I	0-800	5+
O-H bend	II	1000-1550	2-4
O-H bend-stretch	III	1550-2000	2-4
O-H stretch	III	2000+	4-6

Table 2.1: Vibrational bands in spectra of (Al,Fe)-phase H, their corresponding wavenumber regions, and the number of modes (functions) which are fit to infrared spectra at high pressure. M-O refers to vibrations of cation and oxygen bonds, which we do not focus on in this study. Band labels are determined by the primary motions deemed to be present in this wavenumber range. However, combination modes and the effects of pressure complicate an exact labeling (see discussion). Peak broadening due to sample effects may result in a different number of fit modes compared to theoretical calculations.

either (Al,Fe)-phase H or δ-Fe13 at ambient pressure. That is, in neither case are hydrogen bonds symmetric. Additionally, a small shoulder of the primary stretching mode at $\approx$ 1600 cm^{-1} is present in low-pressure infrared spectra of (Al,Fe)-phase H and δ-Fe13. The wavenumber of this mode — between that of the more intense bending modes and the primary O-H stretching mode — may suggest it results from a combination of bending and stretching.

(Al,Fe)-phase H displays a distinct vibrational mode at 3500 cm^{-1}, present in both Raman spectra at 1 bar and infrared spectra (Figures 1 and 2) . This mode is not observed in the 1 bar Raman spectra of δ-Fe13 but is present in the infrared spectra. The precise origin of this mode is unclear. The Raman inactivity of this mode in δ-Fe13 implies that this vibrational mode corresponds to a structural unit which is centrosymmetric in δ-Fe13 but not in (Al,Fe)-phase H. No modes at wavenumbers greater than 3000 cm^{-1} are predicted by Tsuchiya et al. (2008), or reported in studies of oxyhydroxides with a single type of cation (Kagi et al., 2010; Jahn et al., 2012; Ohtani et al., 2001). One possible explanation is that long O-H bonds are present due to hydrogen defects in each of these oxyhydroxides. Studies of O-H vibrational frequencies in rutile (Palfey et al., 2021; Koudriachova et al., 2004) find that OH defects could form on O vacancies and would have infrared-active vibrational frequencies between $\approx$ 3250 and 3350 cm^{-1}. We hypothesize that the distorted rutile structure of (Al,Fe)-phase H increases the frequency of this defect mode to $\approx$ 3500 cm^{-1} although additional measurements or theoretical calculations to confirm this are necessary. Both (Al,Fe)-phase H and δ-Fe13 contain a greater H wt.% than implied by stoichiometry (Kawazoe et al., 2017; Ohira et al., 2019; Strozewski et al., 2023). In particular, for the case of (Al,Fe)-phase H, Mg and Si could enter the crystal structure via the substitution $2Al^{3+} \rightarrow Mg^{2+} + Si^{4+}$. However, these cations are not present in a 1:1 ratio in these samples. The vibrational mode at 3500 cm^{-1} may therefore be evidence of the substitutions $Al^{3+} \rightarrow Mg^{2+} + H^{+}$ and/or $2Al^{3+} \rightarrow Si^{4+} + 2H^{+}$, which could result in OH defects. Similar substitutions may involve Fe^{3+} rather than Al^{3+} and any local order induced as a result could influence transitions in the δ-H-ϵ system.

Effect of pressure on O-H vibrational modes

Selected synchrotron infrared spectra collected at NSLS-II (Upton, NY) at high pressure of (Al,Fe)-phase H and δ-Fe13 are plotted in Figure 3. The entire set of spectra for each composition are plotted in Supplementary Figure S2. In (Al,Fe)-phase H, with increasing pressure, the absorption of stretching modes above 2000 cm^{-1} decreases in intensity while absorption between 1700 and 1900 cm^{-1} increases, commensurate with the calculated infrared spectra of ϵ-FeOOH (Insixiengmay and Stixrude, 2023). The reduction of sample absorption at wavenumbers above 2000 cm^{-1} reveals an artifact from diamond absorption at 2100 cm^{-1}, combined with marked noise due to a fringing effect (i.e. interference between diamond anvils). Nevertheless, ambient-pressure Raman and infrared spectra outside of a diamond anvil cell (Figures 1 and 2) confirm the presence of vibrational modes at ≈ 2100 cm^{-1} at low pressures. Measured spectra of δ-Fe13 show little change at pressures higher than 20 GPa although bending modes cannot be reliably tracked above 6 GPa due to merging of the vibrational modes and saturation of the absorption scale. At 20 GPa, high-wavenumber stretching modes are broad and low in intensity. In (Al,Fe)-phase H, stretching modes are still apparent at 20 GPa and continue to broaden and decrease in intensity to a maximum measured pressure of 42 GPa while the peak at ≈ 1800 cm^{-1} continues to increase in intensity and shift to slightly higher wavenumbers.

The following sections describe results obtained by fitting the measured spectra using the fityk software (Wojdyr, 2010). Vibrational modes are fit with either Gaussian or Voigt profiles. We fit the measured spectra using the minimum number of functions possible to obtain a good (reduced $\chi^2 \approx 1$) statistical description while respecting the observed shape. That is, in some cases multiple peaks are visible but close enough that a fit using a single, very broad function produces similar statistics. In this case, peak positions may be fixed during fitting to maintain the number of peaks which can be discerned from the raw spectra.

For low-symmetry crystal structures with multiple cations such as (Al,Fe)-phase H and δ-Fe13, many vibrational modes may be present within certain spectral bands. For example, the DFT simulations of Jahn et al. (2012) found 8 vibrational modes associated with O-H bending between 1000 and 1600 cm^{-1} in *Pnnm* β-CrOOH at 0 GPa. However, the breadth of the measured vibrational bands precludes the decomposition of the measured band II into vibrational modes associated with particular symmetry properties. Instead, we choose the minimum number of functions necessary to obtain a good statistical fit and in accordance with the number of observable peaks, as described above. At low pressures, infrared absorption with two peaks is observable between 1500 and 1900 cm^{-1} in (Al,Fe)-phase H and δ-Fe13. We label this region as the "bend-stretch" region as it likely is constituted by modes which have some bending (lower frequency) character and some stretching (higher frequency) character (Table 1).

(Al,Fe)-phase H

The O-H bending region (band II) was fit in (Al,Fe)-phase H ($(\text{Al}_{0.84}\text{Fe}^{3+}_{0.07}\text{Mg}_{0.02}\text{Si}_{0.06})\text{OOH}$) over the entire compression and decompression range (Figure 4). Mode centers and pressures are listed in Supplementary Table S3. At pressures below 25 GPa, two

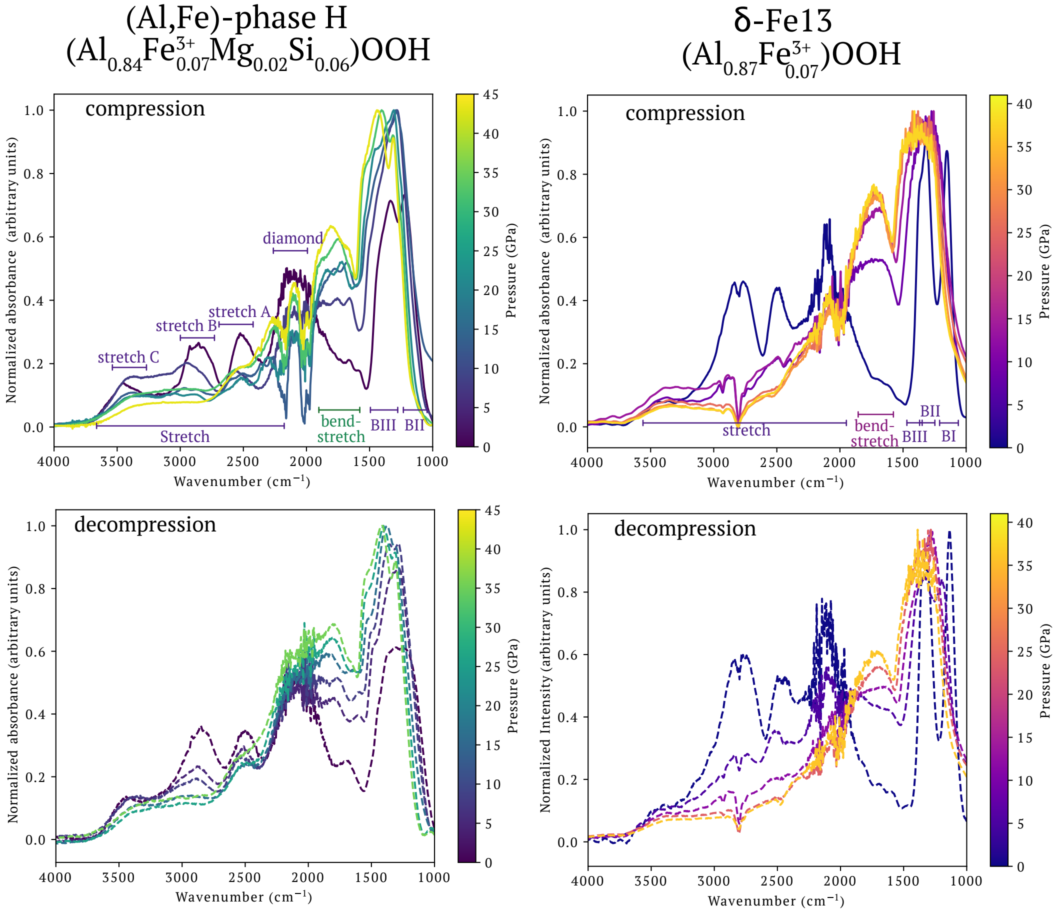

Figure 2.3: Select high-pressure infrared spectroscopy data above 1000 cm^{-1} collected on (Al,Fe)-phase H and δ-(Al$_{0.87}$,Fe$_{0.13}$)OOH (δ-Fe13) at the National Synchrotron Light Source-II, Brookhaven National Laboratory. Spectra were collected on (Al,Fe)-phase H and δ-Fe13 to a maximum pressure of 42 GPa.

Voigt profiles generally provide a good description of the O-H bending frequencies of (Al,Fe)-phase H, consistent with the results of Thompson et al. (2020): ϵ-FeOOH, Jahn et al. (2012): β-CrOOH, and Kagi et al. (2010): δ-AlOOH. At several pressures, a third Voigt profile is required, though it is difficult to ascertain whether this corresponds to the presence of a real vibrational mode. At low pressure ($<$ 25 GPa), the two fit profiles (bend A and bend B1) describe the band II region and have similar pressure dependencies. These modes shift to higher wavenumber with increasing pressure to $\approx$ 12 GPa. At pressures greater than 12 GPa, bend A and bend B1 are relatively insensitive to pressure. The same trend in pressure dependencies was observed for O-H bending modes in β-CrOOH (Jahn et al., 2012) and δ-AlOOH (Kagi et al., 2010) and was interpreted to be due to the disorder of hydrogen bonds (Figure 4b). This interpretation is supported by observations that

δ-AlOOH and δ-(Al,Fe)OOH undergo a $P2_1nm \rightarrow Pnnm$ phase transition between 8 and 12 GPa (Ohira et al., 2019; Satta et al., 2024; Sano-Furukawa et al., 2018), due to disordered hydrogen bonds resulting in an additional glide plane and a change in symmetry of the phase. For the case of (Al,Fe)-phase H ($Pnnm$), hydrogen bonds are disordered even at ambient pressure and no phase transition is observed by X-ray diffraction at high pressure (Strozewski et al., 2023). Nevertheless, the trend in the pressure dependence of O-H bending observed here suggests that (Al,Fe)-phase H undergoes a change in hydrogen bonding environment at 9-13 GPa, similar to other high-pressure oxyhydroxides. In (Al,Fe)-phase H, the plateau-like pressure dependence may indicate merging of several potential wells representing more than two sites for the H atom. We discuss this hypothesis further below.

Modes bend A and bend B1 soften between 20 and 25 GPa, moving to lower wavenumbers (Figure 4). At pressures greater than 25 GPa, it is impossible to obtain a fit of sufficient statistical quality with two Voigt profiles: three are required. Specifically, bend B1 splits into bend B1 and bend B2. The observed splitting of bend B1 could be attributed to a small difference in pressure dependence of two existing modes or softening of O-H stretching modes from higher wavenumbers with increasing pressure. Bend A, bend B1, and bend B2 each increase in wavenumber between 25 and 35 GPa. At 35 GPa, each bending mode appears invariant with pressure to a maximum pressure of 42 GPa. The pressure dependence of the bending modes is similar to that of the modes predicted at these wavenumbers at the pressure of hydrogen bond symmetrization in $P2_1nm$ δ-AlOOH (Tsuchiya et al., 2008) (Figure 4).

The O-H bend-stretch region in (Al,Fe)-phase H (band III), is characterized by a significant gain in absorption with increasing pressure (Figure 3, Supplementary Figure S3). The frequencies of bend-stretch modes at every pressure are plotted in Figure 5a, though we note that this region is complex, particularly at low pressure (Supplementary Table S4). The frequency of bend-stretch A increases with pressure to 12 GPa and softens to lower wavenumbers at higher pressures. The primary stretching mode, labeled "bend-stretch B" in Figure 5, softens significantly at a pressure between 10 an 15 GPa, after which it remains constant. Tsuchiya et al. (2008) predicted that transverse O-H stretching modes would soften from ≈2500 cm^{-1} to ≈1700 cm at the pressure of hydrogen bond symmetrization. Consistent with this prediction, we conclude that the (Al,Fe)-phase H primary stretching mode changes its character from primarily O-H stretching to both bending and stretching

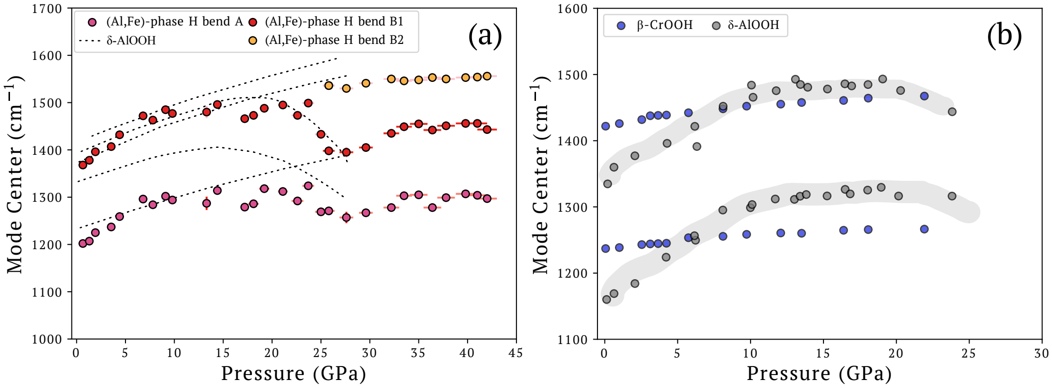

Figure 2.4: (a) Frequencies of fits to (Al,Fe)-phase H infrared bending modes (band II). Mode bend A is assigned to the prominent bending mode with the lowest wavenumber. Modes bend B1 and B2 are at higher wavenumbers. Dashed lines indicate predicted frequencies of several vibrational modes in δ-AlOOH from Tsuchiya et al. (2008). (b) Reported frequencies of bending modes with pressure from infrared spectroscopy measurements on β-CrOOH (Jahn et al., 2012) and δ-AlOOH (Kagi et al., 2010). The shaded gray area serves as a guide to the eye for the plotted δ-AlOOH mode centers.

motions, indicated by the gradient of the shaded region and the name of "bend-stretch B" in Figure 5.

The O-H stretch region (band III) contains modes with a variety of pressure dependencies. Softening of the "stretch A" mode in (Al,Fe)-phase H is observed at approximately 12 GPa, resulting in a splitting of this mode into two modes, both of which are approximately constant with pressure (Figure 5a). This softening could be attributed to that of a longitudinal stretch mode predicted by Tsuchiya et al. (2008), albeit with a different pressure dependence. The second stretching mode ("stretch B", Figure 5b) appears to follow a similar pressure dependence as that of the bending modes, with a kink in the wavenumber vs. pressure trend at 12 GPa. We have labeled this a stretching mode because its wavenumber at ambient pressure falls in the O-H stretching band (band III, Table 1). However, the observed pressure dependence of this mode may indicate that it dominantly involves bending motion of O-H bonds, which could be produced by Fermi resonance with the bending modes at lower wavenumber (Xue et al., 2006). A stretching mode at 3200 cm^{-1} ("stretch C") remains approximately constant with pressure to 12 GPa in (Al,Fe)-phase H but is not fit at higher pressures due to broadening of other absorption features in this region. The center of the "stretch D" mode (3500 cm^{-1}) which we attribute to OH

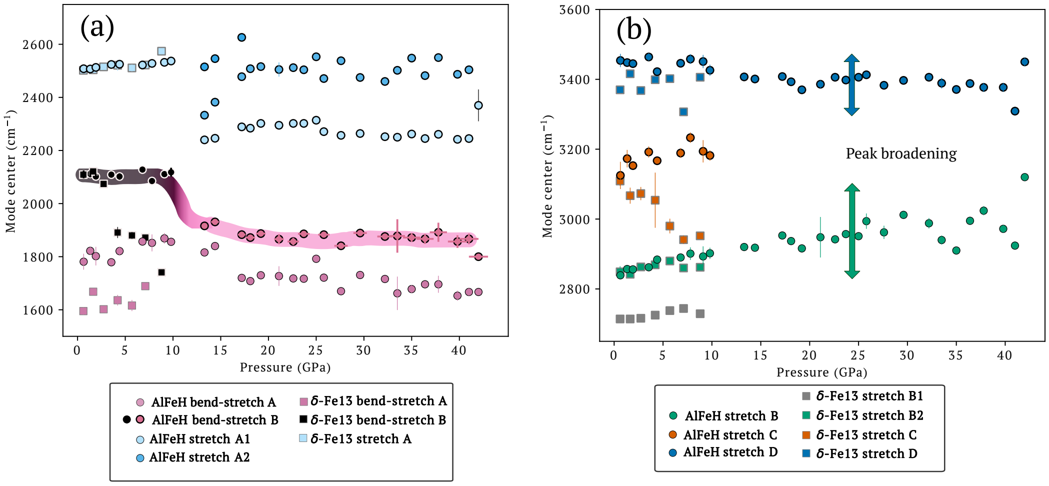

Figure 2.5: Frequencies of O-H vibrational modes determined to be stretching or combination modes of (Al,Fe)-phase H and δ-Fe13. Filled shapes indicate frequencies determined during compression. Empty shapes indicate frequencies of stretching modes measured on decompression in the case of (Al,Fe)-phase H. Fitting procedure and mode assignment is discussed in the main text. In panel (a), the shaded area is drawn as a guide to the eye for the softening of the "bend-stretch B" mode, which may change its character from stretching to bending at 10 GPa. Arrows in panel (b) indicate the apparent disappearance of the "stretch C" mode due to broadening of the surrounding vibrational modes.

defects in (Al,Fe)-phase H remains approximately constant with pressure while the width of the mode increases and its intensity decreases.

Softening of O-H stretching modes (band III) could indicate a widening of the potential minimum in which the H atom sits (Kolesov, 2021). In order to estimate at what pressure softening of O-H stretching modes ceases (if it does), we calculate the fractional intensity of two bands (Supplementary Figure S3): low wavenumbers (1600-2000 cm^{-1}) and high wavenumbers (2200-3700 cm^{-1}), deliberately avoiding the most prominent diamond absorption between 2000 and 2200 cm^{-1}. The fractional intensity is determined by integrating over each band and dividing the summed absorption of that band by the total sum of both. If O-H stretching modes are shifting to lower wavenumbers in a certain pressure range, we expect to see a decrease in the fractional absorption of the high wavenumber region and an increase in the fractional absorption of the low wavenumber region. This calculation confirms that absorption strength shifts with increasing pressure from high wavenumbers to low wavenumberspredominantly at pressures below 15 GPa. The intensity of the 2200-3700 cm^{-1} band reaches a minimum at $\approx$ 35 GPa, although scatter in the values from this calculation make it difficult to discern if intensity exchange from high to low wavenumbers is continuous between 15 and 30 GPa.

δ-(Al,Fe)OOH

O-H bending modes in δ-AlOOH increase significantly in wavenumber with pressure to 10 GPa (Kagi et al. 2010, Figure 4b). At pressures higher than 10 GPa, the centers of these modes depend only weakly on pressure. As discussed above, this change in trend is inferred to be due to the order-disorder transition of hydrogen bonds in δ-AlOOH, which results in a $P2_1nm \rightarrow Pnnm$ transition at this pressure (Ohira et al., 2019; Meier et al., 2022; Trybel et al., 2021; Sano-Furukawa et al., 2018). Band II (O-H bending) in δ-Fe13 is fit to 5 GPa and the mode centers listed in Supplementary Table S3. At higher pressures, merging of the bending modes results in saturation of the absorption spectra in this wavenumber region and fits would not be meaningful. These modes are not plotted in Figure 4b for clarity but generally follow similar trends to those of δ-AlOOH.

O-H stretching modes in δ-Fe13 can be fit to 8 GPa before the breadth of the saturated bending modes becomes a problem for precise fitting (Figure 5). In δ-Fe13, only one mode is required to describe the bend-stretch region to 8 GPa ("bend-stretch A"). With increasing pressure, the mode "bend-stretch B" softens from approximately 2100 cm^{-1} to 1700 cm^{-1}, merging with bend-stretch A. This contrasts with the dramatic softening over a narrow pressure interval of the same mode in (Al,Fe)-phase H. The stretching mode "stretch A" does not soften but is instead relatively invariant with pressure to 8 GPa. Between 2700 and 2900 cm^{-1}, two modes are required for a good fit ("stretch B1" and "stretch B2"), which could be due to an artifact from background removal in the spectra (Figure 3). The two modes have similar dependencies on pressure and the mode stretch B2 follows closely the stretch B mode in (Al,Fe)-phase H. The stretch C mode softens with increasing pressure, similar to the bend-stretch A mode. The highest-wavenumber mode (stretch D) — which is not present in Raman spectra of this phase — may soften with increasing pressure as in (Al,Fe)-phase H but the scatter in its central position at low pressures does not reveal a trend.

2.4 Discussion

Analysis of O-H vibrational modes in (Al,Fe)-phase H and δ-Fe13 indicate a variation in the pressure dependencies of mode centers with increasing pressure. Combined with previous studies, this variation suggests changes in the hydrogen bonding environment. O-H bending modes of (Al,Fe)-phase H have distinct dependencies on presure at (i) low pressure (0 to 9 GPa), (ii) moderate pressure (9 to 23 GPa), (iii) high pressure (23 to 35 GPa), and (iv) highest pressure (above 35 GPa). Diverse trends in O-H stretching modes in both (Al,Fe)-phase H and δ-Fe13 (Figure 5) support the hypothesis that these modes involve a combination of bending and stretching motions, possibly in Fermi resonance with the broad, primary O-H stretching mode (Xue et al., 2006). In the rest of this discussion, we will primarily focus on (Al,Fe)-phase H since its modes can be more thoroughly tracked to high pressure.

It is important to clarify that changes in infrared-active vibrational frequencies associated with O-H bonding are predominantly affected by changes in the force constant of O-H bonds, which in turn affects the dipole moment of the molecule. This differs from studies which employ nuclear magnetic resonance (NMR) to constrain the proton position and mobility (Meier et al., 2022; Trybel et al., 2021) or neutron diffraction, which constrains the position of the nucleus of the H atom (Sano-Furukawa et al., 2018). In the following section, we seek to explain these observations in the context of information provided by additional experimental techniques to form a picture of the O-H--O bonding environment in these oxyhydroxides at high pressure. This discussion is outlined schematically in Figure 6. This schematic shows the potential well of the hydrogen atom in (Al,Fe)-phase H inferred from this study compared to that discerned for δ-AlOOH from the neutron diffraction experiments of Sano-Furukawa et al. (2018). In this schematic, we estimate O-O distances in (Al,Fe)-phase H from previous X-ray diffraction data (Strozewski et al., 2023). We use the constrained a and b unit cell parameters, projected along the vector of the O-O separation at ambient pressure: $\vec{d}_{O-O} = 1/8\mathbf{a} + 1/5\mathbf{b}$ to estimate the change in O-O separation with pressure. O-O distances for δ-AlOOH are taken from Sano-Furukawa et al. (2018) below 20 GPa and estimated from the data of Sano-Furukawa et al. (2009a) at higher pressures.

At low pressures (i: 0 to 9 GPa, Figure 6), O-H bending modes in (Al,Fe)-phase H shift to higher wavenumbers with increasing pressure and O-H–O stretching modes are generally invariant to pressure. In contrast, the primary O-H stretching mode of δ-Fe13 moves to lower wavenumbers monotonically over this pressure range. We interpret the increase in bending mode frequency as a shortening of the O-H bonds, resulting in a higher frequency of vibration (Kagi et al., 2010; Jahn et al., 2012; Tsuchiya et al., 2008; Insixiengmay and Stixrude, 2023). The softening of O-H

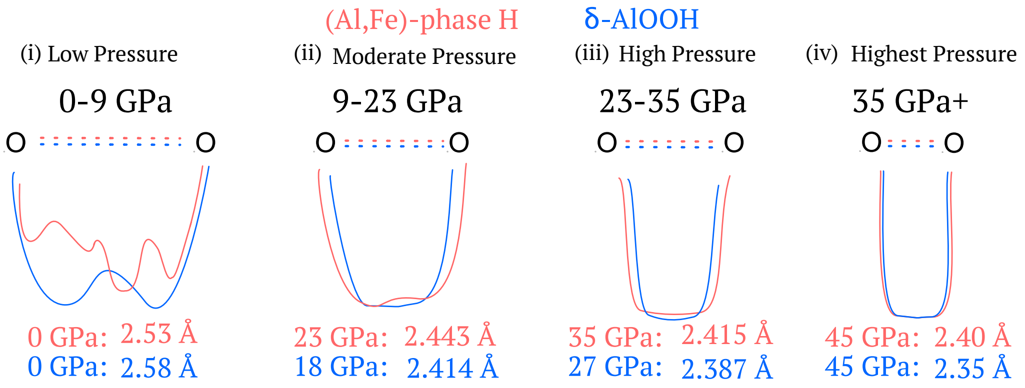

Figure 2.6: A schematic of the proposed change of the potential well of the H atom with pressure in both (Al,Fe)-phase H (red) and δ-AlOOH (blue). Potential wells of δ-AlOOH are taken from the neutron diffraction experiments of Sano-Furukawa et al. (2018). O-O distances at select, important pressures in each phase are given at the bottom of the schematic. O-O distances in (Al,Fe)-phase H are estimated from X-ray diffraction data (Strozewski et al. 2023) as described in the main text. O-O distances in δ-AlOOH to 20 GPa are taken from Sano-Furukawa et al., 2018 and estimated at 40 GPa from the data of Sano-Furukawa et al. (2009a). (i) Occupational disorder of the hydrogen atom over several sites with an O-O distance of 2.53 Å in (Al,Fe)-phase H. The O-O distance in δ-AlOOH is longer and there are two asymmetric sites for the H atom. (ii) Compression of the O-O distance in (Al,Fe)-phase H results in a potential that is wide but asymmetric and with a very small potential barrier. Hydrogen bond symmetrization and the transition to a unimodal potential takes place in δ-AlOOH at 18 GPa. (iii) Further compression of (Al,Fe)-phase H reduces the barrier between potential wells, resulting in a single well potential at 35 GPa and an O-O separation of 2.415 Å. (iv) Compression to pressures greater than 35 GPa narrows a single potential well.

stretching modes in δ-Fe13 indicates a shortening of the O-H–O bonds. As the O-O distance is compressed, the potential barrier between two H sites is reduced and a wider potential well is created that results in a lower frequency of oscillation. This phenomenon is described in general by Kolesov (2021) and predicted using density functional theory for δ-AlOOH by Tsuchiya et al. (2008) and for ϵ-FeOOH by Insixiengmay and Stixrude (2023). Sano-Furukawa et al. (2018) observe shortening of the O-O distance and disorder of hydrogen bonds in δ-AlOOH at 9 GPa via neutron diffraction. The softening of O-H–O stretching modes in δ-Fe13 is commensurate with a softening of the partial, projected density of states observed by Ohira et al. (2021), which ceases after the $P2_1nm \rightarrow Pnnm$ phase transition in this phase (Supplementary Figure S5).

None of the O-H stretching modes in (Al,Fe)-phase H soften between 0 and 9 GPa (Supplementary Figure S5), despite nearly identical pressure dependence of vibrational modes related to O-H bending when compared with δ-AlOOH (Figure 4). We propose that the reason for this difference is that (Al,Fe)-phase H has more than two sites for the hydrogen atom at 0 GPa and that these sites merge into a broad double well with a small potential barrier over a narrower pressure interval than in δ-AlOOH (Figure 6). That is, in both phases, decreased O-O distances lead to O-H distances which are on average shorter, resulting in stiffening of O-H bending modes below 10 GPa. In δ-AlOOH, reducing the O-O distance allows the hydrogen atom to overcome the potential barrier and oscillate with a lower frequency when oscillating in the direction parallel to the O-H bond (stretch). In (Al,Fe)-phase H, the potential is such that tunneling is less probable and the H atoms are more confined (Figure 6i). Between 9 and 13 GPa, these wells merge, resulting in the observed softening of O-H stretching modes (Figure 6ii).

Komatsu et al. (2011) constrained the space group of $(Al_{0.86}Mg_{0.07}Si_{0.07})OOH$ to be *Pnnm* at 1 bar and posited that the dissolution of Mg and Si ions into the crystal structure may result in the disorder of hydrogen atoms, which act as a "valence compensator" to maintain local charge balance, occupying positions closer to ions with lower valence states and farther from those with higher valence states. That is, in a structure with cations of different valences, the H atom may occupy several positions rather than just the two observed in δ-AlOOH (Sano-Furukawa et al., 2018; Kudoh et al., 2004; Kuribayashi et al., 2014) and escape detection by X-rays. Xue et al. (2006) used NMR to observe that in phase egg ($AlSiO_3OH$), Al and Si disorder also provokes H-bond disorder. At ambient pressure, hydrogen atoms in oxyhydroxides with cations of different valences may be occupationally disordered but not dynamically disordered (i.e. no tunneling between sites). Therefore, it is likely that even high-quality X-ray diffraction data would struggle to distinguish multiple hydrogen positions or O-H distances in this context. Indeed, the crystal structures of $Al_{0.86}Mg_{0.07}Si_{0.07}OOH$ (Komatsu et al., 2011) and (Al,Fe)-phase H (Strozewski et al., 2023) were both satisfactorily solved with an assumed single hydrogen position of occupancy 0.5, which necessitates the *Pnnm* space group. This modeled site from X-ray diffraction would represent the most significant concentration of electron density in a potential with several local minima (Figure 6).

Changes in the pressure dependence and position of O-H vibrational modes in (Al,Fe)-phase H at moderate pressure (ii: 9-23 GPa) indicate a clear change in the hydrogen bonding environment. O-H bending modes become invariant to pressure (Figure 4) while O-H stretching modes soften to lower wavenumbers (Figure 5). The plateau-like trend of O-H bending modes due to hydrogen bond disorder has previously been associated with structural phase transitions provoked by hydrogen bond disorder in δ-AlOOH (Kagi et al., 2010) and β-CrOOH (Jahn et al., 2012). In δ-AlOOH, hydrogen bond disorder is observed to occur at an O-O distance of 2.443 Å at approximately 10 GPa (Trybel et al., 2021; Sano-Furukawa et al., 2018; Meier et al., 2022). In compositions more similar to (Al,Fe)-phase H, maximum hydrogen mobility is achieved at the same O-O distance (2.443 Å) but at higher pressure (> 20 GPa) (Meier et al., 2022). This observation agrees with our calculation that the O-O distance reaches 2.443 Å in (Al,Fe)-phase H at 23 GPa. We therefore propose that between 9 and 23 GPa, hydrogen atoms in (Al,Fe)-phase H remain in a state of dynamic disorder whereby there is still a potential barrier (or asymmetry) that is reduced with pressure. At 23 GPa, this barrier or asymmetry is small enough that the hydrogen atoms in (Al,Fe)-phase H achieve maximum mobility in a broad potential well. However, the potential barrier is still present and the hydrogen bonding state remains more accurately described as dynamic disorder. In contrast, the structural transition in δ-AlOOH at approximately 10 GPa results in a reduction of the potential barrier between hydrogen sites such that there is a coincidence between the onset of dynamic disorder and maximum hydrogen mobility (Figures 6 and 7).

The demarcation between moderate pressure (9-23 GPa) and high pressure (iii: 23-35 GPa) is the softening of O-H bending modes in (Al,Fe)-phase H and splitting of bend mode B1,at 25.8 GPa. We propose that between 23 and 35 GPa, the potential well continues to narrow and the potential barrier between minima continues to decrease, resulting in a unimodal potential at 35 GPa which is more narrow than that of the dynamically disordered state. The O-O distance in (Al,Fe)-phase H is 2.415 Å, which is approximately the same as that observed for hydrogen-bond symmetrization in δ-AlOOH at 18 GPa (Sano-Furukawa et al., 2018). This pressure region (23-35 GPa) therefore corresponds to 10-18 GPa in δ-AlOOH, between dynamic disorder of hydrogen bonds and symmetrization. It is unclear whether the softening and splitting we observe here occurs at 18 GPa in δ-AlOOH (Figure 4b). Although Kagi et al. (2010) do not observe softening at 18 GPa, they look only at peaks of two modes and may therefore miss this phenomenon. Previous work has revealed a kink in the plot of normalized pressure vs. eulerian strain (*F*-*f*) (Strozewski et al., 2023) at 35 GPa — which indicates a change in the compressional behavior of (Al,Fe)-phase H — as well as spectral changes in synchrotron Mössbauer spectra that require an additional Fe^{3+} site (Chapter 3). It is possible that two distinct Fe^{3+} sites at pressures greater than 35 GPa points to local cation order. Once the hydrogen atom is confined to a narrow potential well in a symmetric bonding state at 35 GPa, it is no longer free to compensate for differences in electron density provided by different cations, as it could at ambient pressure (Komatsu et al., 2011). Consequently, hydrogen defects or electronegativity differences between Fe atoms and neighboring cations in the crystal structure result in distinct electronic environments surrounding the Fe atoms (Chapter 3).

At pressures greater than 35 GPa (Figure 6iv), there are no observed changes in trends of vibrational modes versus pressure. We hypothesize that this reflects a state of strong, symmetric hydrogen bonding whereby the compression of the crystal structure dominantly occurs due to shortening of bonds other than O-H. Such a change in the accommodation of pressure was observed by Xu et al. (2013) in α-FeOOH and associated with strengthening of hydrogen bonds. We also note that the separation in pressure of H-bond order-disorder and symmetrization from the Fe^{3+} spin crossover in (Al,Fe)-phase H indicates that the these electronic transitions are independent of each other (Figure 7), in agreement with previous studies (Ohira et al., 2019; Meier et al., 2022; Trybel et al., 2021; Sano-Furukawa et al., 2018; Gleason et al., 2013).

2.5 Conclusion

We have performed Raman and infrared spectroscopy measurements on (Al,Fe)-phase H to 42 GPa and on δ-(Al,Fe)OOH to 40 GPa, complimented by constraints derived from nuclear resonant scattering. Our results suggest that hydrogen atoms in (Al,Fe)-phase H become dynamically disordered at approximately 10 GPa but likely achieve maximum mobility at 23 GPa. Structural disorder induced by the substitution of heterovalent Mg^{2+} and Si^{4+} into the crystal structure (Komatsu et al., 2011) results in the additional glide plane of *Pnnm* (Al,Fe)-phase H compared with $P2_1nm$ at ambient pressure and the lack of a soft-mode transition in (Al,Fe)-phase H between 0 and 10 GPa. The softening and splitting of O-H bending modes and calculation of O-O distances at higher pressure support the conclusion of Meier et al. (2022) that dense oxyhydroxides achieve maximum hydrogen mobility in a broad, effectively single potential well between 20 and 25 GPa. We identify the pressure of hydrogen bond symmetrization in (Al,Fe)-phase H as 35 GPa based on the plateau-like trend in frequencies of O-H bending modes above this pressure as well as observed changes in the electronic environment surrounding Fe atoms.

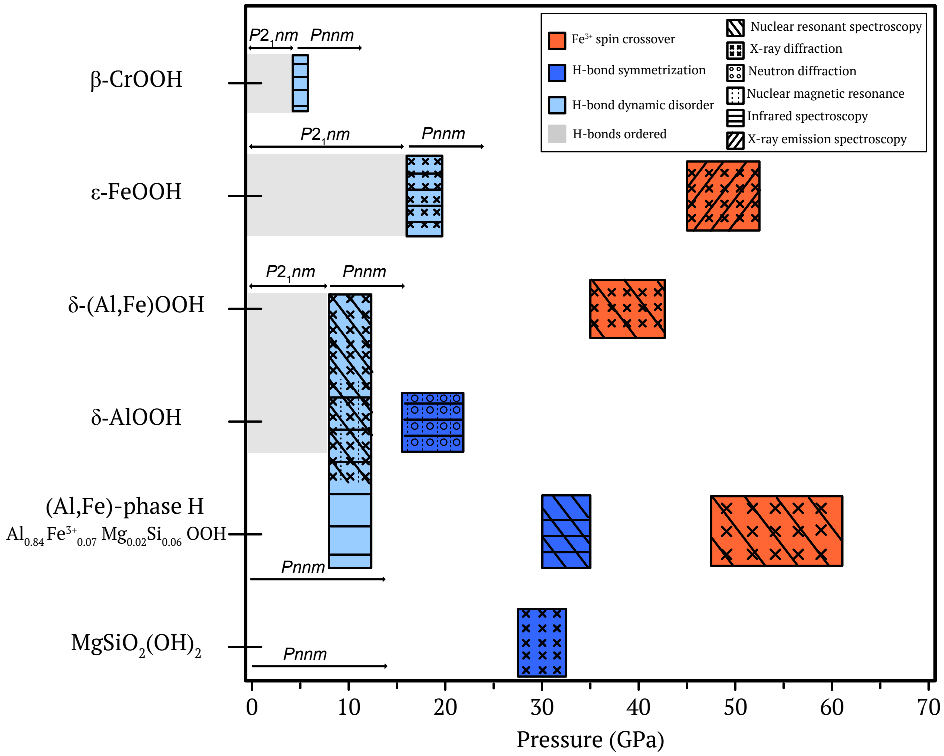

Figure 2.7: Identified or inferred transitions in dense oxyhydroxides at high pressure from experimental data. Theoretical predictions are omitted from this figue. Observation listed for δ-(Al,Fe)OOH include studies of the δ-AlOOH end-member. Interpretations and observations are taken from the following studies: β-CrOOH (Jahn et al., 2012), ϵ-FeOOH (Gleason et al., 2013; Thompson et al., 2020), δ-(Al,Fe)OOH (Kagi et al., 2010; Trybel et al., 2021; Ohira et al., 2019; Ohira et al., 2021; Sano-Furukawa et al., 2018), (Al,Fe)-phase H (Strozewski et al. 2023, and this study), and $MgSiO_2(OH)_2$ (Nishi et al., 2018).

Interestingly, at approximately the same pressure (≈ 35 GPa), a second, distinct Fe^{3+} site is observed in SMS spectra (Strozewski et al., 2023), and a high statistical quality NRIXS spectrum yields a lower Lamb-Mössbauer factor than anticipated by the trend with pressure below 50 GPa. We consider 35 GPa as the maximum pressure at which changes in the hydrogen bonding environment of this phase could be observed or are likely to significantly effect its electronic structure.

Figure 7 summarizes observations on dense oxyhydroxides including changes in the spin state of Fe atoms or hydrogen bonding environment. This diagram demonstrates that hydrogen bond disorder and symmetrization occur at significantly lower pressure than the spin crossover of Fe^{3+}. It is clear that variations in composition of phases in the δ-H-ϵ system have an appreciable effect on both the pressure of hydrogen bond symmetrization and the Fe^{3+} spin crossover. However, additional work focused on intermediate compositions and employing multiple techniques, including neutron diffraction and infrared spectroscopy, would more precisely determine compositional effects. Pairing single crystal X-ray diffraction and infrared spectroscopy at high pressure and temperature would be a powerful approach to discern whether the approximately 20 GPa difference in hydrogen bond symmetrization pressure between δ-AlOOH and (Al,Fe)-phase H results in appreciable effects on the pressure and temperature at which water in these phases could be retained in Earth's mantle.

Evidence that subducted slabs can descend through the mantle transition zone and into the lower mantle implies a need to understand their petrology and seismic velocities at pressures greater than 25 GPa. Previous work (Ohira et al., 2019; Thompson et al., 2017; Duan et al., 2018; Strozewski et al., 2023, Chapter 4) and the current study (Figure 7) indicate that the seismic velocities and electronic transitions in the δ-H-ϵ system are appreciably affected by composition. Hydrogen partitioning between SiO_2 and phases in the δ-H-ϵ system (Ishii et al., 2024) will directly affect the pressure of the post-stishovite transition commonly invoked to explain scattering of seismic waves in the mid-lower mantle (Kaneshima, 2016, Chapter 4) while precise understanding of the mineralogy of a slab is necessary to assess whether scattering may instead occur below the 660 km discontinuity due only to intrinsic heterogeneity within the slab (Mao et al., 2022). If a slab descends to the core-mantle boundary (Sun et al., 2019; Wolf et al., 2024), dense oxyhydroxides may contribute to the observed seismic velocities at the edges of large, low velocity provinces (Ohira et al., 2019; Strozewski et al., 2023, Chapter 4). Further experiments on the crystal chemistry of hydrous minerals that may be involved in H exchange across the core-mantle boundary (Kim et al., 2023; Kawano et al., 2024) would enhance our understanding of the petrology of subducted slabs and place constraints on chemical reactions due to potential slab dehydration in the lowermost mantle. Additional study of intermediate compositions in the δ-H-ϵ system will help to elucidate the variance of seismic velocities in this system as well as the entire range of compositions which may carry hydrogen to the lowermost mantle.

Chapter 3

EQUATION OF STATE AND SPIN CROSSOVER OF (AL,FE)-PHASE H

*This chapter has previously been published as:

Strozewski, Benjamin, Johannes Buchen, Wolfgang Sturhahn, Takayuki Ishii, Itaru Ohira, Stella Chariton, Barbara Lavina, Jiyong Zhao, Thomas S Toellner, and Jennifer M Jackson (2023). “Equation of State and Spin Crossover of (Al,Fe)-Phase H”. In: *Journal of Geophysical Research : Solid Earth*, pp. 1–20. DOI: `10.1029/2022JB026291`.

3.1 Introduction

In Earth’s mantle, the volatile element hydrogen is incorporated into minerals as point defects in nominally anhydrous minerals and in the crystal structures of hydrous minerals (e.g., Bell and Rossman, 1992; Bolfan-Casanova, 2005; Litasov and Ohtani, 2003; Ohtani, 2015; Rossman, 1996). Transport of volatiles in minerals as part of subducted lithosphere results in cycling of hydrogen between Earth’s surface and interior and places important constraints on the chemical and dynamic evolution of the Earth (Crowley et al., 2011; Nakagawa and Tackley, 2015; Parai and Mukhopadhyay, 2018). The presence of hydrogen in mantle minerals has been shown to affect the speed at which seismic waves propagate through the material and alter the properties of key seismic discontinuities in the mantle (Buchen et al., 2018; Jacobsen et al., 2010; Zhou et al., 2022). The release of hydrogen from subducted lithosphere as a result of mineral reactions can affect mantle dynamics by the depression of solidus temperatures and partial melt formation (i.e., arc volcanism), reductions in mantle viscosity, or can result in metasomatic reactions (Palot et al., 2016; Pearson et al., 2014; Tschauner et al., 2018).

While mantle convection models predict a diverse set of possible slab dynamics in the mantle transition zone, these models often agree that subducting slabs can descend through the abrupt change in density at 670 km depth and eventually accumulate at the core-mantle boundary (Brandenburg and Van Keken, 2007; Tan et al., 2011). Regions of positive seismic velocity perturbation, which are inferred to be cold, subducted oceanic lithosphere, have been consistently observed at depths greater than 670 km using seismic tomography (e.g. Durand et al., 2017; Hosseini et al., 2020; Koelemeijer et al., 2016). At higher spatial resolutions, regional seismic studies corroborate dynamic studies in their observations of material with elevated seismic wave speeds throughout the deepest parts of the mantle (Schumacher and Thomas, 2016; Sun et al., 2019). Accurate and quantitative interpretations of seismic studies and inferences of lower mantle structure requires thorough knowledge of the effects of compositional variations on observed seismic velocities and impedance contrasts, constrained in part by the equations of state of relevant mineral phases and their solid solutions.

In the case of subducted slabs, relevant compositions may include hydrous components formed in oceanic lithosphere and carried to greater depth. For example, phase "Egg" ($AlSiO_3(OH)$) has been observed as nanocrystalline inclusions in diamonds recovered from the mantle transition zone (Wirth et al., 2007). The discovery of ice-VII (Tschauner et al., 2018) and hydrous ringwoodite (Pearson et al., 2014) as inclusions in diamonds exhumed from the transition zone also suggests the presence of aqueous fluid in this region. While dense hydrous magnesium silicate phases are expected to dehydrate along typical geotherms in the upper mantle or transition zone (Bolfan-Casanova, 2005), recently synthesized hydrous phases such as δ-AlOOH ("delta phase"), $MgSiO_2(OH)_2$ ("phase H"), and ϵ-FeOOH have been observed to be stable at temperatures and pressures relevant to the lowermost mantle and form from the components of hydrous metabasalts (Liu et al., 2019). In particular, δ-AlOOH has garnered interest as a candidate carrier of hydrogen to the deep mantle (Ohtani, 2020; Ohtani et al., 2018) due to its stability at temperatures potentially as high as those of the ambient mantle near the core-mantle boundary (Sano et al., 2008; Terasaki et al., 2012). However, recent synthesis experiments have revealed δ-AlOOH to be an endmember component of the (δ-AlOOH)-($MgSiO_2(OH)_2$)-(ϵ-FeOOH) solid solution (Komatsu et al., 2011; Liu et al., 2019; Ohira et al., 2014). Therefore, studying the effect of compositional variation in this system will be necessary to understand the seismic signature of subducted lithosphere and distinguish between different hypotheses concerning the origin of seismic reflectors and structure within the lower mantle (e.g., Panero et al. (2020)).

The aluminum oxyhydroxide δ-AlOOH is a high-pressure polymorph of diaspore (α-AlOOH), first synthesized by Suzuki et al., (2000) at 21 GPa and 1273 K with small amounts of magnesium and silicon (δ-$Al_{0.86}Mg_{0.07}Si_{0.07}OOH$). At ambient conditions, δ-AlOOH and ϵ-FeOOH adopt the space group $P2_1nm$ with ordered and asymmetric hydrogen bonds (Gleason et al., 2013; Suzuki et al., 2000; Thompson et al., 2017). These two phases have been further observed to form a solid solution (Kawazoe et al., 2017; Nishi et al., 2017). Changes in hydrogen bonding environment due to compression have been observed in single crystal X-ray diffraction, neutron diffraction, and infrared spectroscopy measurements on δ-AlOOH (Kagi et al., 2010; Kuribayashi et al., 2014; Sano-Furukawa et al., 2018). The symmetrization of hydrogen bonds in ϵ-FeOOH has been inferred from changes in relative compressibilities along different crystallographic directions and prompts a change in space group from $P2_1nm$ to $Pnnm$ near 18 GPa (Thompson et al., 2020), a pressure lower than the symmetrization pressure predicted by density functional theory calculations performed for this composition by Gleason et al. (2013) (42 GPa) but similar to the calculations of Thompson et al. (2017) (17.5 GPa). Similar observations have been used to infer an order-disorder transition of hydrogen bonds in δ-(Al,Fe)OOH near 10 GPa (Ohira et al., 2019). Nuclear magnetic resonance measurements reported by Meier et al. (2022) corroborate the change in space group from $P2_1nm$ to $Pnnm$ observed at $\approx$10 GPa in δ-(Al,Fe)OOH and conclude that hydrogen bond symmetrization occurs at a pressure of approximately 22 GPa.

$MgSiO_2(OH)_2$ (phase H) crystallizes in the space group $Pnnm$ with disordered hydrogen bonds (Bindi et al., 2014a). X-ray diffraction measurements at high pressure revealed changes in relative compressibilities along different crystallographic axes near 30 GPa, indicating that hydrogen bonds in $MgSiO_2(OH)_2$ may become symmetric at this pressure (Nishi et al., 2018). The solid solution between δ-phase and phase H was confirmed to coexist with alumina-depleted bridgmanite in the lower mantle (Ishii et al., 2022a; Ohira et al., 2014). Liu et al. (2019) observed the formation of a solid solution between δ-AlOOH, $MgSiO_2(OH)_2$, and ϵ-FeOOH (referred to as "Al-rich phase H") coexisting with calcium silicate perovskite (or davemaoite, Tschauner et al., 2021), stishovite, magnesiowüstite, and fluid at 25-26.3 GPa and 1273-1473 K from compression and heating of a natural, hydrous basalt. However, the compressional behavior of an intermediate composition in the (δ-AlOOH)-($MgSiO_2(OH)_2$)-(ϵ-FeOOH) solid solution at pressures throughout the lowermost mantle has not yet been described.

The compressibility of this solid solution may be affected by changes in hydrogen bonding environment as well as a spin transition of ferric iron (Fe^{3+}) at high pressure. The formation of short, strong hydrogen bonds by disordering and eventually of symmetric hydrogen bonds is likely important in preventing the dissociation of these hydrous phases at the high temperatures of the lower mantle. A spin transition will affect the elastic properties of Fe-bearing compositions in this solid solution at lower mantle depths. The decreases in bulk modulus across the range of pressures corresponding to a spin crossover have been previously observed in studies of (Mg,Fe)O (Chen et al., 2012; Lin and Tsuchiya, 2008; Solomatova et al., 2016), Fe^{3+}-bearing bridgmanite (Mao et al., 2015; Dorfman et al., 2015), and other Fe-bearing minerals (Liu et al., 2015; Wu et al., 2016). The pressure range of the spin crossover and its effects on compressibility are governed in part by the valence state(s) of the iron atom(s), their coordination environment, and the electric field gradient imposed by the surrounding anions, whose pressure dependence is related to how strain is accommodated within the crystal structure. At quasi-hydrostatic conditions, changes in compressibility reflected in the equation of state of a material should precisely measure the breadth of a Fe^{3+} spin crossover, though the inferred pressures of this crossover may vary by several percent between studies based on the pressure calibrant used (see section 3.2). Additionally, techniques which are directly sensitive to the electronic and magnetic states of Fe atoms (e.g., synchrotron Mössbauer spectroscopy or X-ray emission spectroscopy) can be more sensitive to low proportions of low-spin Fe and may discern broader pressure intervals of the spin crossover. Ohira et al. (2019) inferred a high-low spin transition of Fe^{3+} in δ-(Al,Fe)OOH with two different iron concentrations (Fe/(Al+Fe) = 0.047(10) (δ-Fe5) and Fe/(Al+Fe) = 0.123(2)) (δ-Fe12) near 35 GPa based on synchrotron powder X-ray diffraction measurements and confirmed a change in spin state of the Fe^{3+} atoms by synchrotron Mössbauer spectroscopy on a similar composition with Fe/(Al+Fe) = 0.133(2). Additionally, Nishi et al. (2019) observed a volume collapse due to the Fe^{3+} spin crossover in δ-(Al,Fe)OOH with Fe/(Al+Fe) = 0.21 (δ-Fe21) and Fe/(Al+Fe) = 0.64 (δ-Fe64) at ≈45 GPa using X-ray diffraction. In the (δ-AlOOH)-($MgSiO_2(OH)_2$)-(ϵ-FeOOH) solid-solution, the incorporation of Mg and Si could affect the way in which strain is accommodated by Fe-O bonds and therefore result in important differences in the spin transition characteristics and compressional behavior in comparison to δ-(Al,Fe)OOH. Here, we use synchrotron powder X-ray diffraction to determine the equation of state, including the effects of hydrogen bond symmetrization and the high-low spin transition of iron, of $Al_{0.84}Fe^{3+}{}_{0.07}Mg_{0.02}Si_{0.06}OOH$ (hereafter referred to as "(Al,Fe)-phase H") to 125 GPa. The results are discussed in the context of important transitions in dense oxyhydroxides and their implications for the signature of subducted, hydrous lithosphere in the lower mantle.

3.2 Methods

Synthesis of (Al,Fe)-H crystals

(Al,Fe)-phase H crystals were synthesized with a hydrothermal method using a 1000-ton Kawai-type multi-anvil apparatus installed at the Bayerisches Geoinstitut, University of Bayreuth (BGI). The starting material was a mixture of 80% $Al(OH)_3$, 6% MgO, 6% SiO_2, and 8% Fe_2O_3 (96.64% enriched with 57Fe) by weight. The starting material was compressed to 21 GPa and heated to 1470 K at a rate of 40-50 K/min. This temperature was held constant for a total of 4 hours before rapid quenching. To determine the chemical composition and crystal structure of (Al,Fe)-phase H, a recovered single crystal with dimensions of about 50 x 50 x 50 um was selected based on the absence of twinning observed by X-ray diffraction and sharp optical extinction when viewed between crossed polarizers with a polarizing microscope. The chemical composition of the recovered crystal was measured to be $Al_{0.84}Fe^{3+}{}_{0.07}Mg_{0.02}Si_{0.06}OOH$ using an electron microprobe operating at 15 kV and 10 nA in wavelength-dispersive mode (JEOL, JXA-8200 installed at Tohuku University). Synthetic hematite and corundum were used as standard materials for Fe and Al, respectively. Natural enstatite was employed as a standard material for Mg and Si. The high-pressure experiments described below used grains from this synthesis which were cut into smaller pieces and crushed into a powder. δ-(Al,Fe)OOH crystals with Al/(Al+Fe) = 0.87 (hereafter referred to as “δ-Fe13”) used for synchrotron Mössbauer measurements were synthesized at 27 GPa and 1500 K for 5 hr. using the 1500-ton Kawai-type multi-anvil apparatus with Osugi-type guide block system installed at BGI (Ishii et al., 2016; Ishii et al., 2019). A detailed description of the synthesis of these crystals is given in Buchen et al. (2021).

X-ray diffraction

Single crystal X-ray diffraction patterns of the recovered (Al,Fe)-phase H crystal were collected using a Huber eulerian cradle single-crystal diffractometer with a Mo Kα X-ray source operated at 50 kV and 40 mA and a point detector. The diffractometer was controlled by the SINGLE software (Angel and Finger, 2011). Unit cell parameters of crystals with a half-width of the diffraction peaks less than 0.1° were refined using the vector least-squares method (Ralph and Finger, 1982). The effect of crystal offsets and diffractometer aberrations for each crystal were eliminated using the eight-position centering method (King and Finger, 1979). X-ray diffraction measurements for structural refinement were made separately using an area detector. The WinGX program (Farrugia, 2012) was employed for space group assignment and structure refinement (see section 3.1). The initial structure for the refinement was found using the direct method of the SHELXL-97 program (Sheldrick, 1997). Refinement of the structure was performed against $|F|^2$ using the full-matrix least-squares method with the scattering factors of neutral atoms (International Tables for Crystallography 1992).

Powdered (Al,Fe)-phase H was loaded in a symmetric diamond anvil cell (DAC) for high-pressure X-ray diffraction measurements. Beveled Type IA diamonds with culet diameters of 250 μm were used as the anvils. A rhenium foil with initial thickness of about 250 μm was pre-indented to a thickness of 40 μm for use as the gasket. To form the sample chamber, a 70 μm diameter hole was drilled at the center of the gasket indentation using an electric discharge machine. Powdered (Al,Fe)-phase H was loaded into the sample chamber with a ruby sphere and gold powder to serve as pressure gauges. Compressed helium gas was loaded at 25,000 PSI at the California Institute of Technology to serve as a quasi-hydrostatic pressure-transmitting medium. At beamline 13-ID-D of GSECARS at the Advanced Photon Source at Argonne National Laboratory (Lemont, IL, USA), the DAC was connected to a membrane-driven pressure control system. Angle-dispersive X-ray diffraction patterns were collected on a Pilatus IM CdTe area detector using monochromatic X-rays (λ = 0.3344 Å) focused to a size of 2 μm (vertical) by 3 μm (horizontal) at the sample position. Calibration of the instrument resolution function, sample-detector distance, and detector tilt was performed by collecting a diffraction pattern of LaB_6 powder in air, using the known X-ray wavelength and pixel area. Diffraction patterns of (Al,Fe)-phase H were collected at 159 pressures between 4.0 and 123 GPa. Patterns were collected with an exposure time of 10 seconds, during which the sample was rotated by 10° about its vertical axis. Two-dimensional angle-dispersive X-ray diffraction patterns were integrated to one-dimensional profiles of diffracted intensities versus 2θ-angle using the DIOPTAS software (Prescher and Prakapenka, 2015). Background subtraction was performed using the "sbck" module of the MINUTI software package Sturhahn, 2022 which detects and removes background common to all diffraction profiles in a coherent stack of profiles. By iteratively searching the lowest intensity at specific 2θ angles in the stack of normalized diffraction profiles, sbck yields a refined background function which is subsequently removed from individual diffraction profiles. Inspection of the processed diffraction profiles after background subtraction ensures that sample reflections remain undistorted. An example of the results of the sbck background subtraction routine for a pattern collected at 7 GPa is shown in Figure 1(a). Full-pattern Pawley refinement of each diffraction profile is performed using the GSAS-II software package (Toby and Von Dreele, 2013). An example fit to a pattern collected at 7 GPa is shown in Figure 1(b). All reported pressures for the sample are determined using the refined unit cell volumes of gold and the equation of state given by Fei et al. (2007).

3.3 Equation of State Fitting

The pressure-volume data of (Al,Fe)-phase H obtained from the powder X-ray diffraction measurements was fit to a spin crossover equation of state using the MINUTI software package (Sturhahn, 2022). The MINUTI software package implements an equation of state model which accounts for both the elastic and spin contributions (arising from the spin state of the 3d electrons of the Fe atoms) to the free energy of the sample. For a 3rd order Birch-Murnaghan equation of state, the elastic component of the free energy is given by equations (1) and (2):

$$F_{el}(V) = \frac{9}{2}K_0V_0f^2[1 + f(K_0' - 4)] \tag{3.1}$$

$$f = \frac{1}{2}(\frac{V_0}{V})^{2/3} - 1 \tag{3.2}$$

where K_0 represents the bulk modulus at zero pressure, K'_0 refers to the gradient dK/dP at zero pressure, V_0 is the unit cell volume at zero pressure, and f is the eulerian strain. The component of the free energy attributable to the spin state of the Fe atoms is given by equation (3):

$$F_s(V, T) = -k_BTln(Z_s) \tag{3.3}$$

where k_B is the Boltzmann constant, T is the temperature, and Z_s is the spin partition function, defined for the relevant atom (here Fe^{3+}) by the number of unpaired electrons, volume-dependent energy, and orbital degeneracy. When fit to experimental P-V data, this model locates the region of the spin crossover and describes changes in density and compressibility resulting from the spin transition. Equations of state for the high and low-spin states are fit simultaneously. Additional details are given in the MINUTI manual (Sturhahn, 2021). It is well known that estimates of uncertainties on refined unit cell parameters are typically underestimated by full-profile refinement protocols. Therefore, we follow the procedure recommended by Angel, 2000 and implemented in Morrison et al., 2018 in scaling the uncertainties (σ) on

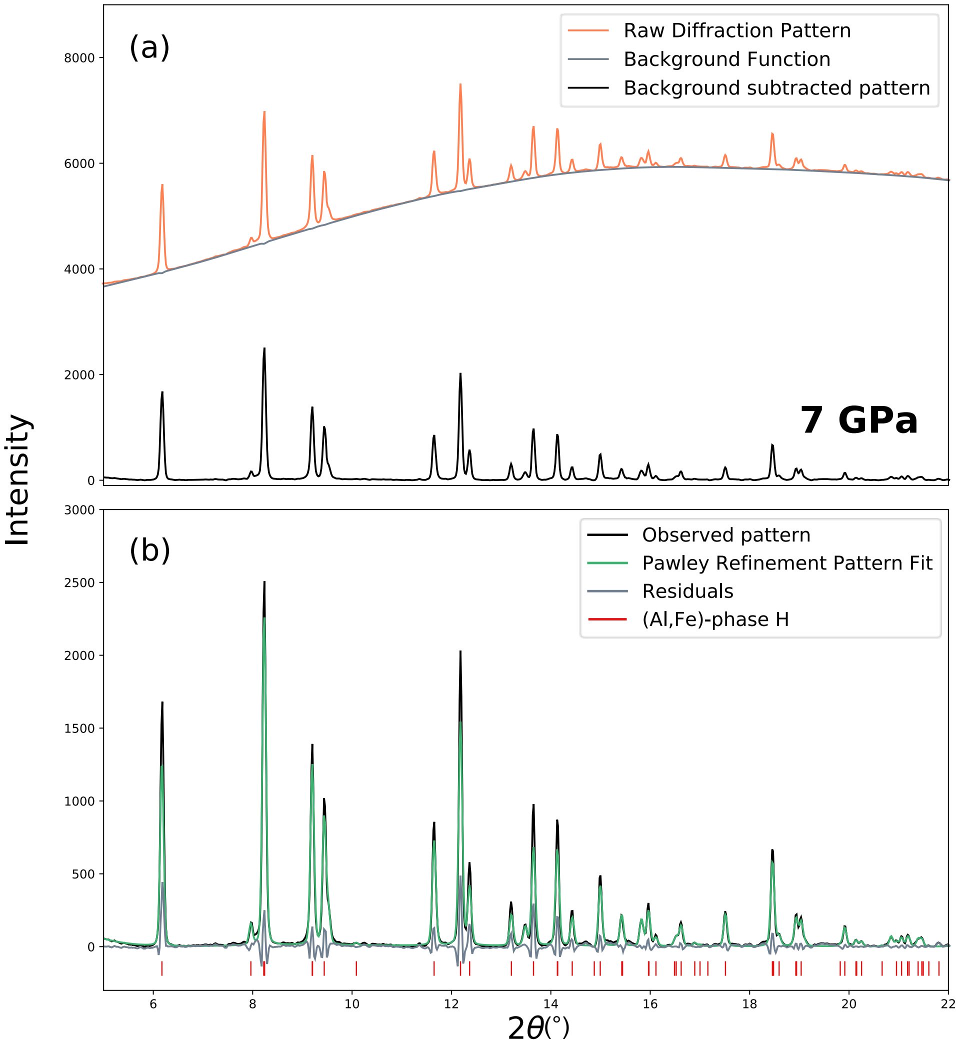

Figure 3.1: a) Example background subtraction using the MINUTI sbck module (nrixs.com). The collected diffraction profile has a substantial but smooth background which can be removed from each profile in the stack to produce a "background subtracted profile" that is more amenable to fitting using whole-profile refinement methods. (b) Example fit to the same background subtracted profile using the Pawley refinement procedure of the GSAS-II software (Toby and Von Dreele, 2013).

unit cell edge lengths by an empirical scaling factor k such that a fit to an appropriate equation of state model produces $\chi^2 \approx 1$. So long as the model used to fit the data is appropriate, χ^2 » 1 indicates that the variance of the data has been underestimated while χ^2 « 1 indicates an overestimate of the variance. Uncertainties on unit cell edge lengths for both the gold pressure calibrant and (Al,Fe)-phase H sample are scaled by a factor of k = 1.5. The scaled uncertainties were subsequently used to calculate the standard deviation of unit cell volumes using standard formulae to propagate experimental uncertainties. Uncertainties in pressure were estimated using the scaled uncertainties of the unit cell volumes of gold, neglecting any uncertainties on the equation of state parameters of gold (Fei et al., 2007a) since their covariance matrix is not reported.

Synchrotron Mössbauer Spectroscopy

Two symmetric diamond anvil cells (DACs) were loaded with powdered (Al,Fe)-phase H and two with δ-(Al,Fe)OOH with Fe/(Al+Fe)=0.13 (δ-Fe13) for synchrotron Mössbauer spectroscopy (SMS) measurements conducted at beamline 3-ID-B of the Advanced Photon Source, Argonne National Laboratory. Each DAC was loaded with a small ruby sphere ($\approx$10 μm diameter) proximal to the center of the gasket hole for online pressure determination using the calibration of (Dewaele et al., 2008). For measurements on (Al,Fe)-phase H, one DAC with 400-μm diameter culets was loaded with compressed He gas at the California Institute of Technology. The measured pressure after gas loading was 1.5 GPa and measurements were performed to a maximum pressure of 22 GPa. A second set of SMS measurements was performed using a DAC with beveled, 300-μm diameter culets at pressures from 0.03 to 53 GPa. For these experiments, the cell was shipped to the Advanced Photon Source and loaded with compressed He gas at the GSECARS/COMPRES gas loading system. Synchrotron Mössbauer spectra were collected on δ-Fe13 samples from 2 to 23 GPa and 15 to 47 GPa using DACs with 400-μm flat and 250-μm beveled culets, respectively, and loaded with compressed He gas at the California Institute of Technology.

Time-domain SMS measurements were performed for the (Al,Fe)-phase H and δ-Fe13 experimental runs during which the storage ring was operated in top-up mode with 24 bunches separated by 153 ns. The beam was focused on an area of 16 x 16 μm^2 at the sample position using a Kirkpatrick-Baez mirror system. A high-resolution monochromator was tuned to the 14.4125 keV nuclear transition energy of ^{57}Fe (Toellner, 2000) and the resonance monitored during collection of time spectra to optimize counting rates. Additional measurements were collected in hybrid mode for (Al,Fe)-phase H at a pressure of 1.5 GPa and δ-Fe13 at 24 GPa, using a focal area of 10 x 10 μm^2. Isomer shifts were derived relative to a stainless steel (SS) reference foil with a natural abundance of ^{57}Fe placed downstream of the sample. Measurements to constrain the isomer shift were taken at the lowest pressure point in each (Al,Fe)-phase H experimental run as well as at 40 GPa. Each reference foil was measured at the APS using a radioactive source to have isomer shifts relative to α-iron metal of -0.100(3) mm/s and -0.094(3) mm/s for the 5 μm and 10 μm thick SS310 foils, respectively (Solomatova et al., 2017).

Synchrotron Mössbauer spectra were fit with version 2.2.2 of the CONUSS software (Sturhahn, 2000) using a time window between 25 and 120 ns in 24-bunch mode and from 50 to 250 ns in hybrid mode. The CONUSS software implements a least-squares algorithm to refine the hyperfine parameters of iron and the effective thickness of the sample. The effective thickness is dimensionless and is the product of the numerical density of the ^{57}Fe atoms, the physical thickness of the sample, the nuclear resonant cross-section (2.56x10^{-22} m^2 for ^{57}Fe), and the Lamb-Mössbauer factor (fraction of recoil-free scattering events). For compression points at which a spectrum was collected with the stainless reference foil, a simultaneous fit of both spectra (with and without the reference foil) was performed. Starting models were informed by the hyperfine parameters of δ-(Al,Fe)OOH reported in Ohira et al. (2019). In fitting SMS spectra of δ-Fe13 in this study, the Lamb-Mössbauer factor at each pressure is interpolated from the Lamb-Mössbauer factors reported in Ohira et al. (2021). The same interpolation is applied to estimate the Lamb-Mössbauer factor of (Al,Fe)-phase H at high pressure, disregarding the transition associated with hydrogen bond disorder in Ohira et al. (2021) as hydrogen bonds are likely disordered at ambient pressure in (Al,Fe)-phase H (see Results and Discussion).

3.4 Results

Crystal Structure of (Al,Fe)-phase H

Single crystal X-ray diffraction patterns of (Al,Fe)-phase H ($Al_{0.84}Fe^{3+}{}_{0.07}Mg_{0.02}Si_{0.06}OOH$) were indexed with the *Pnnm* space group and yielded unit cell parameters at ambient pressure of a_0 = 4.7187(1) Å, b_0 = 4.2285(1) Å, c_0 = 2.8448(1) Å, and V_0 = 56.762(3) Å^3. A rendering of the crystal structure is shown in Figure 2 and a Crystallographic Information File (CIF) file provided in the supporting data (Strozewski et al., 2024). The crystal structure constrained here is similar to that determined for Al-bearing phase H along the δ-AlOOH-$MgSiO_2(OH)_2$ join: $Mg_{0.500}Si_{0.465}Al_{0.035}$

(Bindi et al., 2015), with a_0=4.730(2) Å, b_0 = 4.324(2) Å, c_0 = 2.843(1) Å, and V_0 = 58.15(5) Å^3. (Al,Fe)-phase H crystallizes in the same $CaCl_2$-type structure with edge-sharing octahedra and hydrogen bonds that locate in the a-b plane, albeit with different atomic positions. The substitution of small amounts of Fe^{3+} for Al^{3+} and higher concentration of Al relative to Mg and Si in (Al,Fe)-phase H may be responsible for the observed differences in unit cell edge lengths but does not result in a structural change. In both compositions, cations occupy a single octahedral site and hydrogen bonds are disordered at ambient pressure, as in the end-member $MgSiO_2(OH)_2$ composition (Bindi et al., 2014a). The structure reported here agrees with the observation that a change in space group of δ-AlOOH from $P2_1nm$ to $Pnnm$ is provoked by substitution of even small amounts of Mg and Si for Al (Komatsu et al., 2011). In contrast, the replacement of Al^{3+} by Fe^{3+} substitution does not appear to cause a structural change (Kawazoe et al., 2017; Suzuki et al., 2000).

Powder X-ray Diffraction and Equation of State

A reasonable estimate of the error in pressure when comparing the X-ray diffraction results presented here with previous measurements in the δ-(AlOOH)-($MgSiO_2(OH)_2$)-(ϵ-FeOOH) solid solution is <2%. Pressures reported in Duan et al. (2018) and Gleason et al. (2013) are calibrated with the equation of state of gold reported in Fei et al. (2007a). Thompson et al. (2020) use the Fei et al. (2007a) equation of state for neon. Pressures reported in those studies should therefore be consistent with those reported here. Ohira et al. (2019)) used the calibration of the tungsten pressure scale by Dorogokupets and Oganov (2006), which records pressures that are systematically $\approx$ 1.7% greater than those of the Fei et al., 2007a gold calibration. The Tsuchiya (2003) Au equation of state used to determine pressure in the measurements of Nishi et al. (2019) reports pressures at the relevant pressures and 300 K that are approximately 3% higher than those reported in this study.

Figure 3 shows the normalized unit cell edge lengths and axial ratios of (Al,Fe)-phase H ($Al_{0.84}Fe^{3+}_{0.07}Mg_{0.02}Si_{0.06}OOH$) compared to other compositions in the δ-(AlOOH)-($MgSiO_2(OH)_2$)-(ϵ-FeOOH) solid solution at 300 K (Duan et al., 2018; Gleason et al., 2013; Nishi et al., 2018; Ohira et al., 2019; Thompson et al., 2020). A comparison of normalized unit cell volumes of the same compositions is shown in Figure S1. The linear compressibility of the a-axis is the least sensitive to cation substitution at low pressure (Fe-bearing materials in the high-spin state), as indicated by the similarity in values of a/a_0 between different compositions. The subtle kinks in the compression trends of a/a_0, b/b_0, and c/c_0 in (Al,Fe)-phase H

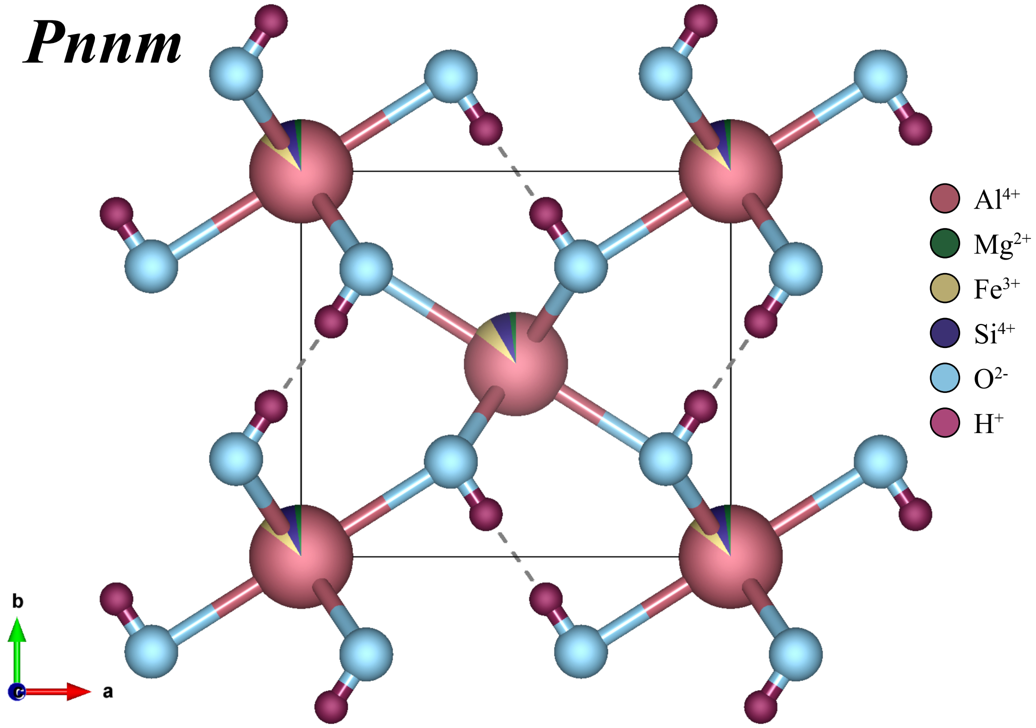

Figure 3.2: Crystal structure of (Al,^{57}Fe)-phase H ($Al_{0.84}{}^{57}Fe^{3+}_{0.07}Mg_{0.02}Si_{0.06}OOH$) (space group *Pnnm*) as determined by single crystal X-ray diffraction. The crystal structure is projected along the crystallographic c-axis. Octahedrally coordinated cations are represented by their colors in proportion to their concentration. A CIF file containing atomic coordinates and structure parameters is available as a supplementary file to the published version of this article. This figure was created with VESTA (Momma and Izumi, 2011).

near 55 GPa are the result of a volume collapse due to a spin transition. There is comparatively little variance in a/a_0 or c/c_0 due to composition in the pressure range shown relative to that observed for b/b_0. The crystal structure of δ-AlOOH appears to be most sensitive along the b-axis to the incorporation of Fe^{3+}: δ-Fe5 exhibits lower values of b/b_0 relative to δ-AlOOH and δ-Fe12 has even lower values. However, this effect does not remain with the substitution of Mg and Si as the length of the crystallographic b-axis in (Al,Fe)-phase H appears to be more invariant to pressure.

Ohira et al. (2019) inferred the symmetrization of hydrogen bonds in δ-(Al,Fe)OOH with Fe/(Al+Fe)=0.12 (δ-Fe12) and Fe/(Al+Fe)=0.05 (δ-Fe5) at approximately 10 GPa based on changes in the trend of the axial ratios as well as on a change in space group from $P2_1nm$ to *Pnnm*. To pressures of about 30 GPa, the trends in ratios of unit

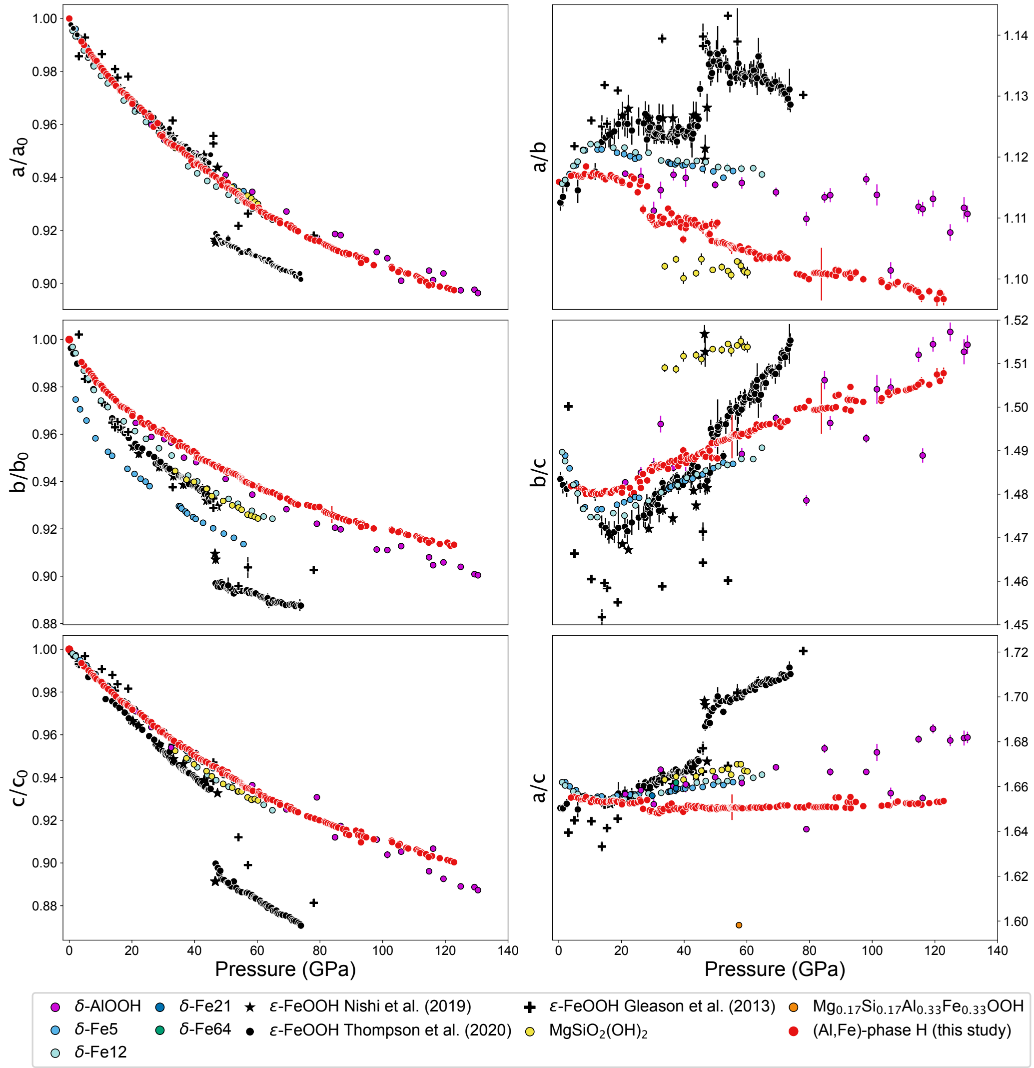

Figure 3.3: Normalized unit cell edge lengths and axial ratios for compositions in the (δ-AlOOH)-($MgSiO_2(OH)_2$)-(ϵ-FeOOH) solid solution at 300K. Measurements at high pressure are obtained from Ohira et al. (2019): δ-$Al_{0.95}Fe_{0.05}OOH$ (δ-Fe5) and δ-$Al_{0.88}Fe_{0.12}OOH$ (δ-Fe12), Nishi et al. (2018): $MgSiO_2(OH)_2$, Duan et al. (2018): δ-AlOOH, and the combined datasets of Gleason et al. (2013), Nishi et al. (2019), and Thompson et al. (2020): ϵ-FeOOH. Unit cell edge lengths at high pressure are normalized by their values at ambient pressure determined by single crystal X-ray diffraction measurements on the same composition: this study (Al,Fe)-phase H, Kawazoe et al. (2017): (δ-Fe5 and δ-Fe12), Bindi et al. (2014a): $MgSiO_2(OH)_2$, Kuribayashi et al. (2014): δ-AlOOH, and Suzuki (2010): ϵ-FeOOH. Values of a/c for δ-$Al_{0.79}Fe_{0.21}OOH$ (δ-Fe21) , δ-$Al_{0.36}Fe_{0.64}OOH$ (δ-Fe64), and $Mg_{0.17}Si_{0.17}Al_{0.33}Fe_{0.63}OOH$ reported by Nishi et al. (2019) are shown in the lower right panel of this figure.

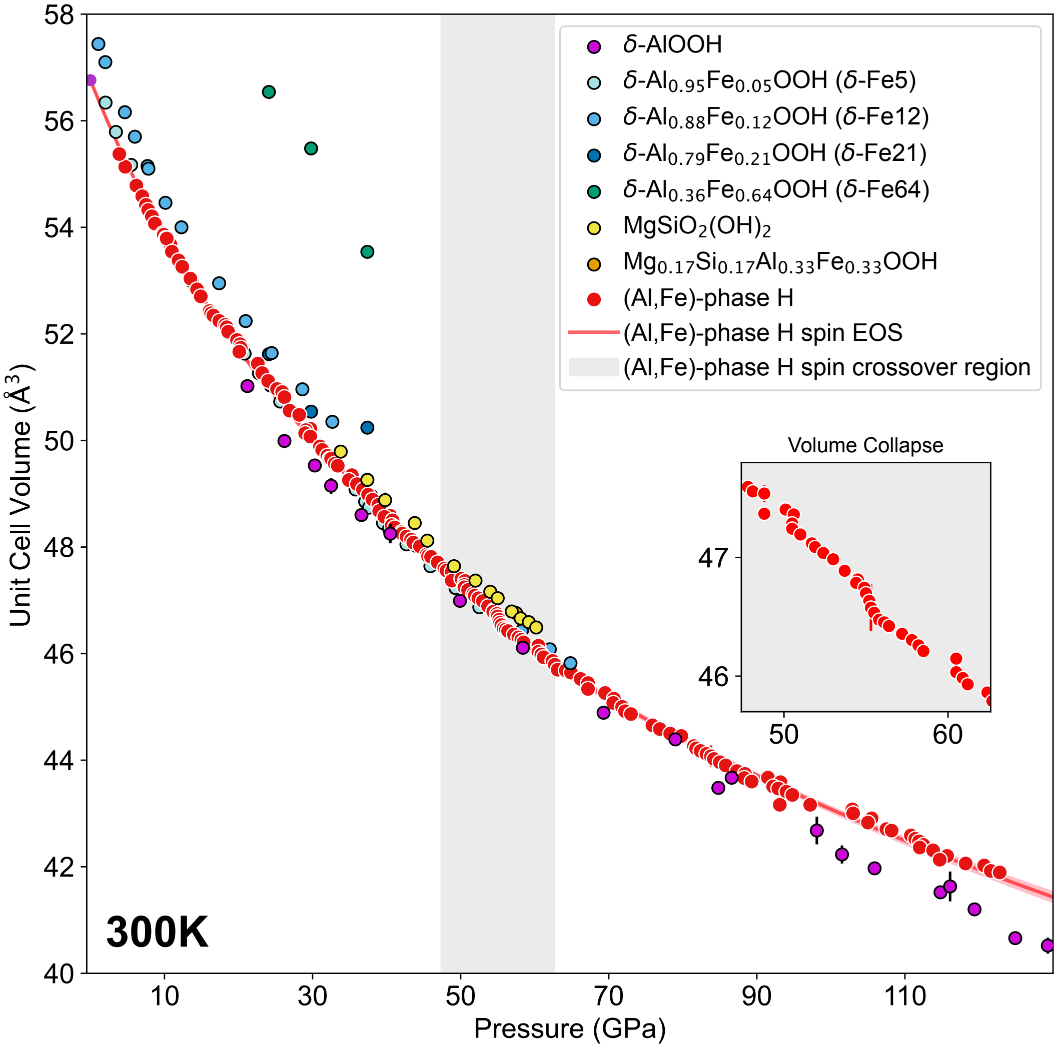

Figure 3.4: *P*-*V* data for (Al,Fe)-phase H fit to a spin equation of state using the MINUTI software package (χ^2 = 1.21(9)). For discussion of uncertainties in fitting *P*-*V* data to an equation of state see the methods section. The gray shaded region indicates the spin crossover region (total width ≈ 15 GPa) determined by fitting the spin equation of state. The equation of state is compared to unit cell volume data for other compositions in the (δ-AlOOH)-($MgSiO_2(OH)_2$)-(ϵ-FeOOH) solid solution at 300 K. *P*-*V* data for other compositions were obtained from Ohira et al. (2019): δ-Fe5 and δ-Fe12, Nishi et al. (2018): $MgSiO_2(OH)_2$, Duan et al. (2018): δ-AlOOH, and Nishi et al. (2019): δ-Fe21 and δ-Fe64. Due to the significantly larger unit cell volume, data for ϵ-FeOOH is omitted from this figure for clarity.

cell edge lengths vs. pressure observed in (Al,Fe)-phase H are flat, especially when compared to the same trends observed in δ-(Al,Fe)OOH (Figure 3). At pressures greater than 30 GPa, the decrease in the ratio *a/b* with pressure is steeper than what is observed for δ-(Al,Fe)OOH, regardless of iron concentration. The ratio *a/c* remains approximately constant to a pressure of 120 GPa whereas the magnitude of the increase of *b/c* with pressure is similar to that observed in δ-(Al,Fe)OOH. The ratio *a/c* of (Al,Fe)-phase H is lower than for δ-(Al,Fe)OOH and is the lowest for $Mg_{0.17}Si_{0.17}Al_{0.33}Fe_{0.63}OOH$, implying that increasing concentration of Mg and Si in δ-(Al,Fe)OOH decreases *a/c*. Axial ratios of δ-AlOOH (Duan et al., 2018) exhibit the same general trends observed for δ-(Al,Fe)OOH to 120 GPa.

Figure 4 shows *P-V* data for compositions in the δ-(AlOOH)-($MgSiO_2(OH)_2$)-(ϵ-FeOOH) solid solution and the equation of state constrained for (Al,Fe)-phase H. For clarity, the much larger unit cell volumes of ϵ-FeOOH are not plotted. Comparison of ϵ-FeOOH to other compositions based on normalized unit cell volumes is shown in Figure S1. Equation of state parameters for compositions plotted in Figure 4 are given in Table 1. In Table 1, the data range for a spin equation of state includes all data used in the fit, with the spin transition pressure and width as free parameters.

The spin transition pressure determined by fitting the spin crossover equation of state is defined as the pressure at which the change in unit cell volume due to the spin transition is 50% complete, constrained here for (Al,Fe)-phase H as 55.5 ± 0.9 GPa. The spin crossover region determined from the equation of state is 48-63 GPa (width of 15 GPa at 300 K). This region does not overlap with the spin crossover determined for δ-(Al,Fe)OOH. On the basis of changes in the unit cell volume, the spin crossover in δ-(Al,Fe)OOH occurs over a pressure range of approximately 8 GPa and is 50% complete in δ-Fe5 at 35(1) GPa, and 36.1(7) GPa, in δ-Fe12 (Ohira et al., 2019). Figure 5 illustrates correlations between unit cell volume and the isothermal bulk modulus of δ-(Al,Fe)OOH and (Al,Fe)-phase H at various pressures as confidence ellipses obtained from the equation of state fits, further discussed below.

Synchrotron Mössbauer Spectroscopy

Fits to (Al,Fe)-phase H ($Al_{0.84}Fe^{3+}_{0.07}Mg_{0.02}Si_{0.06}OOH$) SMS spectra collected in 24-bunch mode are shown in Figure 6. Fits to spectra collected on δ-(Al,Fe)OOH with Fe/(Al+Fe)=0.13 (δ-Fe13) in 24-bunch mode are shown in Figure S2. Hyperfine parameters determined for each phase are given in Tables 2-3 ((Al,Fe)-phase H) and Tables S1-S2 (δ-Fe13). Mössbauer spectra collected in 24 bunch mode (delay

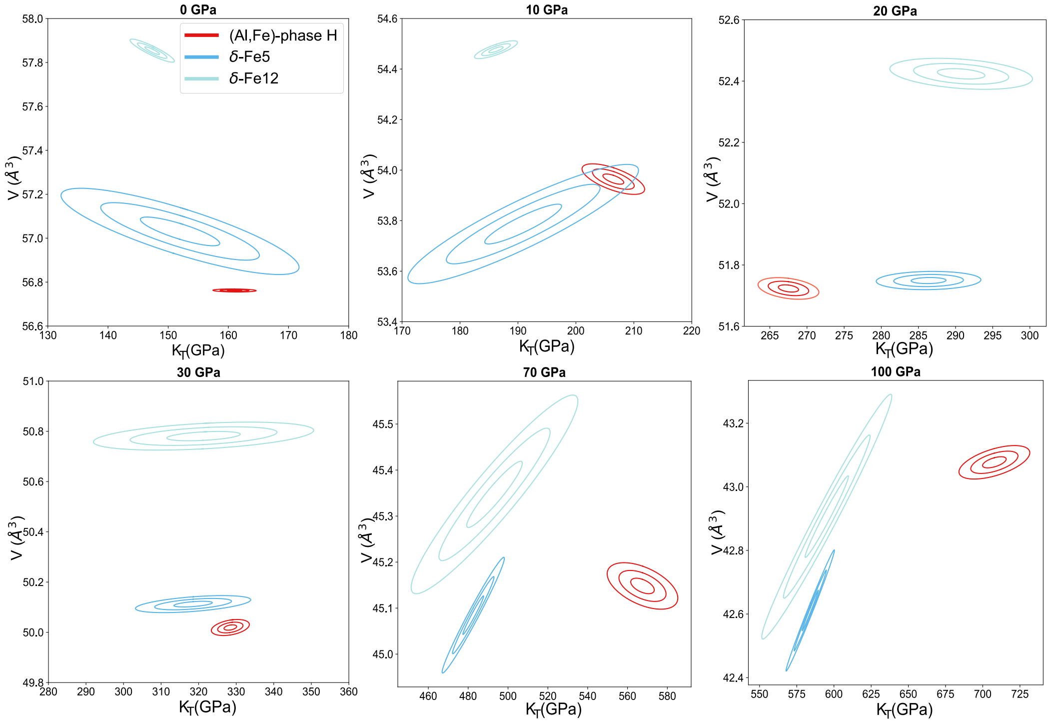

Figure 3.5: Confidence ellipses for correlations between unit cell volume (V) and bulk modulus (K_T) at 0, 10, 20, 30, 70, and 100 GPa from equation of state fits to (Al,Fe)-phase H (this study) and δ-(Al,Fe)OOH (Ohira et al., 2019).The inner ellipses represent the 39% confidence interval of these two parameters at the indicated pressure. The outer ellipses represent the 86% confidence interval and the outermost ellipses represent the 99% confidence interval.

times of 25-150 ns) at low pressures (P < 33 GPa) during both (Al,Fe)-phase H experimental runs are well described using a model with a single ferric iron site (${Fe_A}^{3+}$), in accordance with the single crystallographic site occupied by Fe^{3+} in the crystal structure of (Al,Fe)-phase H. The best-fitting model at pressures higher than 33 GPa requires the introduction of a second site (${Fe_B}^{3+}$) that is distinguishable from ${Fe_A}^{3+}$ by its hyperfine parameters. The spectra collected on δ-Fe13 also require the introduction of a second site at $\approx$ 40 GPa. When multiple sites are required to fit the Mössbauer spectra, we perform a Monte Carlo search over a large parameter space using the CONUSS module kmco. Good models at each pressure cannot be obtained by fixing the weight fractions of the Mössbauer sites over a pressure range as performed in Ohira et al. (2019). Instead, the weight fractions of the two sites at each pressure are obtained by the best sampling in the monte carlo parameter search. Least-squares refinement of hyperfine parameters, physical thickness, and sample texture are then performed using the CONUSS module “kctl” to determine the best model.

Hybrid mode collection allows access to longer delay times than data collected in 24-bunch mode, as shown in Figure S3. Access to longer delay times provides improved spectral resolution and allows for more precise fitting of potentially minor Fe sites or small differences in model parameters, including differences which may arise from deviatoric stresses. In contrast to the data collected in 24-bunch mode, the hybrid mode spectra for both (Al,Fe)-phase H (1.50 GPa) and δ-Fe13 (23.31 GPa) require a second site to obtain the best model (Table 3 and Table S2). At 1.5 GPa in (Al,Fe)-phase H, the two sites have approximately equal weight with distinct hyperfine parameters. Site A has an isomer shift, quadrupole splitting, and full width at half-maximum (FWHM) values of 0.308(3), 0.494(3), and 0.236(1) in units of mm/s. These values are similar to those used in the single site model of the spectrum collected during 24-bunch mode at this pressure. In contrast, site B is broad (FWHM = 1.31(1) mm/s) and has a higher isomer shift (0.574(9) mm/s) and lower quadrupole splitting (0.29(2) mm/s). At 23.31 GPa in δ-Fe13, the hyperfine parameters of the two sites differ only slightly (Table S1). Site A is the dominant contributor to the observed spectrum (wt. fraction = 0.9). A comparison of the two-site model to the best models obtained using a single site is shown in Figure S3.

The quadrupole splittings determined from 24-bunch mode data in this study are compared to those determined for δ-(Al,Fe)OOH (Ohira et al., 2019) in Figure 7a. Comparison of isomer shifts and weight fractions of the Mössbauer sites are plotted in Figure 7b and Figure 7c, respectively. At low pressure, low values of quadrupole splitting and isomer shift confirm the sole presence of ferric iron (Fe^{3+}) (Bromiley and Hilairet, 2005; De Grave et al., 2006; Douvalis et al., 2000; Dyar et al., 2006; Lyubutin et al., 2009) in both (Al,Fe)-phase H and δ-(Al,Fe)OOH. Quadrupole splittings of the A site in (Al,Fe)-phase H exhibit a general decrease with pressure from a value of 0.403(2) to 0.177(2) mm/s at 32.1(3) GPa. Quadrupole splittings of the A site in δ-Fe13 are approximately constant across the same pressure range.

Between 34 and 45 GPa, quadrupole splittings of both ${Fe_A}^{3+}$ and ${Fe_B}^{3+}$ increase for both compositions. Over the same pressure range, the weight fraction of the ${Fe_A}^{3+}$ site (lower quadrupole splitting) in (Al,Fe)-phase H decreases, achieving a minimum value of 0.34 in (Al,Fe)-phase H at 40.1 GPa. The quadrupole splitting of the ${Fe_A}^{3+}$ site in (Al,Fe)-phase H increases disproportionately at pressures higher than 45 GPa relative to that of the ${Fe_B}^{3+}$ site, which plateaus and then increases gradually. In contrast, the quadrupole splittings of each site in δ-Fe13 increase

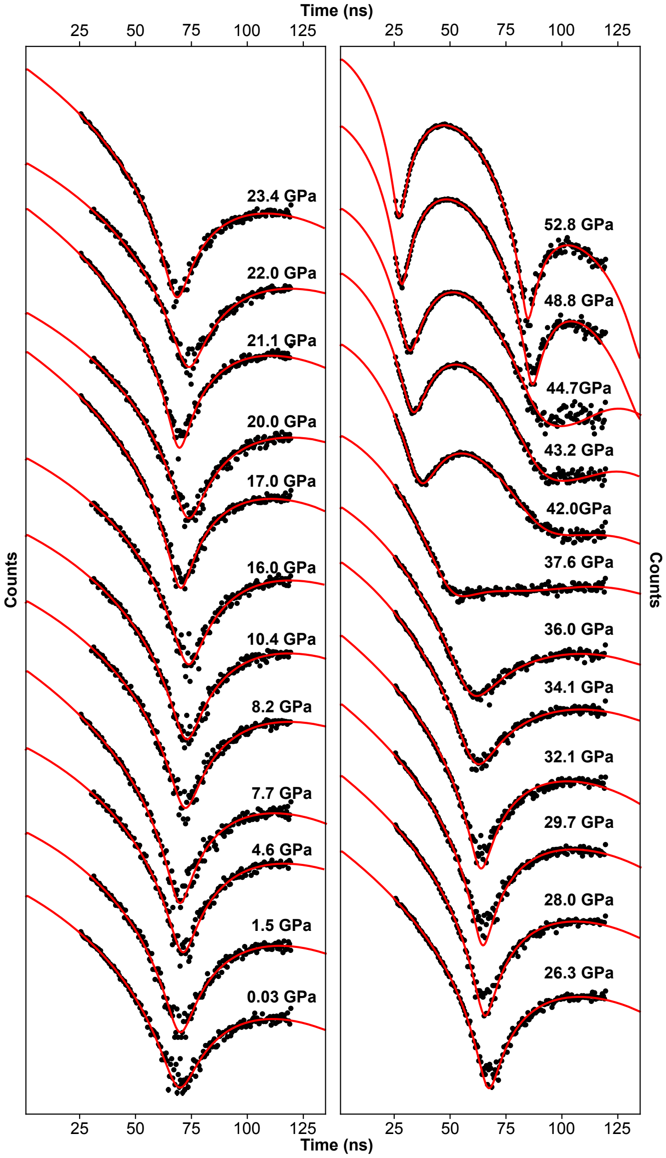

Figure 3.6: SMS spectra of (Al,Fe)-phase H and fits for data collected in 24-bunch mode and without a reference foil are shown at each measured pressure. Spectra are arbitrarily offset for clarity. Fits are performed to time-domain spectra using the CONUSS software package. Resultant hyperfine parameters, uncertainties in pressure, and χ^2 values are given in Tables 2 and 3.

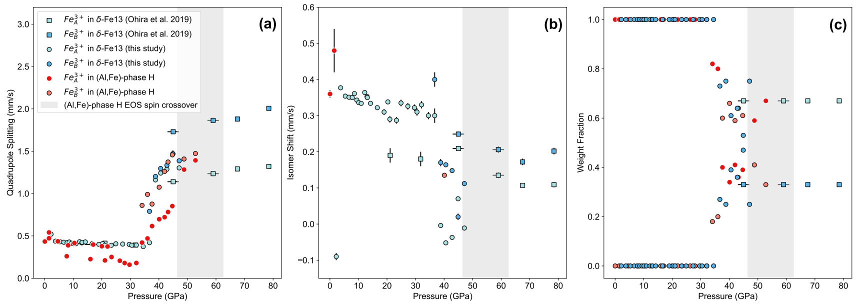

Figure 3.7: Hyperfine parameters and weight fractions of models for Fe^{3+} sites determined from 24-bunch mode data. (a) Quadrupole splittings (QS) of Fe^{3+} in (Al,Fe)-phase H and δ-(Al,Fe)OOH with Fe/(Al+Fe)=0.13(2) (δ-Fe13) compared to those previously reported for δ-(Al,Fe)OOH with Fe/(Al+Fe) = 0.133(3) (δ-Fe13) in Ohira et al. (2019). At low pressures, only one site is necessary to describe the observed SMS data (${Fe_A}^{3+}$). A second Mössbauer site is introduced (${Fe_B}^{3+}$) at pressures higher than 32 GPa for (Al,Fe)-phase H and at 37 GPa for δ-(Al,Fe)OOH. (b) Isomer shifts obtained using a stainless steel reference foil. (c) Weight fractions of the Fe^{3+} sites used to fit synchrotron Mössbauer spectra. Uncertainties (1σ) in pressure and hyperfine parameters are plotted but are generally smaller than the size of the symbols.

relatively smoothly and approach the values determined at higher pressures in Ohira et al. (2019).

Values of the isomer shift decrease with increasing pressure for both (Al,Fe)-phase H and δ-(Al,Fe)OOH (Figure 7b), reflecting an increase in s-electron density at the nucleus of the Fe atom due to compression. At $\approx$ 40 GPa in (Al,Fe)-phase H, the best-fitting model has two sites with identical isomer shifts relative to α-Fe (0.145(6) mm/s), which does not unambiguously determine the spin state of the Fe atoms. In contrast, the fits to δ-(Al,Fe)OOH spectra above 37 GPa require low or negative isomer shifts for site A (Table S2) that identify low-spin Fe^{3+} (Gütlich and Garcia, 2012). Isomer shifts constrained on the same composition in (Ohira et al., 2019) are significantly higher but still reflect values typical of low-spin Fe^{3+}.

3.5 Discussion

Comparison to previous studies

A previous study of δ-($Al_{0.86}Mg_{0.07}Si_{0.07}$)OOH (Komatsu et al., 2011), revealed that substitution of even small amounts of Mg and Si into the structure of δ-AlOOH results in disordering of hydrogen bonds at ambient pressure and in a change in space group from *$P2_1nm$* to *Pnnm*. In contrast, substitution of ferric iron for aluminum does not result in hydrogen bond disorder or a change in space group (Kawazoe et al., 2017). Therefore, the disordering of hydrogen bonds at ambient pressure in (Al,Fe)-phase H is likely due to the incorporation of Mg and Si as confirmed by our crystal structure determination (Figure 2, space group *Pnnm*), and the lack of an order-disorder transition upon compression, as observed for δ-(Al,Fe)OOH (Ohira et al., 2019).

The compressional behavior of (Al,Fe)-phase H ($Al_{0.84}Fe^{3+}{}_{0.07}Mg_{0.02}Si_{0.06}OOH$) is distinct from that of δ-(Al,Fe)OOH as well as that of the end-members δ-AlOOH, $MgSiO_2(OH)_2$, and ϵ-FeOOH, implying the incorporation of Mg and Si into the crystal structure has important effects on bulk elastic properties relative to compositions which contain only Al and Fe. At pressures lower than 10 GPa, the bulk modulus of (Al,Fe)-phase H is comparable to that of δ-(Al,Fe)OOH (Figure 5) and the presence of Mg and Si in (Al,Fe)-phase H does not appear to exert a strong influence. Due to the order-disorder transition of hydrogen bonds, δ-(Al,Fe)OOH becomes less compressible than (Al,Fe)-phase H between 10 and 32 GPa (Figure 5). At 32 GPa, the high to low spin crossover of Fe^{3+} in δ-(Al,Fe)OOH results in increased compressibility compared to (Al,Fe)-phase H. At pressures greater than 70 GPa — where Fe^{3+} in both (Al,Fe)-phase H and δ-(Al,Fe)OOH is in the low-spin state — the bulk moduli and unit cell volumes of the two compositions remain clearly distinguishable, based on the correlations of these parameters from the respective equation of state models (Figure 5). Some of the differences in the constrained isothermal bulk moduli of δ-(Al,Fe)OOH and (Al,Fe)-phase H at pressures greater than 70 GPa may be due to the extrapolation of the equation of state determined in Ohira et al. (2019) from data collected at lower pressure. Ohira et al. (2019) fixed K_T' to a value of 4 in fitting data to the low-spin state of δ-(Al,Fe)OOH due to a lack of data above 70 GPa. This also marks the pressure at which the density, bulk modulus, and bulk sound velocity of (Al,Fe)-phase H begin to deviate from δ-(Al,Fe)OOH due to a considerably higher value of K_T' (Table 1). The larger isothermal bulk modulus of (Al,Fe)-phase H relative to δ-AlOOH, δ-(Al,Fe)OOH, and ϵ-FeOOH may also be attributable to the substitution of Mg and Si into the crystal structure. The mechanism by which this substitution results in a less compressible crystal lattice is presently unclear but could be related to the specific way in which strain is accommodated within each crystal lattice, for which single crystal X-ray diffraction data is needed. With Mg^{2+} having the largest ionic radius of all cations in the δ-(AlOOH)-($MgSiO_2(OH)_2$)-(ϵ-FeOOH) solid solution, the large Mg cations might support the crystal structure and, to some extent, prevent the sites hosting smaller cations from contracting. The relative controls that cation substitution and the high-low spin crossover of Fe^{3+} place on the compressibility of the δ-(AlOOH)-($MgSiO_2(OH)_2$)-(ϵ-FeOOH) solid solution could be clarified by additional constraints on the equation of state of δ-(Al,Fe)OOH to pressures exceeding 70 GPa or an equation of state of another composition in this solid solution.

The onset of the spin transition at a lower pressure in δ-(Al,Fe)OOH (32-40 GPa) compared to ϵ-FeOOH led Ohira et al. (2019) to infer that the spin transition pressure in the (δ-AlOOH)-(ϵ-FeOOH) solid solution would increase with increasing iron concentration, an effect confirmed via Raman spectroscopy (Su et al., 2021b) and also observed for varying concentrations of Fe^{2+} in (Mg,Fe)O (Fei et al., 2007b; Lin et al., 2005; Solomatova et al., 2016). Nishi et al., 2019 observed a spin crossover of Fe^{3+} at approximately 46 GPa in δ-(Al,Fe)OOH with Fe/(Al+Fe) = 0.23 and Fe/(Al+Fe)=0.67. These results corroborate the positive correlation between Fe^{3+} concentration and spin transition pressure in δ-(Al,Fe)OOH at low Fe^{3+} but imply that there may be a critical Fe^{3+} concentration at which this effect becomes negligible. The (Al,Fe)-phase H composition studied here contains 7 wt. % Fe3+, which is within the range of iron concentrations in δ-(Al,Fe)OOH studied in Ohira et al. (2019). We would therefore expect the spin transition to occur at a similar pressure ($\approx$ 35 GPa) if the substitution of Mg and Si did not affect the spin transition pressure. However, the spin crossover inferred from our (Al,Fe)-phase H equation of state occurs at a significantly higher pressure (48-63 GPa) than that in δ-(Al,Fe)OOH and is more similar to that constrained for ϵ-FeOOH (43-47 GPa; Thompson et al., 2020, 46-54 GPa; Gleason et al., 2013) albeit with a larger width. It is therefore apparent that dissolution of Mg and Si into the crystal structure of δ-(Al,Fe)OOH has the same effect as increasing the Fe concentration: stabilization of high-spin Fe^{3+} to higher pressures. The reasons for the persistence of high-spin Fe^{3+} to higher pressures in (Al,Fe)-phase H relative to δ-(Al,Fe)OOH could be related to differences in ionic radii, to how Mg and Si cations affect the hydrogen bonds in the crystal lattice, and to how strain is accommodated at high pressure.

Inferring multiple transitions in the δ-AlOOH -$MgSiO_2(OH)_2$-ϵ-FeOOH system

The inversion of axial compressibility inferred to be a signature of a hydrogen bond-order disorder transition observed in δ-(Al,Fe)OOH at 10 GPa (Figure 3) is not observed in (Al,Fe)-phase H because hydrogen bonds are disordered in (Al,Fe)-

phase H at ambient conditions. Since hydrogen bonds in (Al,Fe)-phase H lie in the *a*-*b* plane, strengthening of these bonds is likely to produce noticeable changes in relative compressibilities along the crystallographic axes. In particular, the compressibility along the crystallographic *a* and *b* axes is expected to decrease while compressibility along the *c*-axis remains largely unaffected by changes in hydrogen bonding. At pressures greater than approximately $\approx$ 30 GPa, the *b*-axis becomes significantly less compressible than either the *a* or *c*-axis in (Al,Fe)-phase H ($Al_{0.84}Fe^{3+}{}_{0.07}Mg_{0.02}Si_{0.06}OOH$) (Figure 3). A decrease in compressibility along the *b*-axis associated with hydrogen bond order-disorder or symmetrization has also been observed in ϵ-FeOOH (18 GPa; Thompson et al. (2020), 43 GPa; Gleason et al. (2013)), $MgSiO_2(OH)_2$ (30 GPa; Nishi et al. (2018)), and δ-AlOOH ($\approx$10 GPa; Sano-Furukawa et al., 2009b; Sano-Furukawa et al., 2018; 8.2 GPa; Kuribayashi et al., 2014).

The compressional behavior observed here for (Al,Fe)-phase H is similar to that of Fe-Al bearing phase D ($MgFe^{3+}{}_{0.15}Al_{0.32}Si_{1.5}H_{2.6}O_6$; Chang et al., 2013), although the two compositions are not isostructural (Fe-Al bearing phase D crystallizes in a trigonal structure with space group *P*31*m*). The spin transition region inferred from our equation of state is similar to that observed for octahedrally coordinated Fe^{3+} in Fe-Al bearing phase D (40-65 GPa) (Chang et al., 2013). Additionally, the pressure at which the *c/a* ratio becomes constant in Fe-Al bearing phase D is $\approx$40 GPa, seemingly unrelated to the Fe^{3+} spin transition (Chang et al., 2013) and comparable to the $\approx$35 GPa observed in this study. A relatively constant ratio of *a/c* reflects similar compressibility along the *a* and *c* axes and has been interpreted to be the result of hydrogen bond symmetrization (Chang et al., 2013; Hushur et al., 2011; Litasov et al., 2007; Shinmei et al., 2008), although this interpretation was not confirmed by infrared spectroscopy measurements, as discussed in Thompson et al., 2020.

The decrease in compressibility of the *b*-axis relative to the *a* and *c* axes in (Al,Fe)-phase H may instead reflect a change in the how strain is accommodated within the crystal structure. Single crystal X-ray diffraction measurements revealed a change in the mechanism by which strain is accommodated in trigonal ϵ-FeOOH at low ($P < 16$ GPa) and high ($P > 16$ GPa) pressure Xu et al., 2013. That is, at pressures below 16 GPa, strain is accommodated along the channels containing the hydrogen bonds which are parallel to the *b*-axis and more compressible relative to the Fe^{3+} octahedra. At pressures greater than 16 GPa, compression of Fe^{3+}

octahedra accommodates a larger proportion of the strain, a change not associated with hydrogen bond symmetrization which occurs at higher pressures. Therefore, the decrease in compressibility of the b-axis in (Al,Fe)-phase H and constant *a/c* ratio observed in this study at 30-35 GPa may indicate a symmetrization of hydrogen bonds. Alternatively, it may represent a change in the dominant mechanism of strain accommodation within the crystal structure without hydrogen bonds becoming fully symmetric at the same pressure.

The best-fitting model to SMS spectra collected in 24-bunch mode at pressures greater than 35 GPa requires the introduction of a second Mössbauer site for ferric iron (Figure 7). Data collected with access to longer delay times (hybrid mode) require a second Mössbauer site at lower pressures in both compositions (Table 3 and Supplementary Table S2, Supplementary Figure S3). The significant difference in hyperfine parameters between Mössbauer sites in δ-Fe13 at $\approx$37 GPa implies a distinct change in the coordination environment and/or the electronic structure of ferric iron. In (Al,Fe)-phase H, the second site at 1.5 GPa could be a result of hydrogen bond disorder. Komatsu et al. (2011) demonstrated that incorporation of Mg and Si into the structure of δ-AlOOH results in disordering of hydrogen bonds and hypothesized that the positions of hydrogen atoms may be affected by the local arrangement of cations. In this context, two Fe^{3+} Mössbauer sites may manifest as a result of two different local arrangements of cations, which may also be important in determining the strength and degree of disordering of hydrogen bonds. This effect may only be observable at low pressures with the longer timing window and more precise measurements conducted in hybrid mode.

The measurements reported here confirm the steep increase in quadrupole splitting of both Fe^{3+} sites in δ-(Al,Fe)OOH that is closely linked to the unit cell volume collapse observed at $\approx$35 GPa. Ohira et al. (2019) found that two low-spin Fe^{3+} sites were necessary to describe SMS spectra collected above 45 GPa. Here we find that two sites are necessary at pressures above approximately 37 GPa, where the low-spin fraction of Fe^{3+} is close to 0.5 based on the equation of state model (Figure 8a).

The quadrupole splittings of ${Fe_A}^{3+}$ and ${Fe_B}^{3+}$ in (Al,Fe)-phase H also increase above 35 GPa. In contrast to δ-(Al,Fe)OOH, the quadrupole splitting of ${Fe_A}^{3+}$ in (Al,Fe)-phase H undergoes a second steep increase at $\approx$50 GPa, close to the lower pressure limit of the spin transition region inferred from our equation of state. Additionally, quadrupole splitting values of both sites in (Al,Fe)-phase H continue to increase at the highest measured pressures (53 GPa), whereas those of δ-(Al,Fe)OOH increase only gradually with pressure beyond 45 GPa, indicating that the spin transition is not complete in (Al,Fe)-phase H at 53 GPa.

Whereas the F-f plot of δ-(Al,Fe)OOH shows a single decrease due to the spin transition of Fe^{3+} at 35 GPa (Figure 8b), values of normalized pressure for (Al,Fe)-phase H decrease separately at 35 and 62 GPa and increase only gradually between 35 and 62 GPa, demarcating 3 separate regions in the compression curve. With the interpretation that hydrogen bond symmetrization occurs at 35 GPa, these regions correspond to (i) high-spin Fe^{3+} with disordered hydrogen bonds ($P < 35$ GPa), (ii) high-spin Fe^{3+} with symmetric hydrogen bonds ($35 < P < 62$ GPa), and (iii) low-spin Fe^{3+} with symmetric hydrogen bonds (Figure 8b). Region (ii) cannot be discerned from the F-f curve for δ-(Al,Fe)OOH, which could be a result of hydrogen bond symmetrization and the spin transition occurring at similar pressures, as noted in Ohira et al. (2019). The appearance of a second Fe^{3+} Mössbauer site in (Al,Fe)-phase H at the boundary between regions (i) and (ii) prior to the spin crossover leads to the conclusion that the second Mössbauer site is unrelated to the spin crossover, at least for (Al,Fe)-phase H. However, a combination of single crystal X-ray diffraction data and infrared spectroscopy measurements at these pressures would better constrain the relationship between hydrogen bond symmetrization and the Fe^{3+} spin crossover in both (Al,Fe)-phase H and δ-(Al,Fe)OOH.

3.6 Implications

The data presented here reveal that the incorporation of Mg and Si into Fe-bearing compositions in the (δ-AlOOH)-($MgSiO_2(OH)_2$)-(ϵ-FeOOH) solid solution decreases their compressibility (Figure 9b). Increasing Fe concentration tends to increase the spin transition pressure, at least for low Fe concentrations (< 30 wt.%) as does increasing concentration of Mg and Si. In the context of the solid solution, the spin transition pressure shifts to higher pressure with a decreasing proportion of δ-AlOOH. Therefore, we predict that the “Al-rich phase H” samples ($Al_{0.63}Fe_{0.03}Mg_{0.11}Si_{0.2}$)OOH synthesized by Liu et al. (2019) would be less compressible and undergo a spin crossover at higher pressures compared to the samples studied here ($Al_{0.84}Fe^{3+}_{0.07}Mg_{0.02}Si_{0.06}OOH$). Additional measurements of compressibility and seismic wavespeeds on non-end-member compositions within this solid solution are needed to provide quantitative constraints on this prediction and its effects on elastic properties. In particular, if (Al,Fe)-phase H forms due to dehydration processes at the base of the lower mantle (Ohtani, 2020), the cation

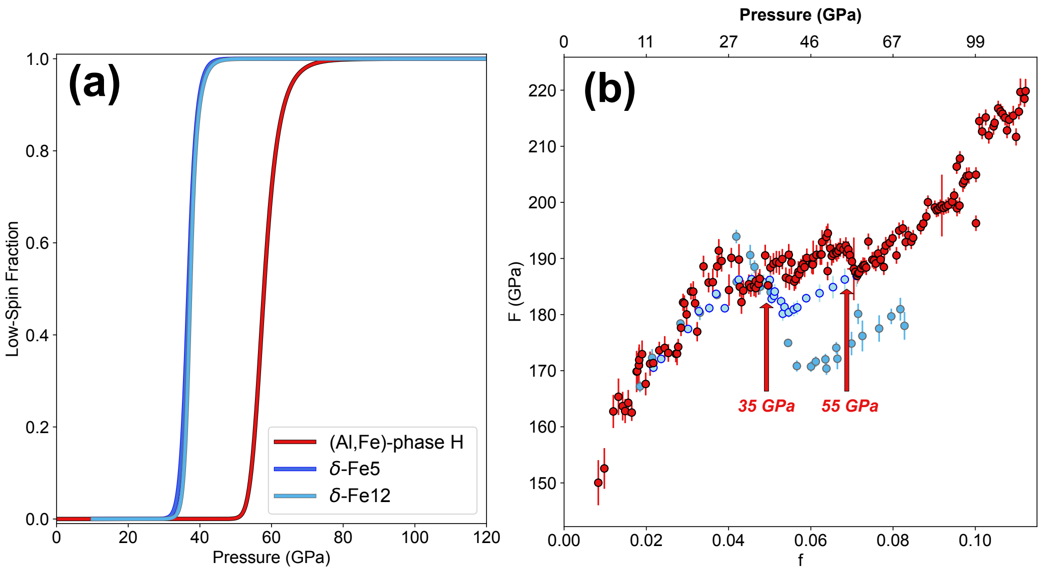

Figure 3.8: (a) Fraction of Fe^{3+} atoms in the low-spin state in (Al,Fe)-phase H and δ-(Al,Fe)OOH determined from the respective equation of state models. Low-spin fraction of δ-Fe5 and δ-Fe12 is determined by refitting the P-V data reported in Ohira et al. (2019) using the same equation of state parameters (within uncertainty). (b) Normalized stress (F) as a function of normalized strain (f) of (Al,Fe)-phase H and δ-(Al,Fe)OOH.

concentration (and consequently, the seismic wavespeeds) may be significantly different from those measured on samples synthesized at pressures and temperatures of the mantle transition zone. Modeling of MORB hydration by formation of phases in the (δ-AlOOH)-($MgSiO_2(OH)_2$)-(ϵ-FeOOH) solid solution may result in increased seismic velocities of hydrous MORB relative to pyrolitic mantle just below the mantle transition zone (≈680-900 km; Satta et al., 2021). However, the V_P and V_S values constrained for δ-($Al_{0.97}Fe_{0.03}$)OOH and used in the modeling for seismic velocities of this solid solution are significantly faster than those constrained for compositions with greater concentrations of Fe: (δ-($Al_{0.87}Fe_{0.13}$)OOH; Ohira et al., 2021, ($Al_{0.956}Fe_{0.044}$)OOH; Su et al., 2021a . Comparison of seismic wavespeeds predicted by these studies reveal a decrease in both V_P and V_S with increasing Fe concentration, complicating the modeled seismic signature of MORB hydration and highlighting the need for additional measurements of seismic wavespeeds of compositions in the (δ-AlOOH)-($MgSiO_2(OH)_2$)-(ϵ-FeOOH) solid solution.

Seismological studies have observed the presence of small-scale seismic scatterers in the mid-lower mantle (1100-1800 km; 43-78 GPa) and attributed the observed scattering to the presence of basaltic material transported into the lower mantle

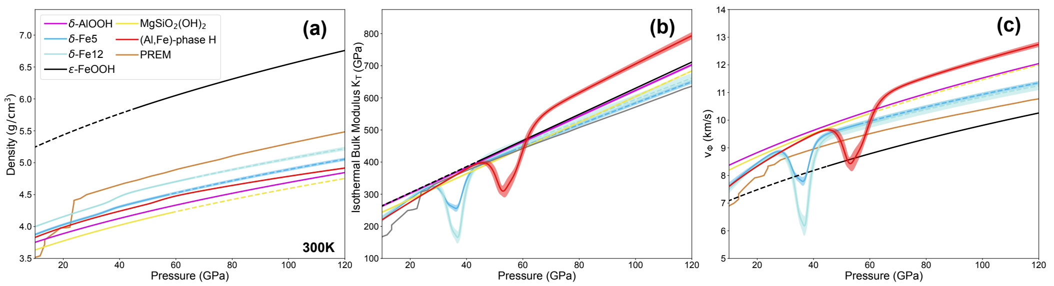

Figure 3.9: (a) Density, (b) Isothermal bulk modulus, and (c) bulk sound velocity of compositions in the (δ-AlOOH)-($MgSiO_2(OH)_2$)-(ϵ-FeOOH) solid solution at 300 K compared to PREM (Dziewonski and Anderson, 1981). Values for δ-Fe5 and δ-Fe12 were determined by refitting the *P-V* data reported in Ohira et al. (2019) with the same equation of state parameters (within uncertainty). Values for δ-AlOOH and $MgSiO_2(OH)_2$ were determined from the equations of state reported by Duan et al. (2018) at 300 K and Nishi et al. (2018), respectively. ϵ-FeOOH is plotted in the low-spin state using the equation of state parameters reported in Thompson et al. (2017). Shaded regions indicate uncertainties at the 68% confidence level (1σ). Extrapolations of values to pressures beyond those of the measured data or applicable pressures of the respective equations of state used are shown as dashed lines.

by a subducting slab (Kaneshima, 2016). For example, Bentham and Rost (2014) observed small-scale scatterers associated with the Mariana slab in the western Pacific to depths of 1480 km (≈65 GPa), as well as at other subduction zones in this region. Similarly, scatterers associated with high velocity anomalies interpreted to be fossil slabs in the mid-lower mantle (≈700-1600 km) were observed by Saki et al. (2022) and Rochira et al. (2022). Chang et al. (2013) discussed the possibility that seismic scatterers in this depth range could be explained by the spin transition of Fe^{3+} in Fe-Al bearing phase D. The spin crossover of (Al,Fe)-phase H (48-63 GPa) spans a similar pressure range as that of Fe-Al bearing phase D (40-65 GPa) (Chang et al., 2013), and gives rise to a large decrease in bulk sound velocity over approximately the same depth range (≈1100 to 1550 km). However, the synthesis experiments of Liu et al. (2019) demonstrated that Fe-Al bearing phase D transforms to Fe-Al bearing phase H above 25 GPa and 1000°C, possibly by the reaction: Fe-Al bearing phase D + garnet = Fe-Al bearing phase H + bridgmanite + davemaoite (Tschauner et al., 2021). At pressures of the spin crossover of Fe^{3+}, (Al,Fe)-phase H is therefore more likely to form as the stable hydrous phase in Earth's mantle. While this study constrains the pressures of the spin transition at ambient temperature, first-principles calculations of the temperature dependence of the spin transition of

Fe^{3+} in the NAL phase suggests that the spin crossover region may broaden with increasing temperature, but not change pressure appreciably (Hsu, 2017).

Modeling of seismic velocities of the major constituents of metabasalt, formed from recycled mid-ocean ridge basalt (MORB) suggests that a thin layer (<10 km) of a metabasaltic aggregate within a subducting slab could scatter seismic waves based on the observation that S-wave velocity (vs) in metabasalt could be $\approx$ 2-4% lower than vs in pyrolite at the top of the lower mantle (Tsuchiya, 2011), resulting in a significant change in vs over a relatively short length scale (<10 km). In (Al,Fe)-phase H, vs may be invariant to pressure across the spin transition and lower than that of ambient mantle at these pressures whereas the P-wave velocity (vp) is expected to decrease, by analogy to seismic wavespeeds reported for δ-(Al,Fe)OOH (Ohira et al., 2021). The concentration of (Al,Fe) phase H in subducted oceanic crust between 1100 and 1550 km could enhance scattering of seismic waves in this region via significant reduction of vp in metabasaltic rocks which are otherwise indistinguishable from pyrolitic mantle by vp in this depth range (Tsuchiya, 2011). However, measurements of the S-wave speed in (Al,Fe) phase H are needed, as well as more precise constraints on the shape and elastic parameters are necessary to better understand scatterers in the lower mantle (Kaneshima, 2016) and formulate a quantitative interpretation of their origin.

Large, low seismic velocity provinces (LLSVPs) are basal mantle structures which may be thermochemical in nature and are defined by negative shear-wave velocity anomalies that are anti-correlated with positive bulk sound velocity anomalies (Garnero et al., 2016; McNamara, 2019). One possible source of chemical heterogeneity is the transport of subducted material carried into the lowermost mantle by slabs (Garnero et al., 2016; Jones et al., 2020; McNamara, 2019; Ohtani, 2020). δ-(Al,Fe)OOH, $MgSiO_2(OH)_2$, and (Al,Fe)-phase H each represent positive perturbations in bulk sound velocity (v_Φ) relative to PREM (Figure 9c). Assuming the same thermal parameters as determined for δ-AlOOH (Duan et al., 2018), a smaller proportion of (Al,Fe)-phase H (1-4 wt.%) than δ-(Al,Fe)OOH (6-8 wt.%) (Ohira et al., 2019) is necessary to produce the v_Φ anomalies observed at the edges of LLSVPs. This small concentration of (Al,Fe)-phase H is 10-14% less than the proportion of (Al,Fe)-phase H in the (δ-AlOOH)-($MgSiO_2(OH)_2$)-(ϵ-FeOOH) system produced by synthesis experiments on hydrous oceanic basalts at pressures of 25-27 GPa and temperatures between 1273 and 1473 K (Liu et al., 2019). If an anti-correlation of v_Φ and v_s is observed in (Al,Fe)-phase H, as in δ-(Al,Fe)OOH, accumulation of this phase as part of subducted basaltic material may contribute to the positive bulk sound velocity and negative shear wave velocity anomalies observed near the edges of LLSVPs.

Chapter 4

SOUND VELOCITIES OF (AL,FE)-PHASE H AND THE SEISMIC VISIBILITY OF DENSE OXYHYDROXIDES IN EARTH'S LOWER MANTLE

*This chapter has been submitted and is currently under review:

Strozewski, Benjamin T., Ojashvi Rautela, Johannes Buchen, Wolfgang Sturhahn, Takayuki Ishii, Itaru Ohira, Olivia Pardo, Jiyong Zhao, Thomas S Toellner, and Jennifer M Jackson (2025). "Sound Velocities of (Al,Fe)-phase H and the seismic visibility of dense oxyhydroxides in Earth's lower mantle ". In: *Physics of Earth and Planetary Interiors [submitted].*

4.1 Introduction

Cycling of 'water' — in the form of hydrogen and hydroxyl in mantle minerals — between different chemical reservoirs of the Earth is a critical process in controlling the evolution of the Earth as a chemical system. Knowledge of the deep Earth water cycle is critical to quantify Earth's total hydrogen budget, which can help constrain models of volatile delivery and accretion of terrestrial planets (Albarède, 2009; Barnes et al., 2020; Piani et al., 2020). In particular, precise understanding of volatile transport in Earth's interior can constrain the amount of 'water' stored as hydrogen or hydroxyl groups in the core and lower mantle (Litasov and Ohtani, 2003; Murakami et al., 2002). Earth's core and lower mantle are volumetrically large and therefore have the potential to store more than five ocean masses of water (Li et al., 2020), although partitioning of hydrogen between the lowermost mantle and core at all relevant conditions remains uncertain. Hydrogen is degassed from Earth's interior by magmatism, primarily at mid-ocean ridges but also by mantle plumes which produce ocean island basalts (OIBs). OIBs can be more hydrogen-rich (e.g. Simons et al. (2002), review by Bolfan-Casanova (2005)), than mid-ocean ridge basalts (MORBs), suggesting that their lower mantle source may either preserve a primordial signature of hydrogen-rich material or a volatile enrichment attributable to subducted material. Modeling of the I/Pu ratio (Liu et al., 2023) — which is lower in the plume reservoir compared to MORB mantle (Mukhopadhyay and Parai, 2019) — suggests that the source of ocean-island basalts (OIBs) could be well described by an undegassed reservoir of volatile-rich material delivered in the late veneer phase of Earth's accretion. However, precise measurement of Xe isotopic ratios (Parai and Mukhopadhyay, 2015) as well as those of Pb and Sr (Doucet et al., 2020) suggest that at least OIBs delivered by plumes arising from the African large, low-velocity province (LLVP) incorporate signatures of recycled oceanic crust. In combination with geochemical observations of mantle rocks, studying seismic velocities of relevant hydrous phases will provide a better understanding of the concentration of hydrous material and volatile cycling in Earth's interior by facilitating more precise comparison to observations from tomographic images (e.g. Koelemeijer et al. (2016) and Hosseini et al. (2020)) as well as regional seismic studies capable of locating small-scale scatterers and heterogeneities (Kaneshima, 2016; Ritsema et al., 2020).

To what depths within Earth's mantle hydrogen can be transported is determined by whether the minerals in which it is stored can retain hydrogen at high pressures and temperatures along the *P-T* path of a subducting slab (e.g., Barber et al. (2022)). The mantle transition zone has generally been considered to be 'wet' (up to 20,000 ppm H_2O) relative to the upper (100-200 ppm H_2O) and lower mantle (100-2,000 ppm H_2O), a paradigm (see review Ohtani (2020)) based in part on the water storage capacities of high-pressure olivine polymorphs and the apparent lack of hydrous phases stable at conditions of the lower mantle (Bercovici and Karato, 2003; Karato, 2011). Inclusions in superdeep ($>$ 410 km depth) diamonds have revealed that the base of the mantle transition zone is at least locally 'wet' (up to 2 wt. % H_2O) and is likely a region of metasomatism within Earth's mantle (Gu et al., 2022; Pearson et al., 2014; Tschauner et al., 2018; Wirth et al., 2007). Recent findings suggest that stishovite (Lin et al., 2020) and other rutile-structured phases may contain up to several wt.% water, even at core-mantle boundary conditions (Tsutsumi et al., 2024), possibly via the occupation of an oxygen vacancy by a hydrogen atom (Palfey et al., 2021) or, in the case of Al-free stishovite, the charge balancing of a Si vacancy by four OH groups (Palfey et al., 2023). The coupled substitution of Al and H for Si likely enhances the water storage capacity of stishovite (Ishii et al., 2022a; Takaichi et al., 2024). However, it was suggested that stishovite remains dry and alumina depleted when an Al-rich hydrous mineral (δ-AlOOH) coexists (Ishii et al., 2024), implying that such a hydrous mineral is an important carrier of water as long as it is thermally stable. The observation that certain hydrous phases may be stable to the core-mantle boundary along a cold slab geotherm implies that the lower mantle may be more 'wet' than implied by the restricted water storage capacities of volumetrically major minerals (Liu et al., 2019; Ohira et al., 2014; Sano et al., 2008; Suzuki et al., 2000).

Mantle convection models and images produced by seismic tomography indicate that in certain cases slabs can descend through the mantle transition zone (Durand et al., 2017; Hosseini et al., 2020; Koelemeijer et al., 2016) and accumulate at the core-mantle boundary (Brandenburg and Van Keken, 2007; Tan et al., 2011). The geographical correlation of basal mantle structures such as LLVPs and ultralow velocity zones (ULVZs) with subduction zones imply that subducted material could interact with these structures either dynamically (i.e. sweeping a ULVZ into an LLVP: (Sun et al., 2019; Wolf et al., 2024)) or thermochemically, influencing the existence of geochemical reservoirs in the deep mantle (McNamara et al., 2010; Tan et al., 2002). Hydrous phases such as $MgSiO_2(OH)_2$ (phase H), ε-FeOOH, δ-AlOOH, and their solid solutions are potential water carriers into the lower mantle (see review Ohtani et al. (2018)). If they form within oceanic lithosphere in the mantle transition zone (Kawazoe et al., 2017; Suzuki et al., 2000; Liu et al., 2019) they could remain stable even at the high pressures and temperatures of the core-mantle boundary region (Ohtani et al., 2018; Sano et al., 2008; Terasaki et al., 2012; Duan et al., 2018) and may also affect seismic wave speeds throughout the lower mantle (Ohira et al., 2021; Thompson et al., 2017). For example, hydrous phases would be concentrated in a basaltic assemblage, which can contribute to scattering of seismic waves in the mid-lower mantle (Kaneshima, 2016; Mao et al., 2022).

Measurement of the seismic velocities of hydrous minerals in the $MgSiO_2(OH)_2$-FeOOH-AlOOH ternary system is critical to understanding the seismic signature of hydrous MORB in the lower mantle (e.g. Satta et al. (2021)). A solid solution between the δ-phase (δ-AlOOH) and phase H ($MgSiO_2(OH)_2$) has been confirmed to coexist with alumina-depleted bridgmanite at conditions of the lower mantle (Ishii et al., 2022b; Ohira et al., 2014) in high-pressure experiments while an intermediate solid solution (referred to as “Al-rich phase H”) between δ-AlOOH, $MgSiO_2(OH)_2$, and ε-FeOOH has been observed to coexist with calcium silicate perovskite (or davemaoite: Tschauner et al. (2021)), stishovite, ferropericlase (Fe/(Fe+Mg) = 0.9), and fluid at 25-26.3 GPa and 1273-1473 K from compression and heating of a natural, hydrous basalt (Liu et al., 2019). Small amounts of cation substitution can produce significant effects on the velocity profile of minerals, particularly those which undergo spin crossovers (e.g. (Mg,Fe)O: Chen et al. (2012), Lin and Tsuchiya (2008), and Solomatova et al. (2016)), or phase transitions at lower mantle pressures and temperatures (e.g. Al-bearing SiO_2; Zhang et al. (2022)). Compression studies have found that δ-(Al,Fe)OOH with up to Fe/(Al+Fe)= 0.15 undergoes a spin crossover of Fe^{3+} at a pressure of approximately 35 GPa (Ohira et al., 2019; Su et al., 2021b). Nishi et al. (2019) observed that for higher concentrations of Fe in δ-(Al,Fe)OOH (Fe/(Al+Fe) = 0.21 and Fe/(Al+Fe) = 0.64), the spin crossover pressure increases to 45 GPa. Strozewski et al. (2023) also observed an increase in the spin transition pressure of Fe^{3+} ($\approx$ 55 GPa) as a result of the incorporation of Mg and Si. Together, these observations reveal that the spin crossover of Fe^{3+} in Fe-bearing phases in the $MgSiO_2(OH)_2$-FeOOH-AlOOH ternary system is affected by compositional variation (Ohira et al., 2019; Thompson et al., 2020; Strozewski et al., 2023) and implies that measurements of the sound velocities of intermediate compositions in this system are required for accurate predictions of its effect on seismic velocities in subducted metabasalt.

In this study, we used nuclear resonant inelastic X-ray scattering (NRIXS) to measure the partial phonon density of states (pDOS) of (Al,Fe)-phase H ($Al_{0.84}Fe^{3+}_{0.07}Mg_{0.02}Si_{0.06}OOH$) at high pressure. Based on the measured pDOS and an equation of state previously constrained by X-ray diffraction (XRD) at high pressures (Strozewski et al., 2023), we calculate P-wave (V_P), S-wave (V_S), and bulk sound (V_Φ) velocities of this hydrous phase throughout Earth's lower mantle, both as a single phase and as a component of hydrous metabasalt along an adiabat corresponding to a cold subducting slab (1173.2 K at 25 GPa). Additionally, we model the wavespeeds of pyrolitic mantle along an ambient mantle adiabat (1900 K at 25 GPa). We compare our constraints on the wavespeeds of hydrous metabasalt and pyrolite to a 1-D Earth model and in this context discuss implications for the mineralogy of basal mantle structures and mid-lower mantle seismic scatterers.

4.2 Methods

Two panoramic diamond anvil cells (panDACs) were loaded with grains of (Al,Fe)-phase H ($Al_{0.84}Fe^{3+}_{0.07}Mg_{0.02}Si_{0.06}OOH$) for nuclear resonant inelastic X-ray scattering (NRIXS) experiments. Synthesis and characterization of these samples is described in Strozewski et al. (2023). One panDAC with 400 μm flat culet anvils was loaded with a 20 μm thick, 50x30 μm grain. A Be gasket was pre-indented to a thickness of 62 μm and drilled with a 210 μm diameter hole. Compressed Ne gas was loaded into the sample chamber as a pressure medium at the California Institute of Technology. A second panDAC with 250 μm beveled culets was loaded with a 30 μm thick, 65 x 60 μm grain and a small (<5 μm) W flake as a pressure calibrant. A Be gasket was pre-indented to a thickness of 41 μm and a 140 μm hole drilled in the center of the indentation. A boron epoxy insert was placed into each drilled Be gasket to stiffen the sample chamber. A ruby sphere approximately 10 μm in diameter was loaded proximal to the sample in each panDAC for pressure determination. Ruby fluorescence measurements were used to determine the pressure in each cell at low pressure ($P < 35$ GPa), using the calibration of Dewaele et al. (2008). Pressure uncertainty was determined from ruby fluorescence measurements performed before and after each series of NRIXS scans. At high pressure ($P > 35$ GPa), Raman spectroscopy of the diamond anvils (diamond edge) was used to determine pressure inside the panDAC and the pressure at 100 GPa verified using X-ray diffraction of W. Raman spectroscopy (including ruby fluorescence measurements) was performed at sector 13, GSECARS of the Advanced Photon Source, Argonne National Laboratory. X-ray diffraction patterns of W were analyzed using the DIOPTAS software (Prescher and Prakapenka, 2015) and pressure determined using the calibration of Dewaele et al. (2004). To determine the uncertainty in pressure arising from stress gradients within the panDAC, diamond edge Raman measurements were taken at four corners of the sample as well as the center. Reported pressures and uncertainties correspond to the average and standard deviation of these measurements, respectively.

NRIXS spectra were collected at sector 3 of the Advanced Photon Source, Argonne National Laboratory. During NRIXS experiments, the storage ring was operated in 24-bunch mode and the X-ray energy was tuned to the Fe resonance energy (14.4125 keV) using a high-resolution monochromator with an energy resolution of 1.1 meV (Toellner, 2000). NRIXS signal was collected using three avalanche photo diodes positioned radially around the panDAC. Nuclear forward scattering signal (critical in determining the resolution function) was collected downstream of the panDAC. At pressures below 30 GPa, energy scans were performed over the energy range -100 to 150 meV. At $\approx$33 GPa, an energy scan range of -80 to 120 meV was used. For most pressures greater than 35 GPa, energy scans were performed over the range -80 to 150 meV. Scans at 78, 91, and 100 GPa were performed over the range -80 to 180 meV.

Examples of raw NRIXS spectra are shown in Supplementary Figure S1 and additional details of the reduction and analysis of NRIXS data explained in Supplementary Text S1. Parameters extracted from the refined spectra (without the elastic peak) are presented in Supplementary Table S1. The PHOENIX software package (version 3.0.4, www.nrixs.com; Sturhahn, 2000) is used to process NRIXS energy scans, construct the partial, projected phonon density of states (pDOS), determine the Debye velocity, and determine seismic wavespeeds. The pDOS at each pressure in the dataset is shown in Figure 1.

4.3 Results

Debye velocities (V_D) of (Al,Fe)-phase H ($Al_{0.84}Fe^{3+}_{0.07}Mg_{0.02}Si_{0.06}OOH$) are extracted from the measured NRIXS pDOS as described in Supplementary Text S1. An example of the collection of fits to the Debye velocity function and the resulting probability distribution for the Debye velocity of (Al,Fe)-phase H at 26(1) GPa is shown in Figure 2. Fits to the Debye velocity function and resulting probability distributions constrained for each pressure are given in Supplementary Figures S2 and S3, respectively. Parameters of the probability distribution are reported in Supplementary Figure S2. Debye velocities of (Al,Fe)-phase H and δ-($Al_{0.87}Fe_{0.13}$)OOH (δ-Fe13) (Ohira et al., 2021) at high pressure are compared in Figure 2. Ohira et al. (2021) observed a shift of features of the pDOS to lower frequencies at pressures between ambient pressure and approximately 10 GPa, indicative of a soft mode transition inferred to be related to the disordering of hydrogen bonds and commensurate with the phase transition from $P2_1nm$ to $Pnnm$ observed in Ohira et al. (2019). (Al,Fe)-phase H has the $Pnnm$ structure and disordered hydrogen bonds at ambient pressure (Strozewski et al., 2023). In agreement with these observations, we do not observe any phonon softening in (Al,Fe)-phase H and Debye velocities monotonically increase with increasing pressure. At comparable pressures, Debye velocities of (Al,Fe)-phase H and δ-Fe13 are generally indistinguishable within error. At approximately 65 GPa, the Debye velocity of δ-Fe13 is slightly higher than that of (Al,Fe)-phase H, though this difference disappears at higher pressure.

Seismic wavespeeds of (Al,Fe)-phase H and other high-pressure oxyhydroxides at 300 K are compared to the preliminary reference Earth model (PREM) (Dziewonski and Anderson, 1981) in Figure 3. In order to discern the effects of cation substitution on the seismic wavespeeds of dense oxyhydroxides, we compare our results to previous measurements on relevant compositions (Mashino et al., 2016; Su et al., 2021a; Ikeda et al., 2019; Ohira et al., 2021). Mashino et al. (2016) and Su et al. (2021a) used Brillouin spectroscopy to constrain the seismic wavespeeds of δ-AlOOH and δ-($Al_{0.956}Fe_{0.044}$)OOH, respectively. Ikeda et al. (2019) determined the seismic wavespeeds of ϵ-FeOOH in a Kawai-type multi-anvil press using an ultrasonic method. As previously mentioned, the seismic wavespeeds of δ-($Al_{0.87}Fe_{0.13}$)OOH (Ohira et al., 2021) are determined by nuclear resonant inelastic X-ray scattering.

At pressures greater than 65 GPa, (Al,Fe)-phase H displays the highest P-wave velocity ($\delta \ln V_P \approx +8\%$ relative to PREM), due mostly to the high bulk modulus of (Al,Fe)-phase H at pressures of the lowermost mantle (Strozewski et al., 2023). The P-wave velocities of (Al,Fe)-phase H and δ-($Al_{0.87}Fe_{0.13}$)OOH (δ-Fe13) are similar from 0 to 30 GPa, at pressures lower than the Fe^{3+} spin crossover in both phases. The more iron-rich δ-Fe13 has lower P-wave velocities than δ-($Al_{0.956}Fe_{0.044}$) (Su et al., 2021a) and δ-AlOOH (Mashino et al., 2016) at all measured pressures. ϵ-FeOOH displays the lowest P-wave velocity and is the only high-pressure oxyhydroxide with a negative δV_P relative to PREM at all pressures.

Both (Al,Fe)-phase H and δ-Fe13 display S-wave velocities lower than those of PREM at 300 K and pressures of the lower mantle ($P > 25$ GPa). S-wave velocities of (Al,Fe)-phase H and δ-Fe13 are generally comparable at pressures greater than 30 GPa. At $\approx$ 100 GPa, the S-wave velocity of (Al,Fe)-phase H is approximately 10% lower than that of PREM at 300 K. In the low-spin state (δ-Fe13: $P > 45$ GPa (Ohira et al., 2019); (Al,Fe)-phase H: $P > 65$ GPa (Strozewski et al., 2023)) dVs/dP is small and S-wave velocities plateau, particularly for pressures above 80 GPa. A plateau in the S-wave velocities of δ-Fe13 at approximately 40 GPa may be attributable to the spin crossover of Fe^{3+} at this pressure. However, the Fe^{3+} spin crossover does not cause a significant decrease in S-wave velocity, in contrast with the bulk sound velocity and P-wave velocity, which decrease substantially over the pressure region of a spin crossover due to the enhanced compressibility of Fe-bearing compositions at pressures of the Fe^{3+} spin crossover.

4.4 Discussion and Implications

Modeling lower mantle seismic velocity profiles of select petrologies

To understand a scenario in which (Al,Fe)-phase H is subducted into the lowermost mantle, we model a hydrous metabasalt that includes (Al,Fe)-phase H (HHMB) assuming that 8 vol.% of bridgmanite is replaced by (Al,Fe)-phase H (Liu et al., 2019). We also model the seismic wavespeeds of pyrolitic mantle. Pyrolite represents a model composition of Earth's mantle that partially melts to produce MORB and leaves behind a peridotite residuum. Chemical bulk compositions of pyrolitic mantle and modeled metabasalt correspond to the depleted MORB mantle (DMM; 'pyrolite') and normal mid-ocean ridge basalt (NMORB) compositions defined in Workman and Hart (2005) + 1 wt.% H_2O in the case of the modeled hydrous metabasalt (HHMB). The phase proportions of each modeled rock are given in Supplementary Table S3. In HHMB, the added 1 wt.% H_2O is assumed to be en-

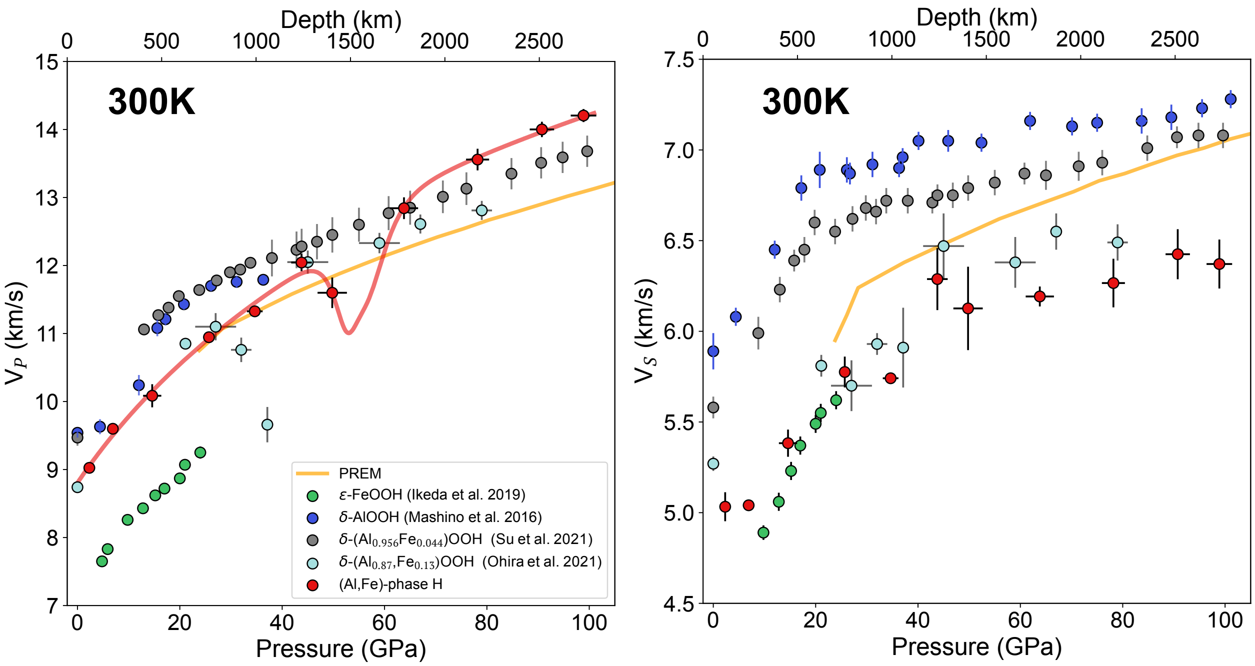

Figure 4.1: Seismic wavespeeds of (Al,Fe)-phase H and other high-pressure oxyhydroxides compared to PREM at high pressure and 300 K. PREM is shown as an orange line. Calculated P-wave velocities (red line) of (Al,Fe)-phase H are determined from the equation of state (Strozewski et al., 2023) and the interpolation of shear modulus values is described in the Supplementary Text S2. Seismic wavespeeds of Fe-bearing oxyhydroxides are shown for compositions with a natural abundance of ^{57}Fe.

tirely in (Al,Fe)-phase H, which could be reasonable based on the observed strong partitioning of water into hydrous phases (Ishii et al., 2024; Ishii et al., 2022b). The seismic velocities of the resulting aggregate are determined as described in Buchen et al. (2021), incorporating the elastic properties and sound wave velocities of (Al,Fe)-phase H reported here and in Strozewski et al. (2023). For incorporation of (Al,Fe)-phase H into our modeling framework, we fit the crystal field model of Buchen et al. (2021) to the unit cell volume and bulk modulus data of Strozewski et al. (2023) as well as the Debye velocities presented in this study. We use the thermal parameters γ_0 = 1.26(9), θ_0 = 1230, and q_0 = 1.21 (0.46), $\eta_{s0} = 2\gamma_0 = 2.52$, constrained by adapting the crystal field modeling and thermal equation of state described in Buchen et al. (in review) to (Al,Fe)-phase H. Additional details regarding the determination of wavespeeds and associated uncertainties of (Al,Fe)-phase H at high temperatures can be found in Supplementary Texts S2 and S3 and additional description of our modeling procedure in Supplementary Text S4. We note here that our models of pyrolite and HHMB do not incorporate the phase transition of bridgmanite to post-perovskite in the lowermost mantle (Murakami et al., 2004; Oganov and Ono, 2004; Tsuchiya et al., 2004) and therefore we restrict our conclusions to pressures lower than 95 GPa ($\approx$ 2200 km depth), approximately the depth at which this phase transition occurs in a metabasalt (Hirose, 2006).

Propagation of uncertainties in the seismic wavespeeds of (Al,Fe)-phase H into modeled hydrous metabasalt at high temperature is described in Supplemental Text S3. Uncertainties computed for (Al,Fe)-phase H are generally less than (+/-) 1%, $\approx$ 1.5%, and $\approx$ 1% for V_Φ, V_S, and V_P, respectively. We assign the same fractional error to our modeled hydrous metabasalt. It has previously been noted that uncertainties in thermoelastic parameters and lower mantle temperature contribute significantly to the uncertainty in the wavespeeds of an aggregate rock from mineral physics properties (Houser et al., 2020; Buchen et al., 2021). The uncertainties determined here reinforce the need for increasingly precise thermoelastic parameters and demonstrate that average wavespeed anomalies of less than 2% remain difficult to assign to any particular composition in Earth's mantle.

Comparison of modeled petrologies to PREM

It remains unclear whether an adiabatically decompressed uniform, peridotitic composition (i.e. pyrolite) in Earth's lower mantle can be reconciled with 1-D global Earth models derived from seismology (Ricolleau et al., 2009), especially given uncertainties in lower mantle temperatures and thermoelastic parameters at lower mantle pressures and temperatures (Houser et al., 2020). Regardless, comparison to a model composition of the ambient mantle remains helpful in discerning whether differences in seismic wave velocities are predominantly thermal, compositional, or both. Deviations of the wavespeeds of (Al,Fe)-phase H and those of pyrolitic mantle from PREM are shown in Figure 4. Pyrolite is plotted along an ambient mantle adiabat (1900 +/- 200 K at 25 GPa) that spans the range consistent with the mantle adiabatic temperature profiles of Katsura (2022). (Al,Fe)-phase H and HHMB are plotted along a "cold" adiabat profile constrained to 1173.2 K (900° C) at 25 GPa, based on the thermal structure of the Tonga slab derived from deep earthquakes (Liu et al., 2021) and consistent with slab temperatures determined from global geodynamic modeling studies (e.g. Bower et al. (2013)). Mantle and cold slab adiabatic temperature profiles are plotted in Supplemental Figure S5. Different adiabats are chosen for pyrolite and HHMB to reflect realistic temperature differences between ambient mantle and a cold subducting slab. That is, comparing these two compositions along different adiabats yields velocity differences attributable to both intrinsic compositional differences and temperature, which more accurately compares velocity differences sensed by propagating seismic waves than considering only compositional differences. In the lower mantle, differences between PREM and other 1-D average Earth models (IASP91: (Kennett and Engdahl, 1991) AK135: (Kennett et al., 1995)) are small so we here compare our results only to PREM for clarity.

Throughout the lower mantle, (Al,Fe)-phase H has significantly higher bulk sound velocity and significantly lower shear wave velocity than pyrolite and PREM. These differences become more extreme with increasing depths, reaching a value of $\delta \ln V_S$ - $\delta \ln V_{\Phi} \approx 25\%$ at 2200 km depth. Similarly, V_P/V_S of (Al,Fe)-phase H is greater than that of pyrolite (Figure 4) and the difference increases more strongly with depth after the completion of the Fe^{3+} spin crossover (65 GPa; 1550 km depth). At approximately 40 GPa, the P-wave velocities of (Al,Fe)-phase H become greater than those of pyrolitic mantle and the difference between the two increases with increasing pressure to $\approx 6\%$ at 100 GPa. The deviations of HHMB along the cold adiabat and pyrolite along the ambient mantle adiabat from PREM are shown in Figure 5. HHMB and pyrolite have low shear wave velocities ($\delta \ln V_S \approx -2\%$ relative to PREM) at 25-50 GPa along these adiabats, implying that these two compositions would be indistinguishable between about 750 and 1300 km depth when only considering V_S. The same is true for pressures greater than 80 GPa (depth > 1800 km). Based on V_S alone, pyrolite and HHMB are distinguishable only between $\approx$ 1300 and 1800 km depth, where the post-stishovite phase transition (Zhang et al., 2022; Umemoto et al., 2016; Fischer et al., 2018; Buchen et al., 2018) in metabasalt decreases the S-wave speed of HHMB. The Fe^{3+} spin crossover in (Al,Fe)-phase H also occurs over a portion of this depth range (48-63 GPa, $\approx$ 1100-1500 km depth: Strozewski et al. (2023)) and contributes to decreasing V_P and V_{Φ} in HHMB, as discussed in section 3. Consequently, structures inferred to be subducted metabasalt should display a significant increase in the ratio V_P/V_S (Figure 5) due to the post-stishovite transition, which can vary with depth (e.g. Zhang et al., 2022; Wang et al., 2023). Given the estimated uncertainties on seismic wavespeeds, HHMB may be difficult to distinguish from PREM at lowermost mantle depths solely by V_P or V_S. However, with additional constraints on V_{Φ}, the subducted metabasalt could be distinguishable from pyrolite ($\delta \ln V_P = +1$ to 3%, $\delta \ln V_{\Phi} = +1$ to 3.5%) throughout the lower mantle. At pressures greater than 80 GPa, after the completion of the post-stishovite transition and the spin crossover in (Al,Fe)-phase

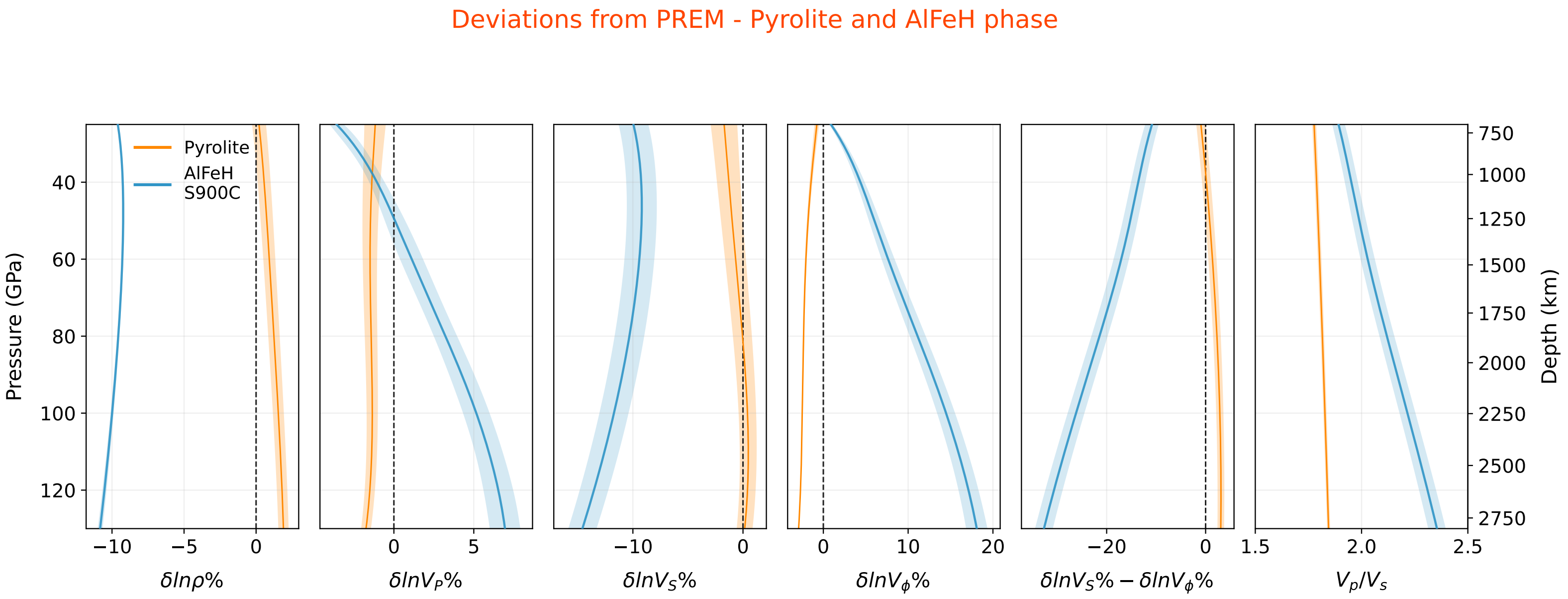

Figure 4.2: Properties of pyrolite and hydrous (Al,Fe)-phase H (AlFeH) in the lower mantle (25-130 GPa). Panels show deviations in density, V_P, V_S, V_Φ, and anti-correlation δlnV_S-δlnV_Φ with respect to PREM, as well as the V_P to V_S ratio. Pyrolite is plotted along an ambient mantle adiabat (1900 K at 25 GPa) and (Al,Fe)-phase H along an adiabat of a cold slab (1173.2 K at 25 GPa) constrained by the thermal structure of the Tonga slab inferred from deep earthquakes (Liu et al., 2021). For pyrolite, in addition to 1900 K, properties are shown for +/- 200 K adiabats (shaded region along the depth profile). See Supplementary Figure S5 for pressure-temperature profiles of both adiabats and Supplementary Figures S6, S7, and S9 for the absolute values of the properties shown in each panel.

H, HHMB shows little deviation from PREM in V_P, V_S, and V_ϕ. The comparatively low values of both V_Φ and V_P of pyrolite relative to PREM imply that although pyrolite and HHMB would not be distinguishable in their effect on S-wave travel times, their presence between 750 and 1300 km depth may be parsed by whether or not slow S-wave anomalies are correlated with fast or slow P-waves (relative to PREM). Considering the anti-correlation of V_S and V_Φ in HHMB (Figure 5), constraints on bulk sound velocity would be even more informative in discerning the presence of subducted metabasalt between 750 and 1300 km. Finally, exchange of less dense (Al,Fe)-phase H ($\delta \ln\rho \approx$ -10% with respect to PREM and pyrolite; Figure 4) in hydrous metabasalt maintains the higher density of metabasalt with respect to pyrolite and PREM. That is, cold, dense hydrous metabasalt will sink into the lowermost mantle.

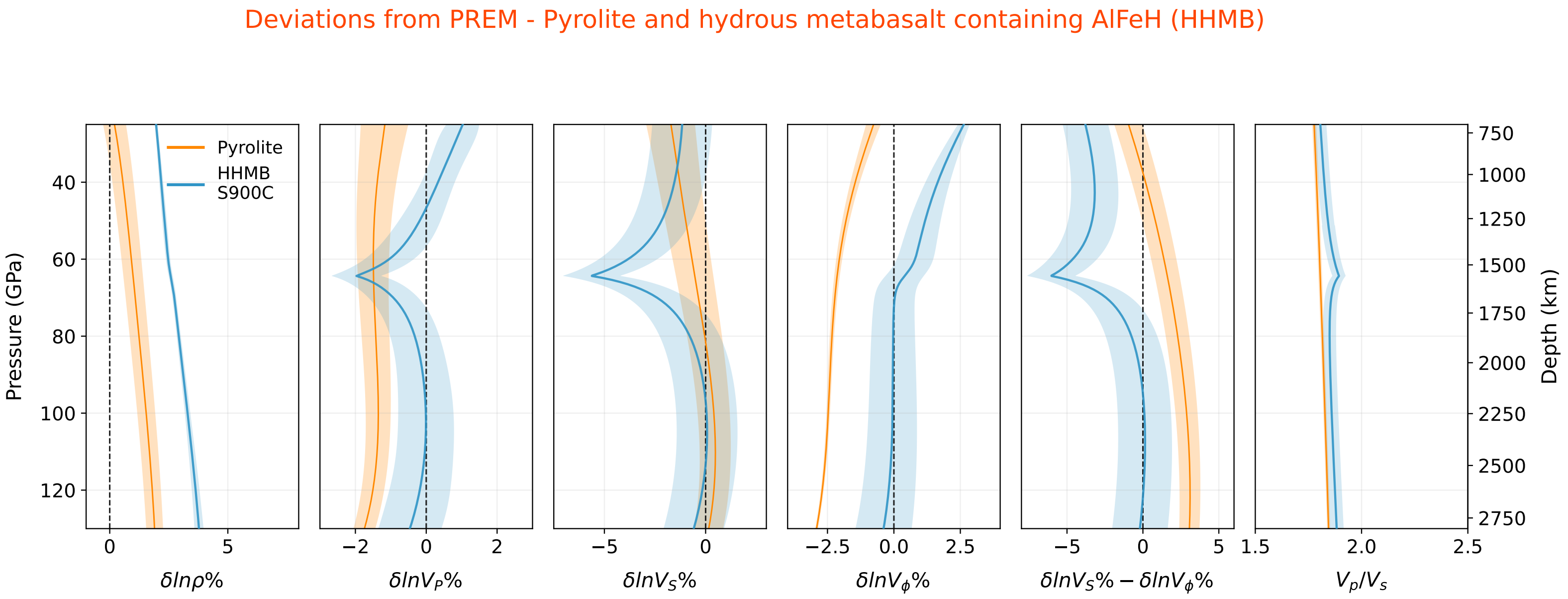

Figure 4.3: Properties of pyrolite and hydrous metabasalt (HHMB) containing (Al,Fe)-phase H in the lower mantle (25-130 GPa). Panels show deviations in density, V_P, V_S, V_Φ, and anti-correlation $\delta \ln V_S$-$\delta \ln V_\Phi$ with respect to PREM, as well as the V_P to V_S ratio. Plotted adiabats are the same as described in Figure 4 and shown in Supplementary Figure S5.

(Al,Fe)-phase H and lower mantle heterogeneity

Understanding the effect of a variable composition in the $MgSiO_2(OH)_2$-FeOOH-AlOOH system on seismic wavespeeds is critical to inferring the presence of hydrous phases in the deep Earth from seismic observations. The present measurements on the solid solution (Al,Fe)-phase H compared to a compilation of other mantle-relevant oxyhydroxides at 300 K (Figure 3) indicate that increasing Fe concentration generally produces both lower P-wave velocities and lower S-wave velocities at pressures of the lower mantle and when Fe is in the high-spin state. Given the lower concentration of Fe in (Al,Fe)-phase H compared to δ-Fe13 (Ohira et al., 2021), their comparable seismic wavespeeds at pressures below 30 GPa imply that incorporation of a $MgSiO_2(OH)_2$ component also serves to decrease the wavespeeds of high-spin Fe-bearing oxyhydroxides. At higher pressures, after the completion of the Fe^{3+} spin crossover in δ-(Al,Fe)OOH (42 GPa) and (Al,Fe)-phase H (65 GPa), increasing Fe concentration in (Al,Fe)OOH results in lower V_P and V_S (Su et al., 2021a), though the effect is more apparent in V_P. (Al,Fe)-phase H is an exception to this trend. That is, (Al,Fe)-phase H exhibits the highest P-wave velocities and lowest S-wave velocities amongst dense oxyhydroxides at pressures of the lowermost mantle. Therefore, while dissolution of $MgSiO_2(OH)_2$ into high-spin δ-(Al,Fe)OOH decreases seismic wavespeeds, the effect of incorporating $MgSiO_2(OH)_2$ into an oxyhydroxide solid solution is to increase the P-wave velocities of low-spin Fe-bearing compositions. Liu et al. (2019) synthesized (Al,Fe)-phase H that is significantly richer in the $MgSi(OH)_2$ component and depleted in Al: ($Mg_{0.11}Fe_{0.03}Si_{0.2}Al_{0.63}OOH$) compared to the samples measured here. Our results suggest that the samples of Liu et al. (2019) would have even higher P-wave velocities and lower S-wave velocities in the lowermost mantle ($P > 65$ GPa) than the samples measured here, exacerbating the difference from PREM in each case. The increased concentration of Mg and Si in the samples of Liu et al. (2019) could stiffen the crystal structure and result in a higher pressure of the Fe^{3+} spin crossover relative to (Al,Fe)-phase H (Strozewski et al., 2023), though additional experiments are needed to clarify the effect.

Regional seismic imaging studies have observed subducting slabs impinging on the edges of LLVPs (Sun et al., 2019; Wolf et al., 2024). HHMB remains denser than surrounding mantle (Figure 5) and should continue to sink into the lowermost mantle. We have not included the post-perovskite (pPv) phase transition in our modeled HHMB, and therefore restrict our conclusions to depths shallower than 95 GPa (2200 km depth), which includes the upper edges of LLVPs. We note that experiments have found oxyhydroxide phases to coexist with post-perovskite (Ohira et al., 2014; Yuan et al., 2019) and that the $\approx 1\%$ density increase associated with the pPv transition (Murakami et al., 2004; Hirose, 2006) would encourage the sinking of subducted metabasalt ($\delta \ln \rho \approx +5\%$) to the core-mantle boundary. The magnitude of this density anomaly leaves open the fate of subducted HHMB: it could either concentrate at the edges of LLVPs or be entrained into mantle upwellings, i.e. plumes (McNamara et al., 2010). Along the chosen cold adiabat at 95 GPa (2200 km depth), our modeled HHMB with 8 vol% (Al,Fe)-phase H exhibits values of V_S and V_Φ similar to those of PREM (Figure 5). It is therefore an unlikely candidate for reproducing the observed seismic anomalies associated with LLVPs (McNamara, 2019) at depths shallower than those of the pPv transition in metabasalt, at least when the subducted HHMB first arrives in the core-mantle boundary region. If the HHMB heats as it accumulates, V_S, V_Φ, and V_P will decrease, resulting in uniformly low seismic wavesspeds associated with HHMB, similar to the low V_S and V_P associated with LLVPs at 2200 km depth (Koelemeijer et al., 2016).

Formation of (Al,Fe)-phase H in a subducted hydrous metabasalt will contribute to seismic heterogeneity in the mid mantle due to its low density, high P-wave speed, and low S-wave speed (Figure 4). Mid-mantle (750-1800 km depth) heterogeneity has been frequently observed via scattered seismic waves, which are presumably caused by thin interfaces with large contrast in wavespeeds relative to the surrounding material (Kaneshima, 2016; Waszek et al., 2018). Although the geometry and wavespeeds of these structures are difficult to constrain, several studies suggest that they are associated with low shear wave velocities (δV_S = 0 to -12%) (Ritsema et al., 2020; Haugland et al., 2017), and they must be thin ($\approx$ 10 km) due to the short period ($<$ 1 s) of the scattered waves. These constraints suggest the presence of subducted metabasalt as a possible cause for the observed scattered waves. Along the adiabat of a cold slab, our modeled HHMB is difficult to distinguish from either PREM or pyrolite in shear wave velocity, except at pressures of the broad post-stishovite transition (40-80 GPa; 1000-2000 km depth). In contrast, differences in wavespeeds of P-waves are largest between our modeled pyrolite and HHMB at depths greater than 1800 km and between 750 and 1300 km.

Fan et al. (2024) used P-wave azimuthal anisotropy tomography to identify structures interpreted to be remnants of the subducted Izanagi plate with modestly high V_P ($\delta V_P \approx +1\%$) between 800 and 1500 km, which generally agrees with the predicted velocity anomalies of our modeled hydrous metabasalt. Given our model for pyrolite, a P-wave will encounter the greatest impedance contrasts between pyrolite and HHMB at depths greater than 1800 km and between 750 and 1300 km, and we would predict a relative paucity of P-P scattering attributable to metabasalt between 1300 and 1800 km depth. In contrast, if the PREM P-wave velocities are representative of ambient mantle surrounding a subducting slab, rather than the modeled pyrolite, the depth range of 1300 to 1800 km should yield the highest efficiency of P-P scattering. The post-stishovite transition increases the contrast between S-wave speed in metabasalt and P-wave speed in the surrounding mantle (Figure 5) and should result in higher amplitudes of S-P scattering that occurs between 1000 and 1800 km depth, making such scattered waves easier to identify, in agreement with the reported frequency of such observations (Kaneshima, 2016).

In addition to temperature (Fischer et al., 2018; Nomura et al., 2010) and deviatoric stress (Wang et al., 2023), the phase boundary of the post-stishovite transition is affected by Al and H concentration (Zhang et al., 2022; Lakshtanov et al., 2007). This phase boundary could therefore be influenced by the formation of (Al,Fe)-phase H. Ishii et al. (2024) found that at 24-28 GPa and 1000° - 1200° C, Al and H would partition into(Al,Fe)-phase H such that stishovite contained < 1 wt.%

Al_2O_3 and $\approx$ 500 ppm H_2O. At the formation conditions of the cold adiabat in this study, stishovite would therefore be Al and H-poor. Similarly, Liu et al. (2019) observed Al_2O_3 contents of 0.3-1.6 wt.% and H_2O contents < 1 wt. % in stishovite when formed with (Al,Fe)-phase H in a metabasalt. Increasing the Al_2O_3 content in stishovite to a maximum 1.6 wt.% (0.63 mol %) would result in a 200 km shallower post-stishovite transition at 1300 km depth ($\approx$ 54 GPa, Zhang et al. (2022)), but not change our models significantly otherwise. A shallower post-stishovite transition raises the potential for S-P scatterers between approximately 800 and 1000 km depth and shifts the spike in V_P/V_S of HHMB to shallower depths, as noted in section 4.2. S-P scatterers associated with low S-wave speeds at depths shallower than 800 km or greater than 1800 km would be difficult to observe in a cold subducting slab in which (Al,Fe)-phase H forms due to the low contrast in S-wave velocity of PREM and pyrolite to HHMB at depths outside the depth interval of the post-stishovite transition. Distinguishing between different dynamic and mineralogical scenarios in this context could be best achieved by advancements in 3-D full waveform simulations at short periods. Additionally, directly building upon the results presented here, a targeted approach of synthetic waveform modeling considering specific mineralogies within a slab at the appropriate depths (e.g. Mao et al. (2022)), could help further develop the understanding of the intra-slab mid-mantle velocity heterogeneity.

Chapter 5

CONCLUSIONS

I describe in this thesis the crystal chemistry and geophysical properties at high pressure of (Al,Fe)-phase H: δ-$Al_{0.84}Fe_{0.07}Mg_{0.02}Si_{0.06}OOH$, a dense oxyhydroxide in the (δ-AlOOH)-($MgSiO_2(OH)_2$)-(ϵ-FeOOH) system which could be an important carrier of water in Earth's deep mantle. In this work, I have demonstrated that even relatively small changes in composition of an oxyhydroxide change the pressures at which it undergoes hydrogen bond symmetrization and the spin crossover of ferric iron. Differences in the pressure of these transitions affect the inferred seismic velocities of a subducted metabasalt containing phases in the (δ-AlOOH)-($MgSiO_2(OH)_2$)-(ϵ-FeOOH) system and may also affect their capacity for retaining water at high temperatures. Studies of different compositions in the system are therefore important as details of the petrology of hydrous, subducted metabasalt at the base of the mantle transition zone and in the rest of the lower mantle remain unclear.

In Chapter 2, I employed Raman and infrared spectroscopy of (Al,Fe)-phase H and δ-$(Al_{0.87},Fe_{0.13})OOH$, complemented by nuclear resonant inelastic X-ray scattering (NRIXS) to constrain the pressure of hydrogen bond disorder and symmetrization in (Al,Fe)-phase H. These measurements demonstrate that substitution of cations with different valences in oxyhydroxides with a distorted rutile structure results in hydrogen bond disorder at ambient pressure and that the pressure of hydrogen bond symmetrization in dense oxyhydroxides depends critically on the distance between oxygens (O-O). The O-O distance is in turn influenced by the incompressibility of the crystal structure on the whole. I also infer that (Al,Fe)-phase H stores additional H as defects in its structure, an observation which warrants further investigation. These measurements motivate additional study of intermediate compositions in the (δ-AlOOH)-($MgSiO_2(OH)_2$)-(ϵ-FeOOH) system to better understand how compositional variance in this system affects the temperatures at which different compositions may retain water and show that hydrogen bond symmetrization likely takes place in all dense oxyhydroxides at lower mantle pressures.

In Chapter 3, I use X-ray diffraction and synchrotron Mössbauer spectroscopy to constrain the equation of state of (Al,Fe)-phase H and the spin state of its Fe^{3+} atoms, respectively. The equation of state provides the most fundamental constraints on the compressional properties of a material and indicates a spin crossover of ferric iron — confirmed by synchrotron Mössbauer measurements — between 48 and 63 GPa, leading to reduced incompressibility over this pressure range and occurs at a significantly higher pressure than δ-(Al,Fe)OOH (35 GPa). These measurements reveal that (Al,Fe)-phase H has a significantly higher bulk sound velocity than PREM or other oxyhydroxides at high pressures. Considering thermal effects, this difference makes it a feasible contributor to the elevated bulk sound velocities (V_Φ) observed at the edges of large, low shear velocity provinces.

Although V_Φ can be determined directly from the equation of state, it provides no constraints on the shear properties. We therefore pursue constraints on V_P and V_S, which are more frequently determined by seismic observations. Chapter 4 describes nuclear resonant inelastic X-ray scattering measurements used to determine V_P and V_S of (Al,Fe)-phase H at high pressure and room temperature. These experimental constraints are incorporated into realistic models of a hydrous metabasalt at high temperature and pressure. We conclude from these models that hydrous metabasalt containing a hydrous phase will be difficult to distinguish from PREM or pyrolitic mantle across a wide range of depths in the lower mantle purely from seismic velocities. However, the modeled impedance contrasts support the hypothesis that subducted metabasalt could result in scattering of seismic waves in the mid-lower mantle. The depth of this scattering also depends on whether ambient mantle velocities are best represented by a pyrolitic model or by a 1-D Earth model derived from observations, such as PREM. We suggest synthetic waveform modeling targeted towards specific mineralogies and which incorporate detailed constraints on mineral assemblages from experimental studies as a way to resolve some of these questions.

The deep Earth presents several challenges to detailed study, foremost among them the often non-unique models used to explain observations and the inevitability that any rocks exhumed from depth have been geochemically reprocessed. Nevertheless, it is clear that certain regions of the Earth deviate substantially from the predictions of an average, 1-D Earth model. Large, low shear velocity provinces and ultra-low velocity zones at the base of the mantle suggest heterogeneity which may be related to subducted material and demand a thorough knowledge of the petrology of this material and its seismic signature. Scattering of seismic waves in the mid-lower mantle imply departures from ambient mantle seismic velocities and hint at potentially complex dynamics of subduction, even in regions of the Earth nominally without chemical and seismic discontinuities. Important, first-order questions about the evolution of the Earth as a whole naturally arise. How much water is sequestered in Earth's interior? Was this water delivered during accretion or by subduction of tectonic plates? What is the origin of basal mantle structures such as large, low velocity provinces? Do we misattribute seismic velocities to temperature variations when those variations could in fact be compositional? Does exsolution of hydrogen at the core-mantle boundary result in complex chemistry such as Fe-H exchange between the core and mantle?

The work contained herein addresses these challenges with fundamental knowledge on lower mantle mineralogy. Lower mantle materials are mineral aggregates; the chemistry and elastic properties of the minerals in these aggregates place fundamental controls on their rheology and the speed at which they propagate seismic waves. The experiments and models discussed in this thesis offer insight into the complex crystal chemistry of dense oxyhydroxides and the influence they may exert on the relevant mineral assemblages. As seismic observations continue to improve, more precise knowledge of the heterogeneous properties of minerals within these aggregates will be required for accurate inferences. Confluence of advances in our understanding of mineral physics, seismology, and geodynamics promises resolution to first-order questions about Earth's interior.

BIBLIOGRAPHY

Akahama, Yuichi and Haruki Kawamura (2010). “Pressure calibration of diamond anvil Raman gauge to 410 GPa”. In: *Journal of Physics: Conference Series* 215. DOI: `10.1088/1742-6596/215/1/012195`.

Albarede, Francis, Chris Ballhaus, Janne Blichert-Toft, Cin Ty Lee, Bernard Marty, Frédéric Moynier, and Qing Zhu Yin (2013). “Asteroidal impacts and the origin of terrestrial and lunar volatiles”. In: *Icarus* 222.1, pp. 44–52. DOI: `10.1016/j.icarus.2012.10.026`.

Albarède, Francis (2009). “Volatile accretion history of the terrestrial planets and dynamic implications”. In: *Nature* 461.7268, pp. 1227–1233. DOI: `10.1038/nature08477`.

Allégre, Claude J., J. P. Poirier, Eric Humler, and Albrecht W. Hofmann (1995). “The chemical composition of the Earth”. In: *Earth and Planetary Science Letters* 134, pp. 515–526. ISSN: 18840884. DOI: `10.5026/jgeography.131.163`.

Angel, R (2000). “Equations of state”. In: *Reviews in mineralogy and geochemistry* 41, pp. 35–59. DOI: `10.2138/rmg.2000.41.2`.

Angel, R. J. and L.W. Finger (2011). “SINGLE: A program to control single-crystal diffractometers”. In: *Journal of Applied Crystallography* 44, pp. 247–251. DOI: `10.1107/S0021889810042305`.

Ballhaus, Chris, Vera Laurenz, Carsten Münker, Raúl O.C. Fonseca, Francis Albarède, Arno Rohrbach, Markus Lagos, Max W. Schmidt, Klaus Peter Jochum, Brigitte Stoll, Ulrike Weis, and Hassan M. Helmy (2013). “The U/Pb ratio of the Earth’s mantle-A signature of late volatile addition”. In: *Earth and Planetary Science Letters* 362, pp. 237–245. DOI: `10.1016/j.epsl.2012.11.049`.

Barber, N.D., M. Edmonds, F. Jenner, and H. Williams (2022). “Global Ba/Nb systematics in arc magmas reflect the depths of mineral dehydration in subducted slabs”. In: *Geology* 50, pp. 1438–1442. DOI: `10.1130/g50447.1`.

Barnes, Jessica J., Francis M. McCubbin, Alison R. Santos, James M. D. Day, Jeremy W. Boyce, Susanne P. Schwenzer, Ulrich Ott, Ian A. Franchi, Scott Messenger, Mahesh Anand, and Carl B. Agee (2020). “Multiple early-formed water reservoirs in the interior of Mars”. In: *Nature Geoscience* 13.April. DOI: `10.1038/s41561-020-0552-y`.

Bell, D.R. and G.R. Rossman (1992). “Water in Earth’s Mantle: The Role of Nominally Anhydrous Minerals”. In: *Science* 255, pp. 1391–1397. DOI: `10.1126/science.255.5050.139`.

Bentham, H. L.M. and S. Rost (2014). “Scattering beneath Western Pacific subduction zones: Evidence for oceanic crust in the mid-mantle”. In: *Geophysical Journal International* 197, pp. 1627–1641. DOI: `10.1093/gji/ggu043`.

Bercovici, D. and S. Karato (2003). “Whole-mantle convection and the transition-zone water filter”. In: *Nature* 425, pp. 39–44. DOI: `10.1038/nature01918`.

Bindi, L., M. Nishi, and T. Irifune (2015). “Partition of Al between Phase D and Phase H at high pressure: Results from a simultaneous structure refinement of the two phases coexisting in a unique grain”. In: *American Mineralogist* 100, pp. 1637–1640. DOI: `10.2138/am-2015-5327`.

Bindi, L., M. Nishi, J. Tsuchiya, and T. Irifune (2014a). “Crystal chemistry of dense hydrous magnesium silicates: The structure of phase H, $MgSiH_2O_4$, synthesized at 45 GPa and 1000°C”. In: *American Mineralogist* 99, pp. 1802–1805. DOI: `10.2138/am.2014.4994`.

Bindi, Luca, Masayuki Nishi, Jun Tsuchiya, and Tetsuo Irifune (2014b). “Crystal chemistry of dense hydrous magnesium silicates: The structure of phase H, $MgSiH_2O_4$, synthesized at 45 GPa and 1000°C”. In: *American Mineralogist* 99, pp. 1802–1805. DOI: `10.2138/am.2014.4994`.

Blackwell, David D, G Bowen, A Hull, and John L Steele (1982). “Heat Flow, Arc Volcanism, and Subduction in Northern Oregon”. In: *Journal of Geophysical Research* 87.B10, pp. 8735–8754.

Bolfan-Casanova, N (2005). “Water in the Earth’s mantle”. In: *Mineralogical Magazine* 69, pp. 229–257. DOI: `10.1180/0026461056930248`.

Bower, Dan J., Michael Gurnis, and Daoyuan Sun (2013). “Dynamic origins of seismic wavespeed variation in D"”. In: *Physics of the Earth and Planetary Interiors* 214, pp. 74–86. DOI: `10.1016/j.pepi.2012.10.004`.

Bower, Dan J., June K. Wicks, Michael Gurnis, and Jennifer M. Jackson (2011). “A geodynamic and mineral physics model of a solid-state ultralow-velocity zone”. In: *Earth and Planetary Science Letters* 303.3-4, pp. 193–202. DOI: `10.1016/j.epsl.2010.12.035`.

Brandenburg, J.P. and P.E. Van Keken (2007). “Deep storage of oceanic crust in a vigorously convecting mantle”. In: *Journal of Geophysical Research* 112.B06403. DOI: `10.1029/2006JB004813`.

Bromiley, G. D. and N. Hilairet (2005). “Hydrogen and minor element incorporation in synthetic rutile”. In: *Mineralogical Magazine* 69, pp. 345–358. DOI: `10.1180/0026461056930256`.

Buchen, Johannes, Hauke Marquardt, Sergio Speziale, Takaaki Kawazoe, Tiziana Boffa Ballaran, and Alexander Kurnosov (2018). “High-pressure single-crystal elasticity of wadsleyite and the seismic signature of water in the shallow transition zone”. In: *Earth and Planetary Science Letters* 498, pp. 77–87. DOI: `10.1016/j.epsl.2018.06.027`.

Buchen, Johannes, Wolfgang Sturhahn, Takayuki Ishii, and Jennifer M Jackson (2021). "Vibrational anisotropy of δ-(Al,Fe)OOH single crystals as probed by nuclear resonant inelastic X-ray scattering". In: *European Journal of Mineralogy* 33, pp. 485–502. DOI: `10.5194/ejm-33-485-2021`.

Chang, Y.Y, S.D. Jacobsen, J.F. Lin, C.R. Bina, S.M. Thomas, J. Wu, G. Shen, Y. Xiao, P. Chow, D.J. Frost, C.A. McCammon, and P. Dera (2013). "Spin transition of Fe^{3+} in Al-bearing phase D: An alternative explanation for small-scale seismic scatterers in the mid-lower mantle". In: *Earth and Planetary Science Letters* 382, pp. 1–9. DOI: `10.1016/j.epsl.2013.08.038`.

Chen, B., J.M. Jackson, W. Sturhahn, D. Zhang, J. Zhao, J.K. Wicks, and C.A. Murphy (2012). "Spin crossover equation of state and sound velocities of $(Mg_{0.65}Fe_{0.35})O$ ferropericlase to 140 GPa". In: *Journal of Geophysical Research: Solid Earth* 117, pp. 1–9. DOI: `10.1029/2012JB009162`.

Creasy, Neala, Maureen D. Long, and Heather A. Ford (2017). "Deformation in the lowermost mantle beneath Australia from observations and models of seismic anisotropy". In: *Journal of Geophysical Research: Solid Earth* 122.7, pp. 5243–5267. DOI: `10.1002/2016JB013901`.

Crowley, John W., Mélanie Gérault, and Richard J. O'Connell (2011). "On the relative influence of heat and water transport on planetary dynamics". In: *Earth and Planetary Science Letters* 310, pp. 380–388. DOI: `10.1016/j.epsl.2011.08.035`.

Dal Zilio, Luca and Taras Gerya (2022). "Subduction earthquake cycles controlled by episodic fluid pressure cycling". In: *Lithos* 426-427.April, p. 106800. DOI: `10.1016/j.lithos.2022.106800`.

De Grave, E., R. E. Vandenberghe, and C. Dauwe (2006). "ILEEMS: Methodology and applications to iron oxides". In: *Hyperfine Interactions* 161.1-4, pp. 147–160. DOI: `10.1007/s10751-005-9177-1`.

Dewaele, Agnes, Paul Loubeyre, and Mohamed Mezouar (2004). "Equations of state of six metals above 94 GPa". In: *Physical Review B - Condensed Matter and Materials Physics* 70.9, pp. 1–8. DOI: `10.1103/PhysRevB.70.094112`.

Dewaele, Agnes, Marc Torrent, Paul Loubeyre, and Mohamed Mezouar (2008). "Compression curves of transition metals in the Mbar range: Experiments and projector augmented-wave calculations". In: *Physical Review B* 78. DOI: `10.1103/PhysRevB.78.104102`.

Dobrosavljevic, Vasilije V., Wolfgang Sturhahn, and Jennifer M. Jackson (2019). "Evaluating the role of iron-rich (Mg,Fe)O in ultralow velocity zones". In: *Minerals* 9.12. DOI: `10.3390/min9120762`.

Dobrosavljevic, Vasilije V., Dongzhou Zhang, Wolfgang Sturhahn, Stella Chariton, Vitali B. Prakapenka, Jiyong Zhao, Thomas S. Toellner, Olivia S. Pardo, and Jennifer M. Jackson (2023). "Melting and defect transitions in FeO up to pressures of Earth's core-mantle boundary". In: *Nature Communications* 14. DOI: `10.1038/s41467-023-43154-w`.

Dobson, David P., Philip G. Meredith, and Stephen A. Boon (2002). "Simulation of subduction zone seismicity by dehydration of serpentine". In: *Science* 298.5597, pp. 1407–1410. DOI: `10.1126/science.1075390`.

Dorfman, Susannah M., James Badro, Jean-Pascal Rueff, Paul Chow, Yuming Xiao, and Philippe Gillet (2015). "Composition dependence of spin transition in (Mg,Fe)SiO_3 bridgmanite". In: *American Mineralogist* 100, pp. 2246–2253. DOI: `10.2138/am-2015-5190`.

Dorogokupets, P. I. and A. R. Oganov (2006). "Equations of state of Al, Au, Cu, Pt, Ta, and W and revised ruby pressure scale". In: *Doklady Earth Sciences* 410, pp. 1091–1095. DOI: `10.1134/S1028334X06070208`.

Doucet, Luc S., Zheng Xiang Li, Hamed Gamal El Dien, Amaury Pourteau, J. Brendan Murphy, William J. Collins, Nadine Mattielli, Hugo K.H. Olierook, Christopher J. Spencer, and Ross N. Mitchell (2020). "Distinct formation history for deep-mantle domains reflected in geochemical differences". In: *Nature Geoscience* 13, pp. 511–515. DOI: `10.1038/s41561-020-0599-9`.

Douvalis, A. P., V. Papaefthymiou, A. Moukarika, and T. Bakas (2000). "Electronic and magnetic properties of the iron borate Fe_2BO_4". In: *Hyperfine Interactions* 126, pp. 319–327.

Duan, Yunfei, Ningyu Sun, Siheng Wang, Xinyang Li, Xuan Guo, Huaiwei Ni, Vitali B. Prakapenka, and Zhu Mao (2018). "Phase stability and thermal equation of state of δ-AlOOH: Implication for water transportation to the Deep Lower Mantle". In: *Earth and Planetary Science Letters* 494, pp. 92–98. DOI: `10.1016/j.epsl.2018.05.003`.

Durand, S., E. Debayle, Y. Ricard, C. Zaroli, and S. Lambotte (2017). "Confirmation of a change in the global shear velocity pattern at around 1000km depth". In: *Geophysical Journal International* 211, pp. 1628–1639. DOI: `10.1093/gji/ggx405`.

Dyar, M. Darby, David G. Agresti, Martha W. Schaefer, Christopher A. Grant, and Elizabeth C. Sklute (2006). "Mössbauer spectroscopy of Earth and planetary materials". In: *Annual Review of Earth and Planetary Sciences* 34, pp. 83–125. DOI: `10.1146/annurev.earth.34.031405.125049`.

Dziewonski, Adam M. and Don L. Anderson (1981). "Preliminary reference Earth model". In: *Physics of the Earth and Planetary Interiors* 25, pp. 297–356. DOI: `10.1016/0031-9201(81)90046-7`.

Fan, Jianke, Dapeng Zhao, Cuilin Li, Lijun Liu, and Dongdong Dong (2024). "Remnants of shifting early Cenozoic Pacific lower mantle flow imaged beneath the Philippine Sea Plate". In: *Nature Geoscience* 17, pp. 347–352. DOI: `10.1038/s41561-024-01404-6`.

Farrugia, L.J. (2012). “WinGX and ORTEP for Windows: an update”. In: *Journal of Applied Crystallography* 45, pp. 849–854. DOI: `10.1107/S0021889812029111`.

Fei, Yingwei, Angele Ricolleau, Mark Frank, Kenji Mibe, Guoyin Shen, and Vitali Prakapenka (2007a). “Toward an internally consistent pressure scale”. In: *Proceedings of the National Academy of Sciences of the United States of America* 104, pp. 9182–9186. DOI: `10.1073/pnas.0609013104`.

Fei, Yingwei, Li Zhang, Alexandre Corgne, Heather Watson, Angele Ricolleau, Yue Meng, and Vitali Prakapenka (2007b). “Spin transition and equations of state of (Mg, Fe)O solid solutions”. In: *Geophysical Research Letters* 34, pp. 1–5. DOI: `10.1029/2007GL030712`.

Férot, Anaïs and Nathalie Bolfan-Casanova (2012). “Water storage capacity in olivine and pyroxene to 14 GPa: Implications for the water content of the Earth’s upper mantle and nature of seismic discontinuities”. In: *Earth and Planetary Science Letters* 349-350, pp. 218–230. DOI: `10.1016/j.epsl.2012.06.022`.

Fialko, Yuri (2004). “Evidence of fluid-filled upper crust from observations of postseismic deformation due to the 1992 Mw7.3 Landers earthquake”. In: *Journal of Geophysical Research: Solid Earth* 109.8, pp. 1–17. DOI: `10.1029/2004JB002985`.

Fischer, Rebecca A., Andrew J. Campbell, Bethany A. Chidester, Daniel M. Reaman, Elizabeth C. Thompson, Jeffrey S. Pigott, Vitali B. Prakapenka, and Jesse S. Smith (2018). “Equations of state and phase boundary for stishovite and $CaCl_2$-type SiO_2”. In: *American Mineralogist* 103, pp. 792–802. DOI: `10.2138/am-2018-6267`.

French, Scott W. and Barbara Romanowicz (2015). “Broad plumes rooted at the base of the Earth’s mantle beneath major hotspots”. In: *Nature* 525, pp. 95–99. DOI: `10.1038/nature14876`.

Garnero, Edward J., Allen K. McNamara, and Sang Heon Shim (2016). “Continent-sized anomalous zones with low seismic velocity at the base of Earth’s mantle”. In: *Nature Geoscience* 9, pp. 481–489. DOI: `10.1038/ngeo2733`.

Gleason, A. E., C. E. Quiroga, A. Suzuki, R. Pentcheva, and W. L. Mao (2013). “Symmetrization driven spin transition in ϵ-FeOOH at high pressure”. In: *Earth and Planetary Science Letters* 379, pp. 49–55. DOI: `10.1016/j.epsl.2013.08.012`.

Gu, Jesse T., Bo Peng, Xuan Ji, Jisheng Zhang, Hong Yang, Susana Hoyos, Marc M. Hirschmann, Edwin S. Kite, and Rebecca A. Fischer (2024). “Composition of Earth’s initial atmosphere and fate of accreted volatiles set by core formation and magma ocean redox evolution”. In: *Earth and Planetary Science Letters* 629. DOI: `10.1016/j.epsl.2024.118618`.

Gu, T., M.G. Pamato, D. Novella, J. Alvaro M.and Fournelle, F.E. Brenker, W. Wang, and F. Nestola (2022). “Hydrous peridotitic fragments of Earth’s mantle 660 km discontinuity sampled by a diamond”. In: *Nature Geoscience* 15, pp. 950–954. DOI: `10.1038/s41561-022-01024-y`.

Gütlich, Philipp and Yann Garcia (2012). *Mössbauer Spectroscopy: Tutorial Book*. Ed. by Y Yoshida and G Langouche. Springer Berlin Heidelberg. DOI: `10.1007/978-3-642-32220-4_2`.

Halliday, Alex N. and Robin M. Canup (2023). “The accretion of planet Earth”. In: *Nature Reviews Earth and Environment* 4.1, pp. 19–35. DOI: `10.1038/s43017-022-00370-0`.

Haugland, S.M., J. Ritsema, S. Kaneshima, and M.S. Thorne (2017). “Estimate of the Rigidity of Eclogite in the Lower Mantle From Waveform Modeling of Broadband S-to-P Wave Conversions”. In: *Geophysical Research Letters* 44, pp. 11, 778–11, 784. DOI: `10.1002/2017GL075463`.

Heimisson, Elías Rafn, John Rudnicki, and Nadia Lapusta (2021). “Dilatancy and Compaction of a Rate-and-State Fault in a Poroelastic Medium: Linearized Stability Analysis”. In: *Journal of Geophysical Research: Solid Earth* 126.8. DOI: `10.1029/2021JB022071`.

Herman, A. (2022). “Granular effects in sea ice rheology in the marginal ice zone”. In: *Philosophical Transactions of the Royal Society A: Mathematical, Physical and Engineering Sciences* 380.2235. DOI: `10.1098/rsta.2021.0260`.

Hernlund, John W. and Christine Houser (2008). “On the statistical distribution of seismic velocities in Earth’s deep mantle”. In: *Earth and Planetary Science Letters* 265, pp. 423–437. DOI: `10.1016/j.epsl.2007.10.042`.

Hirose, Kei (2006). “Postperovskite phase transition and its geophysical implications”. In: *Reviews of Geophysics* 44.3, pp. 1–18. DOI: `10.1029/2005RG000186`.

Hirose, Kei, Stéphane Labrosse, and John Hernlund (2013). “Composition and State of the Core”. In: *Annual Review of Earth and Planetary Sciences* 41.1, pp. 657–691. DOI: `10.1146/annurev-earth-050212-124007`.

Hirschmann, Marc M. (2006). “Water, melting, and the deep Earth H_2O cycle”. In: *Annual Review of Earth and Planetary Sciences* 34, pp. 629–653. DOI: `10.1146/annurev.earth.34.031405.125211`.

Ho, Wai-Ga D., Peng Zhang, Kristjan Haule, Jennifer M. Jackson, Vladimir Dobrosavljevic, and Vasilije V. Dobrosavljevic (2023). “Quantum critical phase of FeO spans conditions of Earth’s lower mantle”. In: pp. 1–8. DOI: `10.1038/s41467-024-47489-w`.

Hosseini, Kasra, Karin Sigloch, Maria Tsekhmistrenko, Afsaneh Zaheri, Tarje Nissen-Meyer, and Heiner Igel (2020). “Global mantle structure from multifrequency tomography using P, PP and P-diffracted waves”. In: *Geophysical Journal International* 220, pp. 96–141. DOI: `10.1093/gji/ggz394`.

Houser, C., J. W. Hernlund, J. Valencia-Cardona, and R. M. Wentzcovitch (2020). "Discriminating lower mantle composition". In: *Physics of the Earth and Planetary Interiors* 308.106552. DOI: `10.1016/j.pepi.2020.106552`.

Hsu, Han (2017). "First-principles study of iron spin crossover in the new hexagonal aluminous phase". In: *Physical Review B* 95.2, pp. 1–7. DOI: `10.1103/PhysRevB.95.020406`.

Hu, Qingyang, Duck Young Kim, Jin Liu, Yue Meng, Liuxiang Yang, Dongzhou Zhang, Wendy L. Mao, and Ho Kwang Mao (2017). "Dehydrogenation of goethite in Earth's deep lower mantle". In: *Proceedings of the National Academy of Sciences of the United States of America* 114.7, pp. 1498–1501. DOI: `10.1073/pnas.1620644114`.

Hushur, Anwar, Murli H. Manghnani, Joseph R. Smyth, Quentin Williams, Eric Hellebrand, Dayana Lonappan, Yu Ye, Przemyslaw Dera, and Daniel J. Frost (2011). "Hydrogen bond symmetrization and equation of state of phase D". In: *Journal of Geophysical Research: Solid Earth* 116, pp. 1–8. DOI: `10.1029/2010JB008087`.

Ikeda, Osamu, Tatsuya Sakamaki, Tomonori Ohashi, Masahisa Goto, Yuji Higo, and Akio Suzuki (2019). "Sound velocity measurements of ϵ-FeOOH up to 24 GPa". In: *Journal of Mineralogical and Petrological Sciences* 114.3, pp. 155–160. DOI: `10.2465/jmps.181115b`.

Insixiengmay, Leslie and Lars Stixrude (2023). "Hydrogen bond symmetrization and high-spin to low-spin transition of ϵ-FeOOH at the pressure of Earth's lower mantle". In: *American Mineralogist* 108.12, pp. 2209–2218. DOI: `10.2138/am-2022-8839`.

Ishii, T., L. Shi, R. Huang, N. Tsujino, D. Druzhbin, R. Myhill, Y. Li, L. Wang, T. Yamamoto, N. Miyajima, T. Kawazoe, N. Nishiyama, Y. Higo, Y. Tange, and T. Katsura (2016). "Generation of pressures over 40 GPa using Kawai-type multi-anvil press with tungsten carbide anvils". In: *Review of Scientific Instruments* 87.2. DOI: `10.1063/1.4941716`.

Ishii, Takayuki, Giacomo Criniti, Eiji Ohtani, Narangoo Purevjav, Hongzhan Fei, Tomoo Katsura, and Ho Kwang Mao (2022a). "Superhydrous aluminous silica phases as major water hosts in high-temperature lower mantle". In: *Proceedings of the National Academy of Sciences of the United States of America* 119.44, pp. 1–6. DOI: `10.1073/pnas.2211243119`.

Ishii, Takayuki, Giacomo Criniti, Narangoo Purevjav, Tomoo Katsura, and Eiji Ohtani (2024). "Hydrogen partitioning between stishovite and hydrous phase δ: implications for water cycle and distribution in the lower mantle". In: *Progress in Earth and Planetary Science* 11.10. DOI: `10.1186/s40645-024-00615-0`.

Ishii, Takayuki, Zhaodong Liu, and Tomoo Katsura (2019). "A Breakthrough in Pressure Generation by a Kawai-Type Multi-Anvil Apparatus with Tungsten Carbide Anvils". In: *Engineering* 5.3, pp. 434–440. DOI: `10.1016/j.eng.2019.01.013`.

Ishii, Takayuki, Eiji Ohtani, and Anton Shatskiy (2022b). “Aluminum and hydrogen partitioning between bridgmanite and high-pressure hydrous phases: Implications for water storage in the lower mantle”. In: *Earth and Planetary Science Letters* 583. DOI: `10.1016/j.epsl.2022.117441`.

Jackson, Jennifer M. and Christine Thomas (2021). *Seismic and Mineral Physics Constraints on the D” Layer*. Ed. by H. Marquardt, M. Ballmer, S. Cottaar, and J. Konter. American Geophysical Union, pp. 193–227. DOI: `10.1002/9781119528609.ch8`.

Jacobsen, S.D., Z. Liu, T. Boffa Ballaran, E.F Littlefield, L. Ehm, and R.J. Hemley (2010). “Effect of H_2O on upper mantle phase transitions in $MgSiO_3$: Is the depth of the seismic X-discontinuity an indicator of mantle water content?” In: *Physics of the Earth and Planetary Interiors* 183, pp. 234–244. DOI: `10.1016/j.pepi.2010.06.015`.

Jacobsen, Steven D. (2018). “Effect of water on the equation of state of nominally anhydrous minerals”. In: *Water in Nominally Anhydrous Minerals* 62.April, pp. 321–342. DOI: `10.2138/rmg.2006.62.14`.

Jahn, Sandro, Bernd Wunder, Monika Koch-Müller, Leïla Tarrieu, Michael Pöhle, Anke Watenphul, and Michael N. Taran (2012). “Pressure-induced hydrogen bond symmetrisation in guyanaite, β-CrOOH: evidence from spectroscopy and ab initio simulations”. In: *European Journal of Mineralogy* 24.5, pp. 839–850. DOI: `10.1127/0935-1221/2012/0024-2228`.

Jones, Timothy D., Ross R. Maguire, Peter E. van Keken, Jeroen Ritsema, and Paula Koelemeijer (2020). “Subducted oceanic crust as the origin of seismically slow lower-mantle structures”. In: *Progress in Earth and Planetary Science* 7.1, pp. 1–16. DOI: `10.1186/s40645-020-00327-1`.

Kagi, H., D. Ushijima, A. Sano-Furukawa, K. Komatsu, R. Iizuka, T. Nagai, and S. Nakano (2010). “Infrared absorption spectra of δ-AlOOH and its deuteride at high pressure and implication to pressure response of the hydrogen bonds”. In: *Journal of Physics: Conference Series* 215. DOI: `10.1088/1742-6596/215/1/012052`.

Kaneshima, Satoshi (2016). “Seismic scatterers in the mid-lower mantle”. In: *Physics of the Earth and Planetary Interiors* 257, pp. 105–114. DOI: `10.1016/j.pepi.2016.05.004`.

Karato, S. (2011). “Water distribution across the mantle transition zone and its implications for global material circulation”. In: *Earth and Planetary Science Letters* 301, pp. 413–423. DOI: `10.1016/j.epsl.2010.11.038`.

Katsura, Tomoo (2022). “A Revised Adiabatic Temperature Profile for the Mantle”. In: *Journal of Geophysical Research: Solid Earth* 127, pp. 1–11. DOI: `10.1029/2021JB023562`.

Kawamoto, Tatsuhiko (2006). “Hydrous phases and water transport in the subducting slab”. In: *Reviews in Mineralogy and Geochemistry* 62, pp. 273–289. DOI: `10.2138/rmg.2006.62.12`.

Kawano, Katsutoshi, Masayuki Nishi, Hideharu Kuwahara, Sho Kakizawa, Toru Inoue, and Tadashi Kondo (2024). "Extensive iron-water exchange at Earth's core-mantle boundary can explain seismic anomalies". In: *Nature communications* 15. DOI: `10.1038/s41467-024-52677-9`.

Kawazoe, T., I. Ohira, T. Ishii, T. Boffa Ballaran, C. McCammon, and A. Suzuki (2017). "Single crystal synthesis of δ-(Al,Fe)OOH". In: *American Mineralogist* 102, pp. 1953–1956. DOI: `10.2138/am-2017-6153`.

Kennett, B. L.N. and E. R. Engdahl (1991). "Traveltimes for global earthquake location and phase identification". In: *Geophysical Journal International* 105, pp. 429–465. DOI: `10.1111/j.1365-246X.1991.tb06724.x`.

Kennett, B. L.N., E. R. Engdahl, and R. Buland (1995). "Constraints on seismic velocities in the Earth from traveltimes". In: *Geophysical Journal International* 122, pp. 108–124. DOI: `10.1111/j.1365-246X.1995.tb03540.x`.

Kim, D., V. Lekić, B. Ménard, D. Baron, and M. Taghizadeh-Popp (2020). "Sequencing seismograms: A panoptic view of scattering in the core-mantle boundary region". In: *Science* 368, pp. 1223–1228. DOI: `10.1126/science.aba8972`.

Kim, Taehyun, Joseph G. O'Rourke, Jeongmin Lee, Stella Chariton, Vitali Prakapenka, Rachel J. Husband, Nico Giordano, Hanns Peter Liermann, Sang Heon Shim, and Yongjae Lee (2023). "A hydrogen-enriched layer in the topmost outer core sourced from deeply subducted water". In: *Nature Geoscience* 16.12, pp. 1208–1214. DOI: `10.1038/s41561-023-01324-x`.

King, H E and L W Finger (1979). "Diffracted beam crystal centering and its application to high-pressure crystallography". In: *Journal of Applied Crystallography* 12, pp. 374–378. DOI: `10.1107/S0021889879012723`.

Koelemeijer, P., J. Ritsema, A. Deuss, and H. J. van Heijst (2016). "SP12RTS: A degree-12 model of shear- and compressional-wave velocity for Earth's mantle". In: *Geophysical Journal International* 204, pp. 1024–1039. DOI: `10.1093/gji/ggv481`.

Kolesov, Boris A. (2021). "Hydrogen bonds: Raman spectroscopic study". In: *International Journal of Molecular Sciences* 22.10. DOI: `10.3390/ijms22105380`.

Komatsu, K., A. Sano-Furukawa, and H. Kagi (2011). "Effects of Mg and Si ions on the symmetry of δ-AlOOH". In: *Physics and Chemistry of Minerals* 38, pp. 727–733. DOI: `10.1007/s00269-011-0445-0`.

Koudriachova, Marina V., Simon W. De Leeuw, and Nicholas M. Harrison (2004). "First-principles study of H intercalation in rutile TiO_2". In: *Physical Review B - Condensed Matter and Materials Physics* 70.16, pp. 1–5. DOI: `10.1103/PhysRevB.70.165421`.

Kruijer, Thomas S., Thorsten Kleine, Mario Fischer-Gödde, and Peter Sprung (2015). "Lunar tungsten isotopic evidence for the late veneer". In: *Nature* 520, pp. 534–537. DOI: `10.1038/nature14360`.

Kudoh, Y., T. Kuribayashi, A. Suzuki, E. Ohtani, and T. Kamada (2004). “Space group and hydrogen sites of δ-AlOOH and implications for a hypothetical high-pressure form of $Mg(OH)_2$”. In: *Physics and Chemistry of Minerals* 31.6, pp. 360–364. DOI: `10.1007/s00269-004-0404-0`.

Kuribayashi, Takahiro, Asami Sano-Furukawa, and Toshiro Nagase (2014). “Observation of pressure-induced phase transition of δ-AlOOH by using single-crystal synchrotron X-ray diffraction method”. In: *Physics and Chemistry of Minerals* 41, pp. 303–312. DOI: `10.1007/s00269-013-0649-6`.

Lai, Voon Hui, Don V. Helmberger, Vasilije V. Dobrosavljevic, Wenbo Wu, Daoyuan Sun, Jennifer M. Jackson, and Michael Gurnis (2022). “Strong ULVZ and Slab Interaction at the Northeastern Edge of the Pacific LLSVP Favors Plume Generation”. In: *Geochemistry, Geophysics, Geosystems* 23.2, pp. 1–19. DOI: `10.1029/2021GC010020`.

Lakshtanov, Dmitry L., Stanislav V. Sinogeikin, Konstantin D. Litasov, Vitali B. Prakapenka, Holger Hellwig, Jingyun Wang, Carmen Sanches-Valle, Jean Philippe Perrillat, Bin Chen, Maddury Somayazulu, Jie Li, Eiji Ohtani, and Jay D. Bass (2007). “The post-stishovite phase transition in hydrous alumina-bearing SiO_2 in the lower mantle of the earth”. In: *Proceedings of the National Academy of Sciences of the United States of America* 104, pp. 13588–13590. DOI: `10.1073/pnas.0706113104`.

Li, Lin, Chao Li, and Sheng-rong Li (2022). “Epidote as a conveyor of water into the Earth’s deep mantle in subduction zones: Insights from coupled high pressure - temperature experiments”. In: *American Mineralogist* 108.January, pp. 120–126. DOI: `10.2138/am-2022-8252`.

Li, Yunguo, L. Vočadlo, T. Sun, and J.P. Brodholt (2020). “The Earth’s core as a reservoir of water”. In: *Nature Geoscience* 13, pp. 453–458. DOI: `10.1038/s41561-020-0578-1`.

Libowitzky, Eugen (1999). “Correlation of O-H stretching frequencies and O-H--O hydrogen bond lengths in minerals”. In: *Monatshefte fur Chemie* 130.8, pp. 1047–1059.

Lin, Jung Fu, Viktor V. Struzhkin, Steven D. Jacobsen, Michael Y. Hu, Paul Chow, Jennifer Kung, Haozhe Liu, Ho Kwang Mao, and Russell J. Hemley (2005). “Spin transition of iron in magnesiowüstite in the Earth’s lower mantle”. In: *Nature* 436, pp. 377–380. DOI: `10.1038/nature03825`.

Lin, Jung Fu and Taku Tsuchiya (2008). “Spin transition of iron in the Earth’s lower mantle”. In: *Physics of the Earth and Planetary Interiors* 170, pp. 248–259. DOI: `10.1016/j.pepi.2008.01.005`.

Lin, Y., Q. Hu, Y. Meng, M. Walter, and H.K. Mao (2020). “Evidence for the stability of ultrahydrous stishovite in Earth’s lower mantle”. In: *Proceedings of the National Academy of Sciences of the United States of America* 117, pp. 184–189. DOI: `10.1073/pnas.1914295117`.

Litasov, K. and E. Ohtani (2003). “Stability of various hydrous phases in CMAS pyrolite-H_2O system up to 25 GPa”. In: *Physics and Chemistry of Minerals* 30.3, pp. 147–156. DOI: `10.1007/s00269-003-0301-y`.

Litasov, Konstantin D., Eiji Ohtani, Akio Suzuki, and Kenichi Funakoshi (2007). “The compressibility of Fe- and Al-bearing phase D to 30 GPa”. In: *Physics and Chemistry of Minerals* 34, pp. 159–167. DOI: `10.1007/s00269-006-0136-4`.

Liu, H., M. Gurnis, W. Leng, Z. Jia, and Z. Zhan (2021). “Tonga Slab Morphology and Stress Variations Controlled by a Relic Slab: Implications for Deep Earthquakes in the Tonga-Fiji Region”. In: *Geophysical Research Letters* 48, pp. 1–10. DOI: `10.1029/2020GL091331`.

Liu, Jin, Jung Fu Lin, and Vitali B. Prakapenka (2015). “High-Pressure Orthorhombic Ferromagnesite as a Potential Deep-Mantle Carbon Carrier”. In: *Scientific Reports* 5, pp. 3–8. DOI: `10.1038/srep07640`.

Liu, W., Y. Zhang, F. Tissot, G. Avice, and Q. Ye Z.and Yin (2023). “I/Pu reveals Earth mainly accreted from volatile-poor differentiated planetesimals”. In: *Science Advances* 9. DOI: `10.1126/sciadv.adg9213`.

Liu, Xingcheng, Kyoko N. Matsukage, Yu Nishihara, Toshihiro Suzuki, and Eiichi Takahashi (2019). “Stability of the hydrous phases of Al-rich phase D and Al-rich phase H in deep subducted oceanic crust”. In: *American Mineralogist* 104, pp. 64–72. DOI: `10.2138/am-2019-6559`.

Lyubutin, I. S., C. R. Lin, Yu V. Korzhetskiy, T. V. Dmitrieva, and R. K. Chiang (2009). “Mössbauer spectroscopy and magnetic properties of hematite/magnetite nanocomposites”. In: *Journal of Applied Physics* 106. DOI: `10.1063/1.3194316`.

Mao, W., M. Gurnis, and W. Wu (2022). “On the Origin of Small-Scale Seismic Scatters at 660-km Depth”. In: *Geochemistry, Geophysics, Geosystems* 23. DOI: `10.1029/2022GC010560`.

Mao, Z., S. D. Jacobsen, F. Jiang, J. R. Smyth, C. M. Holl, and T. S. Duffy (2008). “Elasticity of hydrous wadsleyite to 12 GPa: Implications for Earth’s transition zone”. In: *Geophysical Research Letters* 35.21. DOI: `10.1029/2008GL035618`.

Mao, Zhu, Jung-Fu Lin, Jing Yang, Toru Inoue, and Vitali B. Prakapenka (2015). “Effects of the Fe^{3+} spin transition on the equation of state of bridgmanite”. In: *Geophysical Research Letters* 42, pp. 4335–4342. DOI: `10.1002/2015GL064400`.

Mashino, Izumi, Motohiko Murakami, and Eiji Ohtani (2016). “Sound velocities of δ-AlOOH up to core-mantle boundary pressures with implications for the seismic anomalies in the deep mantle”. In: *Journal of Geophysical Research, Solid Earth* 121, pp. 595–609. DOI: `10.1002/2015JB012477`.

McNamara, A.K. (2019). “A review of large low shear velocity provinces and ultra low velocity zones”. In: *Tectonophysics* 760, pp. 199–220. DOI: `10.1016/j.tecto.2018.04.015`.

McNamara, A.K., E.J. Garnero, and S. Rost (2010). “Tracking deep mantle reservoirs with ultra-low velocity zones”. In: *Earth and Planetary Science Letters* 299, pp. 1–9. DOI: `10.1016/j.epsl.2010.07.042`.

Meer, Douwe G. van der, Douwe J.J. van Hinsbergen, and Wim Spakman (2018). “Atlas of the underworld: Slab remnants in the mantle, their sinking history, and a new outlook on lower mantle viscosity”. In: *Tectonophysics* 723, pp. 309–448. DOI: `10.1016/j.tecto.2017.10.004`.

Meier, Thomas, Florian Trybel, Saiana Khandarkhaeva, Dominique Laniel, Takayuki Ishii, Alena Aslandukova, Natalia Dubrovinskaia, and Leonid Dubrovinsky (2022). “Structural independence of hydrogen-bond symmetrisation dynamics at extreme pressure conditions”. In: *Nature Communications* 13, pp. 1–8. DOI: `10.1038/s41467-022-30662-4`.

Momma, Koichi and Fujio Izumi (2011). “VESTA 3 for three-dimensional visualization of crystal, volumetric and morphology data”. In: *Journal of Applied Crystallography* 44.6, pp. 1272–1276. DOI: `10.1107/S0021889811038970`.

Morrison, Rachel A., Jennifer M. Jackson, Wolfgang Sturhahn, Dongzhou Zhang, and Eran Greenberg (2018). “Equations of State and Anisotropy of Fe-Ni-Si Alloys”. In: *Journal of Geophysical Research: Solid Earth* 123. DOI: `10.1029/2017JB015343`.

Mukhopadhyay, Sujoy (2012). “Early differentiation and volatile accretion recorded in deep-mantle neon and xenon”. In: *Nature* 486, pp. 101–104. DOI: `10.1038/nature11141`.

Mukhopadhyay, Sujoy and Rita Parai (2019). “Noble gases: A record of earth’s evolution and mantle dynamics”. In: *Annual Review of Earth and Planetary Sciences* 47, pp. 389–419. DOI: `10.1146/annurev-earth-053018-060238`.

Murakami, M., K. Hirose, H. Yurimoto, S. Nakashima, and N. Takafuji (2002). “Water in Earth’s Lower Mantle”. In: *Science* 295, pp. 1885–1888. DOI: `10.1126/science.1065998`.

Murakami, Motohiko, Kei Hirose, Katsuyuki Kawamura, Nagayoshi Sata, and Yasuo Ohishi (2004). “Post-Perovskite Phase Transition in $MgSiO_3$”. In: *Science* 304, pp. 855–858. DOI: `10.1126/science.1095932`.

Nakagawa, Takashi and Paul J. Tackley (2015). “Geochemistry, Geophysics, Geosystems”. In: *Geochemistry Geophysics Geosystems* 16.1, pp. 267–300. DOI: `10.1002/2014GC005701`.

Newcombe, M. E., S. G. Nielsen, L. D. Peterson, J. Wang, C. M.O.D. Alexander, A. R. Sarafian, K. Shimizu, L. R. Nittler, and A. J. Irving (2023). “Degassing of early-formed planetesimals restricted water delivery to Earth”. In: *Nature* 615, pp. 854–857. DOI: `10.1038/s41586-023-05721-5`.

Ni, Sidao and Don V. Helmberger (2003). “Seismological constraints on the South African superplume: Could be the oldest distinct structure on earth”. In: *Earth and Planetary Science Letters* 206.1-2, pp. 119–131. DOI: `10.1016/S0012-821X(02)01072-5`.

Ni, Sidao, Eh Tan, Michael Gurnis, and Don Helmberger (2002). “Sharp sides to the African superplume”. In: *Science* 296.5574, pp. 1850–1852. DOI: `10.1126/science.1070698`.

Nishi, M., J. Tsuchiya, Y. Kuwayama, T. Arimoto, Y. Tange, Y. Higo, T. Hatakeyama, and T. Irifune (2019). “Solid Solution and Compression Behavior of Hydroxides in the Lower Mantle”. In: *Journal of Geophysical Research: Solid Earth* 124.10, pp. 10231–10239. DOI: `10.1029/2019JB018146`.

Nishi, Masayuki, Yasuhiro Kuwayama, Jun Tsuchiya, and Taku Tsuchiya (2017). “The pyrite-Type high-pressure form of FeOOH”. In: *Nature* 547.7662, pp. 205–208. DOI: `10.1038/nature22823`.

Nishi, Masayuki, Jun Tsuchiya, Takeshi Arimoto, Sho Kakizawa, Takehiro Kunimoto, Yoshinori Tange, Yuji Higo, and Tetsuo Irifune (2018). “Thermal equation of state of $MgSiO_4H_2$ phase H determined by in situ X-ray diffraction and a multianvil apparatus”. In: *Physics and Chemistry of Minerals* 45, pp. 995–1001. DOI: `10.1007/s00269-018-0980-z`.

Nomura, Ryuichi, Kei Hirose, Nagayoshi Sata, Yasuo Ohishi, Daisuke Suetsugu, Craig Bina, Toru Inoue, Douglas Wiens, and Mark Jellinek (2010). “Precise determination of post-stishovite phase transition boundary and implications for seismic heterogeneities in the mid-lower mantle”. In: *Physics of the Earth and Planetary Interiors* 183.1-2, pp. 104–109. DOI: `10.1016/j.pepi.2010.08.004`.

Oganov, Artem R. and Shigeaki Ono (2004). “Theoretical and experimental evidence for a post-perovskite phase of $MgSiO_3$ in Earth’s D" layer”. In: *Nature* 430, pp. 445–448. DOI: `10.1038/nature02701`.

Ohira, I., J.M. Jackson, N.V. Solomatova, W. Sturhahn, G.J. Finkelstein, S. Kamada, T. Kawazoe, F. Maeda, N. Hirao, S. Nakano, T.S. Toellner, A. Suzuki, and E. Ohtani (2019). “Compressional behavior and spin state of δ-(Al,Fe)OOH at high pressures”. In: *American Mineralogist* 104, pp. 1273–1284. DOI: `10.2138/am-2019-6913`.

Ohira, I., E. Ohtani, T. Sakai, M. Miyahara, N. Hirao, Y. Ohishi, and M. Nishijima (2014). “Stability of a hydrous δ-phase, AlOOH-$MgSiO_2(OH)_2$, and a mechanism for water transport into the base of lower mantle”. In: *Earth and Planetary Science Letters* 401, pp. 12–17. DOI: `10.1016/j.epsl.2014.05.059`.

Ohira, Itaru, Jennifer M. Jackson, Wolfgang Sturhahn, Gregory J. Finkelstein, Takaaki Kawazoe, Thomas S. Toellner, Akio Suzuki, and Eiji Ohtani (2021). “The influence of δ-(Al,Fe)OOH on seismic heterogeneities in Earth’s lower mantle”. In: *Scientific Reports* 11. DOI: `10.1038/s41598-021-91180-9`.

Ohtani, Eiji (2015). “Hydrous minerals and the storage of water in the deep mantle”. In: *Chemical Geology* 418, pp. 6–15. DOI: `10.1016/j.chemgeo.2015.05.005`.

– (2020). “The role of water in Earth’s mantle”. In: *National Science Review* 7, pp. 224–232. DOI: `10.1093/nsr/nwz071`.

Ohtani, Eiji, Konstantin Litasov, Akio Suzuki, and Tadashi Kondo (2001). “Stability field of new hydrous phase δ-AlOOH, for water transport into the deep mantle”. In: *Geophysical Research Letters* 28.20, pp. 3991–3993.

Ohtani, Eiji, Liang Yuan, Itaru Ohira, Anton Shatskiy, and Konstantin Litasov (2018). “Fate of water transported into the deep mantle by slab subduction”. In: *Journal of Asian Earth Sciences* 167, pp. 2–10. DOI: `10.1016/j.jseaes.2018.04.024`.

Omori, Soichi, Tetsuya Komabayashi, and Shigenori Maruyama (2004). “Dehydration and earthquakes in the subducting slab: Empirical link in intermediate and deep seismic zones”. In: *Physics of the Earth and Planetary Interiors* 146.1-2, pp. 297–311. DOI: `10.1016/j.pepi.2003.08.014`.

Palfey, W., G. Rossman, and W. Goddard (2021). “Structure, Energetics, and Spectra for the Oxygen Vacancy in Rutile: Prominence of the Ti-HO-Ti Bond”. In: *Journal of Physical Chemistry Letters* 12, pp. 10175–10181. DOI: `10.1021/acs.jpclett.1c02850`.

Palfey, W., G.R. Rossman, and W.A Goddard (2023). “Behavior of Hydrogarnet-Type Defects in Hydrous Stishovite at Various Temperatures and Pressures”. In: *Journal of Geophysical Research: Solid Earth*, 1–11. DOI: `10.1029/2022JB024980`.

Palot, M., S.D. Jacobsen, J.P. Townsend, F. Nestola, Marquardt K., N. Miyajima, J.W. Harris, T. Stachel, C.A. McCammon, and D.G. Pearson (2016). “Evidence for H_2O-bearing fluids in the lower mantle from diamond inclusion”. In: *Lithos* 265, pp. 237–243. DOI: `10.1016/j.lithos.2016.06.023`.

Panero, W. R., C. Thomas, R. Myhill, and J. S. Pigott (2020). “Dehydration Melting Below the Undersaturated Transition Zone”. In: *Geochemistry, Geophysics, Geosystems* 21. DOI: `10.1029/2019GC008712`.

Panero, Wendy R. and Razvan Caracas (2017). “Stability of phase H in the $MgSiO_4H_2$–AlOOH–SiO_2 system”. In: *Earth and Planetary Science Letters* 463, pp. 171–177. DOI: `10.1016/j.epsl.2017.01.033`.

Parai, R. and S. Mukhopadhyay (2015). “The evolution of MORB and plume mantle volatile budgets: Constraints from fission Xe isotopes in Southwest Indian Ridge basalts”. In: *Geochemistry Geophysics Geosystems* 16, pp. 719–735. DOI: `10.1002/2014GC005566`.

Parai, Rita and Sujoy Mukhopadhyay (2018). “Xenon isotopic constraints on the history of volatile recycling into the mantle”. In: *Nature* 560, pp. 223–227. DOI: `10.1038/s41586-018-0388-4`.

Pearson, D.G., F.E. Brenker, F. Nestola, J. McNeill, L. Nasdala, M.T. Hutchison, S. Matveev, K. Mather, G. Silversmit, S. Schmitz, B. Vekemans, and L. Vincze (2014). “Hydrous mantle transition zone indicated by ringwoodite included within diamond”. In: *Nature* 507, pp. 221–224. DOI: `10.1038/nature13080`.

Peslier, Anne H., Maria Schönbächler, Henner Busemann, and Shun Ichiro Karato (2017). “Water in the Earth’s Interior: Distribution and Origin”. In: *Space Science Reviews* 212.1-2, pp. 743–810. DOI: `10.1007/s11214-017-0387-z`.

Piani, Laurette, Yves Marrocchi, Thomas Rigaudier, Lionel G Vacher, Dorian Thomassin, and Bernard Marty (2020). “Earth’s water may have been inherited from material similar to enstatite chondrite meteorites.” In: *Science* 369.6507, pp. 1110–1113. DOI: `10.1126/science.aba1948`.

Pisconti, Angelo, Neala Creasy, James Wookey, Maureen D. Long, and Christine Thomas (2023). “Mineralogy, fabric and deformation domains in D” across the southwestern border of the African LLSVP”. In: *Geophysical Journal International* 232, pp. 705–724. DOI: `10.1093/gji/ggac359`.

Poirier, Jean-Paul (1994). “Light elements in the Earth’s outer core: A critical review”. In: *Physics of the Earth and Planetary Interiors* 85.3-4, pp. 319–337. DOI: `https://doi.org/10.1016/0031-9201(94)90120-1`.

Prescher, Clemens and Vitali B. Prakapenka (2015). “DIOPTAS: A program for reduction of two-dimensional X-ray diffraction data and data exploration”. In: *High Pressure Research* 35, pp. 223–230. DOI: `10.1080/08957959.2015.1059835`.

Qin, Liping, Conel M.O.D. Alexander, Richard W. Carlson, Mary F. Horan, and Tetsuya Yokoyama (2010). “Contributors to chromium isotope variation of meteorites”. In: *Geochimica et Cosmochimica Acta* 74.3, pp. 1122–1145. DOI: `10.1016/j.gca.2009.11.005`.

Ralph, R L and L W Finger (1982). “A Computer-Program for Refinement of Crystal Orientation Matrix and Lattice-Constants from Diffractometer Data with Lattice Symmetry Constraints”. In: *Journal of Applied Crystallography* 15, pp. 537–539. DOI: `10.1107/S0021889882012539`.

Ranganathan, Meghana and Brent Minchew (2024). “A modified viscous flow law for natural glacier ice: Scaling from laboratories to ice sheets”. In: *Proceedings of the National Academy of Sciences of the United States of America* 121.23, pp. 1–11. DOI: `10.1073/pnas.2309788121`.

Ricolleau, Angele, Yingwei Fei, Elizabeth Cottrell, Heather Watson, Liwei Deng, Li Zhang, Guillaume Fiquet, Anne Line Auzende, Mathieu Roskosz, Guillaume Morard, and Vitali Prakapenka (2009). “Density profile of pyrolite under the lower mantle conditions”. In: *Geophysical Research Letters* 36.6, pp. 1–5. DOI: `10.1029/2008GL036759`.

Ritsema, J., S. Kaneshima, and S. Haugland (2020). "The dimensions of scatterers in the lower mantle using USArray recordings of S-wave to P-wave conversions". In: *Physics of the Earth and Planetary Interiors* 306. DOI: `10.1016/j.pepi.2020.106541`.

Rochira, Federica, Lina Schumacher, and Christine Thomas (2022). "Mapping the edge of subducted slabs in the lower mantle beneath southern Asia". In: *Geophysical Journal International* 230.2, pp. 1239–1252. DOI: `10.1093/gji/ggac110`.

Ross, Zachary E. and Elizabeth S. Cochran (2021). "Evidence for Latent Crustal Fluid Injection Transients in Southern California From Long-Duration Earthquake Swarms". In: *Geophysical Research Letters* 48.12. DOI: `10.1029/2021GL092465`.

Rossman, G. R. (1996). "Studies of OH in nominally anhydrous minerals". In: *Physics and Chemistry of Minerals* 23, pp. 299–304. DOI: `10.1007/BF00207777`.

Rüpke, Lars H., Jason Phipps Morgan, Matthias Hort, and James A.D. Connolly (2004). "Serpentine and the subduction zone water cycle". In: *Earth and Planetary Science Letters* 223.1-2, pp. 17–34. DOI: `10.1016/j.epsl.2004.04.018`.

Russell, Stuart, Jessica C.E. Irving, Lisanne Jagt, and Sanne Cottaar (2023). "Evidence for a Kilometer-Scale Seismically Slow Layer Atop the Core-Mantle Boundary From Normal Modes". In: *Geophysical Research Letters* 50.24. DOI: `10.1029/2023GL105684`.

Saki, Morvarid, Christine Thomas, and Rafael Abreu (2022). "Detection and modelling of strong topography of mid-mantle structures beneath the North Atlantic". In: *Geophysical Journal International* 229.1, pp. 219–234. DOI: `10.1093/gji/ggab465`.

Sano, Asami, Eiji Ohtani, Tadashi Kondo, Naohisa Hirao, Takeshi Sakai, Nagayoshi Sata, Yasuo Ohishi, and Takumi Kikegawa (2008). "Aluminous hydrous mineral δ-AlOOH as a carrier of hydrogen into the core-mantle boundary". In: *Geophysical Research Letters* 35, pp. 1–5. DOI: `10.1029/2007GL031718`.

Sano-Furukawa, Asami, Takanori Hattori, Kazuki Komatsu, Hiroyuki Kagi, Takaya Nagai, Jamie J. Molaison, António M. dos Santos, and Christopher A. Tulk (2018). "Direct observation of symmetrization of hydrogen bond in δ-AlOOH under mantle conditions using neutron diffraction". In: *Scientific Reports* 8. DOI: `10.1038/s41598-018-33598-2`.

Sano-Furukawa, Asami, Hiroyuki Kagi, Takaya Nagai, Satatoshi Nakano, Satatoshi Fukura, Daichi Ushijima, Riko Iizuka, Eiji Ohtahtahtani, and Takehehiko Yagi (2009a). "Change in compressibility of δ-AlOOH and δ-AlOOD at high pressure: A study of isotope effect and hydrogen-bond symmetrization". In: *American Mineralogist* 94, pp. 1255–1261. DOI: `10.2138/am.2009.3109`.

Sano-Furukawa, Asami, Hiroyuki Kagi, Takaya Nagai, Satoshi Nakano, Satoshi Fukura, Daichi Ushijima, Riko Iizuka, Eiji Ohtani, and Takehiko Yagi (2009b). "Change in compressibility of δ-AlOOH and δ-AlOOD at high pressure: A study of isotope effect and hydrogen-bond symmetrization". In: *American Mineralogist* 94, pp. 1255–1261.

Satta, Niccolò, Giacomo Criniti, Alexander Kurnosov, Tiziana Boffa Ballaran, Takayuki Ishii, and Hauke Marquardt (2024). " Elastic anomalies across the $P2_1mn$ –> Pnnm structural phase transition in δ-(Al,Fe)OOH ". In: *American Mineralogist* 109, pp. 1934–1944. DOI: `10.2138/am-2023-9129`.

Satta, Niccolò, Giacomo Criniti, Alexander Kurnosov, Tiziana Boffa Ballaran, Takayuki Ishii, and Hauke Marquardt (2021). "High-Pressure Elasticity of δ-(Al,Fe)OOH Single Crystals and Seismic Detectability of Hydrous MORB in the Shallow Lower Mantle". In: *Geophysical Research Letters* 48.23, pp. 1–10. DOI: `10.1029/2021GL094185`.

Scheller, E. L., B. L. Ehlmann, Renyu Hu, D. J. Adams, and Y. L. Yung (2021). "Long-term drying of Mars by sequestration of ocean-scale volumes of water in the crust". In: *Science* 372.6537, pp. 56–62. DOI: `10.1126/science.abc7717`.

Schmandt, Brandon, Steven D. Jacobsen, Thorsten W Becker, Zhenxian Liu, and Kenneth G. Dueker (2014). "Dehydration melting at the top of the lower mantle". In: *Science* 344, pp. 1265–1268. DOI: `10.1126/science.1253358`.

Schuberth, B. S.A. and H. P. Bunge (2009). "Tomographic filtering of high-resolution mantle circulation models: Can seismic heterogeneity be explained by temperature alone?" In: *Geochemistry, Geophysics, Geosystems* 10. DOI: `10.1029/2009GC002401`.

Schumacher, L. and C. Thomas (2016). "Detecting lower-mantle slabs beneath Asia and the Aleutians". In: *Geophysical Journal International* 205, pp. 1512–1524. DOI: `10.1093/gji/ggw098`.

Sheldrick, G.M. (1997). *SHELX-97*.

Shen, Guoyin, Yanbin Wang, Agnes Dewaele, Christine Wu, Dayne E. Fratanduono, Jon Eggert, Stefan Klotz, Kamil F. Dziubek, Paul Loubeyre, Oleg V. Fat'yanov, Paul D. Asimow, Tsutomu Mashimo, and Renata M.M. Wentzcovitch (2020). "Toward an international practical pressure scale: A proposal for an IPPS ruby gauge (IPPS-Ruby2020)". In: *High Pressure Research* 40.3, pp. 299–314. DOI: `10.1080/08957959.2020.1791107`.

Shinmei, Toru, Tetsuo Irifune, Jun Tsuchiya, and Ken-Ichi Funakoshi (2008). "Phase transition and compression behavior of phase D up to 46 GPa using multi-anvil apparatus with sintered diamond anvils". In: *High Pressure Research* 28, pp. 363–373.

Simons, Kyla, Jacqueline Dixon, Jean-Guy Schilling, Richard Kingsley, and Robert Poreda (2002). "Volatiles in basaltic glasses from the Easter-Salas y Gomez Seamount Chain and Easter Microplate: Implications for geochemical cycling of volatile elements". In: *Geochemistry, Geophysics, Geosystems* 3.7, pp. 1–29. DOI: `10.1029/2001gc000173`.

Smyth, Joseph R., Christopher M. Holl, Daniel J. Frost, Steven D. Jacobsen, Falko Langenhorst, and Catherine A. Mccammon (2003). “Structural systematics of hydrous ringwoodite and water in Earth’s interior”. In: *American Mineralogist* 88.10, pp. 1402–1407. DOI: `10.2138/am-2003-1001`.

Solomatova, Natalia V., Jennifer M. Jackson, Wolfgang Sturhahn, George R. Rossman, and Mathieu Roskosz (2017). “Electronic environments of ferrous iron in rhyolitic and basaltic glasses at high pressure”. In: *Journal of Geophysical Research: Solid Earth* 122, pp. 6306–6322. DOI: `10.1002/2017JB014363`.

Solomatova, Natalia V., Jennifer M. Jackson, Wolfgang Sturhahn, June K. Wicks, Jiyong Zhao, Thomas S. Toellner, Bora Kalkan, and William M. Steinhardt (2016). “Equation of state and spin crossover of (Mg,Fe)O at high pressure, with implications for explaining topographic relief at the core-mantle boundary”. In: *American Mineralogist* 101, pp. 1084–1093. DOI: `10.2138/am-2016-5510`.

Spasojevic, Sonja, Michael Gurnis, and Rupert Sutherland (2010). “Mantle upwellings above slab graveyards linked to the global geoid lows”. In: *Nature Geoscience* 3.6, pp. 435–438. DOI: `10.1038/ngeo855`.

Stevenson, DJ (1981). “Models of the Earth’s core”. In: *Science* 214.4521, pp. 611–619. DOI: `https://doi.org/10.1126/science.214.4521.611`.

Stixrude, Lars and Carolina Lithgow-Bertelloni (2005). “Thermodynamics of mantle minerals - I. Physical properties”. In: *Geophysical Journal International* 162, pp. 610–632. DOI: `10.1111/j.1365-246X.2005.02642.x`.

Strozewski, Benjamin, Johannes Buchen, Wolfgang Sturhahn, Takayuki Ishii, Itaru Ohira, Stella Chariton, Barbara Lavina, Jiyong Zhao, Thomas S Toellner, and Jennifer M Jackson (2023). “Equation of State and Spin Crossover of (Al,Fe)-Phase H”. In: *Journal of Geophysical Research : Solid Earth*, pp. 1–20. DOI: `10.1029/2022JB026291`.

Strozewski, Benjamin, Ojashvi Rautela, Johannes Buchen, Wolfgang Sturhahn, Takayuki Ishii, Itaru Ohira, Olivia Pardo, Barbara Lavina, Jiyong Zhao, Thomas S. Toellner, and Jennifer Jackson (2024). *Data supporting "Sound velocities of (Al,Fe)-phase H and the seismic visibility of dense oxyhydroxides in Earth’s lower mantle"*. Dataset. DOI: `10.22002/8v9yv-9mm73`.

Sturhahn, W. (2000). “CONUSS and PHOENIX: Evaluation of nuclear resonant scattering data”. In: *Hyperfine Interactions* 125.1-4, pp. 149–172. DOI: `10.1023/A:1012681503686`.

– (2022). *MINUTI (MINeral physics UTIlities)*. `http://www.nrixs.com`.

Sturhahn, Wolfgang (2021). “PHOENIX, version 3.0.4”. In: URL: `www.nrixs.com`.

Su, Xiaowan, Chaoshuai Zhao, Chaojia Lv, Yukai Zhuang, Nilesh Salke, Liangxu Xu, Hu Tang, Huiyang Gou, Xiaohui Yu, Qiang Sun, and Jin Liu (2021a). “The effect of iron on the sound velocities of δ-AlOOH up to 135 GPa”. In: *Geoscience Frontiers* 12.2, pp. 937–946. DOI: `10.1016/j.gsf.2020.08.012`.

Su, Xiaowan, Chaoshuai Zhao, Liangxu Xu, Chaojia Lv, Xitong Song, Takayuki Ishii, Yuming Xiao, Paul Chow, Qiang Sun, and Jin Liu (2021b). "Spectroscopic evidence for the Fe^{3+} spin transition in iron-bearing δ-AlOOH at high pressure". In: *American Mineralogist* 106.11, pp. 1709–1716. DOI: `10.2138/am-2021-7541`.

Sun, D., D. Helmberger, V. H. Lai, M. Gurnis, J. M. Jackson, and H. Y. Yang (2019). "Slab Control on the Northeastern Edge of the Mid-Pacific LLSVP Near Hawaii". In: *Geophysical Research Letters* 46, pp. 3142–3152. DOI: `10.1029/2018GL081130`.

Sun, Daoyuan, Don Helmberger, Meghan S. Miller, and Jennifer M. Jackson (2016). "Major disruption of D" beneath Alaska". In: *Journal of Geophysical Research: Solid Earth* 121.5, pp. 3534–3556. DOI: `10.1002/2015JB012534`.

Suzuki, A., E. Ohtani, and T. Kamada (2000). "A new hydrous phase δ-AlOOH synthesized at 21 GPa and 1000°C". In: *Physics and Chemistry of Minerals* 27.10, pp. 689–693. DOI: `10.1007/s002690000120`.

Suzuki, Akio (2010). "High-pressure X-ray diffraction study of ϵ-FeOOH". In: *Physics and Chemistry of Minerals* 37.3, pp. 153–157. DOI: `10.1007/s00269-009-0319-x`.

Takaichi, Goru, Yu Nishihara, Kyoko N. Matsukage, Masayuki Nishi, Yuji Higo, Yoshinori Tange, Noriyoshi Tsujino, and Sho Kakizawa (2024). "Limited stability of hydrous SiO_2 stishovite in the deep mantle". In: *Earth and Planetary Science Letters* 640. DOI: `10.1016/j.epsl.2024.118790`.

Tan, Eh, Michael Gurnis, and Lijie Han (2002). "Slabs in the lower mantle and their modulation of plume formation". In: *Geochemistry, Geophysics, Geosystems* 3, pp. 1–24. DOI: `10.1029/2001GC000238`.

Tan, Eh, Wei Leng, Shijie Zhong, and Michael Gurnis (2011). "On the location of plumes and lateral movement of thermochemical structures with high bulk modulus in the 3-D compressible mantle". In: *Geochemistry, Geophysics, Geosystems* 12, pp. 1–13. DOI: `10.1029/2011GC003665`.

Terasaki, H., E. Ohtani, T. Sakai, S. Kamada, H. Asanuma, Y. Shibazaki, N. Hirao, N. Sata, Y. Ohishi, T. Sakamaki, A. Suzuki, and K. Funakoshi (2012). "Stability of Fe-Ni hydride after the reaction between Fe-Ni alloy and hydrous phase (δ-AlOOH) up to 1.2Mbar: Possibility of H contribution to the core density deficit". In: *Physics of the Earth and Planetary Interiors* 194-195, pp. 18–24. DOI: `10.1016/j.pepi.2012.01.002`.

Thompson, E. C., A. J. Campbell, and J. Tsuchiya (2017). "Elasticity of ϵ-FeOOH: Seismic implications for Earth's lower mantle". In: *Journal of Geophysical Research: Solid Earth* 122, pp. 5038–5047. DOI: `10.1002/2017JB014168`.

Thompson, Elizabeth C., Anne H. Davis, Nigel M. Brauser, Zhenxian Liu, Vitali B. Prakapenka, and Andrew J. Campbell (2020). "Phase transitions in ϵ-FeOOH at high pressure and ambient temperature". In: *American Mineralogist* 105, pp. 1769–1777. DOI: `10.2138/am-2020-7468`.

Toby, Brian H. and Robert B. Von Dreele (2013). "GSAS-II: The genesis of a modern open-source all purpose crystallography software package". In: *Journal of Applied Crystallography* 46, pp. 544–549. DOI: `10.1107/S0021889813003531`.

Toellner, T. S. (2000). "Monochromatization of synchrotron radiation for nuclear resonant scattering experiments". In: *Hyperfine Interactions* 125, pp. 3–28. DOI: `10.1023/A:1012621317798`.

Trinquier, A., J. L. Birck, C. J. Allègre, C. Göpel, and D. Ulfbeck (2008). "53Mn-53Cr systematics of the early Solar System revisited". In: *Geochimica et Cosmochimica Acta* 72.20, pp. 5146–5163. DOI: `10.1016/j.gca.2008.03.023`.

Trybel, Florian, Thomas Meier, Biao Wang, and Gerd Steinle-Neumann (2021). "Absence of proton tunneling during the hydrogen-bond symmetrization in". In: *Physical Review B* 104.10, pp. 1–6. DOI: `10.1103/PhysRevB.104.104311`.

Tschauner, O., S. Huang, E. Greenberg, V. B. Prakapenka, C. Ma, G. R. Rossman, A. H. Shen, D. Zhang, M. Newville, A. Lanzirotti, and K. Tait (2018). "Ice-VII inclusions in diamonds: Evidence for aqueous fluid in Earth's deep mantle". In: *Science* 359, pp. 1136–1139. DOI: `10.1126/science.aao3030`.

Tschauner, Oliver, Shichun Huang, Shuying Yang, Munir Humayun, Wenjun Liu, Stephanie N. Gilbert Corder, Hans A. Bechtel, Jon Tischler, and George R. Rossman (2021). "Discovery of davemaoite, $CaSiO_3$-perovskite, as a mineral from the lower mantle". In: *Science* 374.6569, pp. 891–894. DOI: `10.1126/science.abl8568`.

Tsuchiya, Jun and Elizabeth C. Thompson (2022). "The role of hydrogen bonds in hydrous minerals stable at lower mantle pressure conditions". In: *Progress in Earth and Planetary Science* 9. DOI: `10.1186/s40645-022-00521-3`.

Tsuchiya, Jun, Taku Tsuchiya, and Renata M. Wentzcovitch (2008). "Vibrational properties of δ-AlOOH under pressure". In: *American Mineralogist* 93.2-3, pp. 477–482. DOI: `10.2138/am.2008.2627`.

Tsuchiya, T. (2011). "Elasticity of subducted basaltic crust at the lower mantle pressures: Insights on the nature of deep mantle heterogeneity". In: *Physics of the Earth and Planetary Interiors* 188.3-4, pp. 142–149. DOI: `10.1016/j.pepi.2011.06.018`.

Tsuchiya, Taku (2003). " First-principles prediction of the P-V-T equation of state of gold and the 660-km discontinuity in Earth's mantle ". In: *Journal of Geophysical Research: Solid Earth* 108, pp. 1–9. DOI: `10.1029/2003jb002446`.

Tsuchiya, Taku, Jun Tsuchiya, Koichiro Umemoto, and Renata M. Wentzcovitch (2004). “Phase transition in $MgSiO_3$ perovskite in the earth’s lower mantle”. In: *Earth and Planetary Science Letters* 224.3-4, pp. 241–248. DOI: `10.1016/j.epsl.2004.05.017`.

Tsutsumi, Yutaro, Naoya Sakamoto, Kei Hirose, Shoh Tagawa, Koichiro Umemoto, Yasuo Ohishi, and Hisayoshi Yurimoto (2024). “Retention of water in subducted slabs under core–mantle boundary conditions”. In: *Nature Geoscience* 17. DOI: `10.1038/s41561-024-01464-8`.

Turner, Stephen J. and Charles H. Langmuir (2022). “An Evaluation of Five Models of Arc Volcanism”. In: *Journal of Petrology* 63.3, pp. 1–25. DOI: `10.1093/petrology/egac010`.

Ulmer, Peter and Volkmar Trommsdorff (1995). “Serpentine stability to mantle depths and subduction-related magmatism”. In: *Science* 268.5212, pp. 858–861. DOI: `10.1126/science.268.5212.858`.

Umemoto, Koichiro, Katsuyuki Kawamura, Kei Hirose, and Renata M. Wentzcovitch (2016). “Post-stishovite transition in hydrous aluminous SiO_2”. In: *Physics of the Earth and Planetary Interiors* 255, pp. 18–26. DOI: `10.1016/j.pepi.2016.03.008`.

Van Der Hilst, R.D., S Widiyantorot, and E.R. Engdahl (1997). “Evidence for deep mantle circulation from global tomography”. In: *Nature* 386. DOI: `10.1038/386578a0`.

Walker, Richard J. (2009). “Highly siderophile elements in the Earth, Moon and Mars: Update and implications for planetary accretion and differentiation”. In: *Chemie der Erde* 69.2, pp. 101–125. DOI: `10.1016/j.chemer.2008.10.001`.

Wang, Biao, Johannes Buchen, Alba San José Méndez, Alexander Kurnosov, Giacomo Criniti, Hanns Peter Liermann, and Hauke Marquardt (2023). “Strong Effect of Stress on the Seismic Signature of the Post-Stishovite Phase Transition in the Earth’s Lower Mantle”. In: *Geophysical Research Letters* 50.10, pp. 1–9. DOI: `10.1029/2023GL102740`.

Wang, W. and Z. Wu (2022). “A first-principles study of water in wadsleyite and ringwoodite: Implication for the 520 km discontinuity”. In: *American Mineralogist* 107, pp. 1361–1368. DOI: `10.2138/am-2021-7929`.

Waszek, Lauren, Nicholas C. Schmerr, and Maxim D. Ballmer (2018). “Global observations of reflectors in the mid-mantle with implications for mantle structure and dynamics”. In: *Nature Communications* 9.1, pp. 1–13. DOI: `10.1038/s41467-017-02709-4`.

Wicks, J. K., J. M. Jackson, and W. Sturhahn (2010). “Very low sound velocities in iron-rich (Mg,Fe)O: Implications for the core-mantle boundary region”. In: *Geophysical Research Letters* 37.15, pp. 1–5. DOI: `10.1029/2010GL043689`.

Wicks, June K., Jennifer M. Jackson, Wolfgang Sturhahn, and Dongzhou Zhang (2017). “Sound velocity and density of magnesiowüstites: Implications for ultralow-velocity zone topography”. In: *Geophysical Research Letters* 44.5, pp. 2148–2158. DOI: `10.1002/2016GL071225`.

Wirth, R., C. Vollmer, F. Brenker, S. Matsyuk, and F. Kaminsky (2007). “Inclusions of nanocrystalline hydrous aluminium silicate "Phase Egg" in superdeep diamonds from Juina (Mato Grosso State, Brazil)”. In: *Earth and Planetary Science Letters* 259, pp. 384–399. DOI: `10.1016/j.epsl.2007.04.041`.

Wojdyr, Marcin (2010). “*Fityk*: a general-purpose peak fitting program”. In: *Journal of Applied Crystallography* 43.5, pp. 1126–1128. DOI: `10.1107/S0021889810030499`.

Wolf, J., M.D. Long, and D.A. Frost (2024). “Ultralow velocity zone and deep mantle flow beneath the Himalayas linked to subducted slab”. In: *Nature Geoscience* 17, pp. 302–308. DOI: `10.1038/s41561-024-01386-5`.

Workman, Rhea K. and Stanley R. Hart (2005). “Major and trace element composition of the depleted MORB mantle (DMM)”. In: *Earth and Planetary Science Letters* 231, pp. 53–72. DOI: `10.1016/j.epsl.2004.12.005`.

Wu, Ye, Xiang Wu, Jung Fu Lin, Catherine A. McCammon, Yuming Xiao, Paul Chow, Vitali B. Prakapenka, Takashi Yoshino, Shuangmeng Zhai, and Shan Qin (2016). “Spin transition of ferric iron in the NAL phase: Implications for the seismic heterogeneities of subducted slabs in the lower mantle”. In: *Earth and Planetary Science Letters* 434, pp. 91–100. DOI: `10.1016/j.epsl.2015.11.011`.

Xu, Weiming, Eran Greenberg, Gregory Kh Rozenberg, Moshe P. Pasternak, Elena Bykova, Tiziana Boffa-Ballaran, Leonid Dubrovinsky, Vitali Prakapenka, Michael Hanfland, Olga Yu Vekilova, Sergei I. Simak, and Igor A. Abrikosov (2013). “Pressure-induced hydrogen bond symmetrization in iron oxyhydroxide”. In: *Physical Review Letters* 111, pp. 1–5. DOI: `10.1103/PhysRevLett.111.175501`.

Xue, Xianyu, Masami Kanzaki, Hiroshi Fukui, Eiji Ito, and Takafumi Hashimoto (2006). “Cation order and hydrogen bonding of high-pressure phases in the Al_2O_3-SiO_2-H_2O system: An NMR and Raman study”. In: *American Mineralogist* 91.5-6, pp. 850–861. DOI: `10.2138/am.2006.2064`.

Yuan, Hongsheng, Li Zhang, Eiji Ohtani, Yue Meng, Eran Greenberg, and Vitali B. Prakapenka (2019). “Stability of Fe-bearing hydrous phases and element partitioning in the system $MgO–Al_2O_3–Fe_2O_3–SiO_2–H_2O$ in Earth’s lowermost mantle”. In: *Earth and Planetary Science Letters* 524, p. 115714. DOI: `10.1016/j.epsl.2019.115714`.

Yuan, Y., D. Sun, W. Leng, and Z. Wu (2021). “Southeastward dipping mid-mantle heterogeneities beneath the sea of Okhotsk”. In: *Earth and Planetary Science Letters* 573. DOI: `10.1016/j.epsl.2021.117151`.

Zhang, Y., S. Fu, S.I. Karato, T. Okuchi, S. Chariton, V.B. Prakapenka, and J.F. Lin (2022). “Elasticity of Hydrated Al-Bearing Stishovite and Post-Stishovite: Implications for Understanding Regional Seismic V_S Anomalies Along Subducting Slabs in the Lower Mantle”. In: *Journal of Geophysical Research: Solid Earth* 127, pp. 1–16. DOI: `10.1029/2021JB023170`.

Zhou, Wen Yi, Jin S. Zhang, Quancheng Huang, Xiaojing Lai, Bin Chen, Przemyslaw Dera, and Brandon Schmandt (2022). “High pressure-temperature single-crystal elasticity of ringwoodite: Implications for detecting the 520 discontinuity and metastable ringwoodite at depths greater than 660 km”. In: *Earth and Planetary Science Letters* 579. DOI: `10.1016/j.epsl.2021.117359`.

SUPPLEMENTARY MATERIAL TO CHAPTER 2

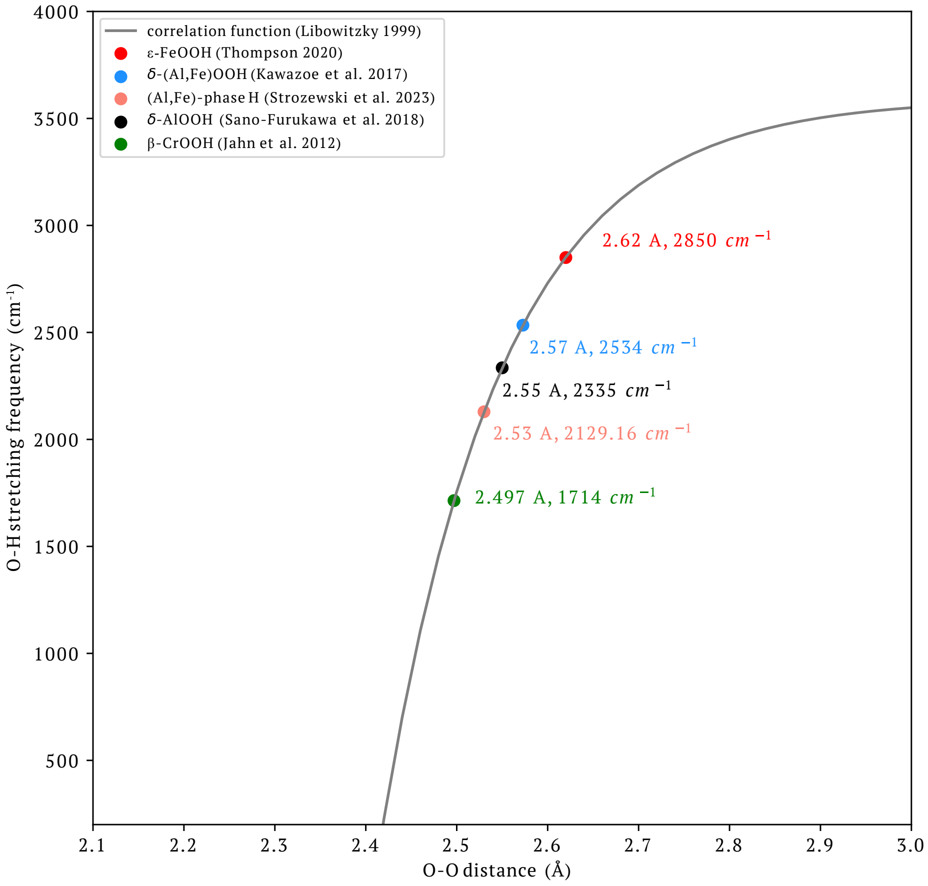

Supplementary Figure S1: Correlation function (Libowitzky 1999) of infrared-active O-H stretching modes of various oxyhydroxides. In each case, the predicted O-H stretching frequency at ambient pressure is determined from the O–O distance measured by single-crystal X-ray diffraction.

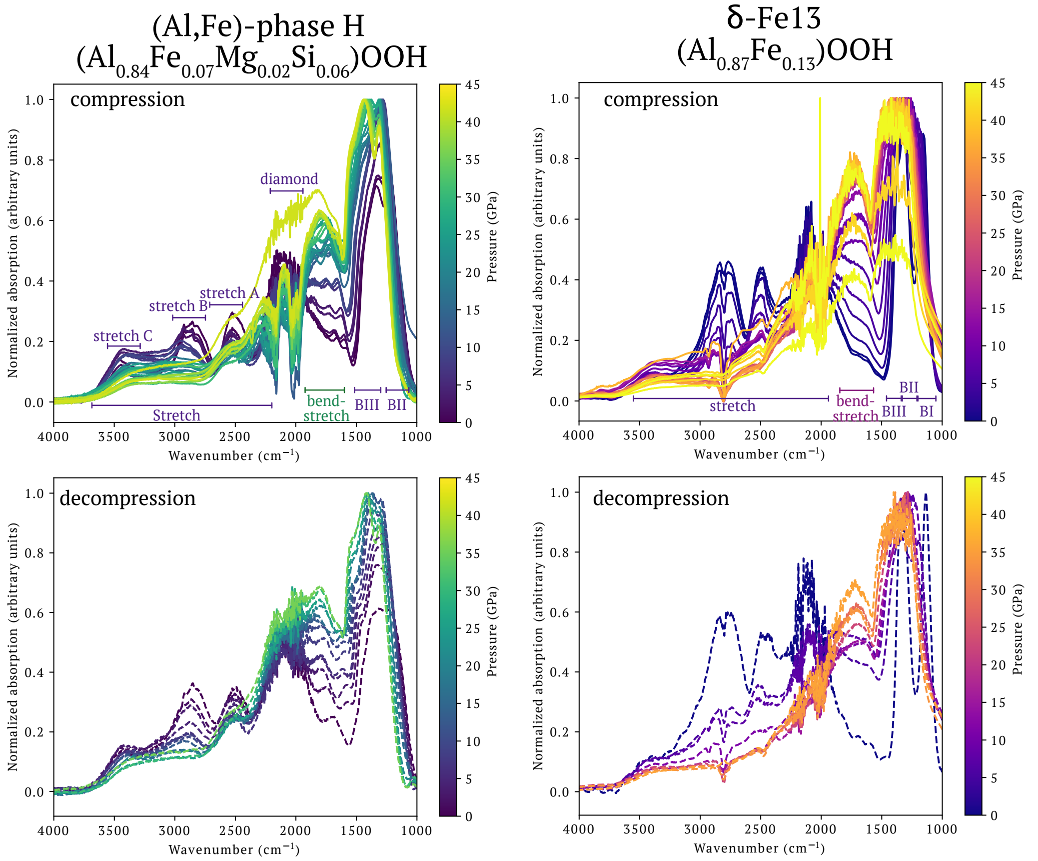
(Al,Fe)-phase H $(Al_{0.84}Fe_{0.07}Mg_{0.02}Si_{0.06})OOH$

δ-Fe13 $(Al_{0.87}Fe_{0.13})OOH$

Supplementary Figure S2: High-pressure infrared absorption spectra above 1000 cm^{-1} collected on (Al,Fe)-phase H ($(Al_{0.84}Fe_{0.07}Mg_{0.02}Si_{0.06})OOH$) and δ-$(Al_{0.87},Fe_{0.13})OOH$ (δ-Fe13) at the National Synchrotron Light Source-II, Brookhaven National Laboratory. Spectra were collected on compression of (Al,Fe)-phase H and δ-Fe13 to a maximum pressure of 42 GPa and upon decompression.

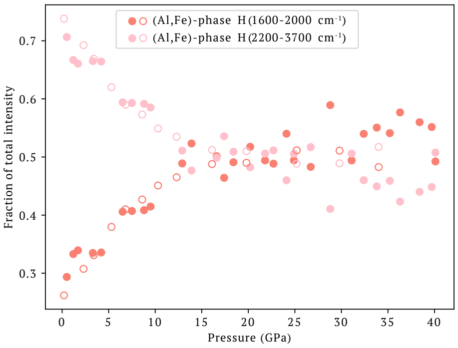

Supplementary Figure S3: Relative intensities of the low wavenumber (1600 to 2000 cm^{-1}) stretching region and the high (2200 to 3700 cm^{-1}) wavenumber region in (Al,Fe)-phase H. Fractions were calculated by integrating the two regions (deliberately avoiding the diamond absorption region) and taking the ratio of each integrated intensity to the summed total.

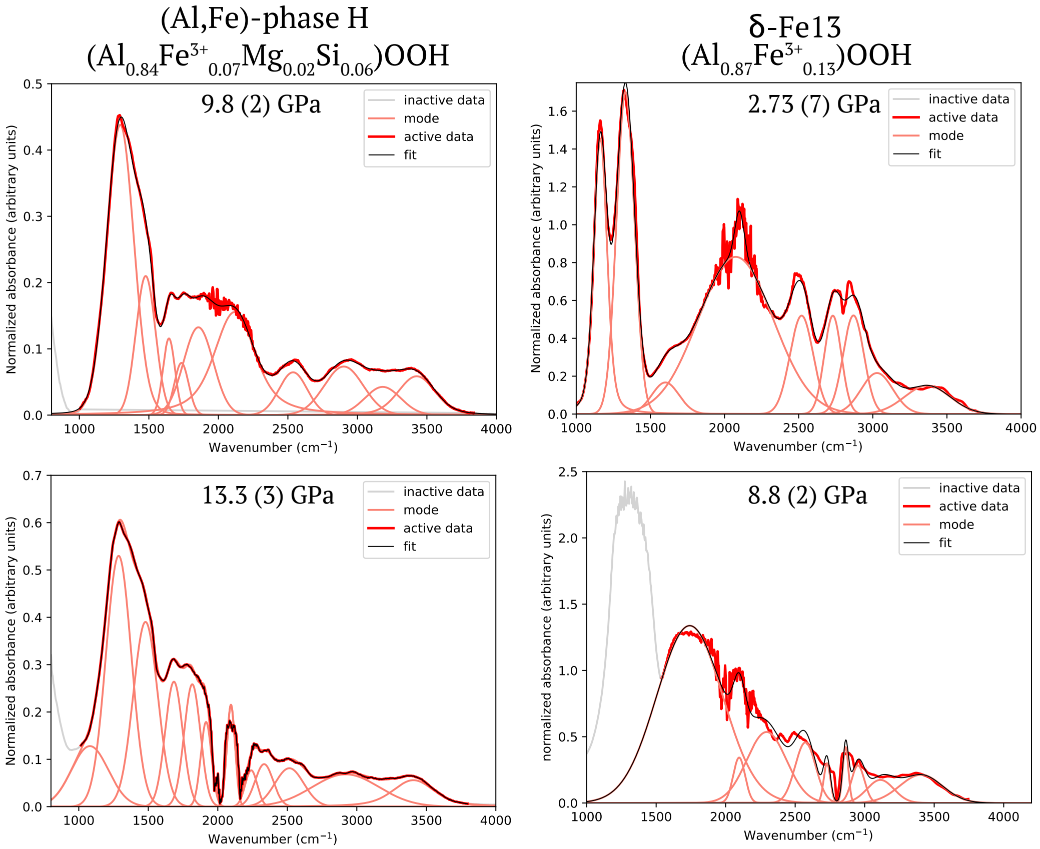

Supplementary Figure S4: Data and fit examples demonstrating the softening of O-H stretching modes above 10 GPa in (Al,Fe)-phase H and below 10 GPa in δ-Fe13. Individual functions used for fitting are plotted in pink while the summed fit model is plotted in black. "Active data" refers to the data used for fitting while "inactive data" is not used.

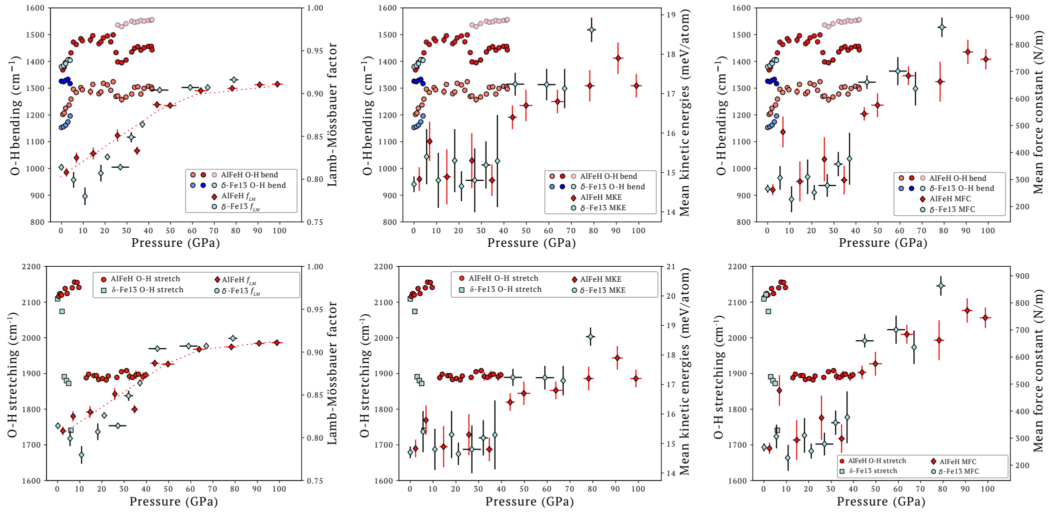

Supplementary Figure S5: Vibrational frequencies of O-H modes in (Al,Fe)-phase H and δ-$Al_{0.87}Fe_{0.13}OOH$ compared with trends in Lamb-Mössbauer factor, mean force constant, and mean kinetic energy determined by nuclear resonant inelastic X-ray scattering (NRIXS) after refinement of the spectra (see Chapter 4). For clarity, only the compression run and primary O-H stretching mode for each phase are plotted.

Pressure (GPa)	**bend A** (cm^{-1})	**bend B1** (cm^{-1})	**bend B2** (cm^{-1})	bend C (cm^{-1})	χ^2
0.64 (2)	1202 (3)	1368 (3)	-	1056 (2)	1.7
1.3 (3)	1207 (4)	1378 (4)	-	-	2.1
1.92 (5)	1225 (3)	1396 (3)	-	-	0.82
3.54 (9)	1237 (3)	1407 (4)	-	-	1.54
4.4 (1)	1259 (3)	1432 (3)	-	-	0.92
5.5 (1)	1296 (5)	1472 (3)	-	-	0.97
6.8 (2)	1284 (2)	1463 (3)	-	-	0.42
8.9 (2)	1302 (3)	1485 (3)	-	-	0.96
9.6 (2)	1294 (2)	1477 (2)	-	-	0.43
13.3 (3)	1287 (14)	1480 (13)	-	1080 (0)	4.4
14.4 (4)	1314 (2)	1496 (2)	-	-	1.15
17.2 (4)	1279 (4)	1466 (5)	-	1062 (3)	0.66
18.1 (5)	1286 (4)	1473 (4)	-	1061 (1)	0.91
19.2 (5)	1318 (2)	1488 (2)	-	-	2.29
21.1 (5)	1312 (4)	1495 (4)	-	-	1.02
22.6 (6)	1292 (7)	1473 (7)	-	-	2.34
23.7 (6)	1324 (3)	1499 (4)	-	-	1.57
25.0 (6)	1269 (3)	1433 (4)	-	-	1.19
25.8 (6)	1271 (3)	1398 (5)	1536 (2)	-	2.77
27.6 (7)	1257 (12)	1395 (11)	1530 (2)	-	0.7
29.6 (7)	1267 (2)	1405 (3)	1541 (2)	-	2.14
32.2 (8)	1278 (1)	1435 (3)	1550 (1)	-	1.09
33.5 (8)	1303 (7)	1449 (4)	1546 (2)	1108 (2)	1.45
35.0 (9)	1305 (4)	1455 (3)	1548 (2)	1117 (2)	0.73
36.4 (9)	1278 (2)	1442 (2)	1553 (1)	1134 (2)	0.7
37.8 (9)	1299 (7)	1451 (5)	1550 (2)	1126 (8)	1.7
39 (1)	1307 (3)	1456 (2)	1553 (1)	1112 (1)	0.92
41.2 (1.0)	1304 (4)	1456 (2)	1554 (1)	1127 (2)	0.88
41.5 (1.0)	1297 (4)	1443 (3)	1556 (3)	1246 (21)	1.66
*0.44 (1)	1181 (4)	-	1366 (4)	-	0.5
*2.6 (1)	1164 (3)	-	1340 (3)	-	0.74
*3.7 (1)	1205 (9)	-	1373 (13)	-	0.6
*5.7 (1)	1142 (14)	1264 (14)	1424 (42)	-	1.7
*7.2 (2)	1137 (3)	1258 (4)	1414 (9)	-	1.1
*8.9 (2)	1239 (14)	1399 (13)	1511 (2)	-	0.6
*10.8 (3)	1249 (8)	1400 (7)	1516 (2)	-	1.48
*12.8 (3)	1250 (12)	1398 (11)	1525 (2)	-	0.6
*16.7 (4)	1324 (4)	1440 (5)	1532 (2)	-	0.8
*20.6 (5)	1289 (4)	1428 (3)	1534 (2)	-	0.61
*26.1 (7)	1238 (30)	1368 (14)	1515 (41)	-	3.7
*30.7 (8)	1269 (3)	1430 (5)	1550 (2)	-	0.61
*35.2 (9)	1301 (3)	1451 (2)	1554 (1)	-	0.38

Supplementary Table S1: Frequencies of O-H vibrational modes in (Al,Fe)-phase H ($Al_{0.84}Fe_{0.07}Mg_{0.02}Si_{0.06}OOH$) nominally in the O-H bending wavenumber region for this phase. 1σ uncertainty is given in parentheses for each vibrational mode. * indicates a measurement on decompression while a dash indicates that this mode was not fit at this pressure. Modes in bold are plotted in Figure 4 of the main text. In this table, they are ordered from left to right with increasing wavenumber.

Pressure (GPa)	bend-stretch A1 (cm^{-1})	bend-stretch A2 (cm^{-1})	**bend-stretch A** (cm^{-1})	**bend-stretch B** (cm^{-1})	diamond (cm^{-1})	**stretch A** (cm^{-1})	**stretch A2** (cm^{-1})	stretch A3 (cm^{-1})	**stretch B** (cm^{-1})	**stretch C** (cm^{-1})	**stretch D** (cm^{-1})
0.64 (2)	1664 (3)	-	1781 (30)	2110 (15)	-	2508 (5)	-	-	2839 (7)	3125 (39)	3454 (19)
1.3 (3)	1592 (0)	1667 (4)	1822 (16)	2112 (13)	-	2507 (2)	-	-	2857 (4)	3173 (25)	3448 (4)
1.92 (5)	1592 (3)	1667 (6)	1802 (35)	2102 (10)	-	2513 (1)	-	-	2856 (3)	3153 (6)	3445 (6)
3.54 (9)	-	1628 (2)	1779 (8)	2109 (11)	-	2524 (2)	-	-	2862 (9)	3192 (16)	3464 (11)
4.4 (1)	1617 (4)	1696 (10)	1821 (17)	2102 (12)	-	2525 (2)	-	-	2884 (4)	3167 (6)	3422 (7)
5.5 (1)	1629 (17)	1734 (16)	1852 (32)	2085 (8)	-	2528 (2)	-	-	2901 (18)	3233 (15)	3458 (14)
6.8 (2)	1631 (4)	1713 (12)	1857 (10)	2128 (8)	-	2522 (2)	-	-	2890 (10)	3189 (14)	3446 (8)
8.9 (2)	1641 (11)	1742 (14)	1869 (20)	2111 (11)	-	2532 (3)	-	-	2893 (29)	3194 (32)	3451 (19)
9.6 (2)	1645 (6)	1734 (12)	1856 (12)	2118 (17)	-	2537 (4)	-	-	2902 (16)	3182 (15)	3426 (16)
13.3 (3)	-	1684 (18)	1816 (13)	1916 (6)	2095 (1)	2240 (6)	2333 (11)	2515 (11)	2920 (9)	-	3407 (7)
14.4 (4)	-	1669 (3)	1840 (7)	1931 (1)	2097 (1)	2246 (5)	2382 (10)	2546 (10)	2918 (6)	-	3401 (2)
17.2 (4)	-	-	1720 (2)	1883 (3)	2096 (1)	2289 (2)	2478 (2)	2626 (2)	2953 (3)	-	3408 (2)
18.1 (5)	-	-	1708 (3)	1872 (4)	2097 (1)	2284 (3)	2508 (3)	-	2937 (3)	-	3393 (5)
19.2 (5)	-	-	1730 (3)	1887 (1)	2099 (1)	2302 (2)	2516 (3)	-	2916 (5)	-	3370 (9)
21.1 (5)	-	1644 (48)	1727 (37)	1866 (19)	2103 (3)	2295 (3)	2505 (27)	-	2948 (58)	-	3386 (11)
22.6 (6)	-	1639 (5)	1718 (6)	1857 (14)	2107 (4)	2302 (2)	2512 (4)	-	2942 (7)	-	3406 (8)
23.7 (6)	-	1619 (4)	1717 (10)	1886 (8)	2105 (9)	2302 (2)	2504 (4)	-	2957 (10)	-	3398 (8)
25.0 (6)	-	-	1792 (7)	-	2117 (3)	2314 (4)	2553 (3)	-	2951 (8)	-	3406 (2)
25.8 (6)	-	-	1721 (8)	1883 (7)	2094 (1)	2271 (2)	2471 (8)	-	2994 (22)	-	3413 (4)
27.6 (7)	-	-	1670 (4)	1841 (4)	2092 (1)	2257 (4)	2538 (6)	-	2962 (19)	-	3383 (9)
29.6 (7)	-	-	1731 (5)	1889 (4)	2094 (1)	2264 (2)	2475 (5)	-	3012 (8)	-	3397 (6)
32.2 (8)	-	-	1716 (5)	1876 (6)	2095 (1)	2252 (3)	2460 (6)	-	2988 (15)	-	3406 (4)
33.5 (8)	-	-	1662 (63)	1878 (63)	2096 (1)	2250 (4)	2502 (9)	-	2940 (13)	-	3389 (15)
35.0 (9)	-	-	1678 (15)	1872 (17)	2093 (1)	2262 (3)	2548 (6)	-	2910 (10)	-	3371 (5)
36.4 (9)	-	-	1696 (9)	1867 (19)	2096 (1)	2245 (5)	2482 (7)	-	2995 (7)	-	3388 (8)
37.8 (9)	-	-	1696 (32)	1892 (36)	2094 (1)	2261 (2)	2550 (6)	-	3024 (13)	-	3377 (13)
39 (1)	-	-	1653 (19)	1857 (24)	2097 (1)	2242 (4)	2487 (5)	-	2972 (11)	-	3377 (13)
41.2 (1.0)	-	-	1667 (16)	1867 (20)	2095 (1)	2245 (4)	2504 (6)	-	2924 (8)	-	3309 (8)
41.5 (1.0)	-	-	1667 (6)	1800 (9)	2144 (16)	2370 (60)	-	-	3120 (10)	-	3450 (12)
* 0.44 (1)	-	-	1674 (3)	-	2085 (2)	-	2507 (1)	-	2847 (2)	3194 (5)	3455 (3)
*2.6 (1)	-	1585 (3)	1719 (16)	-	2110 (17)	-	2522 (2)	-	2859 (9)	3184 (13)	3461 (11)
*3.7 (1)	-	1598 (2)	1747 (17)	-	2106 (33)	-	2539 (2)	-	2871 (3)	-	3403 (4)
*5.7 (1)	-	1618 (4)	1747 (8)	-	2106 (12)	-	2522 (2)	-	2896 (16)	3240 (7)	3431 (3)
*7.2 (2)	-	1621 (2)	1733 (5)	-	2087 (9)	-	2527 (1)	-	2918 (8)	-	3425 (2)
*8.9 (2)	-	1595 (4)	1719 (5)	-	2077 (7)	-	2533 (1)	-	2913 (8)	-	3415 (2)
*10.8 (3)	-	1599 (6)	1736 (26)	-	2125 (34)	-	2532 (3)	-	2932 (14)	-	3417 (2)
*12.8 (3)	-	1608 (4)	1751 (18)	-	2129 (25)	-	2532 (3)	-	2943 (16)	-	3415 (2)
*16.7 (4)	-	1621 (6)	1840 (5)	-	2183 (5)	-	2497 (9)	-	2971 (41)	-	3407 (4)
*20.6 (5)	-	-	1728 (33)	-	2049 (40)	2222 (6)	2494 (26)	-	2979 (7)	-	3405 (6)
*26.1 (7)	-	-	1796 (22)	-	2123 (26)	-	2431 (111)	-	3052 (14)	-	3372 (7)
*30.7 (8)	-	-	1772 (14)	1974 (10)	2164 (15)	-	2471 (10)	-	3004 (7)	-	3395 (8)
*35.2 (9)	-	-	1775 (12)	-	2171 (15)	-	2540 (5)	-	2897 (13)	-	3373 (4)

Supplementary Table S2: Frequencies of O-H vibrational modes in (Al,Fe)-phase H ($Al_{0.84}Fe_{0.07}Mg_{0.02}Si_{0.06}OOH$) nominally in the O-H stretching wavenumber region for this phase. 1σ uncertainty is given in parentheses for each vibrational mode. * indicates a measurement on decompression while a dash indicates that this mode was not fit at this pressure. Modes in bold are plotted in Figure 5 of the main text. In this table, they are ordered from left to right with increasing wavenumber.

Pressure (GPa)	bend A (cm^{-1})	bend B (cm^{-1})	bend C (cm^{-1})	χ^2
0.61 (0.02)	1153 (1)	1326 (1)	1380 (2)	1.75
1.64 (0.04)	1156 (1)	1324 (2)	1384 (2)	1.25
2.73 (0.07)	1162 (1)	1329 (1)	1392 (3)	2.4
4.2 (0.1)	1174 (1)	1333 (5)	1406 (3)	1.53
5.7 (0.1)	1196 (5)	1317 (9)	1404 (12)	1.91
*0.5 (0.02)	1133 (1)	1311 (6)	1364 (2)	0.4
*5.6 (0.1)	1142 (2)	1264 (14)	1424 (42)	1.7

Supplementary Table S3: Frequencies of O-H vibrational modes in δ-Fe13 ($Al_{0.87}Fe_{0.13}OOH$) nominally in the O-H bending wavenumber region for this phase. 1σ uncertainty is given in parentheses for each vibrational mode. * indicates a measurement on decompression while a dash indicates that this mode was not fit at this pressure. Vibrational modes are ordered from left to right with increasing wavenumber.

Pressure (GPa)	**bend-stretch A** (cm^{-1})	**bend-stretch B** (cm^{-1})	diamond (cm^{-1})	**stretch A** (cm^{-1})	**stretch B** (cm^{-1})	**stretch B2** (cm^{-1})	**stretch C** (cm^{-1})	**stretch D** (cm^{-1})
0.61 (0.02)	1595 (14)	2109 (7)	2101 (0)	2502 (3)	2714 (3)	2849 (16)	3109 (14)	3370 (2)
1.64 (0.04)	1668 (5)	2121 (2)	2097 (0)	2504 (1)	2714 (3)	2842 (6)	3067 (23)	3416 (5)
2.73 (0.07)	1602 (7)	2074 (3)	2101 (0)	2515 (2)	2716 (4)	2863 (6)	3073 (19)	3368 (2)
4.2 (0.1)	1636 (20)	1891 (21)	2192 (4)	2521 (10)	2725 (2)	2869 (8)	3054 (79)	3399 (2)
5.7 (0.1)	1616 (21)	1880 (13)	2100 (3)	2511 (2)	2738 (1)	2880 (2)	2980 (21)	3402 (3)
7.1 (0.2)	1689 (7)	1872 (3)	2116 (5)	2522 (4)	2744 (3)	2860 (2)	2941 (12)	3307 (9)
8.8 (0.2)	-	1741 (6)	2097 (5)	2574 (6)	2729 (1)	2862 (1)	2952 (3)	3406 (3)
*0.5 (0.02)	1645 (5)	2115 (2)	-	2462 (2)	-	2783 (6)	3088 (17)	3417 (11)
*5.6 (0.1)	1671 (11)	2113 (6)	-	2499 (7)	-	2802 (7)	3071 (23)	3338 (8)

Supplementary Table S4: Frequencies of O-H vibrational modes in δ-Fe13 ($Al_{0.87}Fe_{0.13}OOH$) nominally in the O-H stretching wavenumber region for this phase. 1σ uncertainty is given in parentheses for each vibrational mode. * indicates a measurement on decompression while a dash indicates that this mode was not fit at this pressure. Modes in bold are plotted in Figure 5 of the main text. In this table, they are ordered from left to right with increasing wavenumber.

SUPPLEMENTARY MATERIAL TO CHAPTER 3

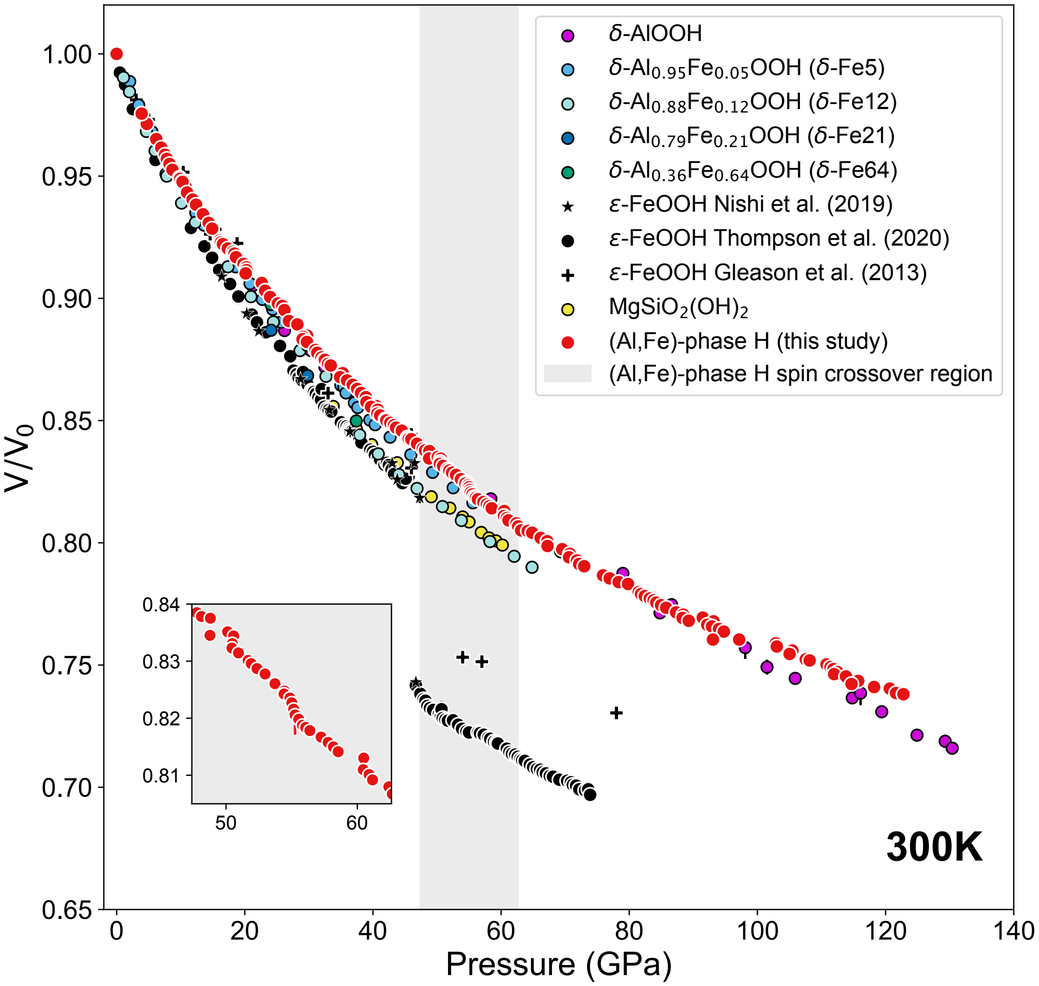

Supplementary Figure S1: Normalized unit cell volumes of different compositions in the (δ-AlOOH)-(MgSiO$_2$(OH)$_2$)-(ϵ-FeOOH) solid solution at 300K. Measurements on δ-(Al,Fe)OOH with Fe/(Fe+Al) = 0.05 and Fe/(Fe+Al) = 0.12 are obtained from Ohira et al. (2019). Data on other compositions are obtained from Nishi et al. (2014): MgSiO$_2$(OH)$_2$, Duan et al. (2018): δ-AlOOH, Nishi et al. (2019): δ-Al$_{0.79}$Fe$_{0.21}$OOH and δ-Al$_{0.36}$Fe$_{0.64}$OOH, and the combined datasets of Gleason et al., 2013), Nishi et al., 2019, and Thompson et al., 2020 for ϵ-FeOOH. Unit cell volumes are normalized by the zero-pressure volume determined by single crystal X-ray diffraction measurements on the same composition: this study: (Al,Fe)-phase H, Kawazoe et al., 2017: (δ-Fe5 and δ-Fe12), Bindi et al., 2014a: MgSiO$_2$(OH)$_2$, Kuribayashi et al., (2014): δ-AlOOH, and Suzuki (2010): ϵ-FeOOH. Unit cell volumes of δ-Al$_{0.79}$Fe$_{0.21}$OOH and δ-Al$_{0.36}$Fe$_{0.64}$OOH are normalized by the ambient pressure measurements of the same study (Nishi et al. (2019).) Error bars (1σ) are generally smaller than the points.

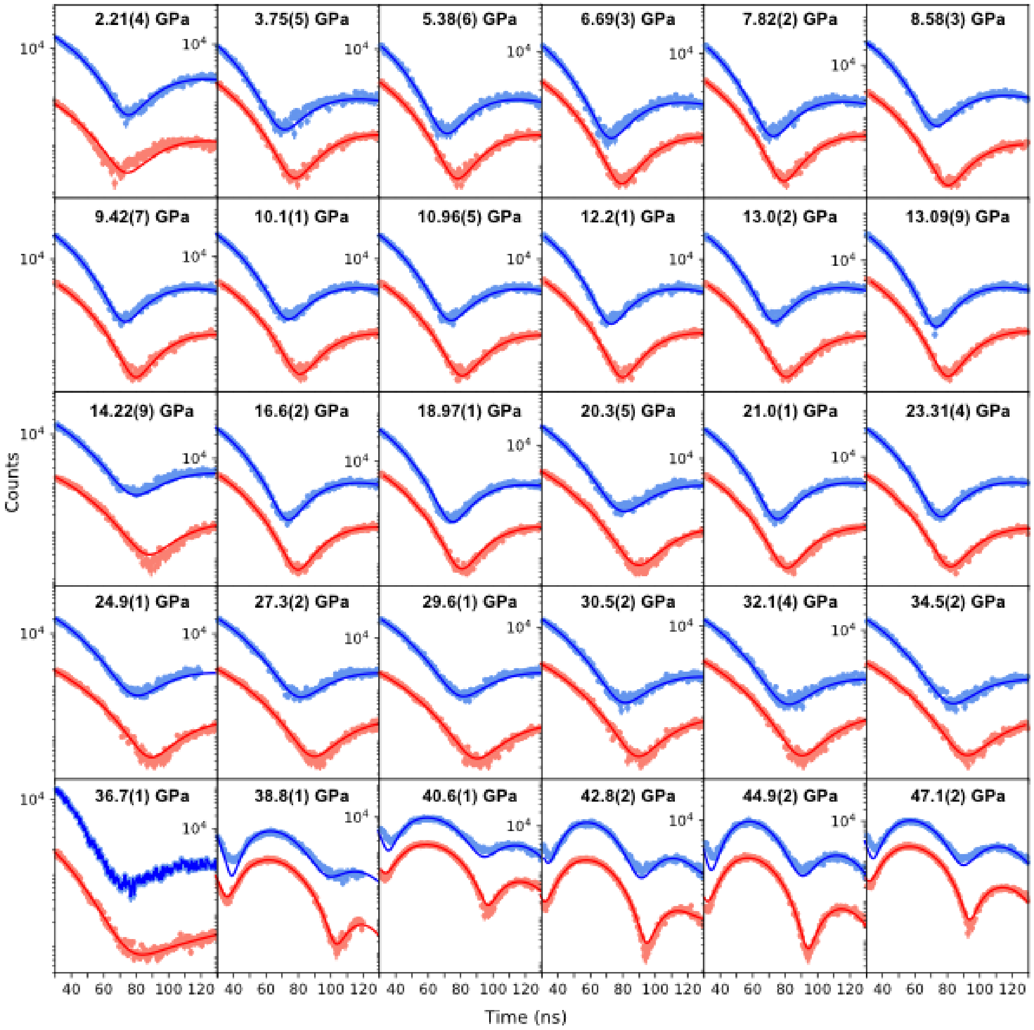

Supplementary Figure S2: Fits to SMS spectra collected on δ-(Al,^{57}Fe)OOH with Fe/(Fe+Al)=0.13(3). Spectra and fits of the sample alone are shown in red, spectra and fits to the sample and the stainless steel reference foil are shown in blue. Spectra and fits to the reference foil and sample are offset from those of only the sample by a factor of 10 for clarity. Hyperfine parameters and χ^2 values are given in supplementary Tables S1 and S2 (below). Data collection times were generally between 30 and 50 minutes

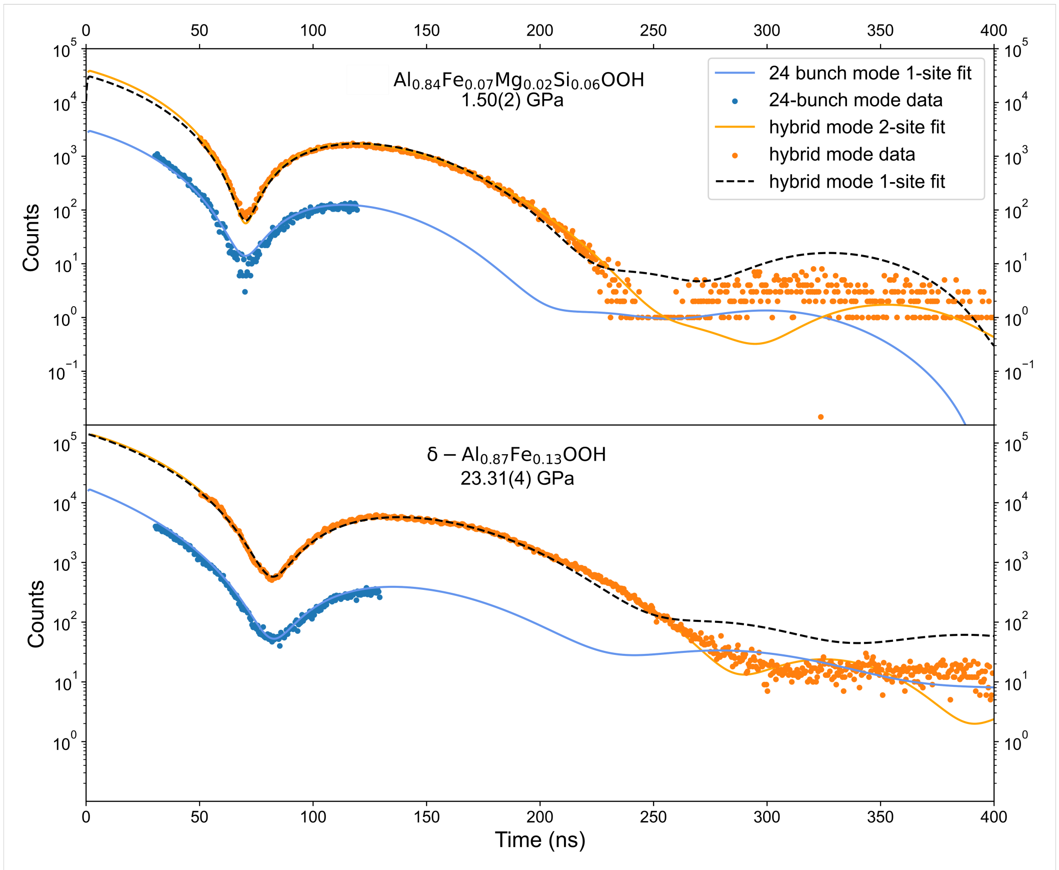

Supplementary Figure S3: Models constrained using hybrid mode measurements compared to those obtained by fitting 24-bunch mode data. Hybrid mode data is fit to 250 ns but all data out to 400 ns is shown here. Data and fits are arbitrarily scaled to facilitate comparison and represent measurements conducted without a stainless steel reference foil. Isomer shifts constrained using a reference foil are described in the main text. Each hybrid mode spectrum requires two distinct Mössbauer sites whereas data obtained in 24-bunch mode do not justify a second site in fitting an appropriate model. Weight fractions and hyperfine parameters from hybrid mode fits are reported in Table 3 of the main text and Table S2.

Pressure (GPa)	WT$_A$	IS$_A$ (mm/s)	QS$_A$ (mm/s)	FWHM$_A$	Thickness (μm)	Reduced χ^2	Reference
2.21(4)	1.00	-0.088(1)	0.520(2)	0.137(5)	10.5(1)	3.78(1)	SS310 (10μm)
3.75(5)	1.00	0.377(6)	0.438(1)	0.056(6)	14.5(1)	1.78(7)	SS310 (10μm)
5.38(6)	1.00	0.354(6)	0.431(1)	0.104(4)	14.64(9)	2.04(7)	SS310 (10μm)
6.69(3)	1.00	0.351(6)	0.425(1)	0.108(4)	14.29(9)	2.25(7)	SS310 (10μm)
7.82(2)	1.00	0.350(6)	0.420(9)	0.122(3)	14.68(8)	2.20(7)	SS310 (10μm)
8.58(3)	1.00	0.361(5)	0.428(1)	0.147(3)	12.68(7)	3.13(9)	SS310 (10μm)
9.42(7)	1.00	0.343(5)	0.414(9)	0.121(3)	14.55(8)	2.70(8)	SS310 (10μm)
10.1(1)	1.00	0.336(5)	0.409(1)	0.116(3)	14.44(8)	2.55(8)	SS310 (10μm)
10.96(5)	1.00	0.334(6)	0.408(1)	0.113(3)	14.56(8)	3.00(9)	SS310 (10μm)
12.2(1)	1.00	0.364(5)	0.431(1)	0.162(3)	12.35(7)	3.85(1)	SS310 (10μm)
13.0(2)	1.00	0.353(7)	0.418(3)	0.087(8)	9.5(4)	2.37(8)	SS310 (10μm)
13.09(9)	1.00	0.350(5)	0.424(1)	0.153(3)	12.45(7)	3.7(1)	SS310 (10μm)
14.22(9)	1.00	0.334(6)	0.429(1)	0.161(3)	12.13(6)	3.9(1)	SS310 (10μm)
16.6(2)	1.00	0.322(6)	0.407(1)	0.125(3)	13.98(7)	3.50(9)	SS310 (10μm)
18.97(1)	1.00	0.310(8)	0.400(4)	0.113(10)	13.8(4)	4.1(1)	SS310 (10μm)
20.3(5)	1.00	0.338(6)	0.409(1)	0.078(5)	9.24(6)	3.5(1)	SS310 (10μm)
21.0(1)	1.00	0.290(9)	0.390(4)	0.086(1)	14.2(4)	3.7(1)	SS310 (10μm)
23.31(4)	1.00	0.287(9)	0.389(4)	0.093(1)	13.7(4)	3.6(1)	SS310 (10μm)
24.9(1)	1.00	0.335(9)	0.407(4)	0.07(1)	9.2(4)	3.0(1)	SS310 (10μm)
27.3(2)	1.00	0.326(9)	0.404(4)	0.07(1)	9.2(4)	2.72(9)	SS310 (10μm)
29.6(1)	1.00	0.322(9)	0.400(4)	0.06(1)	9.3(4)	2.90(9)	SS310 (10μm)
30.5(2)	1.00	0.31(1)	0.390(5)	0.05(2)	10.2(4)	2.53(8)	SS310 (10μm)
32.1(4)	1.00	0.33(1)	0.392(5)	0.05(1)	9.7(4)	2.54(8)	SS310 (10μm)
34.5(2)	1.00	0.30(1)	0.374(5)	0.02(2)	10.2(4)	2.79(9)	SS310 (10μm)

Supplementary Table S1: Hyperfine parameters of ^{57}Fe^{3+} in δ-Fe13 and full-widths at half maximum (FWHM) of the measured spectra determined by fitting SMS spectra collected in 24-bunch mode using a model with a single Fe^{3+} site (QS = quadrupole splitting, IS = isomer shift). Isomer shifts are reported relative to α-Fe based on the measured isomer shift of the stainless steel reference foil (see methods section of the main text). For measurements which use a reference foil, the reported χ^2 indicates the combined value for a fit to the reference and data.

Pressure (GPa)	WT$_A$	IS$_A$ (mm/s)	QS$_A$ (mm/s)	FWHM$_A$	WT$_A$	IS$_A$ (mm/s)	QS$_A$ (mm/s)	FWHM$_A$	Thickness (μm)	Reduced χ^2	Reference
23.31 (4)	0.90	-	0.448(1)	0.109(1)	0.1	-	0.418(4)	0.13(1)	9.22(9)	10.1(1)	-
36.7(5)	0.73	0.30(2)	0.420(7)	0.059(2)	0.27	0.40(2)	0.79(2)	0.38(5)	7.23(1)	2.90(9)	SS310 (10μm)
38.8(1)	0.75	-0.004(6)	1.161(4)	0.52(2)	0.25	0.17(1)	1.202(6)	0.05(1)	6.01(9)	5.6(1)	SS310 (10μm)
40.6(1)	0.61	-0.052(5)	1.242(5)	0.50(2)	0.39	0.164(5)	1.296(5)	0.124(5)	5.56(9)	4.4(1)	SS310 (10μm)
42.8(2)	0.64	-0.037(6)	1.287(6)	0.50(1)	0.36	0.148(6)	1.333(6)	1.181(5)	6.03	4.3(1)	SS310 (10μm)
44.9(2)	0.47	0.07(2)	1.47(4)	0.41(6)	0.53	0.02(9)	1.47(4)	0.23(2)	6.7(3)	6.7(1)	SS310 (10μm)
47.1(2)	0.75	-0.011(5)	1.303(7)	0.50(1)	0.25	0.112(7)	1.387(8)	0.074(2)	5.56(7)	5.2(1)	SS310 (10μm)

Supplementary Table S2: Hyperfine parameters of ^{57}Fe^{3+} in δ-Fe13 and full-widths at half maximum of the measured spectra determined by fitting SMS spectra using a model with two Mössbauer sites. Isomer shifts are reported relative to α-Fe based on the measured isomer shift of the stainless steel reference foil (see methods section of the main text). For measurements which use a reference foil, the reported χ^2 indicates the combined value for a fit to the reference and data. Hybrid mode measurements are denoted with an asterisk (*).

SUPPLEMENTARY MATERIAL TO CHAPTER 4

Reduction and analysis of NRIXS data

Between 15 and 25 energy scans (collection time of approximately 1.5 hours for each scan) at each compression point were summed to form each NRIXS spectrum. Raw spectra without the elastic peak removed are shown in Figure S1. The PHOENIX software package was used to remove the elastic peak of each spectrum, after which the Lamb-Mössbauer factor, mean-force constant, and mean kinetic energy are determined (Table S1). The mean kinetic energy and mean force constant can be determined from the second and third-order moments of the spectrum, respectively. Additional details of the implemented procedure can be found in Sturhahn (2000) and Buchen et al. (2021). The partial, projected phonon density of states (pDOS) — the portion of the phonon density of states involving vibrations of the Fe atoms — is then determined from the NRIXS spectrum with the elastic peak removed (Sturhahn, 2000). The dependence of the Debye velocity on energy can be calculated using equation (1):

$$v(E) = [\frac{mE^2}{2\pi^2\hbar^3\rho D(E)}]^{1/3} \tag{5.1}$$

where ρ is the density of the enriched sample, m is the mass of the nuclear resonant isotope (^{57}Fe), D(E) is the pDOS in the low-energy region (< 20 meV), and $\hbar$ is the reduced Planck constant. v(E) is equal to v$_D$ in the limit E→0, the low-energy region of the pDOS. To determine v$_D$, a probability distribution is formed by many different possible fits to v(E) using an empirical power-law formulation:

$$v(E) = v_D[1 - (E/p_1)]^{p_2} \tag{5.2}$$

where p$_1$ and p$_2$ are fit parameters. One fit provides a single estimate of v$_D$ and hundreds of fits are performed over different energy ranges between a minimum and maximum energy (Table S2) to determine the probability distributions (Figure S2). The Debye and bulk sound velocities are related to the compressional (V$_P$) and shear (V$_S$) wave velocities through equations (3) and (4), respectively:

$$\frac{3}{v_D^3} = \frac{1}{V_P^3} + \frac{2}{V_S^3} \tag{5.3}$$

$$(\frac{K_s}{\rho})^2 = V_P^2 - \frac{4}{3}V_S^3 \tag{5.4}$$

where K_S is the adiabatic bulk modulus of the sample, determined at a given pressure from an equation of state of the material of interest: (Al,Fe)-phase H (Strozewski et al., 2023) in this case. Equations (3) and (4) are solved within PHOENIX to determine V_P and V_S, which can in turn be used to calculate the shear modulus (μ) using equations (5) and (6):

$$V_P = \sqrt{\frac{K_S + \frac{4}{3}\mu}{\rho}} \tag{5.5}$$

$$V_S = \sqrt{\frac{\mu}{\rho}} \tag{5.6}$$

Determination of the bulk sound velocity (V_Φ) from the equation of state (Strozewski et al., 2023) yields a complete picture of seismologically relevant acoustic wave velocities for a given material.

Supplementary Text S2. Parameterization of shear properties

To incorporate the shear properties of the hydrous phases, we explicitly parameterize the NRIXS results by fitting a polynomial to the shear modulus (μ). A 3rd-order polynomial, which is found to describe NRIXS-derived values of shear modulus well (Figure S4), is used for the (Al,Fe)-phase H data:

$$\mu(P) = 90.06 + 2.05P - 0.013P^2 + (3.35 * 10^{-5})P^3 \tag{5.7}$$

where P is pressure in GPa. For determination of uncertainty in shear properties at high pressure and temperature (see below), an estimate of 3% relative uncertainty is used, commensurate with the uncertainty from NRIXS experiments (Figure S4). Similarly, the shear modulus values (Ohira et al., 2021) of (Al,Fe)OOH are fit with the 5th-order polynomial:

$$\mu(P) = 104.659+0.248P+0.076P^2-0.0014P^3+(9.15*10^{-6})P^4-(2.144*10^{-8})P^5 \tag{5.8}$$

Each polynomial is used to calculate the shear modulus at the *P,T* conditions of the prescribed adiabat using the appropriate thermal parameters (discussed in Supplementary Text S3 below). The associated uncertainty in shear modulus, along with that determined for the bulk modulus and density (see below) is then propagated into equations (5) and (6) in order to estimate the uncertainty on wavespeeds of (Al,Fe)-phase H at high temperature.

Supplementary Text S3. Model of uncertainties at high P-T

To determine uncertainties on seismic velocities of (Al,Fe)-phase H at high temperature and when incorporated into our modeled HHMB rock, we use a monte carlo approach which resamples the equation of state of Strozewski et al. (2023) and the thermal parameters of Buchen et al. (in review) to determine the unit cell volume and associated uncertainty at each *P,T* value along a given adiabat. That is, the total pressure at high pressure and temperature can be written as:

$$P(V,T) = P_{300K}(V) + \Delta P_{th}(V,T) \tag{5.9}$$

where P_{300K} represents the contribution from an isothermal equation of state at 300 K and ΔP_{th}(V,T) represents the thermal pressure. Calculation of the thermal pressure requires constraints on the Gruneisen parameter γ_0, Debye temperature θ_0, and the parameter q_0. We use the thermal parameters γ_0 = 1.26(9), θ_0 = 1230, and q_0 = 1.21 (0.46), $\eta_{s0} \approx 2\gamma_0 = 2.52$, constrained by adapting the crystal field modeling and thermal equation of state described in Buchen et al. (in review) to (Al,Fe)-phase H.

Along a given adiabat, total pressure (P) and temperature (T) are specified, along with all other requisite equation of state parameters besides the unit cell volume (V). For each (P,T) pair, we resample each thermal equation of state parameter 1000 times and perform a numerical solution for the unit cell volume (V). The covariance of parameters derived from fits to unit cell volume data is not explicitly included in this resampling but is accounted for by the constraint that P_{300K} calculated from the obtained unit cell volume using the ambient temperature equation of state parameters must be within 5σ of the constrained unit cell volume (Strozewski et al., 2023) at the specified pressure on the adiabat. An isothermal bulk modulus and associated uncertainty can be determined from the calculated unit cell volumes in the usual manner: $K_T = -V(\frac{dP}{dV})$. To calculate $(\frac{dP}{dV})$, we again solve for the unit cell volume but at a pressure perturbed from the target pressure by 0.1%, keeping temperature constant. This calculation is performed for each resampling of the equation of state parameters to determine the uncertainty on K_T at a given pressure. In calculating the sound velocities of (Al,Fe)-phase H, the adiabatic bulk modulus K_S is used. For the purpose of uncertainty estimation, we assume that the relative uncertainty of K_S is the same as that determined for K_T. With V, K_S, μ, and associated uncertainties computed, standard error propagation formulae are applied to determine uncertainties on the sound velocities of (Al,Fe)-phase H using equations (5) and (6).

Supplementary Text S4. Modeling of lower mantle rocks

To determine the influence of Fe-bearing hydrous phases on the bulk properties of rock assemblages stable at Earth's lower mantle conditions, we build on the mineral physics modeling framework delineated in Buchen et al. (2021). That is, the post-stishovite phase transition and spin transitions are modeled using a Landau theory approach and a crystal field model, respectively, and Voigt-Reuss-Hill averaging is used to compute the elastic properties and wavespeeds of a given rock. In addition to the mineral phases of the lower mantle described in Table 3.1 of Buchen et al. (2021), we have incorporated the hydrous phases (Al,Fe)-phase H and (Al,Fe)OOH. We use the bulk compositions of the depleted MORB mantle (DMM) and N-MORB from Workman and Hart (2005) for pyrolite and metabasalt, respectively, which are the same compositions discussed in Buchen et al. (2021). Volume fractions of constituent minerals in each rock are shown in Supplementary Table S3.

In this way, we have adopted a reasonable model for pyrolite that agrees with geochemical constraints on total oxide percentages. However, we note that this approach differs fundamentally from that implemented in the HeFESTo software (Stixrude and Lithgow-Bertelloni, 2005), which self-consistently computes phase equilibria for a prescribed P,T profile and bulk composition. The motivation for the modeling pursued in this study was to enable the exchange of (Al,Fe)-phase H in specific proportions corresponding to those discerned in previous studies (e.g. (Liu et al., 2019)), which cannot be done with HeFESTo as the underlying thermodynamic database does not include hydrous phases. We apply the same modeling framework to pyrolite and metabasalt, to maintain consistency within our own models. Although a thermodynamic framework which incorporates the requisite physics and chemistry for phase equilibria is extremely useful, it does necessitate precise constraints on thermodynamic properties which are not always available. For this reason, it is not the goal of this study to assert a specific composition for pyrolite but rather to highlight the effects of oxyhydroxide phases on wavespeeds in the lower mantle via reference to specific benchmarks (i.e. PREM and the DMM pyrolite of (Workman and Hart, 2005) as modeled by (Buchen et al., 2021). Different models of pyrolitic mantle can be compared to the hydrous metabasalt and pyrolite presented here with reference to their deviations from PREM.

The Fe-bearing delta phase ($Al_{0.87}Fe_{0.13}OOH$) is modeled using bulk properties from Buchen et al. (in review). Shear properties are from Ohira et al. (2021), with shear modulus parameterized as a function of pressure with a polynomial function as described above in Supplementary Text S2. (Al,Fe)-phase H is modeled using the bulk properties presented in Strozewski et al. (2023) and shear properties constrained in this paper. For thermal properties of both the hydrous phases, we use the properties of Buchen et al. (in review), refitted for the modeling framework of Buchen et al. (2021). The temperature dependence of the spin transition implemented in the models is explained in Buchen (2021). Uncertainties on the wavespeeds of the modeled HHMB rock are assumed to be the same relative uncertainty as those determined for the included hydrous phase. That is, we do not assume that the wavespeeds of the other components in the aggregate can be determined exactly, which would artificially deflate this uncertainty. The resultant uncertainties for the HHMB aggregate are comparable to other calculations of the elastic properties of metabasalt (Tsuchiya, 2011).

Pressure (GPa)	MFC (N/m)	MKE (meV/atom)	f_{LM}
2.32 (5)	262 (21)	14.8 (3)	0.808 (5)
6.9 (2)	476 (57)	15.8 (5)	0.825 (6)
15 (2)	293 (74)	14.9 (7)	0.830 (7)
26 (1)	375 (82)	15.3 (7)	0.851 (7)
35 (2)	298 (53)	14.8 (4)	0.833 (5)
44 (2)	543 (25)	16.4 (3)	0.887 (4)
50 (3)	575 (44)	16.7 (4)	0.886 (3)
64 (3)	684 (35)	16.8 (3)	0.903(3)
78 (3)	662 (74)	17.2 (4)	0.906 (3)
91 (2)	772 (45)	17.9 (4)	0.910 (3)
100 (3)	745 (38)	17.2 (3)	0.911 (3)

Supplementary Table S1: Parameters obtained from the NRIXS spectra of (Al,Fe)-phase H after data refinement. MFC = mean force constant, MKE = mean kinetic energy, and f_{LM} = Lamb-Mössbauer factor. In all cases, parameters are determined using an energy cutoff of 150 meV, which is the maximum energy for the majority of the measured NRIXS spectra.

Pressure (GPa)	E_{min} (meV)	E_{max} (meV)	Avg. V_D (km/s)	RMS of V_D (km/s)	Skewness	Kurtosis	Fitted v_D (km/s)
2.32 (5)	3.0	15.0	5.617	0.085	-0.427	5.843	5.60 (9)
6.9 (2)	1.1	17.0	5.972	0.020	0.799	4.831	5.98 (2)
15 (2)	1.7	20.0	6.005	0.028	1.467	7.058	6.01 (8)
26 (1)	8.9	21.6	6.438	0.129	0.158	4.309	6.45 (9)
35 (2)	9.0	20.6	6.437	0.034	-0.290	3.686	6.43 (3)
44 (2)	12.6	22.4	6.998	0.210	-0.619	4.522	7.03 (18)
50 (3)	9.3	21.8	6.852	0.106	0.071	2.882	6.8 (3)
64 (3)	10.9	29.6	6.957	0.119	0.279	5.934	6.96 (6)
78 (3)	10.0	33.0	7.046	0.18	-0.352	4.893	7.05 (10)
91 (2)	12.2	33.2	7.250	0.106	0.014	3.264	7.24 (15)
99 (3)	13.1	32.6	7.229	0.148	0.796	4.327	7.18 (15)

Supplementary Table S2: Parameters and fits to the debye velocity function, used to determine the Debye Velocity (V_D). E_{min} and E_{max} represent the energy bounds of the debye velocity function, between which many fits are performed to determine the debye velocity PDF, parameterized by the average V_D, skewness, and kurtosis. An asymmetric function is fit to the V_D values determined from the collection of fits to the debye velocity function, yielding the reported fitted V_D given in Table 1 of the main text.

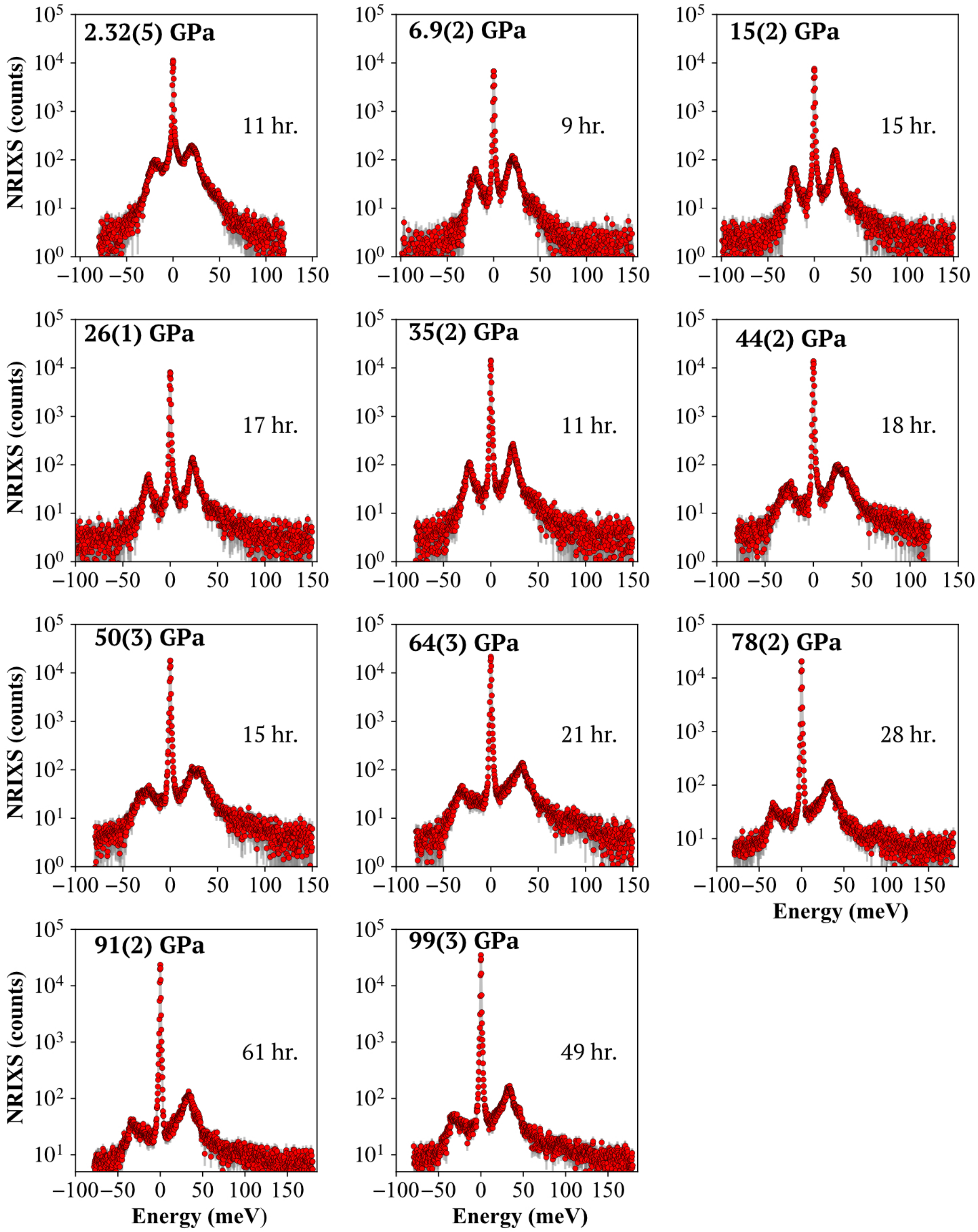

Supplementary Figure S1: Raw NRIXS spectra collected at each pressure with total collection times in hours (hr.). Pressure was determined using a combination of ruby fluorescence and diamond edge Raman as described in the main text. Longer collection times at high pressure result from lower count rates due to sample thinning as well as the effects of the spin crossover.

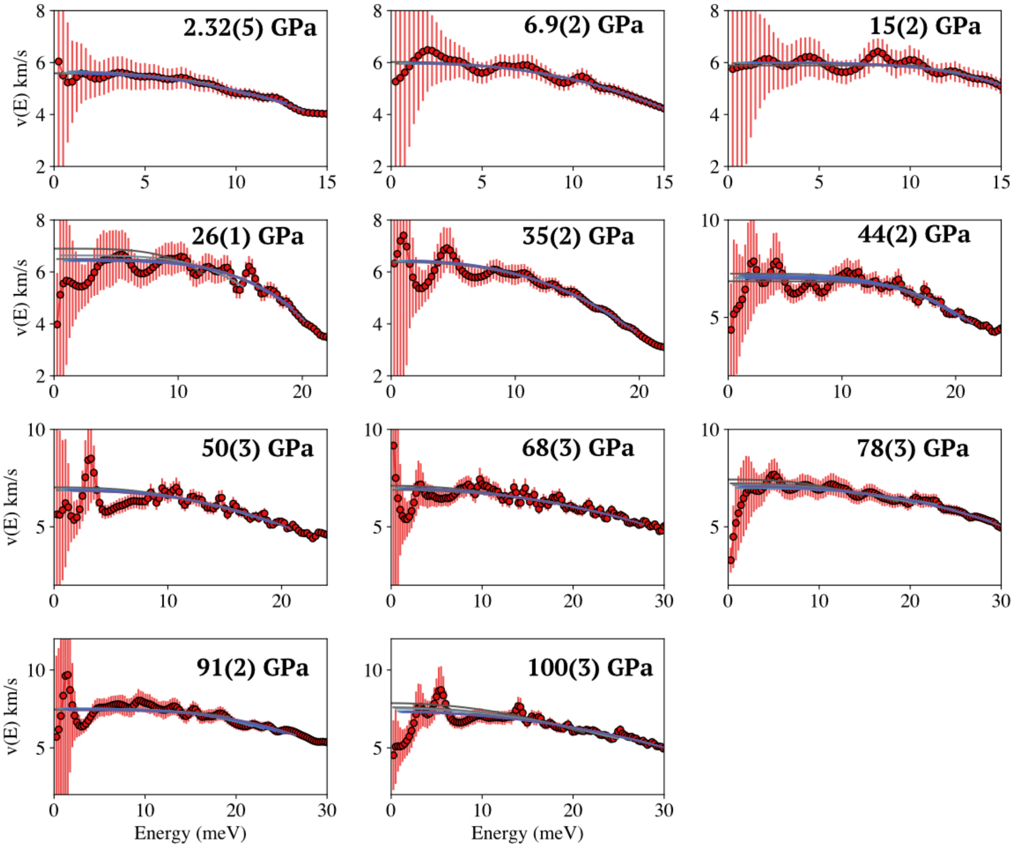

Supplementary Figure S2: Fits to debye velocity functions at each pressure. A collection of fits are used to better determine the debye velocity at low energies as described in Supplemental Text S1 above.

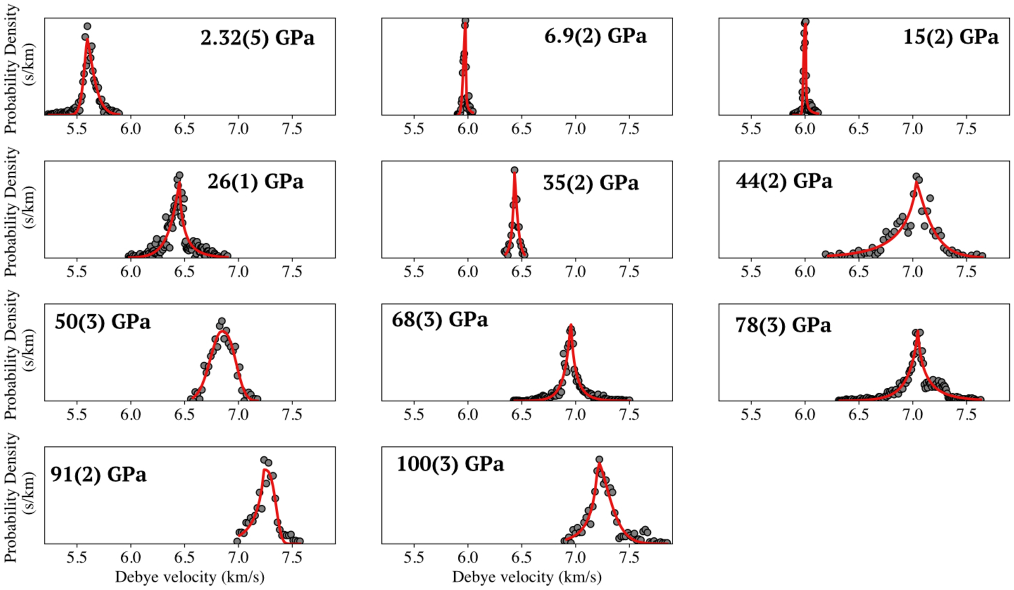

Supplementary Figure S3: Probability density functions resulting from the collection of fits at each pressure presented in Figure S2. The x-axis of each figure is scaled to the same range of Debye velocities to demonstrate the increase in Debye velocity with pressure.

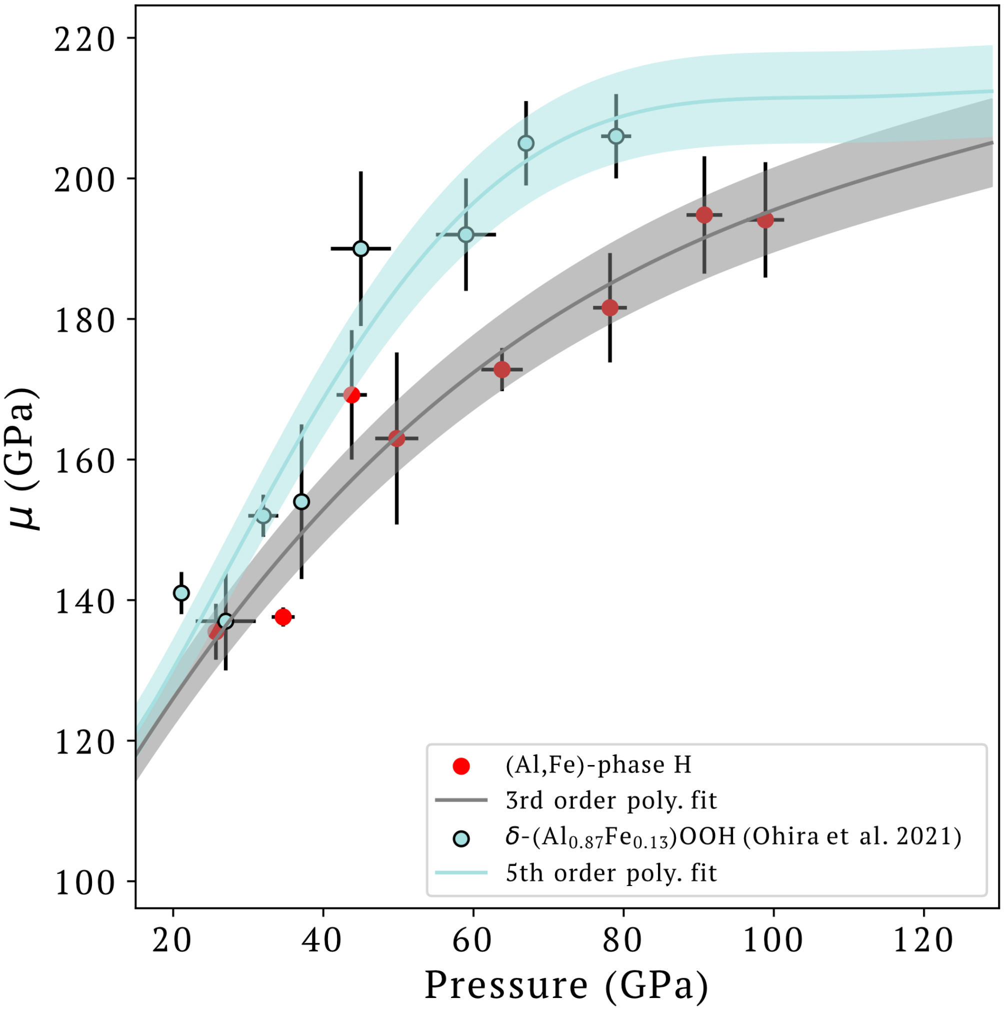

Supplementary Figure S4: Shear moduli (μ) of (Al,Fe)-phase H (this study) and δ-(Al,Fe)OOH (Ohira et al., 2021) determined from NRIXS experiments. The gray line and shaded area delineate a fit of a 3rd order polynomial to the shear moduli of (Al,Fe)-phase H and the estimated uncertainty of 3%, respectively. The light blue line and shaded area show the fit and uncertainty for δ-(Al,Fe)OOH. In constructing models of lower mantle rocks, we only analyze wavespeeds above 25 GPa and therefore fit each polynomial only to data above 20 GPa. Description of the parametrization of the shear modulus is given in Supplementary Text S2.

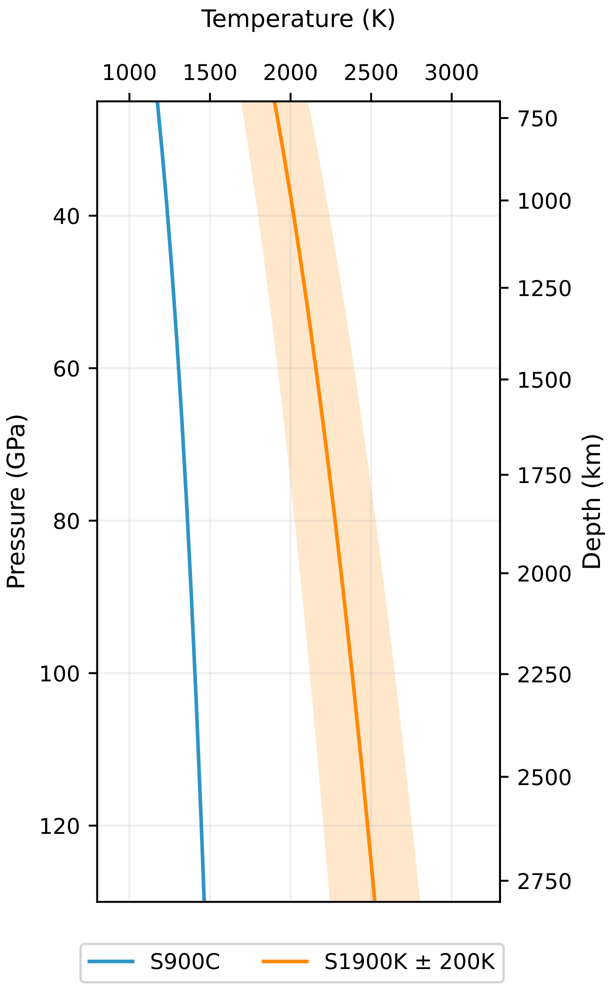

Supplementary Figure S5: Cold slab (S900C) and ambient mantle adiabats (S1900K), used to model hydrous metabasalt and pyrolitic mantle, respectively. The colder geotherm for slabs in the lower mantle, (900°C at 25 GPa), is based on results of a seismic-geodynamic study of the Tonga subduction zone (Liu et al., 2021). This slab temperature is also consistent with previous geodynamic models (Bower et al., 2013). The mantle adiabatic path (1900+/-200K at 25 GPa) spans the range described in Katsura (2022)

.

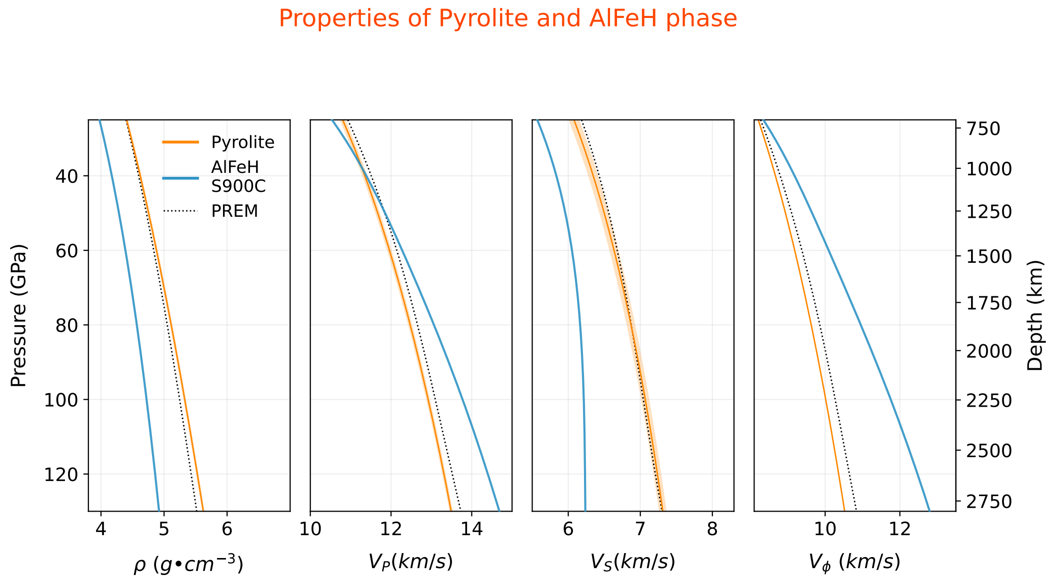

Supplementary Figure S6: Absolute values of density and seismic wavespeeds of pyrolitic mantle and (Al,Fe)-phase H (AlFeH) computed along the adiabatic profiles shown in Figure S5 and compared to PREM. Deviations of pyrolite and HHMB from PREM are plotted in Figure 4 of the main text.

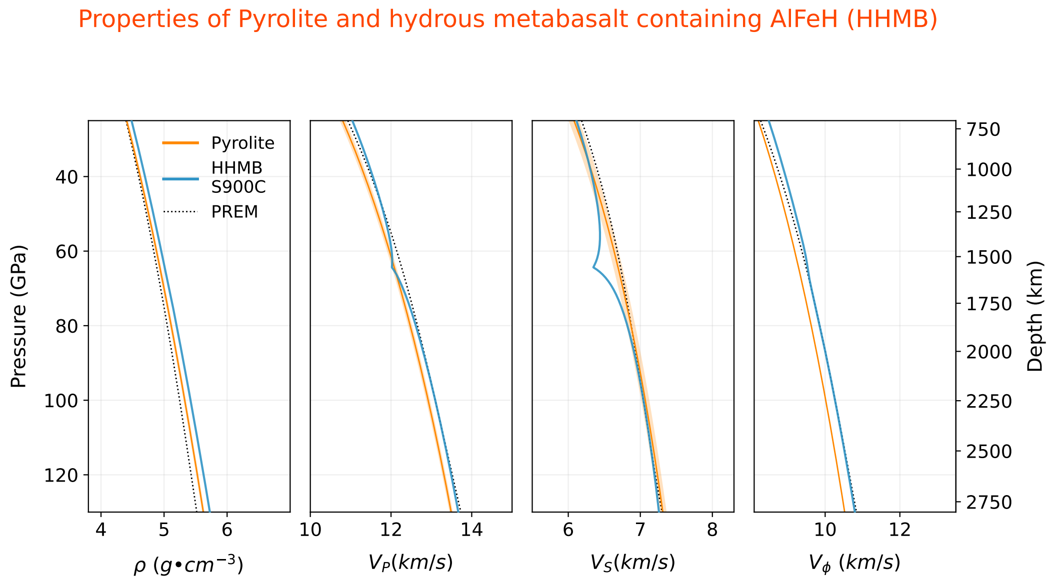

Supplementary Figure S7: Absolute values of density and seismic wavespeeds of pyrolitic mantle and (Al,Fe)-phase H containing hydrous metabasalt (HHMB) computed along the adibatic profiles shown in Figure S5 and compared to PREM. Deviations of pyrolite and AlFeH from PREM are plotted in Figure 5 of the main text.

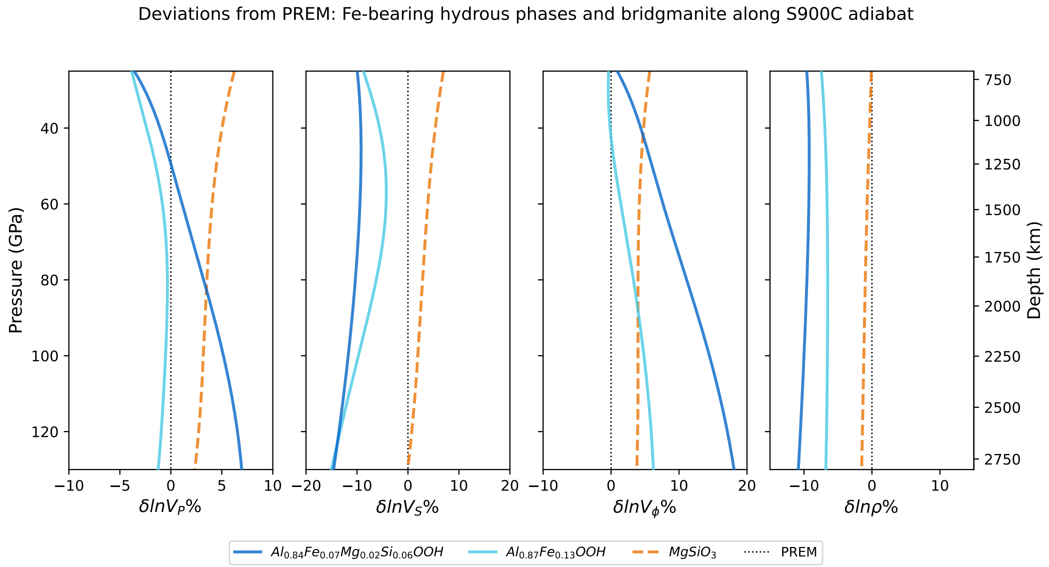

Supplementary Figure S8: Deviations of seismic wavespeeds and density of selected compositions from PREM: (Al,Fe)-phase H, Fe-bearing delta phase ($Al_{0.87}Fe_{0.13}OOH$; (Ohira et al., 2021), and $MgSiO_3$ bridgmanite. Each phase is plotted along the cold adiabat shown in Figure S4 and compared to PREM.

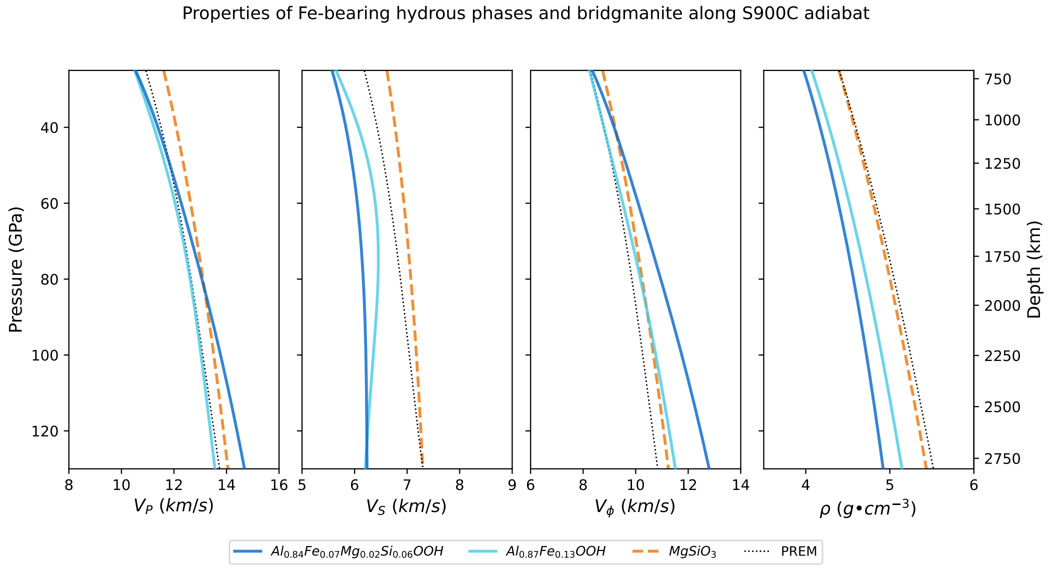

Supplementary Figure S9: Absolute values of seismic wavespeeds and density of selected compositions from PREM: (Al,Fe)-phase H, Fe-bearing delta phase ($Al_{0.87}Fe_{0.13}OOH$; (Ohira et al., 2021), and $MgSiO_3$ bridgmanite. Each phase is plotted along the cold adiabat shown in Figure S4 and compared to PREM.

Phase	End member	Mole fraction of end member in pyrolite	phase vol. % in pyrolite	Mole fraction of end member in HHMB	phase vol. % in HHMB
bm	$MgSiO_3$	0.89	77%	0.62	37%
bm	$FeSiO_3$	0.04		0.13	
bm	Al_2O_3	0.03		0.12	
bm	$FeAlO_3$	0.04		0.13	
fp	MgO	0.85	16%	-	-
fp	FeO	0.15			
cp	$CaSiO_3$	1.0	7%	1.0	26%
cf	$MgAl_2O_4$	-	-	0.17	14%
cf	$MgFe_2O_4$			0.05	
cf	$NaAlSiO_4$			0.78	
st	SiO_2	-	-	1.0	15 %
AlFeH	$Al_{0.84}Fe^{3+}_{0.07}Mg_{0.02}Si_{0.06}OOH$	-	-	1.0	8%

Supplementary Table S3: Mineralogies of modeled lower mantle rocks whose seismic velocities are presented in the main text of this paper (bm = bridgmanite, fp = ferropericlase, cp = calcium silicate perovskite, cf = calcium ferrite phase, st = stishovite, and AlFeH = (Al,Fe)-phase H). The bulk composition of pyrolite and hydrous metabasalt are based on the depleted MORB mantle (DMM) and N-MORB (Workman and Hart, 2005) + approximately 1 wt.% H_2O for hydrous metabasalt. Hydrous metabasalt (HHMB) incorporates (Al,Fe)-phase H and represents a portion of the subducted slab. Pyrolite represents the composition of ambient mantle. In both rocks, $Fe^{3+}/\Sigma Fe = 0.5$ for bridgmanite. Mg/(Mg + Fe) = 0.683 in HHMB, resulting in a total ferric iron proportion of $Fe^{3+}/\Sigma Fe = 0.6$. In pyrolite, the partitioning of Fe between bridgmanite and ferropericlase is $K_{Fe/Mg}^{bm/fp} = 0.5$, resulting in a total ferric iron content of the rock of $Fe^{3+}/\Sigma Fe = 0.25$. The chemical compositions of solid solutions are described by the mole fraction of the phase end-members compiled in this table. The elastic properties for the rock assemblages are then calculated using the workflow described in Buchen et al. (2021). In addition to the hydrous phases discussed in this paper, experimentally, theoretically, and computationally derived finite strain parameters of various lower mantle mineral phases used in the modeling are listed and referenced in Buchen (2021).

BIBLIOGRAPHY

Akahama, Yuichi and Haruki Kawamura (2010). “Pressure calibration of diamond anvil Raman gauge to 410 GPa”. In: *Journal of Physics: Conference Series* 215. DOI: `10.1088/1742-6596/215/1/012195`.

Albarede, Francis, Chris Ballhaus, Janne Blichert-Toft, Cin Ty Lee, Bernard Marty, Frédéric Moynier, and Qing Zhu Yin (2013). “Asteroidal impacts and the origin of terrestrial and lunar volatiles”. In: *Icarus* 222.1, pp. 44–52. DOI: `10.1016/j.icarus.2012.10.026`.

Albarède, Francis (2009). “Volatile accretion history of the terrestrial planets and dynamic implications”. In: *Nature* 461.7268, pp. 1227–1233. DOI: `10.1038/nature08477`.

Allégre, Claude J., J. P. Poirier, Eric Humler, and Albrecht W. Hofmann (1995). “The chemical composition of the Earth”. In: *Earth and Planetary Science Letters* 134, pp. 515–526. ISSN: 18840884. DOI: `10.5026/jgeography.131.163`.

Angel, R (2000). “Equations of state”. In: *Reviews in mineralogy and geochemistry* 41, pp. 35–59. DOI: `10.2138/rmg.2000.41.2`.

Angel, R. J. and L.W. Finger (2011). “SINGLE: A program to control single-crystal diffractometers”. In: *Journal of Applied Crystallography* 44, pp. 247–251. DOI: `10.1107/S0021889810042305`.

Ballhaus, Chris, Vera Laurenz, Carsten Münker, Raúl O.C. Fonseca, Francis Albarède, Arno Rohrbach, Markus Lagos, Max W. Schmidt, Klaus Peter Jochum, Brigitte Stoll, Ulrike Weis, and Hassan M. Helmy (2013). “The U/Pb ratio of the Earth’s mantle-A signature of late volatile addition”. In: *Earth and Planetary Science Letters* 362, pp. 237–245. DOI: `10.1016/j.epsl.2012.11.049`.

Barber, N.D., M. Edmonds, F. Jenner, and H. Williams (2022). “Global Ba/Nb systematics in arc magmas reflect the depths of mineral dehydration in subducted slabs”. In: *Geology* 50, pp. 1438–1442. DOI: `10.1130/g50447.1`.

Barnes, Jessica J., Francis M. McCubbin, Alison R. Santos, James M. D. Day, Jeremy W. Boyce, Susanne P. Schwenzer, Ulrich Ott, Ian A. Franchi, Scott Messenger, Mahesh Anand, and Carl B. Agee (2020). “Multiple early-formed water reservoirs in the interior of Mars”. In: *Nature Geoscience* 13.April. DOI: `10.1038/s41561-020-0552-y`.

Bell, D.R. and G.R. Rossman (1992). “Water in Earth’s Mantle: The Role of Nominally Anhydrous Minerals”. In: *Science* 255, pp. 1391–1397. DOI: `10.1126/science.255.5050.139`.

Bentham, H. L.M. and S. Rost (2014). “Scattering beneath Western Pacific subduction zones: Evidence for oceanic crust in the mid-mantle”. In: *Geophysical Journal International* 197, pp. 1627–1641. DOI: `10.1093/gji/ggu043`.

Bercovici, D. and S. Karato (2003). “Whole-mantle convection and the transition-zone water filter”. In: *Nature* 425, pp. 39–44. DOI: `10.1038/nature01918`.

Bindi, L., M. Nishi, and T. Irifune (2015). “Partition of Al between Phase D and Phase H at high pressure: Results from a simultaneous structure refinement of the two phases coexisting in a unique grain”. In: *American Mineralogist* 100, pp. 1637–1640. DOI: `10.2138/am-2015-5327`.

Bindi, L., M. Nishi, J. Tsuchiya, and T. Irifune (2014a). “Crystal chemistry of dense hydrous magnesium silicates: The structure of phase H, $MgSiH_2O_4$, synthesized at 45 GPa and 1000°C”. In: *American Mineralogist* 99, pp. 1802–1805. DOI: `10.2138/am.2014.4994`.

Bindi, Luca, Masayuki Nishi, Jun Tsuchiya, and Tetsuo Irifune (2014b). “Crystal chemistry of dense hydrous magnesium silicates: The structure of phase H, $MgSiH_2O_4$, synthesized at 45 GPa and 1000°C”. In: *American Mineralogist* 99, pp. 1802–1805. DOI: `10.2138/am.2014.4994`.

Blackwell, David D, G Bowen, A Hull, and John L Steele (1982). “Heat Flow, Arc Volcanism, and Subduction in Northern Oregon”. In: *Journal of Geophysical Research* 87.B10, pp. 8735–8754.

Bolfan-Casanova, N (2005). “Water in the Earth’s mantle”. In: *Mineralogical Magazine* 69, pp. 229–257. DOI: `10.1180/0026461056930248`.

Bower, Dan J., Michael Gurnis, and Daoyuan Sun (2013). “Dynamic origins of seismic wavespeed variation in D"”. In: *Physics of the Earth and Planetary Interiors* 214, pp. 74–86. DOI: `10.1016/j.pepi.2012.10.004`.

Bower, Dan J., June K. Wicks, Michael Gurnis, and Jennifer M. Jackson (2011). “A geodynamic and mineral physics model of a solid-state ultralow-velocity zone”. In: *Earth and Planetary Science Letters* 303.3-4, pp. 193–202. DOI: `10.1016/j.epsl.2010.12.035`.

Brandenburg, J.P. and P.E. Van Keken (2007). “Deep storage of oceanic crust in a vigorously convecting mantle”. In: *Journal of Geophysical Research* 112.B06403. DOI: `10.1029/2006JB004813`.

Bromiley, G. D. and N. Hilairet (2005). “Hydrogen and minor element incorporation in synthetic rutile”. In: *Mineralogical Magazine* 69, pp. 345–358. DOI: `10.1180/0026461056930256`.

Buchen, Johannes, Hauke Marquardt, Sergio Speziale, Takaaki Kawazoe, Tiziana Boffa Ballaran, and Alexander Kurnosov (2018). “High-pressure single-crystal elasticity of wadsleyite and the seismic signature of water in the shallow transition zone”. In: *Earth and Planetary Science Letters* 498, pp. 77–87. DOI: `10.1016/j.epsl.2018.06.027`.

Buchen, Johannes, Wolfgang Sturhahn, Takayuki Ishii, and Jennifer M Jackson (2021). “Vibrational anisotropy of δ-(Al,Fe)OOH single crystals as probed by nuclear resonant inelastic X-ray scattering”. In: *European Journal of Mineralogy* 33, pp. 485–502. DOI: `10.5194/ejm-33-485-2021`.

Chang, Y.Y, S.D. Jacobsen, J.F. Lin, C.R. Bina, S.M. Thomas, J. Wu, G. Shen, Y. Xiao, P. Chow, D.J. Frost, C.A. McCammon, and P. Dera (2013). “Spin transition of Fe^{3+} in Al-bearing phase D: An alternative explanation for small-scale seismic scatterers in the mid-lower mantle”. In: *Earth and Planetary Science Letters* 382, pp. 1–9. DOI: `10.1016/j.epsl.2013.08.038`.

Chen, B., J.M. Jackson, W. Sturhahn, D. Zhang, J. Zhao, J.K. Wicks, and C.A. Murphy (2012). “Spin crossover equation of state and sound velocities of $(Mg_{0.65}Fe_{0.35})O$ ferropericlase to 140 GPa”. In: *Journal of Geophysical Research: Solid Earth* 117, pp. 1–9. DOI: `10.1029/2012JB009162`.

Creasy, Neala, Maureen D. Long, and Heather A. Ford (2017). “Deformation in the lowermost mantle beneath Australia from observations and models of seismic anisotropy”. In: *Journal of Geophysical Research: Solid Earth* 122.7, pp. 5243–5267. DOI: `10.1002/2016JB013901`.

Crowley, John W., Mélanie Gérault, and Richard J. O’Connell (2011). “On the relative influence of heat and water transport on planetary dynamics”. In: *Earth and Planetary Science Letters* 310, pp. 380–388. DOI: `10.1016/j.epsl.2011.08.035`.

Dal Zilio, Luca and Taras Gerya (2022). “Subduction earthquake cycles controlled by episodic fluid pressure cycling”. In: *Lithos* 426-427.April, p. 106800. DOI: `10.1016/j.lithos.2022.106800`.

De Grave, E., R. E. Vandenberghe, and C. Dauwe (2006). “ILEEMS: Methodology and applications to iron oxides”. In: *Hyperfine Interactions* 161.1-4, pp. 147–160. DOI: `10.1007/s10751-005-9177-1`.

Dewaele, Agnes, Paul Loubeyre, and Mohamed Mezouar (2004). “Equations of state of six metals above 94 GPa”. In: *Physical Review B - Condensed Matter and Materials Physics* 70.9, pp. 1–8. DOI: `10.1103/PhysRevB.70.094112`.

Dewaele, Agnes, Marc Torrent, Paul Loubeyre, and Mohamed Mezouar (2008). “Compression curves of transition metals in the Mbar range: Experiments and projector augmented-wave calculations”. In: *Physical Review B* 78. DOI: `10.1103/PhysRevB.78.104102`.

Dobrosavljevic, Vasilije V., Wolfgang Sturhahn, and Jennifer M. Jackson (2019). “Evaluating the role of iron-rich (Mg,Fe)O in ultralow velocity zones”. In: *Minerals* 9.12. DOI: `10.3390/min9120762`.

Dobrosavljevic, Vasilije V., Dongzhou Zhang, Wolfgang Sturhahn, Stella Chariton, Vitali B. Prakapenka, Jiyong Zhao, Thomas S. Toellner, Olivia S. Pardo, and Jennifer M. Jackson (2023). “Melting and defect transitions in FeO up to pressures of Earth's core-mantle boundary". In: *Nature Communications* 14. DOI: `10.1038/s41467-023-43154-w`.

Dobson, David P., Philip G. Meredith, and Stephen A. Boon (2002). "Simulation of subduction zone seismicity by dehydration of serpentine". In: *Science* 298.5597, pp. 1407–1410. DOI: `10.1126/science.1075390`.

Dorfman, Susannah M., James Badro, Jean-Pascal Rueff, Paul Chow, Yuming Xiao, and Philippe Gillet (2015). "Composition dependence of spin transition in (Mg,Fe)SiO_3 bridgmanite". In: *American Mineralogist* 100, pp. 2246–2253. DOI: `10.2138/am-2015-5190`.

Dorogokupets, P. I. and A. R. Oganov (2006). "Equations of state of Al, Au, Cu, Pt, Ta, and W and revised ruby pressure scale". In: *Doklady Earth Sciences* 410, pp. 1091–1095. DOI: `10.1134/S1028334X06070208`.

Doucet, Luc S., Zheng Xiang Li, Hamed Gamal El Dien, Amaury Pourteau, J. Brendan Murphy, William J. Collins, Nadine Mattielli, Hugo K.H. Olierook, Christopher J. Spencer, and Ross N. Mitchell (2020). "Distinct formation history for deep-mantle domains reflected in geochemical differences". In: *Nature Geoscience* 13, pp. 511–515. DOI: `10.1038/s41561-020-0599-9`.

Douvalis, A. P., V. Papaefthymiou, A. Moukarika, and T. Bakas (2000). "Electronic and magnetic properties of the iron borate Fe_2BO_4". In: *Hyperfine Interactions* 126, pp. 319–327.

Duan, Yunfei, Ningyu Sun, Siheng Wang, Xinyang Li, Xuan Guo, Huaiwei Ni, Vitali B. Prakapenka, and Zhu Mao (2018). "Phase stability and thermal equation of state of δ-AlOOH: Implication for water transportation to the Deep Lower Mantle". In: *Earth and Planetary Science Letters* 494, pp. 92–98. DOI: `10.1016/j.epsl.2018.05.003`.

Durand, S., E. Debayle, Y. Ricard, C. Zaroli, and S. Lambotte (2017). "Confirmation of a change in the global shear velocity pattern at around 1000km depth". In: *Geophysical Journal International* 211, pp. 1628–1639. DOI: `10.1093/gji/ggx405`.

Dyar, M. Darby, David G. Agresti, Martha W. Schaefer, Christopher A. Grant, and Elizabeth C. Sklute (2006). "Mössbauer spectroscopy of Earth and planetary materials". In: *Annual Review of Earth and Planetary Sciences* 34, pp. 83–125. DOI: `10.1146/annurev.earth.34.031405.125049`.

Dziewonski, Adam M. and Don L. Anderson (1981). "Preliminary reference Earth model". In: *Physics of the Earth and Planetary Interiors* 25, pp. 297–356. DOI: `10.1016/0031-9201(81)90046-7`.

Fan, Jianke, Dapeng Zhao, Cuilin Li, Lijun Liu, and Dongdong Dong (2024). "Remnants of shifting early Cenozoic Pacific lower mantle flow imaged beneath the Philippine Sea Plate". In: *Nature Geoscience* 17, pp. 347–352. DOI: `10.1038/s41561-024-01404-6`.

Farrugia, L.J. (2012). "WinGX and ORTEP for Windows: an update". In: *Journal of Applied Crystallography* 45, pp. 849–854. DOI: `10.1107/S0021889812029111`.

Fei, Yingwei, Angele Ricolleau, Mark Frank, Kenji Mibe, Guoyin Shen, and Vitali Prakapenka (2007a). "Toward an internally consistent pressure scale". In: *Proceedings of the National Academy of Sciences of the United States of America* 104, pp. 9182–9186. DOI: `10.1073/pnas.0609013104`.

Fei, Yingwei, Li Zhang, Alexandre Corgne, Heather Watson, Angele Ricolleau, Yue Meng, and Vitali Prakapenka (2007b). "Spin transition and equations of state of (Mg, Fe)O solid solutions". In: *Geophysical Research Letters* 34, pp. 1–5. DOI: `10.1029/2007GL030712`.

Férot, Anaïs and Nathalie Bolfan-Casanova (2012). "Water storage capacity in olivine and pyroxene to 14 GPa: Implications for the water content of the Earth's upper mantle and nature of seismic discontinuities". In: *Earth and Planetary Science Letters* 349-350, pp. 218–230. DOI: `10.1016/j.epsl.2012.06.022`.

Fialko, Yuri (2004). "Evidence of fluid-filled upper crust from observations of postseismic deformation due to the 1992 Mw7.3 Landers earthquake". In: *Journal of Geophysical Research: Solid Earth* 109.8, pp. 1–17. DOI: `10.1029/2004JB002985`.

Fischer, Rebecca A., Andrew J. Campbell, Bethany A. Chidester, Daniel M. Reaman, Elizabeth C. Thompson, Jeffrey S. Pigott, Vitali B. Prakapenka, and Jesse S. Smith (2018). "Equations of state and phase boundary for stishovite and $CaCl_2$-type SiO_2". In: *American Mineralogist* 103, pp. 792–802. DOI: `10.2138/am-2018-6267`.

French, Scott W. and Barbara Romanowicz (2015). "Broad plumes rooted at the base of the Earth's mantle beneath major hotspots". In: *Nature* 525, pp. 95–99. DOI: `10.1038/nature14876`.

Garnero, Edward J., Allen K. McNamara, and Sang Heon Shim (2016). "Continent-sized anomalous zones with low seismic velocity at the base of Earth's mantle". In: *Nature Geoscience* 9, pp. 481–489. DOI: `10.1038/ngeo2733`.

Gleason, A. E., C. E. Quiroga, A. Suzuki, R. Pentcheva, and W. L. Mao (2013). "Symmetrization driven spin transition in ϵ-FeOOH at high pressure". In: *Earth and Planetary Science Letters* 379, pp. 49–55. DOI: `10.1016/j.epsl.2013.08.012`.

Gu, Jesse T., Bo Peng, Xuan Ji, Jisheng Zhang, Hong Yang, Susana Hoyos, Marc M. Hirschmann, Edwin S. Kite, and Rebecca A. Fischer (2024). "Composition of Earth's initial atmosphere and fate of accreted volatiles set by core formation and magma ocean redox evolution". In: *Earth and Planetary Science Letters* 629. DOI: `10.1016/j.epsl.2024.118618`.

Gu, T., M.G. Pamato, D. Novella, J. Alvaro M.and Fournelle, F.E. Brenker, W. Wang, and F. Nestola (2022). "Hydrous peridotitic fragments of Earth's mantle 660 km discontinuity sampled by a diamond". In: *Nature Geoscience* 15, pp. 950–954. DOI: `10.1038/s41561-022-01024-y`.

Gütlich, Philipp and Yann Garcia (2012). *Mössbauer Spectroscopy: Tutorial Book*. Ed. by Y Yoshida and G Langouche. Springer Berlin Heidelberg. DOI: `10.1007/978-3-642-32220-4_2`.

Halliday, Alex N. and Robin M. Canup (2023). "The accretion of planet Earth". In: *Nature Reviews Earth and Environment* 4.1, pp. 19–35. DOI: `10.1038/s43017-022-00370-0`.

Haugland, S.M., J. Ritsema, S. Kaneshima, and M.S. Thorne (2017). "Estimate of the Rigidity of Eclogite in the Lower Mantle From Waveform Modeling of Broadband S-to-P Wave Conversions". In: *Geophysical Research Letters* 44, pp. 11, 778–11, 784. DOI: `10.1002/2017GL075463`.

Heimisson, Elías Rafn, John Rudnicki, and Nadia Lapusta (2021). "Dilatancy and Compaction of a Rate-and-State Fault in a Poroelastic Medium: Linearized Stability Analysis". In: *Journal of Geophysical Research: Solid Earth* 126.8. DOI: `10.1029/2021JB022071`.

Herman, A. (2022). "Granular effects in sea ice rheology in the marginal ice zone". In: *Philosophical Transactions of the Royal Society A: Mathematical, Physical and Engineering Sciences* 380.2235. DOI: `10.1098/rsta.2021.0260`.

Hernlund, John W. and Christine Houser (2008). "On the statistical distribution of seismic velocities in Earth's deep mantle". In: *Earth and Planetary Science Letters* 265, pp. 423–437. DOI: `10.1016/j.epsl.2007.10.042`.

Hirose, Kei (2006). "Postperovskite phase transition and its geophysical implications". In: *Reviews of Geophysics* 44.3, pp. 1–18. DOI: `10.1029/2005RG000186`.

Hirose, Kei, Stéphane Labrosse, and John Hernlund (2013). "Composition and State of the Core". In: *Annual Review of Earth and Planetary Sciences* 41.1, pp. 657–691. DOI: `10.1146/annurev-earth-050212-124007`.

Hirschmann, Marc M. (2006). "Water, melting, and the deep Earth H_2O cycle". In: *Annual Review of Earth and Planetary Sciences* 34, pp. 629–653. DOI: `10.1146/annurev.earth.34.031405.125211`.

Ho, Wai-Ga D., Peng Zhang, Kristjan Haule, Jennifer M. Jackson, Vladimir Dobrosavljevic, and Vasilije V. Dobrosavljevic (2023). "Quantum critical phase of FeO spans conditions of Earth's lower mantle". In: pp. 1–8. DOI: `10.1038/s41467-024-47489-w`.

Hosseini, Kasra, Karin Sigloch, Maria Tsekhmistrenko, Afsaneh Zaheri, Tarje Nissen-Meyer, and Heiner Igel (2020). "Global mantle structure from multifrequency tomography using P, PP and P-diffracted waves". In: *Geophysical Journal International* 220, pp. 96–141. DOI: `10.1093/gji/ggz394`.

Houser, C., J. W. Hernlund, J. Valencia-Cardona, and R. M. Wentzcovitch (2020). "Discriminating lower mantle composition". In: *Physics of the Earth and Planetary Interiors* 308.106552. DOI: `10.1016/j.pepi.2020.106552`.

Hsu, Han (2017). "First-principles study of iron spin crossover in the new hexagonal aluminous phase". In: *Physical Review B* 95.2, pp. 1–7. DOI: `10.1103/PhysRevB.95.020406`.

Hu, Qingyang, Duck Young Kim, Jin Liu, Yue Meng, Liuxiang Yang, Dongzhou Zhang, Wendy L. Mao, and Ho Kwang Mao (2017). "Dehydrogenation of goethite in Earth's deep lower mantle". In: *Proceedings of the National Academy of Sciences of the United States of America* 114.7, pp. 1498–1501. DOI: `10.1073/pnas.1620644114`.

Hushur, Anwar, Murli H. Manghnani, Joseph R. Smyth, Quentin Williams, Eric Hellebrand, Dayana Lonappan, Yu Ye, Przemyslaw Dera, and Daniel J. Frost (2011). "Hydrogen bond symmetrization and equation of state of phase D". In: *Journal of Geophysical Research: Solid Earth* 116, pp. 1–8. DOI: `10.1029/2010JB008087`.

Ikeda, Osamu, Tatsuya Sakamaki, Tomonori Ohashi, Masahisa Goto, Yuji Higo, and Akio Suzuki (2019). "Sound velocity measurements of ϵ-FeOOH up to 24 GPa". In: *Journal of Mineralogical and Petrological Sciences* 114.3, pp. 155–160. DOI: `10.2465/jmps.181115b`.

Insixiengmay, Leslie and Lars Stixrude (2023). "Hydrogen bond symmetrization and high-spin to low-spin transition of ϵ-FeOOH at the pressure of Earth's lower mantle". In: *American Mineralogist* 108.12, pp. 2209–2218. DOI: `10.2138/am-2022-8839`.

Ishii, T., L. Shi, R. Huang, N. Tsujino, D. Druzhbin, R. Myhill, Y. Li, L. Wang, T. Yamamoto, N. Miyajima, T. Kawazoe, N. Nishiyama, Y. Higo, Y. Tange, and T. Katsura (2016). "Generation of pressures over 40 GPa using Kawai-type multi-anvil press with tungsten carbide anvils". In: *Review of Scientific Instruments* 87.2. DOI: `10.1063/1.4941716`.

Ishii, Takayuki, Giacomo Criniti, Eiji Ohtani, Narangoo Purevjav, Hongzhan Fei, Tomoo Katsura, and Ho Kwang Mao (2022a). "Superhydrous aluminous silica phases as major water hosts in high-temperature lower mantle". In: *Proceedings of the National Academy of Sciences of the United States of America* 119.44, pp. 1–6. DOI: `10.1073/pnas.2211243119`.

Ishii, Takayuki, Giacomo Criniti, Narangoo Purevjav, Tomoo Katsura, and Eiji Ohtani (2024). "Hydrogen partitioning between stishovite and hydrous phase δ: implications for water cycle and distribution in the lower mantle". In: *Progress in Earth and Planetary Science* 11.10. DOI: `10.1186/s40645-024-00615-0`.

Ishii, Takayuki, Zhaodong Liu, and Tomoo Katsura (2019). "A Breakthrough in Pressure Generation by a Kawai-Type Multi-Anvil Apparatus with Tungsten Carbide Anvils". In: *Engineering* 5.3, pp. 434–440. DOI: `10.1016/j.eng.2019.01.013`.

Ishii, Takayuki, Eiji Ohtani, and Anton Shatskiy (2022b). “Aluminum and hydrogen partitioning between bridgmanite and high-pressure hydrous phases: Implications for water storage in the lower mantle”. In: *Earth and Planetary Science Letters* 583. DOI: `10.1016/j.epsl.2022.117441`.

Jackson, Jennifer M. and Christine Thomas (2021). *Seismic and Mineral Physics Constraints on the D” Layer*. Ed. by H. Marquardt, M. Ballmer, S. Cottaar, and J. Konter. American Geophysical Union, pp. 193–227. DOI: `10.1002/9781119528609.ch8`.

Jacobsen, S.D., Z. Liu, T. Boffa Ballaran, E.F Littlefield, L. Ehm, and R.J. Hemley (2010). “Effect of H_2O on upper mantle phase transitions in $MgSiO_3$: Is the depth of the seismic X-discontinuity an indicator of mantle water content?” In: *Physics of the Earth and Planetary Interiors* 183, pp. 234–244. DOI: `10.1016/j.pepi.2010.06.015`.

Jacobsen, Steven D. (2018). “Effect of water on the equation of state of nominally anhydrous minerals”. In: *Water in Nominally Anhydrous Minerals* 62.April, pp. 321–342. DOI: `10.2138/rmg.2006.62.14`.

Jahn, Sandro, Bernd Wunder, Monika Koch-Müller, Leïla Tarrieu, Michael Pöhle, Anke Watenphul, and Michael N. Taran (2012). “Pressure-induced hydrogen bond symmetrisation in guyanaite, β-CrOOH: evidence from spectroscopy and ab initio simulations”. In: *European Journal of Mineralogy* 24.5, pp. 839–850. DOI: `10.1127/0935-1221/2012/0024-2228`.

Jones, Timothy D., Ross R. Maguire, Peter E. van Keken, Jeroen Ritsema, and Paula Koelemeijer (2020). “Subducted oceanic crust as the origin of seismically slow lower-mantle structures”. In: *Progress in Earth and Planetary Science* 7.1, pp. 1–16. DOI: `10.1186/s40645-020-00327-1`.

Kagi, H., D. Ushijima, A. Sano-Furukawa, K. Komatsu, R. Iizuka, T. Nagai, and S. Nakano (2010). “Infrared absorption spectra of δ-AlOOH and its deuteride at high pressure and implication to pressure response of the hydrogen bonds”. In: *Journal of Physics: Conference Series* 215. DOI: `10.1088/1742-6596/215/1/012052`.

Kaneshima, Satoshi (2016). “Seismic scatterers in the mid-lower mantle”. In: *Physics of the Earth and Planetary Interiors* 257, pp. 105–114. DOI: `10.1016/j.pepi.2016.05.004`.

Karato, S. (2011). “Water distribution across the mantle transition zone and its implications for global material circulation”. In: *Earth and Planetary Science Letters* 301, pp. 413–423. DOI: `10.1016/j.epsl.2010.11.038`.

Katsura, Tomoo (2022). “A Revised Adiabatic Temperature Profile for the Mantle”. In: *Journal of Geophysical Research: Solid Earth* 127, pp. 1–11. DOI: `10.1029/2021JB023562`.

Kawamoto, Tatsuhiko (2006). “Hydrous phases and water transport in the subducting slab”. In: *Reviews in Mineralogy and Geochemistry* 62, pp. 273–289. DOI: `10.2138/rmg.2006.62.12`.

Kawano, Katsutoshi, Masayuki Nishi, Hideharu Kuwahara, Sho Kakizawa, Toru Inoue, and Tadashi Kondo (2024). “Extensive iron-water exchange at Earth’s core-mantle boundary can explain seismic anomalies”. In: *Nature communications* 15. doi: `10.1038/s41467-024-52677-9`.

Kawazoe, T., I. Ohira, T. Ishii, T. Boffa Ballaran, C. McCammon, and A. Suzuki (2017). “Single crystal synthesis of δ-(Al,Fe)OOH”. In: *American Mineralogist* 102, pp. 1953–1956. doi: `10.2138/am-2017-6153`.

Kennett, B. L.N. and E. R. Engdahl (1991). “Traveltimes for global earthquake location and phase identification”. In: *Geophysical Journal International* 105, pp. 429–465. doi: `10.1111/j.1365-246X.1991.tb06724.x`.

Kennett, B. L.N., E. R. Engdahl, and R. Buland (1995). “Constraints on seismic velocities in the Earth from traveltimes”. In: *Geophysical Journal International* 122, pp. 108–124. doi: `10.1111/j.1365-246X.1995.tb03540.x`.

Kim, D., V. Lekić, B. Ménard, D. Baron, and M. Taghizadeh-Popp (2020). “Sequencing seismograms: A panoptic view of scattering in the core-mantle boundary region”. In: *Science* 368, pp. 1223–1228. doi: `10.1126/science.aba8972`.

Kim, Taehyun, Joseph G. O’Rourke, Jeongmin Lee, Stella Chariton, Vitali Prakapenka, Rachel J. Husband, Nico Giordano, Hanns Peter Liermann, Sang Heon Shim, and Yongjae Lee (2023). “A hydrogen-enriched layer in the topmost outer core sourced from deeply subducted water”. In: *Nature Geoscience* 16.12, pp. 1208–1214. doi: `10.1038/s41561-023-01324-x`.

King, H E and L W Finger (1979). “Diffracted beam crystal centering and its application to high-pressure crystallography”. In: *Journal of Applied Crystallography* 12, pp. 374–378. doi: `10.1107/S0021889879012723`.

Koelemeijer, P., J. Ritsema, A. Deuss, and H. J. van Heijst (2016). “SP12RTS: A degree-12 model of shear- and compressional-wave velocity for Earth’s mantle”. In: *Geophysical Journal International* 204, pp. 1024–1039. doi: `10.1093/gji/ggv481`.

Kolesov, Boris A. (2021). “Hydrogen bonds: Raman spectroscopic study”. In: *International Journal of Molecular Sciences* 22.10. doi: `10.3390/ijms22105380`.

Komatsu, K., A. Sano-Furukawa, and H. Kagi (2011). “Effects of Mg and Si ions on the symmetry of δ-AlOOH”. In: *Physics and Chemistry of Minerals* 38, pp. 727–733. doi: `10.1007/s00269-011-0445-0`.

Koudriachova, Marina V., Simon W. De Leeuw, and Nicholas M. Harrison (2004). “First-principles study of H intercalation in rutile TiO_2”. In: *Physical Review B - Condensed Matter and Materials Physics* 70.16, pp. 1–5. doi: `10.1103/PhysRevB.70.165421`.

Kruijer, Thomas S., Thorsten Kleine, Mario Fischer-Gödde, and Peter Sprung (2015). “Lunar tungsten isotopic evidence for the late veneer”. In: *Nature* 520, pp. 534–537. doi: `10.1038/nature14360`.

Kudoh, Y., T. Kuribayashi, A. Suzuki, E. Ohtani, and T. Kamada (2004). "Space group and hydrogen sites of δ-AlOOH and implications for a hypothetical high-pressure form of $Mg(OH)_2$". In: *Physics and Chemistry of Minerals* 31.6, pp. 360–364. DOI: `10.1007/s00269-004-0404-0`.

Kuribayashi, Takahiro, Asami Sano-Furukawa, and Toshiro Nagase (2014). "Observation of pressure-induced phase transition of δ-AlOOH by using single-crystal synchrotron X-ray diffraction method". In: *Physics and Chemistry of Minerals* 41, pp. 303–312. DOI: `10.1007/s00269-013-0649-6`.

Lai, Voon Hui, Don V. Helmberger, Vasilije V. Dobrosavljevic, Wenbo Wu, Daoyuan Sun, Jennifer M. Jackson, and Michael Gurnis (2022). "Strong ULVZ and Slab Interaction at the Northeastern Edge of the Pacific LLSVP Favors Plume Generation". In: *Geochemistry, Geophysics, Geosystems* 23.2, pp. 1–19. DOI: `10.1029/2021GC010020`.

Lakshtanov, Dmitry L., Stanislav V. Sinogeikin, Konstantin D. Litasov, Vitali B. Prakapenka, Holger Hellwig, Jingyun Wang, Carmen Sanches-Valle, Jean Philippe Perrillat, Bin Chen, Maddury Somayazulu, Jie Li, Eiji Ohtani, and Jay D. Bass (2007). "The post-stishovite phase transition in hydrous alumina-bearing SiO_2 in the lower mantle of the earth". In: *Proceedings of the National Academy of Sciences of the United States of America* 104, pp. 13588–13590. DOI: `10.1073/pnas.0706113104`.

Li, Lin, Chao Li, and Sheng-rong Li (2022). "Epidote as a conveyor of water into the Earth's deep mantle in subduction zones: Insights from coupled high pressure - temperature experiments". In: *American Mineralogist* 108.January, pp. 120–126. DOI: `10.2138/am-2022-8252`.

Li, Yunguo, L. Vočadlo, T. Sun, and J.P. Brodholt (2020). "The Earth's core as a reservoir of water". In: *Nature Geoscience* 13, pp. 453–458. DOI: `10.1038/s41561-020-0578-1`.

Libowitzky, Eugen (1999). "Correlation of O-H stretching frequencies and O-H--O hydrogen bond lengths in minerals". In: *Monatshefte fur Chemie* 130.8, pp. 1047–1059.

Lin, Jung Fu, Viktor V. Struzhkin, Steven D. Jacobsen, Michael Y. Hu, Paul Chow, Jennifer Kung, Haozhe Liu, Ho Kwang Mao, and Russell J. Hemley (2005). "Spin transition of iron in magnesiowüstite in the Earth's lower mantle". In: *Nature* 436, pp. 377–380. DOI: `10.1038/nature03825`.

Lin, Jung Fu and Taku Tsuchiya (2008). "Spin transition of iron in the Earth's lower mantle". In: *Physics of the Earth and Planetary Interiors* 170, pp. 248–259. DOI: `10.1016/j.pepi.2008.01.005`.

Lin, Y., Q. Hu, Y. Meng, M. Walter, and H.K. Mao (2020). "Evidence for the stability of ultrahydrous stishovite in Earth's lower mantle". In: *Proceedings of the National Academy of Sciences of the United States of America* 117, pp. 184–189. DOI: `10.1073/pnas.1914295117`.

Litasov, K. and E. Ohtani (2003). “Stability of various hydrous phases in CMAS pyrolite-H_2O system up to 25 GPa”. In: *Physics and Chemistry of Minerals* 30.3, pp. 147–156. DOI: `10.1007/s00269-003-0301-y`.

Litasov, Konstantin D., Eiji Ohtani, Akio Suzuki, and Kenichi Funakoshi (2007). “The compressibility of Fe- and Al-bearing phase D to 30 GPa”. In: *Physics and Chemistry of Minerals* 34, pp. 159–167. DOI: `10.1007/s00269-006-0136-4`.

Liu, H., M. Gurnis, W. Leng, Z. Jia, and Z. Zhan (2021). “Tonga Slab Morphology and Stress Variations Controlled by a Relic Slab: Implications for Deep Earthquakes in the Tonga-Fiji Region”. In: *Geophysical Research Letters* 48, pp. 1–10. DOI: `10.1029/2020GL091331`.

Liu, Jin, Jung Fu Lin, and Vitali B. Prakapenka (2015). “High-Pressure Orthorhombic Ferromagnesite as a Potential Deep-Mantle Carbon Carrier”. In: *Scientific Reports* 5, pp. 3–8. DOI: `10.1038/srep07640`.

Liu, W., Y. Zhang, F. Tissot, G. Avice, and Q. Ye Z.and Yin (2023). “I/Pu reveals Earth mainly accreted from volatile-poor differentiated planetesimals”. In: *Science Advances* 9. DOI: `10.1126/sciadv.adg9213`.

Liu, Xingcheng, Kyoko N. Matsukage, Yu Nishihara, Toshihiro Suzuki, and Eiichi Takahashi (2019). “Stability of the hydrous phases of Al-rich phase D and Al-rich phase H in deep subducted oceanic crust”. In: *American Mineralogist* 104, pp. 64–72. DOI: `10.2138/am-2019-6559`.

Lyubutin, I. S., C. R. Lin, Yu V. Korzhetskiy, T. V. Dmitrieva, and R. K. Chiang (2009). “Mössbauer spectroscopy and magnetic properties of hematite/magnetite nanocomposites”. In: *Journal of Applied Physics* 106. DOI: `10.1063/1.3194316`.

Mao, W., M. Gurnis, and W. Wu (2022). “On the Origin of Small-Scale Seismic Scatters at 660-km Depth”. In: *Geochemistry, Geophysics, Geosystems* 23. DOI: `10.1029/2022GC010560`.

Mao, Z., S. D. Jacobsen, F. Jiang, J. R. Smyth, C. M. Holl, and T. S. Duffy (2008). “Elasticity of hydrous wadsleyite to 12 GPa: Implications for Earth’s transition zone”. In: *Geophysical Research Letters* 35.21. DOI: `10.1029/2008GL035618`.

Mao, Zhu, Jung-Fu Lin, Jing Yang, Toru Inoue, and Vitali B. Prakapenka (2015). “Effects of the Fe^{3+} spin transition on the equation of state of bridgmanite”. In: *Geophysical Research Letters* 42, pp. 4335–4342. DOI: `10.1002/2015GL064400`.

Mashino, Izumi, Motohiko Murakami, and Eiji Ohtani (2016). “Sound velocities of δ-AlOOH up to core-mantle boundary pressures with implications for the seismic anomalies in the deep mantle”. In: *Journal of Geophysical Research, Solid Earth* 121, pp. 595–609. DOI: `10.1002/2015JB012477`.

McNamara, A.K. (2019). “A review of large low shear velocity provinces and ultra low velocity zones”. In: *Tectonophysics* 760, pp. 199–220. DOI: `10.1016/j.tecto.2018.04.015`.

McNamara, A.K., E.J. Garnero, and S. Rost (2010). "Tracking deep mantle reservoirs with ultra-low velocity zones". In: *Earth and Planetary Science Letters* 299, pp. 1–9. DOI: `10.1016/j.epsl.2010.07.042`.

Meer, Douwe G. van der, Douwe J.J. van Hinsbergen, and Wim Spakman (2018). "Atlas of the underworld: Slab remnants in the mantle, their sinking history, and a new outlook on lower mantle viscosity". In: *Tectonophysics* 723, pp. 309–448. DOI: `10.1016/j.tecto.2017.10.004`.

Meier, Thomas, Florian Trybel, Saiana Khandarkhaeva, Dominique Laniel, Takayuki Ishii, Alena Aslandukova, Natalia Dubrovinskaia, and Leonid Dubrovinsky (2022). "Structural independence of hydrogen-bond symmetrisation dynamics at extreme pressure conditions". In: *Nature Communications* 13, pp. 1–8. DOI: `10.1038/s41467-022-30662-4`.

Momma, Koichi and Fujio Izumi (2011). "VESTA 3 for three-dimensional visualization of crystal, volumetric and morphology data". In: *Journal of Applied Crystallography* 44.6, pp. 1272–1276. DOI: `10.1107/S0021889811038970`.

Morrison, Rachel A., Jennifer M. Jackson, Wolfgang Sturhahn, Dongzhou Zhang, and Eran Greenberg (2018). "Equations of State and Anisotropy of Fe-Ni-Si Alloys". In: *Journal of Geophysical Research: Solid Earth* 123. DOI: `10.1029/2017JB015343`.

Mukhopadhyay, Sujoy (2012). "Early differentiation and volatile accretion recorded in deep-mantle neon and xenon". In: *Nature* 486, pp. 101–104. DOI: `10.1038/nature11141`.

Mukhopadhyay, Sujoy and Rita Parai (2019). "Noble gases: A record of earth's evolution and mantle dynamics". In: *Annual Review of Earth and Planetary Sciences* 47, pp. 389–419. DOI: `10.1146/annurev-earth-053018-060238`.

Murakami, M., K. Hirose, H. Yurimoto, S. Nakashima, and N. Takafuji (2002). "Water in Earth's Lower Mantle". In: *Science* 295, pp. 1885–1888. DOI: `10.1126/science.1065998`.

Murakami, Motohiko, Kei Hirose, Katsuyuki Kawamura, Nagayoshi Sata, and Yasuo Ohishi (2004). "Post-Perovskite Phase Transition in $MgSiO_3$". In: *Science* 304, pp. 855–858. DOI: `10.1126/science.1095932`.

Nakagawa, Takashi and Paul J. Tackley (2015). "Geochemistry, Geophysics, Geosystems". In: *Geochemistry Geophysics Geosystems* 16.1, pp. 267–300. DOI: `10.1002/2014GC005701`.

Newcombe, M. E., S. G. Nielsen, L. D. Peterson, J. Wang, C. M.O.D. Alexander, A. R. Sarafian, K. Shimizu, L. R. Nittler, and A. J. Irving (2023). "Degassing of early-formed planetesimals restricted water delivery to Earth". In: *Nature* 615, pp. 854–857. DOI: `10.1038/s41586-023-05721-5`.

Ni, Sidao and Don V. Helmberger (2003). “Seismological constraints on the South African superplume: Could be the oldest distinct structure on earth”. In: *Earth and Planetary Science Letters* 206.1-2, pp. 119–131. DOI: `10.1016/S0012-821X(02)01072-5`.

Ni, Sidao, Eh Tan, Michael Gurnis, and Don Helmberger (2002). “Sharp sides to the African superplume”. In: *Science* 296.5574, pp. 1850–1852. DOI: `10.1126/science.1070698`.

Nishi, M., J. Tsuchiya, Y. Kuwayama, T. Arimoto, Y. Tange, Y. Higo, T. Hatakeyama, and T. Irifune (2019). “Solid Solution and Compression Behavior of Hydroxides in the Lower Mantle”. In: *Journal of Geophysical Research: Solid Earth* 124.10, pp. 10231–10239. DOI: `10.1029/2019JB018146`.

Nishi, Masayuki, Yasuhiro Kuwayama, Jun Tsuchiya, and Taku Tsuchiya (2017). “The pyrite-Type high-pressure form of FeOOH”. In: *Nature* 547.7662, pp. 205–208. DOI: `10.1038/nature22823`.

Nishi, Masayuki, Jun Tsuchiya, Takeshi Arimoto, Sho Kakizawa, Takehiro Kunimoto, Yoshinori Tange, Yuji Higo, and Tetsuo Irifune (2018). “Thermal equation of state of $MgSiO_4H_2$ phase H determined by in situ X-ray diffraction and a multianvil apparatus”. In: *Physics and Chemistry of Minerals* 45, pp. 995–1001. DOI: `10.1007/s00269-018-0980-z`.

Nomura, Ryuichi, Kei Hirose, Nagayoshi Sata, Yasuo Ohishi, Daisuke Suetsugu, Craig Bina, Toru Inoue, Douglas Wiens, and Mark Jellinek (2010). “Precise determination of post-stishovite phase transition boundary and implications for seismic heterogeneities in the mid-lower mantle”. In: *Physics of the Earth and Planetary Interiors* 183.1-2, pp. 104–109. DOI: `10.1016/j.pepi.2010.08.004`.

Oganov, Artem R. and Shigeaki Ono (2004). “Theoretical and experimental evidence for a post-perovskite phase of $MgSiO_3$ in Earth’s D" layer”. In: *Nature* 430, pp. 445–448. DOI: `10.1038/nature02701`.

Ohira, I., J.M. Jackson, N.V. Solomatova, W. Sturhahn, G.J. Finkelstein, S. Kamada, T. Kawazoe, F. Maeda, N. Hirao, S. Nakano, T.S. Toellner, A. Suzuki, and E. Ohtani (2019). “Compressional behavior and spin state of δ-(Al,Fe)OOH at high pressures”. In: *American Mineralogist* 104, pp. 1273–1284. DOI: `10.2138/am-2019-6913`.

Ohira, I., E. Ohtani, T. Sakai, M. Miyahara, N. Hirao, Y. Ohishi, and M. Nishijima (2014). “Stability of a hydrous δ-phase, AlOOH-$MgSiO_2(OH)_2$, and a mechanism for water transport into the base of lower mantle”. In: *Earth and Planetary Science Letters* 401, pp. 12–17. DOI: `10.1016/j.epsl.2014.05.059`.

Ohira, Itaru, Jennifer M. Jackson, Wolfgang Sturhahn, Gregory J. Finkelstein, Takaaki Kawazoe, Thomas S. Toellner, Akio Suzuki, and Eiji Ohtani (2021). “The influence of δ-(Al,Fe)OOH on seismic heterogeneities in Earth’s lower mantle”. In: *Scientific Reports* 11. DOI: `10.1038/s41598-021-91180-9`.

Ohtani, Eiji (2015). “Hydrous minerals and the storage of water in the deep mantle”. In: *Chemical Geology* 418, pp. 6–15. DOI: `10.1016/j.chemgeo.2015.05.005`.

– (2020). “The role of water in Earth’s mantle”. In: *National Science Review* 7, pp. 224–232. DOI: `10.1093/nsr/nwz071`.

Ohtani, Eiji, Konstantin Litasov, Akio Suzuki, and Tadashi Kondo (2001). “Stability field of new hydrous phase δ-AlOOH, for water transport into the deep mantle”. In: *Geophysical Research Letters* 28.20, pp. 3991–3993.

Ohtani, Eiji, Liang Yuan, Itaru Ohira, Anton Shatskiy, and Konstantin Litasov (2018). “Fate of water transported into the deep mantle by slab subduction”. In: *Journal of Asian Earth Sciences* 167, pp. 2–10. DOI: `10.1016/j.jseaes.2018.04.024`.

Omori, Soichi, Tetsuya Komabayashi, and Shigenori Maruyama (2004). “Dehydration and earthquakes in the subducting slab: Empirical link in intermediate and deep seismic zones”. In: *Physics of the Earth and Planetary Interiors* 146.1-2, pp. 297–311. DOI: `10.1016/j.pepi.2003.08.014`.

Palfey, W., G. Rossman, and W. Goddard (2021). “Structure, Energetics, and Spectra for the Oxygen Vacancy in Rutile: Prominence of the Ti-HO-Ti Bond”. In: *Journal of Physical Chemistry Letters* 12, pp. 10175–10181. DOI: `10.1021/acs.jpclett.1c02850`.

Palfey, W., G.R. Rossman, and W.A Goddard (2023). “Behavior of Hydrogarnet-Type Defects in Hydrous Stishovite at Various Temperatures and Pressures”. In: *Journal of Geophysical Research: Solid Earth*, 1–11. DOI: `10.1029/2022JB024980`.

Palot, M., S.D. Jacobsen, J.P. Townsend, F. Nestola, Marquardt K., N. Miyajima, J.W. Harris, T. Stachel, C.A. McCammon, and D.G. Pearson (2016). “Evidence for H_2O-bearing fluids in the lower mantle from diamond inclusion”. In: *Lithos* 265, pp. 237–243. DOI: `10.1016/j.lithos.2016.06.023`.

Panero, W. R., C. Thomas, R. Myhill, and J. S. Pigott (2020). “Dehydration Melting Below the Undersaturated Transition Zone”. In: *Geochemistry, Geophysics, Geosystems* 21. DOI: `10.1029/2019GC008712`.

Panero, Wendy R. and Razvan Caracas (2017). “Stability of phase H in the $MgSiO_4H_2$–AlOOH–SiO_2 system”. In: *Earth and Planetary Science Letters* 463, pp. 171–177. DOI: `10.1016/j.epsl.2017.01.033`.

Parai, R. and S. Mukhopadhyay (2015). “The evolution of MORB and plume mantle volatile budgets: Constraints from fission Xe isotopes in Southwest Indian Ridge basalts”. In: *Geochemistry Geophysics Geosystems* 16, pp. 719–735. DOI: `10.1002/2014GC005566`.

Parai, Rita and Sujoy Mukhopadhyay (2018). “Xenon isotopic constraints on the history of volatile recycling into the mantle”. In: *Nature* 560, pp. 223–227. DOI: `10.1038/s41586-018-0388-4`.

Pearson, D.G., F.E. Brenker, F. Nestola, J. McNeill, L. Nasdala, M.T. Hutchison, S. Matveev, K. Mather, G. Silversmit, S. Schmitz, B. Vekemans, and L. Vincze (2014). "Hydrous mantle transition zone indicated by ringwoodite included within diamond". In: *Nature* 507, pp. 221–224. DOI: `10.1038/nature13080`.

Peslier, Anne H., Maria Schönbächler, Henner Busemann, and Shun Ichiro Karato (2017). "Water in the Earth's Interior: Distribution and Origin". In: *Space Science Reviews* 212.1-2, pp. 743–810. DOI: `10.1007/s11214-017-0387-z`.

Piani, Laurette, Yves Marrocchi, Thomas Rigaudier, Lionel G Vacher, Dorian Thomassin, and Bernard Marty (2020). "Earth's water may have been inherited from material similar to enstatite chondrite meteorites." In: *Science* 369.6507, pp. 1110–1113. DOI: `10.1126/science.aba1948`.

Pisconti, Angelo, Neala Creasy, James Wookey, Maureen D. Long, and Christine Thomas (2023). "Mineralogy, fabric and deformation domains in D" across the southwestern border of the African LLSVP". In: *Geophysical Journal International* 232, pp. 705–724. DOI: `10.1093/gji/ggac359`.

Poirier, Jean-Paul (1994). "Light elements in the Earth's outer core: A critical review". In: *Physics of the Earth and Planetary Interiors* 85.3-4, pp. 319–337. DOI: `https://doi.org/10.1016/0031-9201(94)90120-1`.

Prescher, Clemens and Vitali B. Prakapenka (2015). "DIOPTAS: A program for reduction of two-dimensional X-ray diffraction data and data exploration". In: *High Pressure Research* 35, pp. 223–230. DOI: `10.1080/08957959.2015.1059835`.

Qin, Liping, Conel M.O.D. Alexander, Richard W. Carlson, Mary F. Horan, and Tetsuya Yokoyama (2010). "Contributors to chromium isotope variation of meteorites". In: *Geochimica et Cosmochimica Acta* 74.3, pp. 1122–1145. DOI: `10.1016/j.gca.2009.11.005`.

Ralph, R L and L W Finger (1982). "A Computer-Program for Refinement of Crystal Orientation Matrix and Lattice-Constants from Diffractometer Data with Lattice Symmetry Constraints". In: *Journal of Applied Crystallography* 15, pp. 537–539. DOI: `10.1107/S0021889882012539`.

Ranganathan, Meghana and Brent Minchew (2024). "A modified viscous flow law for natural glacier ice: Scaling from laboratories to ice sheets". In: *Proceedings of the National Academy of Sciences of the United States of America* 121.23, pp. 1–11. DOI: `10.1073/pnas.2309788121`.

Ricolleau, Angele, Yingwei Fei, Elizabeth Cottrell, Heather Watson, Liwei Deng, Li Zhang, Guillaume Fiquet, Anne Line Auzende, Mathieu Roskosz, Guillaume Morard, and Vitali Prakapenka (2009). "Density profile of pyrolite under the lower mantle conditions". In: *Geophysical Research Letters* 36.6, pp. 1–5. DOI: `10.1029/2008GL036759`.

Ritsema, J., S. Kaneshima, and S. Haugland (2020). “The dimensions of scatterers in the lower mantle using USArray recordings of S-wave to P-wave conversions”. In: *Physics of the Earth and Planetary Interiors* 306. DOI: `10.1016/j.pepi.2020.106541`.

Rochira, Federica, Lina Schumacher, and Christine Thomas (2022). “Mapping the edge of subducted slabs in the lower mantle beneath southern Asia”. In: *Geophysical Journal International* 230.2, pp. 1239–1252. DOI: `10.1093/gji/ggac110`.

Ross, Zachary E. and Elizabeth S. Cochran (2021). “Evidence for Latent Crustal Fluid Injection Transients in Southern California From Long-Duration Earthquake Swarms”. In: *Geophysical Research Letters* 48.12. DOI: `10.1029/2021GL092465`.

Rossman, G. R. (1996). “Studies of OH in nominally anhydrous minerals”. In: *Physics and Chemistry of Minerals* 23, pp. 299–304. DOI: `10.1007/BF00207777`.

Rüpke, Lars H., Jason Phipps Morgan, Matthias Hort, and James A.D. Connolly (2004). “Serpentine and the subduction zone water cycle”. In: *Earth and Planetary Science Letters* 223.1-2, pp. 17–34. DOI: `10.1016/j.epsl.2004.04.018`.

Russell, Stuart, Jessica C.E. Irving, Lisanne Jagt, and Sanne Cottaar (2023). “Evidence for a Kilometer-Scale Seismically Slow Layer Atop the Core-Mantle Boundary From Normal Modes”. In: *Geophysical Research Letters* 50.24. DOI: `10.1029/2023GL105684`.

Saki, Morvarid, Christine Thomas, and Rafael Abreu (2022). “Detection and modelling of strong topography of mid-mantle structures beneath the North Atlantic”. In: *Geophysical Journal International* 229.1, pp. 219–234. DOI: `10.1093/gji/ggab465`.

Sano, Asami, Eiji Ohtani, Tadashi Kondo, Naohisa Hirao, Takeshi Sakai, Nagayoshi Sata, Yasuo Ohishi, and Takumi Kikegawa (2008). “Aluminous hydrous mineral δ-AlOOH as a carrier of hydrogen into the core-mantle boundary”. In: *Geophysical Research Letters* 35, pp. 1–5. DOI: `10.1029/2007GL031718`.

Sano-Furukawa, Asami, Takanori Hattori, Kazuki Komatsu, Hiroyuki Kagi, Takaya Nagai, Jamie J. Molaison, António M. dos Santos, and Christopher A. Tulk (2018). “Direct observation of symmetrization of hydrogen bond in δ-AlOOH under mantle conditions using neutron diffraction”. In: *Scientific Reports* 8. DOI: `10.1038/s41598-018-33598-2`.

Sano-Furukawa, Asami, Hiroyuki Kagi, Takaya Nagai, Satatoshi Nakano, Satatoshi Fukura, Daichi Ushijima, Riko Iizuka, Eiji Ohtahtahtani, and Takehehiko Yagi (2009a). “Change in compressibility of δ-AlOOH and δ-AlOOD at high pressure: A study of isotope effect and hydrogen-bond symmetrization”. In: *American Mineralogist* 94, pp. 1255–1261. DOI: `10.2138/am.2009.3109`.

Sano-Furukawa, Asami, Hiroyuki Kagi, Takaya Nagai, Satoshi Nakano, Satoshi Fukura, Daichi Ushijima, Riko Iizuka, Eiji Ohtani, and Takehiko Yagi (2009b). “Change in compressibility of δ-AlOOH and δ-AlOOD at high pressure: A study of isotope effect and hydrogen-bond symmetrization". In: *American Mineralogist* 94, pp. 1255–1261.

Satta, Niccolò, Giacomo Criniti, Alexander Kurnosov, Tiziana Boffa Ballaran, Takayuki Ishii, and Hauke Marquardt (2024). " Elastic anomalies across the $P2_1mn$ –> Pnnm structural phase transition in δ-(Al,Fe)OOH ". In: *American Mineralogist* 109, pp. 1934–1944. DOI: `10.2138/am-2023-9129`.

Satta, Niccolò, Giacomo Criniti, Alexander Kurnosov, Tiziana Boffa Ballaran, Takayuki Ishii, and Hauke Marquardt (2021). "High-Pressure Elasticity of δ-(Al,Fe)OOH Single Crystals and Seismic Detectability of Hydrous MORB in the Shallow Lower Mantle". In: *Geophysical Research Letters* 48.23, pp. 1–10. DOI: `10.1029/2021GL094185`.

Scheller, E. L., B. L. Ehlmann, Renyu Hu, D. J. Adams, and Y. L. Yung (2021). "Long-term drying of Mars by sequestration of ocean-scale volumes of water in the crust". In: *Science* 372.6537, pp. 56–62. DOI: `10.1126/science.abc7717`.

Schmandt, Brandon, Steven D. Jacobsen, Thorsten W Becker, Zhenxian Liu, and Kenneth G. Dueker (2014). "Dehydration melting at the top of the lower mantle". In: *Science* 344, pp. 1265–1268. DOI: `10.1126/science.1253358`.

Schuberth, B. S.A. and H. P. Bunge (2009). "Tomographic filtering of high-resolution mantle circulation models: Can seismic heterogeneity be explained by temperature alone?" In: *Geochemistry, Geophysics, Geosystems* 10. DOI: `10.1029/2009GC002401`.

Schumacher, L. and C. Thomas (2016). "Detecting lower-mantle slabs beneath Asia and the Aleutians". In: *Geophysical Journal International* 205, pp. 1512–1524. DOI: `10.1093/gji/ggw098`.

Sheldrick, G.M. (1997). *SHELX-97*.

Shen, Guoyin, Yanbin Wang, Agnes Dewaele, Christine Wu, Dayne E. Fratanduono, Jon Eggert, Stefan Klotz, Kamil F. Dziubek, Paul Loubeyre, Oleg V. Fat'yanov, Paul D. Asimow, Tsutomu Mashimo, and Renata M.M. Wentzcovitch (2020). "Toward an international practical pressure scale: A proposal for an IPPS ruby gauge (IPPS-Ruby2020)". In: *High Pressure Research* 40.3, pp. 299–314. DOI: `10.1080/08957959.2020.1791107`.

Shinmei, Toru, Tetsuo Irifune, Jun Tsuchiya, and Ken-Ichi Funakoshi (2008). "Phase transition and compression behavior of phase D up to 46 GPa using multi-anvil apparatus with sintered diamond anvils". In: *High Pressure Research* 28, pp. 363–373.

Simons, Kyla, Jacqueline Dixon, Jean-Guy Schilling, Richard Kingsley, and Robert Poreda (2002). "Volatiles in basaltic glasses from the Easter-Salas y Gomez Seamount Chain and Easter Microplate: Implications for geochemical cycling of volatile elements". In: *Geochemistry, Geophysics, Geosystems* 3.7, pp. 1–29. DOI: `10.1029/2001gc000173`.

Smyth, Joseph R., Christopher M. Holl, Daniel J. Frost, Steven D. Jacobsen, Falko Langenhorst, and Catherine A. Mccammon (2003). “Structural systematics of hydrous ringwoodite and water in Earth’s interior”. In: *American Mineralogist* 88.10, pp. 1402–1407. DOI: `10.2138/am-2003-1001`.

Solomatova, Natalia V., Jennifer M. Jackson, Wolfgang Sturhahn, George R. Rossman, and Mathieu Roskosz (2017). “Electronic environments of ferrous iron in rhyolitic and basaltic glasses at high pressure”. In: *Journal of Geophysical Research: Solid Earth* 122, pp. 6306–6322. DOI: `10.1002/2017JB014363`.

Solomatova, Natalia V., Jennifer M. Jackson, Wolfgang Sturhahn, June K. Wicks, Jiyong Zhao, Thomas S. Toellner, Bora Kalkan, and William M. Steinhardt (2016). “Equation of state and spin crossover of (Mg,Fe)O at high pressure, with implications for explaining topographic relief at the core-mantle boundary”. In: *American Mineralogist* 101, pp. 1084–1093. DOI: `10.2138/am-2016-5510`.

Spasojevic, Sonja, Michael Gurnis, and Rupert Sutherland (2010). “Mantle upwellings above slab graveyards linked to the global geoid lows”. In: *Nature Geoscience* 3.6, pp. 435–438. DOI: `10.1038/ngeo855`.

Stevenson, DJ (1981). “Models of the Earth’s core”. In: *Science* 214.4521, pp. 611–619. DOI: `https://doi.org/10.1126/science.214.4521.611`.

Stixrude, Lars and Carolina Lithgow-Bertelloni (2005). “Thermodynamics of mantle minerals - I. Physical properties”. In: *Geophysical Journal International* 162, pp. 610–632. DOI: `10.1111/j.1365-246X.2005.02642.x`.

Strozewski, Benjamin, Johannes Buchen, Wolfgang Sturhahn, Takayuki Ishii, Itaru Ohira, Stella Chariton, Barbara Lavina, Jiyong Zhao, Thomas S Toellner, and Jennifer M Jackson (2023). “Equation of State and Spin Crossover of (Al,Fe)-Phase H”. In: *Journal of Geophysical Research : Solid Earth*, pp. 1–20. DOI: `10.1029/2022JB026291`.

Strozewski, Benjamin, Ojashvi Rautela, Johannes Buchen, Wolfgang Sturhahn, Takayuki Ishii, Itaru Ohira, Olivia Pardo, Barbara Lavina, Jiyong Zhao, Thomas S. Toellner, and Jennifer Jackson (2024). *Data supporting "Sound velocities of (Al,Fe)-phase H and the seismic visibility of dense oxyhydroxides in Earth’s lower mantle"*. Dataset. DOI: `10.22002/8v9yv-9mm73`.

Sturhahn, W. (2000). “CONUSS and PHOENIX: Evaluation of nuclear resonant scattering data”. In: *Hyperfine Interactions* 125.1-4, pp. 149–172. DOI: `10.1023/A:1012681503686`.

– (2022). *MINUTI (MINeral physics UTIlities)*. `http://www.nrixs.com`.

Sturhahn, Wolfgang (2021). “PHOENIX, version 3.0.4”. In: URL: `www.nrixs.com`.

Su, Xiaowan, Chaoshuai Zhao, Chaojia Lv, Yukai Zhuang, Nilesh Salke, Liangxu Xu, Hu Tang, Huiyang Gou, Xiaohui Yu, Qiang Sun, and Jin Liu (2021a). “The effect of iron on the sound velocities of δ-AlOOH up to 135 GPa”. In: *Geoscience Frontiers* 12.2, pp. 937–946. DOI: `10.1016/j.gsf.2020.08.012`.

Su, Xiaowan, Chaoshuai Zhao, Liangxu Xu, Chaojia Lv, Xitong Song, Takayuki Ishii, Yuming Xiao, Paul Chow, Qiang Sun, and Jin Liu (2021b). "Spectroscopic evidence for the Fe^{3+} spin transition in iron-bearing δ-AlOOH at high pressure". In: *American Mineralogist* 106.11, pp. 1709–1716. DOI: `10.2138/am-2021-7541`.

Sun, D., D. Helmberger, V. H. Lai, M. Gurnis, J. M. Jackson, and H. Y. Yang (2019). "Slab Control on the Northeastern Edge of the Mid-Pacific LLSVP Near Hawaii". In: *Geophysical Research Letters* 46, pp. 3142–3152. DOI: `10.1029/2018GL081130`.

Sun, Daoyuan, Don Helmberger, Meghan S. Miller, and Jennifer M. Jackson (2016). "Major disruption of D" beneath Alaska". In: *Journal of Geophysical Research: Solid Earth* 121.5, pp. 3534–3556. DOI: `10.1002/2015JB012534`.

Suzuki, A., E. Ohtani, and T. Kamada (2000). "A new hydrous phase δ-AlOOH synthesized at 21 GPa and 1000°C". In: *Physics and Chemistry of Minerals* 27.10, pp. 689–693. DOI: `10.1007/s002690000120`.

Suzuki, Akio (2010). "High-pressure X-ray diffraction study of ϵ-FeOOH". In: *Physics and Chemistry of Minerals* 37.3, pp. 153–157. DOI: `10.1007/s00269-009-0319-x`.

Takaichi, Goru, Yu Nishihara, Kyoko N. Matsukage, Masayuki Nishi, Yuji Higo, Yoshinori Tange, Noriyoshi Tsujino, and Sho Kakizawa (2024). "Limited stability of hydrous SiO_2 stishovite in the deep mantle". In: *Earth and Planetary Science Letters* 640. DOI: `10.1016/j.epsl.2024.118790`.

Tan, Eh, Michael Gurnis, and Lijie Han (2002). "Slabs in the lower mantle and their modulation of plume formation". In: *Geochemistry, Geophysics, Geosystems* 3, pp. 1–24. DOI: `10.1029/2001GC000238`.

Tan, Eh, Wei Leng, Shijie Zhong, and Michael Gurnis (2011). "On the location of plumes and lateral movement of thermochemical structures with high bulk modulus in the 3-D compressible mantle". In: *Geochemistry, Geophysics, Geosystems* 12, pp. 1–13. DOI: `10.1029/2011GC003665`.

Terasaki, H., E. Ohtani, T. Sakai, S. Kamada, H. Asanuma, Y. Shibazaki, N. Hirao, N. Sata, Y. Ohishi, T. Sakamaki, A. Suzuki, and K. Funakoshi (2012). "Stability of Fe-Ni hydride after the reaction between Fe-Ni alloy and hydrous phase (δ-AlOOH) up to 1.2Mbar: Possibility of H contribution to the core density deficit". In: *Physics of the Earth and Planetary Interiors* 194-195, pp. 18–24. DOI: `10.1016/j.pepi.2012.01.002`.

Thompson, E. C., A. J. Campbell, and J. Tsuchiya (2017). "Elasticity of ϵ-FeOOH: Seismic implications for Earth's lower mantle". In: *Journal of Geophysical Research: Solid Earth* 122, pp. 5038–5047. DOI: `10.1002/2017JB014168`.

Thompson, Elizabeth C., Anne H. Davis, Nigel M. Brauser, Zhenxian Liu, Vitali B. Prakapenka, and Andrew J. Campbell (2020). “Phase transitions in ϵ-FeOOH at high pressure and ambient temperature”. In: *American Mineralogist* 105, pp. 1769–1777. DOI: `10.2138/am-2020-7468`.

Toby, Brian H. and Robert B. Von Dreele (2013). “GSAS-II: The genesis of a modern open-source all purpose crystallography software package”. In: *Journal of Applied Crystallography* 46, pp. 544–549. DOI: `10.1107/S0021889813003531`.

Toellner, T. S. (2000). “Monochromatization of synchrotron radiation for nuclear resonant scattering experiments”. In: *Hyperfine Interactions* 125, pp. 3–28. DOI: `10.1023/A:1012621317798`.

Trinquier, A., J. L. Birck, C. J. Allègre, C. Göpel, and D. Ulfbeck (2008). “53Mn-53Cr systematics of the early Solar System revisited”. In: *Geochimica et Cosmochimica Acta* 72.20, pp. 5146–5163. DOI: `10.1016/j.gca.2008.03.023`.

Trybel, Florian, Thomas Meier, Biao Wang, and Gerd Steinle-Neumann (2021). “Absence of proton tunneling during the hydrogen-bond symmetrization in”. In: *Physical Review B* 104.10, pp. 1–6. DOI: `10.1103/PhysRevB.104.104311`.

Tschauner, O., S. Huang, E. Greenberg, V. B. Prakapenka, C. Ma, G. R. Rossman, A. H. Shen, D. Zhang, M. Newville, A. Lanzirotti, and K. Tait (2018). “Ice-VII inclusions in diamonds: Evidence for aqueous fluid in Earth’s deep mantle”. In: *Science* 359, pp. 1136–1139. DOI: `10.1126/science.aao3030`.

Tschauner, Oliver, Shichun Huang, Shuying Yang, Munir Humayun, Wenjun Liu, Stephanie N. Gilbert Corder, Hans A. Bechtel, Jon Tischler, and George R. Rossman (2021). “Discovery of davemaoite, $CaSiO_3$-perovskite, as a mineral from the lower mantle”. In: *Science* 374.6569, pp. 891–894. DOI: `10.1126/science.abl8568`.

Tsuchiya, Jun and Elizabeth C. Thompson (2022). “The role of hydrogen bonds in hydrous minerals stable at lower mantle pressure conditions”. In: *Progress in Earth and Planetary Science* 9. DOI: `10.1186/s40645-022-00521-3`.

Tsuchiya, Jun, Taku Tsuchiya, and Renata M. Wentzcovitch (2008). “Vibrational properties of δ-AlOOH under pressure”. In: *American Mineralogist* 93.2-3, pp. 477–482. DOI: `10.2138/am.2008.2627`.

Tsuchiya, T. (2011). “Elasticity of subducted basaltic crust at the lower mantle pressures: Insights on the nature of deep mantle heterogeneity”. In: *Physics of the Earth and Planetary Interiors* 188.3-4, pp. 142–149. DOI: `10.1016/j.pepi.2011.06.018`.

Tsuchiya, Taku (2003). “ First-principles prediction of the P-V-T equation of state of gold and the 660-km discontinuity in Earth’s mantle ”. In: *Journal of Geophysical Research: Solid Earth* 108, pp. 1–9. DOI: `10.1029/2003jb002446`.

Tsuchiya, Taku, Jun Tsuchiya, Koichiro Umemoto, and Renata M. Wentzcovitch (2004). “Phase transition in $MgSiO_3$ perovskite in the earth’s lower mantle”. In: *Earth and Planetary Science Letters* 224.3-4, pp. 241–248. DOI: `10.1016/j.epsl.2004.05.017`.

Tsutsumi, Yutaro, Naoya Sakamoto, Kei Hirose, Shoh Tagawa, Koichiro Umemoto, Yasuo Ohishi, and Hisayoshi Yurimoto (2024). “Retention of water in subducted slabs under core–mantle boundary conditions”. In: *Nature Geoscience* 17. DOI: `10.1038/s41561-024-01464-8`.

Turner, Stephen J. and Charles H. Langmuir (2022). “An Evaluation of Five Models of Arc Volcanism”. In: *Journal of Petrology* 63.3, pp. 1–25. DOI: `10.1093/petrology/egac010`.

Ulmer, Peter and Volkmar Trommsdorff (1995). “Serpentine stability to mantle depths and subduction-related magmatism”. In: *Science* 268.5212, pp. 858–861. DOI: `10.1126/science.268.5212.858`.

Umemoto, Koichiro, Katsuyuki Kawamura, Kei Hirose, and Renata M. Wentzcovitch (2016). “Post-stishovite transition in hydrous aluminous SiO_2”. In: *Physics of the Earth and Planetary Interiors* 255, pp. 18–26. DOI: `10.1016/j.pepi.2016.03.008`.

Van Der Hilst, R.D., S Widiyantorot, and E.R. Engdahl (1997). “Evidence for deep mantle circulation from global tomography”. In: *Nature* 386. DOI: `10.1038/386578a0`.

Walker, Richard J. (2009). “Highly siderophile elements in the Earth, Moon and Mars: Update and implications for planetary accretion and differentiation”. In: *Chemie der Erde* 69.2, pp. 101–125. DOI: `10.1016/j.chemer.2008.10.001`.

Wang, Biao, Johannes Buchen, Alba San José Méndez, Alexander Kurnosov, Giacomo Criniti, Hanns Peter Liermann, and Hauke Marquardt (2023). “Strong Effect of Stress on the Seismic Signature of the Post-Stishovite Phase Transition in the Earth’s Lower Mantle”. In: *Geophysical Research Letters* 50.10, pp. 1–9. DOI: `10.1029/2023GL102740`.

Wang, W. and Z. Wu (2022). “A first-principles study of water in wadsleyite and ringwoodite: Implication for the 520 km discontinuity”. In: *American Mineralogist* 107, pp. 1361–1368. DOI: `10.2138/am-2021-7929`.

Waszek, Lauren, Nicholas C. Schmerr, and Maxim D. Ballmer (2018). “Global observations of reflectors in the mid-mantle with implications for mantle structure and dynamics”. In: *Nature Communications* 9.1, pp. 1–13. DOI: `10.1038/s41467-017-02709-4`.

Wicks, J. K., J. M. Jackson, and W. Sturhahn (2010). “Very low sound velocities in iron-rich (Mg,Fe)O: Implications for the core-mantle boundary region”. In: *Geophysical Research Letters* 37.15, pp. 1–5. DOI: `10.1029/2010GL043689`.

Wicks, June K., Jennifer M. Jackson, Wolfgang Sturhahn, and Dongzhou Zhang (2017). “Sound velocity and density of magnesiowüstites: Implications for ultralow-velocity zone topography”. In: *Geophysical Research Letters* 44.5, pp. 2148–2158. DOI: `10.1002/2016GL071225`.

Wirth, R., C. Vollmer, F. Brenker, S. Matsyuk, and F. Kaminsky (2007). “Inclusions of nanocrystalline hydrous aluminium silicate "Phase Egg" in superdeep diamonds from Juina (Mato Grosso State, Brazil)”. In: *Earth and Planetary Science Letters* 259, pp. 384–399. DOI: `10.1016/j.epsl.2007.04.041`.

Wojdyr, Marcin (2010). “*Fityk*: a general-purpose peak fitting program”. In: *Journal of Applied Crystallography* 43.5, pp. 1126–1128. DOI: `10.1107/S0021889810030499`.

Wolf, J., M.D. Long, and D.A. Frost (2024). “Ultralow velocity zone and deep mantle flow beneath the Himalayas linked to subducted slab”. In: *Nature Geoscience* 17, pp. 302–308. DOI: `10.1038/s41561-024-01386-5`.

Workman, Rhea K. and Stanley R. Hart (2005). “Major and trace element composition of the depleted MORB mantle (DMM)”. In: *Earth and Planetary Science Letters* 231, pp. 53–72. DOI: `10.1016/j.epsl.2004.12.005`.

Wu, Ye, Xiang Wu, Jung Fu Lin, Catherine A. McCammon, Yuming Xiao, Paul Chow, Vitali B. Prakapenka, Takashi Yoshino, Shuangmeng Zhai, and Shan Qin (2016). “Spin transition of ferric iron in the NAL phase: Implications for the seismic heterogeneities of subducted slabs in the lower mantle”. In: *Earth and Planetary Science Letters* 434, pp. 91–100. DOI: `10.1016/j.epsl.2015.11.011`.

Xu, Weiming, Eran Greenberg, Gregory Kh Rozenberg, Moshe P. Pasternak, Elena Bykova, Tiziana Boffa-Ballaran, Leonid Dubrovinsky, Vitali Prakapenka, Michael Hanfland, Olga Yu Vekilova, Sergei I. Simak, and Igor A. Abrikosov (2013). “Pressure-induced hydrogen bond symmetrization in iron oxyhydroxide”. In: *Physical Review Letters* 111, pp. 1–5. DOI: `10.1103/PhysRevLett.111.175501`.

Xue, Xianyu, Masami Kanzaki, Hiroshi Fukui, Eiji Ito, and Takafumi Hashimoto (2006). “Cation order and hydrogen bonding of high-pressure phases in the Al_2O_3-SiO_2-H_2O system: An NMR and Raman study”. In: *American Mineralogist* 91.5-6, pp. 850–861. DOI: `10.2138/am.2006.2064`.

Yuan, Hongsheng, Li Zhang, Eiji Ohtani, Yue Meng, Eran Greenberg, and Vitali B. Prakapenka (2019). “Stability of Fe-bearing hydrous phases and element partitioning in the system MgO–Al_2O_3–Fe_2O_3–SiO_2–H_2O in Earth’s lowermost mantle”. In: *Earth and Planetary Science Letters* 524, p. 115714. DOI: `10.1016/j.epsl.2019.115714`.

Yuan, Y., D. Sun, W. Leng, and Z. Wu (2021). “Southeastward dipping mid-mantle heterogeneities beneath the sea of Okhotsk”. In: *Earth and Planetary Science Letters* 573. DOI: `10.1016/j.epsl.2021.117151`.

Zhang, Y., S. Fu, S.I. Karato, T. Okuchi, S. Chariton, V.B. Prakapenka, and J.F. Lin (2022). “Elasticity of Hydrated Al-Bearing Stishovite and Post-Stishovite: Implications for Understanding Regional Seismic V_S Anomalies Along Subducting Slabs in the Lower Mantle”. In: *Journal of Geophysical Research: Solid Earth* 127, pp. 1–16. DOI: `10.1029/2021JB023170`.

Zhou, Wen Yi, Jin S. Zhang, Quancheng Huang, Xiaojing Lai, Bin Chen, Przemyslaw Dera, and Brandon Schmandt (2022). “High pressure-temperature single-crystal elasticity of ringwoodite: Implications for detecting the 520 discontinuity and metastable ringwoodite at depths greater than 660 km”. In: *Earth and Planetary Science Letters* 579. DOI: `10.1016/j.epsl.2021.117359`.